Characterization of the Conformation and Internal Backbone Dynamics of α-Polyglucans by Pyrene Excimer Fluorescence

by

Damin Kim

A thesis

presented to the University of Waterloo

in fulfillment of the

thesis requirement for the degree of

Doctor of Philosophy

in

Chemistry

Waterloo, Ontario, Canada, 2021

Examining Committee Membership

The following served on the Examining Committee for this thesis. The decision of the Examining Committee is by majority vote.

External Examiner   Dr. Robert G. Gilbert
Professor
Centre for Nutrition and Food Science
The University of Queensland

Supervisor   Dr. Jean Duhamel
Professor
Chemistry
University of Waterloo

Internal Member   Dr. Mario Gauthier
Professor
Chemistry
University of Waterloo

Internal Member   Dr. Xiaosong Wang
Professor
Chemistry
University of Waterloo

Internal-external Member   Dr. Michael K.C. Tam
Professor
Chemical Engineering
University of Waterloo

Author's Declaration

I hereby declare that I am the sole author of this thesis. This is a true copy of the thesis, including any required final revisions, as accepted by my examiners.

I understand that my thesis may be made electronically available to the public.

Abstract

The conformation and internal backbone dynamics (IBD) of several pyrene-labeled polysaccharides (Py-PSs), namely Py-Amylopectin, Py-Glycogen, Py-Dextran, and Py-Pullulan, were successfully examined with a combination of pyrene excimer formation (PEF), fluorescence blob model (FBM) analysis of fluorescence decays, and molecular mechanics optimizations (MMOs). The four Py-PSs were investigated by analysing their fluorescence response resulting from the formation of an excimer upon encounter between an excited and a ground-state pyrene. The fluorescence parameters, namely the fluorescence intensity ratio of the excimer over the monomer, the I_E/I_M ratio, and the number (N_{blob}^{exp}) of anhydroglucose units (AGUs) found in the volume probed by an excited pyrene were determined from the analysis of the fluorescence spectra and decays of the Py-PS samples, respectively. MMOs conducted on Py-PS constructs built *in silico* with the program HyperChem yielded the theoretical number N_{blob}^{theo} of AGUs separating two pyrenyl labels, while still allowing for successful PEF. A satisfying match between N_{blob}^{theo} and N_{blob}^{exp} supported the selection of a given conformation of the macromolecule used to conduct the MMOs. These concepts were applied as follows.

At first, the compressibility of Py-Amylopectin and three pyrene-labeled Nanosized Amylopectin Fragments (Py-NAFs) with a hydrodynamic diameter (D_h) of 227, 56, 20, and 8 nm was investigated. PEF was applied to probe the changes in d_{h-h} as the side chains of amylopectin were compressed by adding unlabeled NAF(56) (NAF with $D_h = 56$ nm) to the Py-PSs dispersions to increase the [NAF(56)] from the dilute to the semi-dilute regime. I_E/I_M and N_{blob}^{exp} began to increase at a [NAF(56)] of 12 wt%, which was one order of magnitude larger than the overlap concentration. The magnitude of I_E/I_M and N_{blob}^{exp} as a function of [NAF(56)] increased with particle size, which suggested that the magnitude of the change in PEF was related to the size of

the clusters of helical side chains in the amylopectin interior. MMOs were conducted on a hexagonal close packed array of oligosaccharide helices to assess how $N_{\text{blob}}^{\text{theo}}$ would change as a function of $d_{\text{h-h}}$ and the size of a cluster of helices. By matching the $N_{\text{blob}}^{\text{exp}}$ values, obtained as a function of [NAF(56)], with the $N_{\text{blob}}^{\text{theo}}$ values, obtained as a function of $d_{\text{h-h}}$ and cluster size, a relationship was obtained between [NAF(56)] and $d_{\text{h-h}}$, which allowed the assignment of the number of helices per cluster. Py-Amylopectin, Py-NAF(56), Py-NAF(20), and Py-NAF(8) were found to be made of clusters constituted of 37, 37, 6, and 3 helices, respectively. Considering that all models aiming to describe amylopectin focus on the clusters of side chains found in the amylopectin interior, the methodology developed to determine the size of side chain clusters in amylopectin is expected to become an important analytical tool in the characterization of amylopectin.

Second, the combination of PEF, FBM, and MMOs was applied to investigate the density profile of the side chains across the interior of glycogen. Fluorescence Resonance Energy Transfer (FRET) experiments demonstrated that the pyrenyl pendants were distributed throughout the glycogen molecules. PEF experiments on two glycogen samples, that had been labeled with 1-pyrenebutyric acid (Py-Glycogen), yielded an $<N_{\text{blob}}^{\text{exp}}>$ value of 34 (± 2), which was higher than the $<N_{\text{blob}}^{\text{exp}}>$ value of 18 (± 1) for Py-Amylopectin. The increase in $<N_{\text{blob}}^{\text{exp}}>$ reflected the higher degree of branching of glycogen. MMOs yielded the relationship between $N_{\text{blob}}^{\text{theo}}$ and the local density of a glycogen molecule. Two density distributions based on the Melendez-Hevia model and the Gilbert model were considered to examine the interior of glycogen. According to the Melendez-Hevia model, glycogen is constituted of oligosaccharide branches, that are arranged in concentric tiers with the local density of side chains increasing from the inner to the outer tier. On the other hand, SAXS experiments indicated that the density is highest toward the center of a

glycogen particle, as predicted by the Gilbert model. Two density distributions of the local distribution of side chains in glycogen were considered based on both models. The parameters used to model these distributions were optimized to match $<N_{\text{blob}}^{\text{theo}}>$ with $<N_{\text{blob}}^{\text{exp}}>$. Both density distributions resulted in a good agreement between $<N_{\text{blob}}^{\text{theo}}>$ and $<N_{\text{blob}}^{\text{exp}}>$ as long as the side chains located in the interior of glycogen experienced a higher density. This study successfully established the PEF-based methodology to examine the density distribution of side chains constituting the interior of glycogen.

Finally, two linear polysaccharides adopting a random coil conformation in solution were examined. Dextran and pullulan were randomly labeled with 1-pyrenebutyric acid to yield Py-Dextran and Py-Pullulan, whose $N_{\text{blob}}^{\text{exp}}$ were found to equal 9.1 ($\pm$0.4) and 11 ($\pm$1), respectively. MMOs were carried out to determine $N_{\text{blob}}^{\text{theo}}$ for dextran and pullulan. The good agreement between $N_{\text{blob}}^{\text{theo}}$ and $N_{\text{blob}}^{\text{exp}}$ indicated that Py-Dextran and Py-Pullulan were randomly coiled in solution and that Py-Dextran was more extended than Py-Pullulan in DMSO. The IBD of these two polysaccharides were examined with the product $k_{\text{blob}} \times N_{\text{blob}}^{\text{exp}} \times l_{\text{SU}}$, where k_{blob} represents the rate constant for diffusive encounters between pyrene labels and l_{SU} is the length of a structural unit (SU). The $k_{\text{blob}} \times N_{\text{blob}}^{\text{exp}} \times l_{\text{SU}}$ values obtained for Py-Dextran and Py-Pullulan were compared to those obtained for a series of pyrene-labeled poly(oligo(ethylene glycol) methyl ether methacrylate)s (Py-PEG$_n$MAs), where n varied from 0 to 19. $k_{\text{blob}} \times N_{\text{blob}}^{\text{exp}} \times l_{\text{SU}}$ of the two polysaccharides was smaller than the $k_{\text{blob}} \times N_{\text{blob}}^{\text{exp}} \times l_{\text{SU}}$ value of a hypothetical Py-PEG$_n$MA sample having a SU with a same molar mass per backbone atom as the Py-PSs. The smaller $k_{\text{blob}} \times N_{\text{blob}}^{\text{exp}} \times l_{\text{SU}}$ product suggested that these polysaccharides had a more rigid backbone than the PEG$_n$MA samples, which was attributed to the cyclic nature of their SU. Comparison of the products $N_{\text{blob}}^{\text{exp}} \times l_{\text{SU}}$ and $k_{\text{blob}} \times N_{\text{blob}}^{\text{exp}} \times l_{\text{SU}}$ indicated that Py-Dextran was more extended and

dynamic than Py-Pullulan in DMSO. The more dynamic backbone of dextran was attributed to the more mobile α-(1,6) glycosidic bonds constituting the backbone of dextran.

In summary, this thesis represents the first example in the literature where PEF has been applied to characterize the conformation and IBD of such a wide variety of polysaccharides in solution. It has extended the realm of PEF applications to a new family of macromolecules and demonstrated the value of PEF-based methods to probe polysaccharides at the molecular level.

Acknowledgements

I want to sincerely express my deepest gratitude to my supervisor, Prof. Jean Duhamel, for being an outstanding role model as a scientist and as a supervisor. His way of treating students with respect and approaching a research problem with patience and determination has been a valuable life lesson.

I would like to thank my advisory committee members, Profs. Mario Gauthier, Michael Tam, and Xiaosong Wang for valuable discussions and advice regarding my research.

I would like to thank all my former and current lab members in the Duhamel and Gauthier groups for making the work environment joyful and having a positive influence.

I would like to thank the University of Waterloo, EcoSynthetix, and the Natural Sciences and Engineering Research Council of Canada (NSERC) for their financial support.

Finally, I would like to thank my family and friends for their unconditional support during my time at the University of Waterloo.

Dedication

To any scientists who find useful information in this thesis.

Table of Contents

List of Figures

List of Tables

List of Abbreviations

AFM	Atomic force microscopy
AGUs	Anhydroglucose units
BBBM	Building block backbone model
CL	Chain length
CLM	Cluster model
ECL	External chain length
FBM	Fluorescence *blob* model
FRET	Fluorescence resonance energy transfer
FT-IR	Fourier-transform infrared spectroscopy
GPC	Gel permeation chromatography
HCP	Hexagonal close packed
IBD	Internal backbone dynamics
ICL	Internal chain length
IRF	Instrument response function
Lm	Leuconostoc mesenteroides
MHS	Mark-Houwink-Sakurada
MMOs	Molecular mechanics optimizations
MW	Molecular weight
MWD	Molecular weight distribution
NAFs	Nanosized amylopectin fragments
NMR	Nuclear magnetic resonance
Np	Naphthalene
Np-Dextran	Naphthalene-labeled dextran
Np-Glycogen (O)	Naphthalene-labeled glycogen from oysters
PAMA	Poly(alkyl methacrylate)
PDI	Polydispersity index

PEF	Pyrene excimer fluorescence/formation
PEG	Poly(ethylene glycol)
PEG_nMA	Poly(oligo(ethylene glycol) methyl ether methacrylate)
PGA	Poly(*L*-glutamic acid)
PS	Polysaccharide
Py	Pyrene
Py-Amylopectin	Pyrene-labeled amylopectin
PyBA	1-Pyrenebutyric acid
Py-Dextran	Pyrene-labeled dextran
Py-Glycogen (C)	Pyrene-labeled glycogen from corn
Py-Glycogen (O)	Pyrene-labeled glycogen from oysters
Py-NAF	Pyrene-labeled nanosized amylopectin fragment
$Py-PEG_nMA$	Pyrene-labeled poly(oligo(ethylene glycol) methyl ether methacrylate)
Py-P*L*GAs	Pyrene-labeled poly(*L*-glutamic acid)s
Py-PS	Pyrene-labeled polysaccharide
Py-Pullulan	Pyrene-labeled pullulan
RBF	Round bottom flask
SAFM	Single molecule atomic force microscopy
SAXS	Small-angle X-ray scattering
SCL	Side chain length
SCLCP	Side chain liquid crystalline polymer
SI	Supporting information
Sol-CL	Solution cluster model
SU	Structural unit
TRF	Time-resolved fluorescence
UV-Vis	Ultraviolet-visible

List of Symbols

a	Mark-Houwink-Sakurada exponent
C*	Overlap concentration
D	Diffusion coefficient
D*	Poorly-stacked pyrene dimers
Da	Dalton
D_h	Hydrodynamic diameter
d_{h-h}	Distance separating two helical oligosaccharide side chains
DP_n	Number-average degree of polymerization
DP_{stub}	Number of glucose units in a stub
$E0$*	Well-stacked pyrene dimers
ES*	Short-lived pyrene excimer species
f_{diff}	Molar fraction of pyrenes forming Py_{k2}* via diffusion in solution
f_{E0}	Molar fraction of aggregated pyrenes in solution
f_{Ediff}	Molar fraction of pyrene species in an excimer decay, which form Py_{k2}* by diffusion
f_{EE0}	Molar fraction of pyrene species in an excimer decay, which are properly stacked and form an excimer $E0$* quasi-instantaneously upon direct excitation
f_{EES}	Molar fraction of pyrene species in an excimer decay, which yield short-lived ground-state aggregates ES*
f_{Ek2}	Molar fraction of pyrene species in an excimer decay, which form excimer with a rapid rate constant k_2
f_{free}	Molar fraction of isolated pyrenes in solution
f_{k2}	Molar fraction of pyrenes forming excimer via rapid arrangement
f_{Mdiff}	Molar fraction of pyrene species in a monomer decay, which form Py_{k2}* by diffusion
f_{Mfree}	Molar fraction of pyrene species in a monomer decay, which do not form excimer

f_{Mk2}	Molar fraction of pyrene species in a monomer decay, which form excimer with a rapid rate constant k_2
g	Branching factor
H_{total}	Total number of helices constituting a cluster of helices
I_{340}	Fluorescence intensity at 340 nm
I_{379}	Fluorescence intensity at 379 nm
I_E	Fluorescence intensity of the pyrene excimer
I_M	Fluorescence intensity of the pyrene monomer
k_{-1}	Dissociation rate constant of pyrene excimer
k_1	Rate constant for diffusive encounters between an excited and a ground-state pyrene
k_2	Rate constant of excimer formation by fast arrangement between an excited and a ground-state pyrene
k_{blob}	Rate constant for the formation of $Py_{k2}*$ between one excited and one ground-state pyrene inside a same *blob*
L	Path length of a quartz cuvette for absorption measurements
l_{SU}	Length of a structural unit
M	Molar mass
M_n	Number-average molecular weight
M_v	Viscosity-average molecular weight
M_w	Weight-average molecular weight
$<n>$	Average number of pyrenes per *blob*
N_A	Avogadro's number
n_{bb}	Number of atoms in a structural unit
N_{blob}	Number of monomer units encompassed within a blob
N_{blob}^{exp}	Experimentally determined N_{blob}
N_{blob}^{theo}	Theoretically determined N_{blob}
$N_{blob,\text{internal}}^{theo}$	Theoretically determined N_{blob} for an internal helix
$N_{blob,\text{side}}^{theo}$	Theoretically determined N_{blob} for a side helix in a HCP array

$N_{blob,\text{corner}}^{theo}$	Theoretically determined N_{blob} for a corner helix in a HCP array
$N_{\text{blob}}^{theo}(t)$	Theoretically determined N_{blob} for the tth tier of a glycogen molecule
$< N_{\text{blob}}^{theo} >$	Theoretically determined N_{blob} for a glycogen molecule comprised of t tiers
n_{L}	Number of atoms in the contour length
Py_{agg}^{*}	Aggregated pyrenes
Py_{diff}^{*}	Pyrenes diffusing in the solution according to the motion of the SU, to which they are bound
Py_{free}^{*}	Isolated pyrenes
Py_{k2}^{*}	Pyrenes forming excimer with a rate constant k_2
$[Py]_{\text{loc}}$	Local pyrene concentration
r	Degree of branching
R	Particle radius
R_0	Förster radius
r_{EE}	End-to-end distance
R_{g}	Radius of gyration
R_{h}	Hydrodynamic radius
t	Number of tiers
tt	Tier thickness
V_{h}	Hydrodynamic volume
α	Sector of a helix that forms excimer inter-helically (Chapter 2)
β	β-Amylase (Chapter 1)
β	Sector of a helix that only forms excimer intra-helically (Chapter 2)
ε	Molar extinction coefficient
φ	Relative orientation of a helix with respect to the x-axis
ϕ, φ	Torsion angles
ϕ	Fluorescence quantum yield
ϕ	Refers to Phosphorylase a (Chapter 1)
η	Viscosity

$[\eta]$	Intrinsic viscosity
λ	Wavelength
λ_{em}	Emission wavelength
λ_{ex}	Excitation wavelength
λ_{Py}	Pyrene content
ω	Torsion angle
θ	Angle between the x-axis and the line joining the centers of helices
ρ	Density
τ_0	Natural lifetime of a dye
τ_E	Fluorescence lifetime of a pyrene excimer
τ_M	Fluorescence lifetime of an excited pyrene monomer

Chapter 1

Literature Review

1.1 Introduction

Polysaccharides are the most abundant natural biopolymers on earth and are used in two main types of applications, namely for energy storage and structural support.[1] For instance, dextran and pullulan are linear polysaccharides used in structural applications, whereas amylopectin and glycogen are branched polysaccharides used for energy storage. The structure of polysaccharides has been characterized at the molecular level by determining the type of glycosidic bonds connecting their structural units and their chain length, in an effort to better understand their properties. The term glucan refers to polysaccharides whose structural unit is a glucose molecule.[2] Dextran, pullulan, amylose, amylopectin, and glycogen are examples of polyglucans and their chemical structure is shown in Figure 1.1. Although they share a same monomeric unit, other structural features distinguish them from each other. For example, amylose is a linear polyglucan, that is composed of anhydroglucose units (AGUs) joined by α-(1,4) glycosidic bonds, while dextran is made of AGUs joined by α-(1,6) glycosidic bonds. The nature of the glycosidic bonds has important implications on the properties of a given polysaccharide. In the case of dextran and amylose, the difference in glycosidic bonds is the reason why amylose is poorly soluble in water while dextran is water-soluble. In turn, the water-solubility of dextran enables its use as a blood plasma expander.[3] In contrast, the AGUs of pullulan are linked to each other by a mixture of α-(1,4) and α-(1,6) glycosidic bonds in a 2:1 ratio. Consequently, a variety of techniques, that include Atomic Force Microscopy (AFM),[4] computational simulations,[5,6] and nuclear magnetic resonance (NMR)[7] have been applied to examine the effects, that the different types and contents of glycosidic bonds have on the properties of amylose, dextran, and pullulan.

The structure of the branched polyglucans is also quite varied as they exhibit different degrees of branching and side chain lengths,[8] which lead to different properties. The side chains of amylopectin can be 20-25 AGUs-long,[8] long enough to form double helices in the crystalline domains generated by amylopectin in the solid state. The average side chain length of glycogen is about half that of amylopectin,[8] which prevents side chain crystallization and the formation of double helices.[9] Beside the ability of the side chains of branched polysaccharides to crystallize or not, their architectural variations also lead to surprisingly important differences in their properties. For instance, the longer side chains of amylopectin, which induce the formation of double helices, result in the poor solubility of amylopectin in water compared to glycogen, which is water-soluble thanks to its shorter side chains, that cannot crystallize. In turn, the inability to produce glycogen with short side chains can lead to glycogen storage disease,[10] since abnormally long side chains form insoluble double helices, which cannot be degraded into glucose.[10]
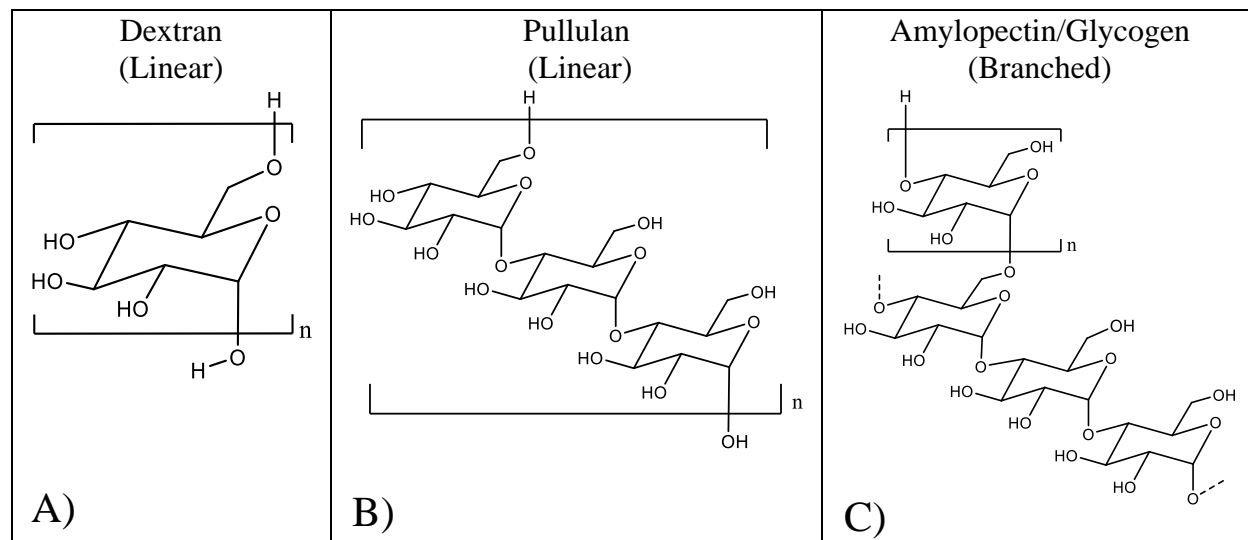
Figure 1.1 Chemical structure of polysaccharides. A) Dextran, B) pullulan, and C) amylopectin/glycogen

The various properties of polysaccharides resulting from their different structures mean that the techniques to characterize the parameters defining the different physical properties of a given polysaccharide need to be tailored for that specific polysaccharide. For instance, the ability of some polysaccharides like amylopectin to crystallize enables their study in the solid state by X-ray diffraction.[11] Of course, X-ray diffraction is of little use for polysaccharides like glycogen,[12] that do not crystallize. Similarly, gel permeation chromatography (GPC) is a powerful technique to characterize the molecular weight distribution (MWD) of polymers. In a GPC experiment, a polymer solution is injected into a column packed with porous beads, that separate the different polymer molecules according to their hydrodynamic volume (V_h). GPC is thus very useful to determine the MWD of all polysaccharides, except amylopectin, whose hydrodynamic diameter (D_h) is typically in the hundreds of nm, larger than the size limit of the pores in GPC column beads reported to exclude macromolecules of D_h greater than 100 nm.[13]

These considerations explain why the characterization of polysaccharides relies heavily on a wide range of analytical techniques capable of probing macromolecules at different length scales. In this context, pyrene excimer fluorescence/formation (PEF) would be a nice addition to this battery of techniques due to its is well-known ability to probe the conformation and internal backbone dynamics (IBD) of macromolecules at the molecular level over a length scale of a few nanometers. In particular, it has been used to characterize the IBD of a series of pyrene-labeled poly(alkyl methacrylate)s[14] and polypeptides[15] and the random coil[16] and helical[16,17] conformation of several polypeptides. While PEF has been recently applied to confirm the helical conformation of amylose in DMSO[18] and determine the inter-helical distance of clusters of helices for amylopectin in solution,[19] its application to the study of polyglucans remains fairly limited. The

goal of this thesis is thus to generalize the applicability of PEF to the study of polyglucans by expanding its realm of applications beyond amylose and amylopectin to glycogen, dextran, and pullulan. Consequently, this chapter will provide a general overview of polyglucans focusing mainly on dextran, pullulan, glycogen, and amylopectin, which will be followed by an introduction on PEF and how it can be applied to probe polyglucans.

1.2 sic Structural Elements of α-Polyglucans.

Polyglucans or glucans are polysaccharides, that are most widespread in nature and whose structural unit is D-glucose.[2] Polyglucans are further divided into α– or β–glucans depending on whether the C1-hydroxyl of D-glucose in a chair conformation is in the axial or equatorial position, respectively (see Figure 1.2).
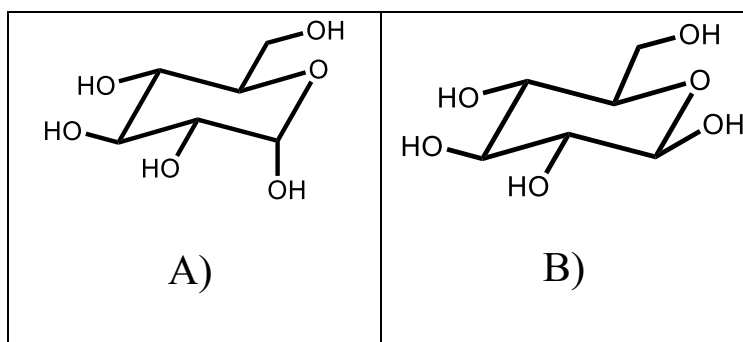
Figure 1.2. Structure of A) α-D-glucose and B) β-D-glucose

Examples of α–glucans include starch (amylose and amylopectin), pullulan, dextran, and glycogen. In comparison, cellulose is an example of β–glucan. This section will mainly focus on α–glucans. Although all α–glucans are constituted of a same D-glucose structural unit (SU), the large number of functional groups afforded by this SU leads to a wide range of spatial placements for AGUs with respect to each other, which is associated with a wide range of structures and thus categories of polyglucans, that have been identified based on their type of glycosidic bond, chain length, or

degree of branching. The glucose unit, glycosidic bond type, and chain length of α–glucans will be briefly discussed in this section.

1.1.1 Structural Unit

Acid hydrolysis is commonly used to depolymerize polyglucans into glucose. The reaction conditions, including the strength and amount of acid, must account for the type of polyglucan being considered and the purpose of the experiment.[20] For instance, dilute acid conditions or insufficient reaction times result in the partial acid hydrolysis of a polyglucan into oligosaccharides instead of glucose monomers.[21,22] Complete acid hydrolysis of polyglucans involves the treatment of the polysaccharides with either 2~3 % sulfuric acid for 4-6 hours[23,24] or 1 M HCl for 40-120 minutes at temperatures higher than 100 $^{\circ}$C.[25,26] Completion of the acid hydrolysis of polysaccharides can be assessed by monitoring the anomeric glucose carbon, whose signal can be identified by Nuclear Magnetic Resonance (NMR),[27] Fourier-Transform Infrared spectroscopy (FT-IR),[28] and optical rotation,[24] depending on whether glucose is characterized as the SU of a polysaccharide or an individual molecule.

1.1.2 Glycosidic Bonds

Glucose has five hydroxyl groups available for conducting a condensation reaction. Methylation can be applied to identify the hydroxyls in a given polysaccharide, that are involved in glycosidic linkages.[29] The general reaction scheme of methylation is shown in Figure 1.3. Since any hydroxyl group not involved in glycosidic linkages can be methylated, this procedure allows the identification of the types of hydroxyls involved in glycosidic linkages. The methylation can be monitored by FT-IR over time to determine its completion.[2] It is then followed by acid hydrolysis

to depolymerize the polysaccharide into methylated monosaccharides, whose chemical composition can be identified by gas chromatography and mass spectrometry.
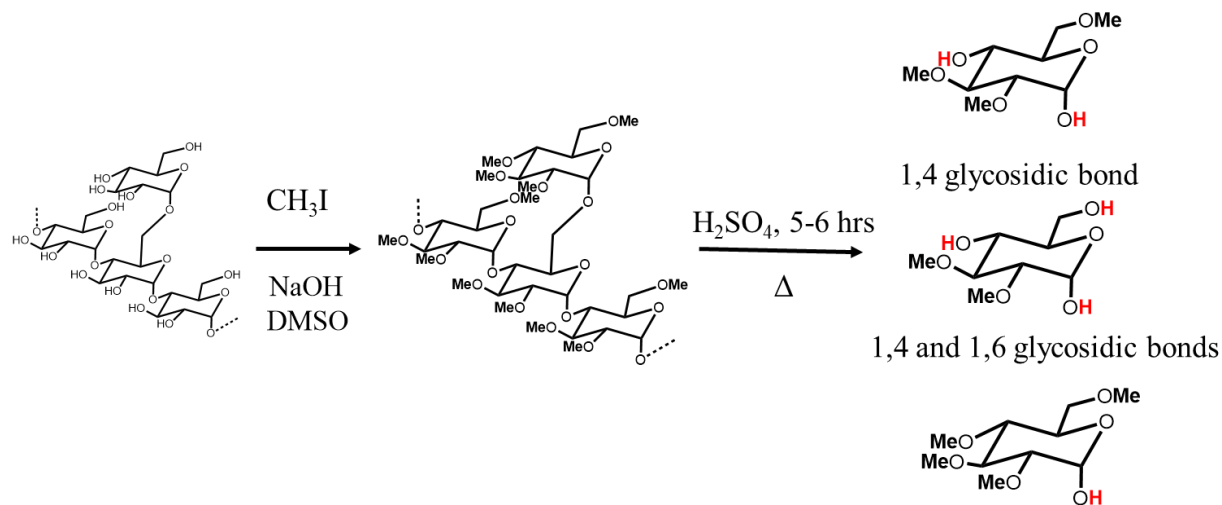
Figure 1.3. Reaction scheme for the methylation of a branched α-glucan followed by acid hydrolysis.

As one example of this methodology, the major product for the methylation of water-soluble dextran was identified as 2,3,4-tri-O-methyl-D-glucose, which indicated that the C1- and C6-hydroxyls are involved in the formation of α−(1,6) glycosidic bonds. Consequently, this result suggested that the AGUs in dextran are joined by α−(1,6) glycosidic bonds to generate a linear polysaccharide.[30,31] However, dimethyl glucoses such as 2,3-di-O-methyl-D-glucose, 2,4-di-O-methyl-D-glucose, or 3,4-di-O-methyl-D-glucose were also found, whose functionality of 3 implied the existence of branching points involving either α−(1,2), α−(1,3), or α−(1,4) glycosidic linkages. Since the population of 2,4-di-O-methyl-D-glucose is higher than the other dimethyl glucoses, it was concluded that the branches of dextran are mostly the result of α−(1,3) glycosidic linkages.[30,31] In contrast, the complete methylation of amylose only gave 2,3,6-tri-O-methyl-D-

glucose, which demonstrated that amylose is a linear polyglucan, whose AGUs are joined by α−(1,4) glycosidic linkages.[32] In the case of pullulan, the glycosidic linkage pattern of pullulan was not determined by acid hydrolysis, but rather from an enzymatic treatment with pullulanase,[33] followed by complete methylation.[34] Pullulanase is an enzyme, that cleaves α−(1,6) glycosidic linkages.[35] The hydrolysis of pullulan with pullulanase produced the trisaccharide maltotriose as the major product, with the tetrasaccharide maltotetraose representing up to 7% of the final product.[33,34,36] Since the proportion of maltotetraose in pullulan is low, pullulan is generally considered to be a polymaltotriose.[37] the methylation of maltotriose yielded 32 % methyl 2,3,4-tri-O-methyl-D-glucose and 67 % methyl 2,3,6-tri-O-methyl-D-glucose, which confirmed that three AGUs are linked by two α−(1,4) glycosidic bonds to form maltotriose, whereas the maltotriose units are linked by α−(1,6) glycosidic linkages.[34]

1.3. Structure and Conformation of α−Polyglucans
1.3.1. Dextran
1.3.1.1. *Chemical Structure of Dextran*
Dextran is a polysaccharide produced by lactic acid bacteria, such as *Leuconostoc mesenteroides* (*Lm*).[38] The AGUs of dextran are mostly joined by α-(1,6) glycosidic bonds.[39] However, branched dextran has been found, where the type of glycosidic linkage for the branching points and the degree of branching depend on the bacterial strains.[40] In the case of dextran produced by *Lm* B-512F, the AGUs are mainly linked by α-(1,6) glycosidic bonds with branches being generated by α-(1,3) glycosidic bonds.[41–43] Branching via α-(1,2) or α-(1,4) glycosidic bonds has also been observed for dextran produced from *Lm* B-742 [41,44] and *Lm* B-1299, [40,41] respectively. The lowest degree of branching equal to 2 % was reported for dextran produced by *Lm* FT 045B, whereas *Lm*

B-1501 produces dextran with the highest degree of branching reported to equal 50%.[41] Branches in dextran are typically one or two AGUs long.[30,45] Consequently, since branches with one or two AGUs should yield a dextran sample, that behaves as a linear polysaccharide, the finding, that some dextran samples behave like branched polymers, suggests the existence of some longer branches.[46]

Jeanes et al. classified dextran samples into three groups based on their percentage of α-(1,3) glycosidic bonds.[39] Classes A, B, and C have been defined for dextrans containing 0-2%, 3-6% and > 6% of α-(1,3) glycosidic bonds, respectively. Class A and B dextrans are water-soluble, whereas dextrans from Class C with a percentage of α-(1,3) glycosidic bonds higher than 43 % are water-insoluble.[47] Dextran with a higher percentage of α-(1,6) glycosidic bonds is commonly used as a blood plasma expander, since α-(1,6) glycosidic bonds are hydrolyzed more slowly than other glycosidic bonds and such dextran samples are more water-soluble. The optimal molecular weight (MW) for dextran used as blood plasma expander is 40,000-100,000 Da.[48] Dextran with a higher MW is not suitable for clinical purposes, as it prolongs the bleeding time by interfering with blood coagulation. However, it can be used as a food ingredient in bakery.[38] Furthermore, since α-(1,2) glycosidic bonds show a high resistance to hydrolysis by digestive enzymes,[49] dextrans with α-(1,2) glycosidic bonds could be beneficial to microorganisms in the human gut. As a matter of fact, low molecular weight dextrans with branches generated by α-(1,2) glycosidic bonds have been shown to exhibit prebiotic effects in continuous gut models.[49]

1.3.1.2. Conformation of Dextran in Dilute Solution

The conformation in solution and degree of branching of dextran have been investigated by specific optical rotation,[50] intrinsic viscosity,[21,51] and small-angle X-ray scattering (SAXS) measurements.[52] The random coil conformation of dextran was confirmed by specific optical rotation in DMSO.[50.] The specific optical rotation of dextran was investigated in the absence and presence of tetramethylurea, which is a hydrogen bonding disruptor. The addition of tetramethylurea to an amylose dispersion in DMSO caused a decrease in the specific optical rotation of amylose from 166° to 151° by disrupting intra-molecular hydrogen bonding in amylose, whereas a constant specific optical rotation of 190° was observed for dextran.[50] This result suggested that dextran is a random coil while amylose adopts a helical conformation in DMSO.

The conformation of macromolecules can also be predicted from the exponent (*a*) of the Mark-Houwink-Sakurada (MHS) relationship given in Equation 1.1 between the intrinsic viscosity ($[\eta]$) of a macromolecule and its viscosity-average molecular weight (M_v). A polymer with a random coil conformation in a good or θ-solvent is expected to have an *a* value ranging from 0.5 to 0.8, which can increase to ~2 and decrease to 0 if the shape of a macromolecule approaches that of a rigid rod or a hard sphere, respectively.[53]

$$[\eta] = K M_v^a \tag{1.1}$$

A plot of $\log[\eta]$ as a function of $\log(MW)$ for dextran in water yielded a straight line for molecular weight (MW) values lower than ~10 kDa with a slope equal to 0.50, which represented the MHS exponent.[54] The MHS exponent of dextran in DMSO[21,51] and DMF/water mixtures[55] was found to equal 0.51~0.53 and 0.51, respectively. These exponents led to the conclusion, that dextran with a

low MW adopts a random coil conformation in solution. The $\log[\eta]$-*vs*-$\log(MW)$ relationship was found to deviate from linearity by showing a downward trend at higher MW's, for which higher degrees of branching were obtained.[54,56] As a result, the *a* exponent decreased below 0.5.[54,56] The mathematical expression of the factor *g*, reflecting the reduction in radius of gyration (R_g) for a branched macromolecule compared to the R_g of a linear chain of equivalent MW, is shown in Equation 1.2.[57] Due to its definition, *g* decreases with increasing degree of branching. *g* was determined as a function of MW for dextran to characterize its degree of branching.

$$g = \frac{R_g^2(branched)}{R_g^2(linear)} \qquad (1.2)$$

To determine *g*, R_g was determined by light scattering for a series of dextran samples. Using Equation 1.3 to represent the R_g of linear dextran,[56] the *g* value of dextran was found to decrease from 0.94 to 0.75 as the MW of dextran increased from 11 to 253 kDa, respectively, which suggested that the degree of branching increases with increasing MW.[52]

$$R_g^2(linear) = 0.19 \times MW^{0.56} \qquad (1.3)$$

In summary, low MW dextran is a mostly linear polysaccharide made of AGUs connected by α-(1,6) glycosidic bonds. Higher MW dextran shows branching points generated by α-(1,3) glycosidic bonds, whose branching frequency increases with increasing MW. In solution, dextran adopts a random coil conformation.

1.3.2. Pullulan

1.3.2.1. Chemical Structure and Conformation of Pullulan in Dilute Solution

Pullulan is made of maltotriose units, which are trisaccharides, where the AGUs are joined by α-(1,4) glycosidic bonds, and where the maltotriose units are connected by α-(1,6) glycosidic bonds.[58] The conformation of pullulan in solution was investigated by intrinsic viscosity measurements and its MHS values are summarized in Table 1.1. The exponent *a* was higher than 0.5 but lower than 0.8 in water and DMSO, which indicated that pullulan adopts a random coil conformation in solution.

Table 1.1. Mark-Houwink-Sakurada (MHS) parameters reported for pullulan in the literature.

Solvent	Temperature, ºC	K, mL/g	a	Reference
0.02 wt% NaN$_3$ in water	25	0.035	0.61	Nishinari [59]
0.02 wt% NaN$_3$ in water	25	0.032	0.63	Kawahara 1984 [60]
0.2 wt% NaN$_3$ in water	25	0.022	0.66	Kato 1982 [61]
0.02 wt% NaN$_3$ in water	25	0.019	0.67	Kato 1984 [62]
DMSO	21	0.016	0.75	Pavlov 1998 [63]
0.5 wt% LiBr in DMSO	50	0.020	0.69	Isenberg 2010 [64]
0.5 wt% LiBr in DMSO	80	0.024	0.68	Sullivan 2014 [65]

Since the AGUs of pullulan are linked by α-(1,4) and α-(1,6) glycosidic bonds in a 2:1 ratio, pullulan has been compared with amylose and dextran, whose AGUs are connected by α-(1,4) and α-(1,6) glycosidic linkages, respectively. The additional torsion angle ω available to an α-(1,6) glycosidic bond provides extra conformational freedom compared to an α-(1,4) glycosidic bond, for which the two torsion angles φ and ϕ are available.[66] Based on this argument, polysaccharides should experience increased conformational freedom according to the sequence dextran > pullulan > amylose. Unfortunately, amylose is a special case as it adopts a helical conformation in DMSO

as was observed by pyrene fluorescence,[18] NMR, [67] and intrinsic viscosity [68] measurements. Intramolecular hydrogen bonding between the C2- and C3-hydroxyls of amylose may be responsible for the helical conformation of amylose.[67] Pullulan on the other hand is randomly coiled in solution due to the heterogeneity of its glycosidic linkages,[69] which is responsible for the good solubility of pullulan in water and some organic solvents such as DMSO and DMF.[58] Dextran is also a random coil in solution. The backbone of pullulan has been found to be less and more mobile than that of dextran[70] and amylose,[71] respectively. The flexibility of pullulan in water has been examined by computational simulations,[5,6] SAXS,[52,72] and intrinsic viscosity and sedimentation[73] measurements. The persistence lengths of pullulan and dextran were simulated by fixing the torsion angle ω to equal either $\pm\,60°$, $180°$, or with a torsional function. The persistence length of dextran was found to increase from 0.6 to 1.3 nm, while the persistence length of pullulan changed from 1.3 nm to 1.2 nm, as a torsional function was applied instead of a fixed torsion angle. The experimentally determined persistence length of pullulan[72,73] and dextran[52] were found to be between 1.0 and 1.9 nm and between 2.0 and 2.8 nm, respectively. It should be noted that the persistence length of dextran was found to decrease with increasing MW as the degree of branching increased.[52] The persistence length of 2.8 nm corresponded to a dextran sample with a MW of 11,200 g/mol, which should be short enough to have a linear structure with little to no branches.[74] The shorter persistence length of pullulan suggested that the backbone of pullulan is less extended than the backbone of dextran.

1.3.3. Enzymes Used to Degrade Branched Polyglucans

Enzymes have been instrumental in assessing whether polysaccharides are linear or branched. For instance, the fact that amylose was completely hydrolyzed by α-amylase was taken as evidence

that amylose is a non-branched linear polysaccharide.[75,76] In contrast, amylopectin and glycogen cannot be completely hydrolyzed by α-amylase, which reflects their branched structure. The stepwise depolymerization of polysaccharides by multiple enzymes is required to study the structural units of branched polyglucans. In particular, the size distribution of the side chains of branched polyglucans has been characterized by applying a stepwise enzymatic treatment to these polysaccharides. The enzymes that have been most widely used to hydrolyze polysaccharides and their mode of action are summarized in Table 1.2.

Table 1.2. List of enzymes used to depolymerize polysaccharides.

Enzyme	Function	Attack Features
α-amylase	Hydrolysis of α−(1,4) glycosidic bonds (Endo acting)	- In the first stage, the hydrolysis with α-amylase generates oligosaccharides consisting of 6-10 AGUs, which are hydrolyzed further into sugars at the second stage of the α-amylase treatment.[77] - End products vary depending on the origin of amylase.[77]
β-amylase	Hydrolysis of α−(1,4) glycosidic bonds (Exo acting)	- Generates maltosyl, maltotriosyl residues.[77]
Phosphorylase a	Phosphorolysis of α−(1,4) glycosidic bonds	- Phosphorolysis leaves 4 and 3 glycosyl units on the A and B chains of branched polysaccharides, respectively.[78] - Generates glucose-1-phosphate.
Isoamylase	Hydrolysis of *non terminal* α−(1,6) glycosidic bonds[77] (endo acting)	- It can debranch amylopectin and glycogen but not pullulan.[79] - It works only if the chain contains more than 3 AGUs before the branching point.[80]
Amylo-1,6 glycosidase	Hydrolysis of *terminal* α−(1,6) glycosidic bonds (Exo acting)	- It can hydrolyze one glucose unit remaining on the A chain of branched polyglucans after treatment with phosphorylase a.[77]
Pullulanase	Hydrolysis of α−(1,6) glycosidic bonds	- The debranching efficiency is low for glycogen[81] - Pullulanase attacks short maltosyl chain stubs better than isoamylase.[82] - Hydrolysis works only if there are neighboring α−(1,4) glycosidic bonds.[83]

1.3.3.1. Side Chain Profiles of Branched Polyglucans

The structural features of branched polyglucans are often described in terms of chain type and chain length (*CL*). The chains found in branched polyglucans can be classified into A-, B-, and C-chains. A-Chains refer to unbranched chains, whereas B-chains are chains with branches. The C-chain is the chain carrying the sole reducing end and can be regarded as a B-chain.[84] Debranching enzymes such as isoamylase can hydrolyze a branch point and yield the unit chains, as shown in Figure 1.4. The average *CL* or unit *CL* can be determined by NMR,[85] methylation,[86] and periodate oxidation,[87] from which the population of non-reducing ends can be estimated. The average *CL* equals the total number of glucose molecules generated by the hydrolysis divided by the number of non-reducing ends. The complete methylation of a hydrolyzed polysaccharide produces tetra-O-methyl-D-glucose from the non-reducing group,[86] while periodate oxidation generates formic acid from its action on the non-reducing group.[87]

The *CL* can be further classified into internal (*ICL*) and external (*ECL*) chain lengths as shown in Figure 1.5. The *ICL* represents the number of AGUs present between two branching points in the interior of polyglucans. The *ECL* represents the number of AGUs from the chain end to the outermost branching point. B-Chains are represented by *ICL* and *ECL*, whereas A-chains are described by their *ECL* only. The determination of an *ECL* involves the enzymatic treatment with an exo-enzyme, which depolymerizes a polyglucan from its non-reducing chain end up to a certain number of AGUs from the branch point. The action of β-amylase[84] or phosphorylase a[78] on a branched polysaccharide leaves behind stubs comprised of 2 or 3.5 AGUs, respectively. A step-by-step hydrolysis of a polyglucan with phosphorylase a followed by treatment with β-amylase leaves 1.5 AGUs on average.[78] Assuming that the *CL* of an A-chain equals the *ECL* of a B-chain,

15

the *ECL* can be determined from Equation 1.4, where the *x*-limit represents the fraction of the branched polyglucan, that remains after hydrolysing the branched polyglucan with an enzyme that cannot digest $\alpha-(1,6)$ glycosidic bonds.[84] The *x*-limit is referred to as the β-, ϕ-, or β/ϕ-limit depending on whether the enzyme involved in the amylolysis is β-amylase, phosphorylase a, or a combination of β-amylase and phosphorylase a, respectively. DP_{stub} in Equation 1.4 represents the number of AGUs in a stub.

$$ECL = CL \times \frac{\% \, x - limit \, value}{100} + DP_{stub} \qquad (1.4)$$

In turn, the *ICL* can be calculated from Equation 1.5,[84] where one AGU is subtracted, since a branching point is not part of the external nor the internal chains.

$$ICL = CL - ECL - 1 \qquad (1.5)$$

The *CL* varies depending on the source of polyglucan. The average *CL* of amylopectin is about 20-25 AGUs, with the *ICL* and *ECL* containing 6-8 and 13-16 AGUs, respectively. The average *CL* of glycogen is about half that of amylopectin. The *ICL* and *ECL* of glycogen equal 3-5 AGUs and 6-8 AGUs, respectively, resulting in an overall *CL* of 10-14 AGUs.[8]
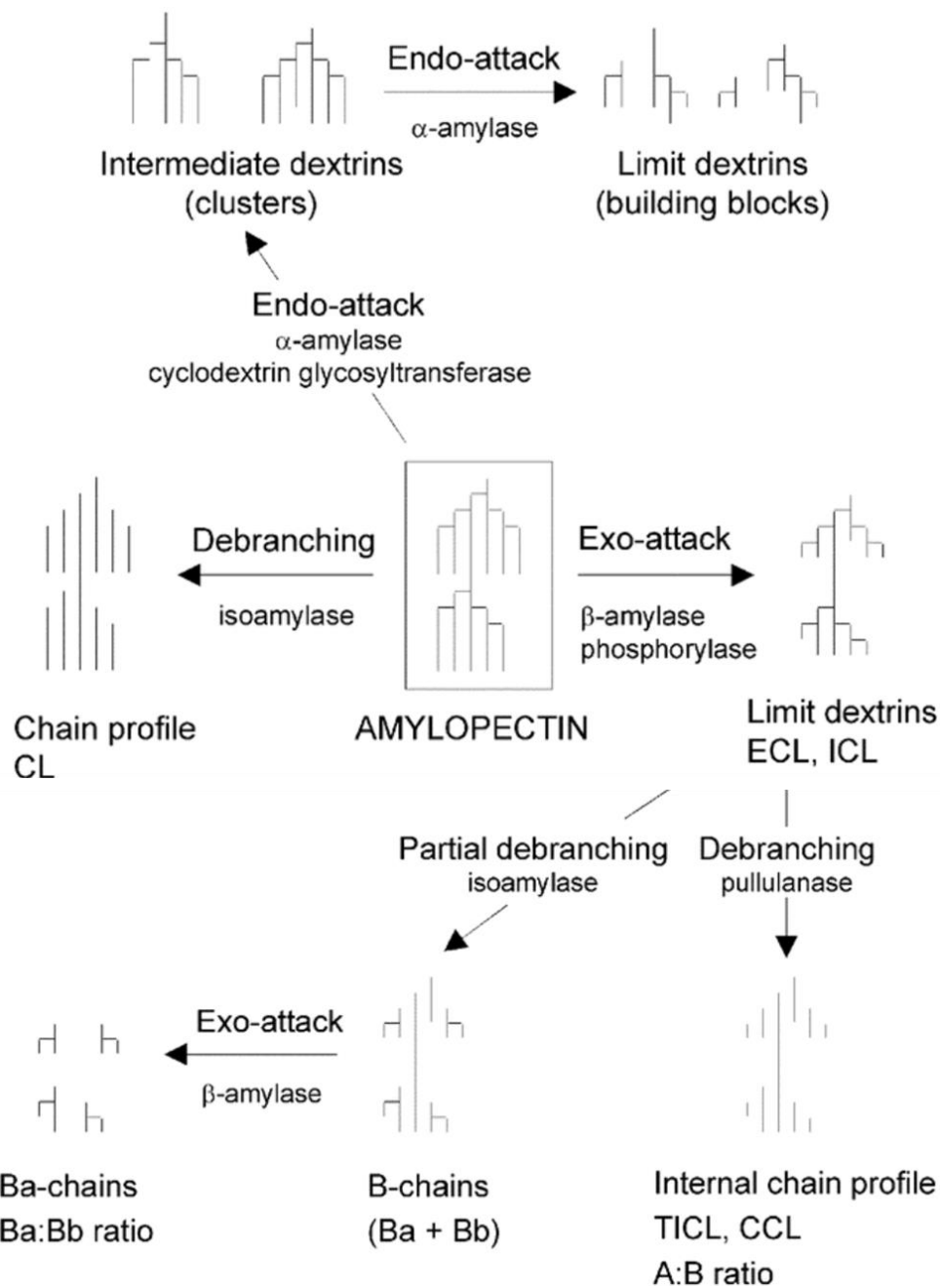
Figure 1.4. Principles of the structural study of branched polysaccharides with enzymatic hydrolysis. [Reprinted from *Starch in Food: Structure, Function and Applications*, 1, Bertoft, E. 2 – Analysing Starch Structure., 57-96, Copyright (2021), with permission from Elsevier. https://www.sciencedirect.com/science/article/pii/B9780081008683000020]
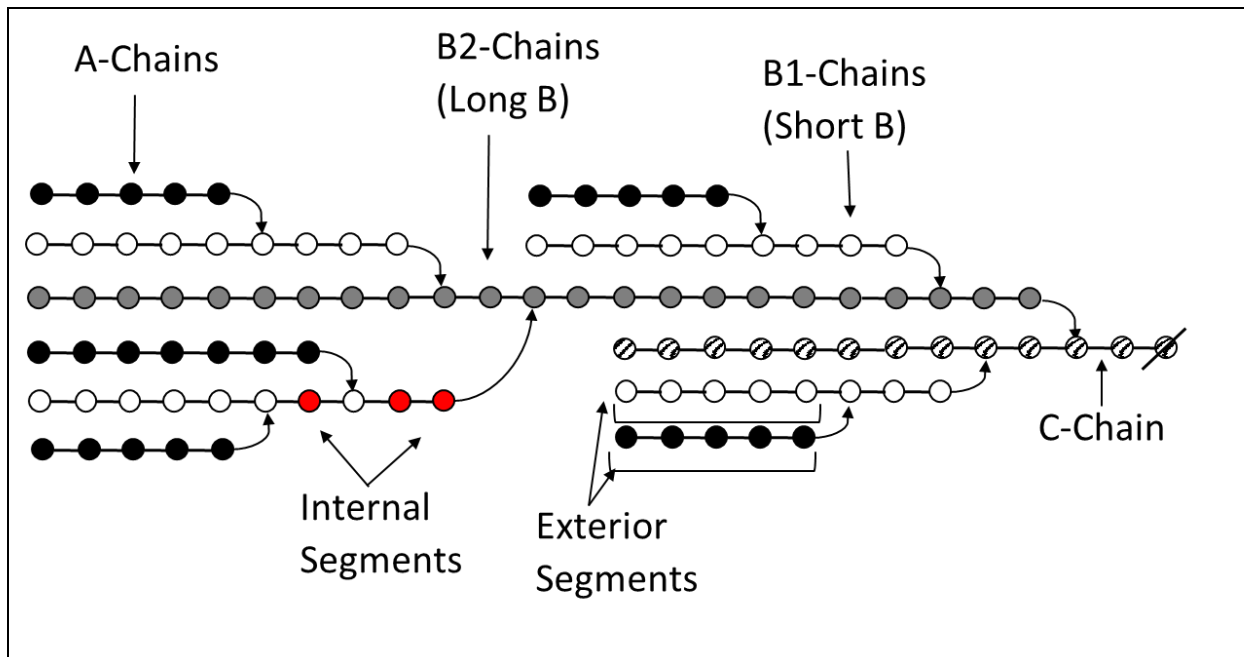
Figure 1.5. Definition of the different types of chains. AGUs are represented by circles (● in A-chain, ◔ in long B-chain, ○ in short B-chain, ◉ in C-chain) in a branched polyglucan. α-(1-4) and α-(1-6) linkages are expressed by horizontal lines and bent arrows, respectively. The reducing-end residue is the AUG at the most far-right. [Reprinted from *Starch/Stärke*, 62, Perez, S.; Bertoft, E. The Molecular Structures of Starch Components and Their Contribution to the Architecture of Starch Granules: A Comprehensive Review. 389-420, Copyright (2021), with permission from John Wiley and Sons. https://onlinelibrary.wiley.com/doi/abs/10.1002/star.201000013]

The A:B ratio estimates the degree of branching of polyglucans. The numbers of A- and B-chains are proportional to the number of sugars generated from the debranching of the limit-dextrin, which is the polyglucan fragment remaining after hydrolysis of a branched polysaccharide. For instance, β-amylolysis turns A-chains into stubs 2-3 AGUs long. The length of the A-chain stubs depends on the length of the original A-chain. If the original A-chain contains an odd or even number of AGUs, the A-chain stub would have three or two AGUs, respectively. On the other

18

hand, β-amylolysis of the B-chain generates stubs with 6 or more AGUs,[88] as described with the exo-attack by β-amylase/phosphorylase a in Figure 1.4. Debranching of the limit-dextrin generates maltose, maltotriose, and other oligosaccharides. The sum of the number of sugars and trisaccharides is proportional to the number of A-chains, while the number of oligosaccharides represents the number of B-chains. The A:B ratio can thus be determined from these experiments. The A:B ratios of amylopectin and glycogen have been reported to vary from 1.5:1.0 to 2.6:1.0 and from 0.6:1.0 to 1.2:1.0, respectively.[8] The B-chains of glycogen carry one or more A-chains, while the B-chains of amylopectin can carry only one A-chain. The A:B ratio indicates that the degree of branching is higher for glycogen than for amylopectin.

1.3.4.   Multiply Branched Polyglucans – Glycogen

1.3.4.1. The Tier Model for Glycogen

Glycogen was first discovered by Claude, who investigated its function in the liver as part of his doctoral thesis. The advancements made by Claude on glycogen were well-reviewed by Young.[89] Working with a dog, which had been fed a low-carbohydrate diet, Bernard Claude found that the blood sugar level was lower in the portal vein, bringing blood to the liver, than in the hepatic vein, which takes blood out of the liver. This observation led him to the conclusion that the liver could produce sugar, which was identified as glucose through several experiments including fermentation with yeast. In 1857, Claude successfully extracted the sugar-forming substance from livers and named it "la matière glycogène". Enzyme treatment with amylases indicated that glycogen is made of glucose, found under the form of AGUs mainly joined by α-(1,4) glycosidic bonds. Methylation of glycogen followed by acid hydrolysis resulted in the production of di-, tri-, and tetra-methyl glucose.[90,91] The dimethyl glucose derivatives were the methylation products of

the C2- and C3-hydroxyls, which suggested that branches are generated in glycogen by the formation of α-(1,6) glycosidic bonds. The branches of glycogen were accounted for by early structural modelling, which resulted in the proposals of a laminated and comb arrangement of the branches by Haworth (Figure 1.6 A)[90] and Staudinger (Figure 1.6B) in 1937,[8] respectively.
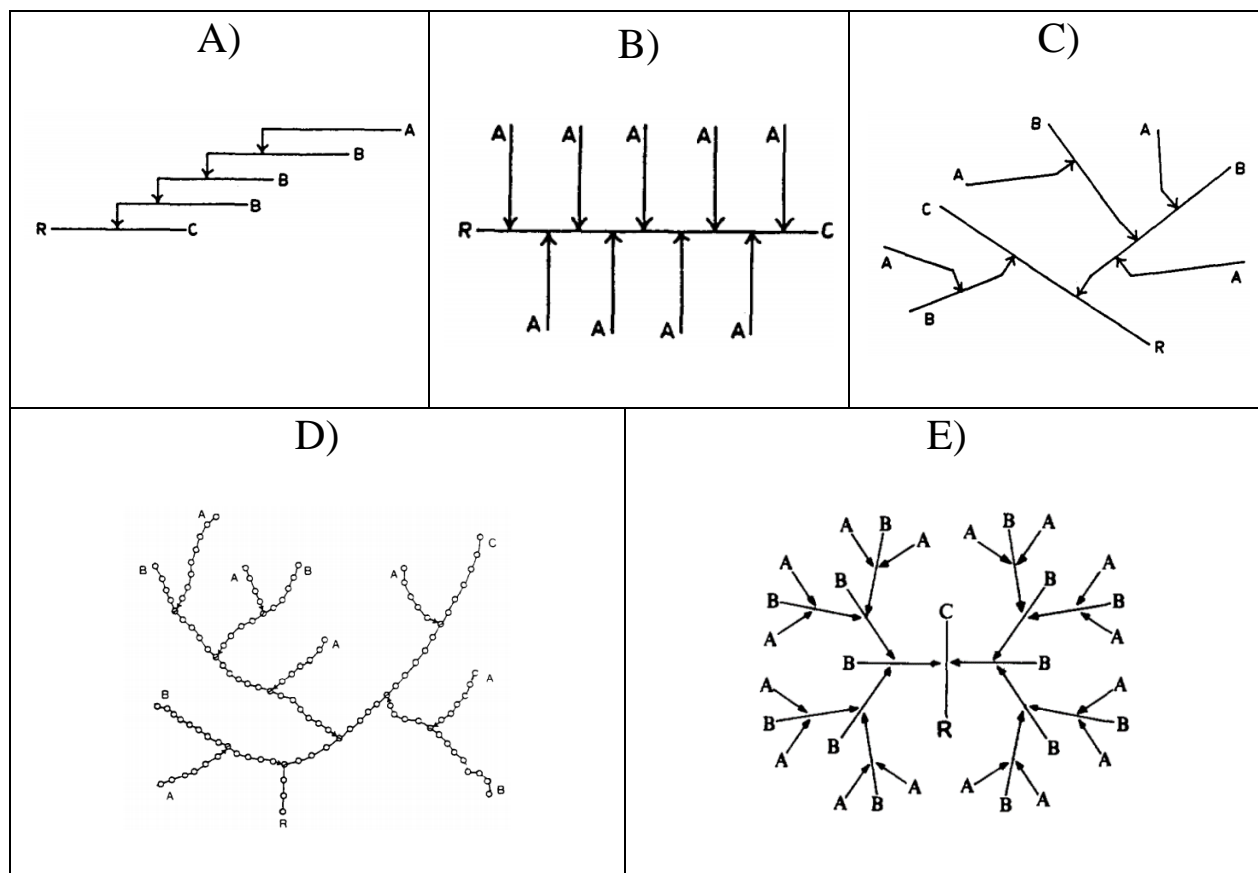
Figure 1.6. Proposed molecular arrangements for glycogen: (A) Laminated form proposed by Haworth.[90] (B) Comb form proposed by Staudinger.[8] (C) Tree form proposed by Meyer.[93] (D) Model of a segment of muscle glycogen based on its enzymatic degradation.[95] (E) Revised Meyer's tree form[88] [Reprinted from *Carbohydr. Polym.,* 16, Manners, D.J. Recent Developments in Our Understanding of Glycogen Structure., 37-82, Copyright (2021), with permission from Elsevier. https://www.sciencedirect.com/science/article/abs/pii/014486179190071J]

The laminated arrangement for the branches of glycogen is described as a singly branched structure. The comb arrangement suggests that glycogen is constituted of a single main chain with multiple branching points like a bottlebrush polymer.[92] Both Haworth's and Staudinger's proposals were based on the methylation method, which cannot distinguish between a singly or multiply branched structure. The tree form, with the multiply branched structure shown for glycogen in Figure 1.6C, was proposed by Meyer.[93] It was based on considerations regarding the ability of an end group generated by a branching enzyme to polymerize. When one end group created by a branching enzyme has a better affinity for polymerization, a singly branched structure will be obtained. A multiply branched structure is achieved when all the chain ends generated by branching enzymes have an equal chance at polymerization. A kinetic study of the chain growth of glycogen supported the latter case, which led to Meyer's tree-like model for glycogen.[94] Meyer's proposal was further supported by a stepwise enzymatic degradation of glycogen, where phosphorylase a and amylo-(1,6)-glucosidase were used to cleave α-(1,4) and α-(1,6) glycosidic bonds, respectively.[95] If glycogen adopted the laminated or comb form, its complete degradation would be achieved by the second enzymatic treatment of the ϕ-limit dextrin of glycogen. In contrast, the complete hydrolysis of glycogen with a multiply branched structure would require multiple repetitions of the enzymatic degradation by phosphorylase a followed by amylo-(1,6)-glucosidase. The first enzymatic treatment of glycogen with phosphorylase a yielded about 35% degradation of the original material, where further degradation was prevented by the branching points of glycogen. After the removal of the branching points with amylo-(1,6)-glucosidase, a second enzymatic treatment of the limit dextrin with phosphorylase a yielded an additional 25 % degradation instead of a complete degradation. This experiment confirmed that glycogen does not

have a singly branched structure. The enzymatic degradation needed to be repeated 3-4 times in order to reach 90% degradation of the original glycogen molecules. The multiply branched structure of glycogen based on Meyer's tree form viewed the branching points as being arranged in "tiers" (Figure 1.6D), where the number of branching points increases from the inner to the outer tier.

The tree form describes glycogen as a regularly branched structure, which may not be entirely valid when the molecular weight of glycogen increases. This complication arises with dendritic macromolecules, where the mass of the macromolecule increases much more quickly than its volume.[96] Meyer proposed the tree form using 178 glucose units, in which case glycogen has a regularly branched structure without experiencing any spatial congestion. The steric limitation on branching becomes significant as the size of glycogen increases. High molecular weights result in a densely packed periphery, which prevents further growth. Thus, the regularity in the branching of glycogen proposed by Meyer was not suitable for glycogen particles with a molecular weight larger than 20 million Daltons. Meyer's tree form with a regularly rebranched structure was revised by Whelan,[97] who introduced buried chains (Figure 1.6E). Some chains may be terminated deeper within the macromolecule, thereby allowing further growth of other chains.[8,98] According to this model, one half of the B-chains of glycogen carry two A-chains in average, while the other half carries two B-chains.

1.3.4.2. Self-Limitation of Size Growth of Glycogen

The highly branched compact structure of glycogen enables it to store the most glucose in the smallest possible volume. The large number of side chains present at the periphery increases the number of active sites for enzymes such as phosphorylase a and synthase. This allows living

animals to store or release glucose as efficiently as possible. According to the Tier Model initially proposed by Meyer,[93] the density of glycogen increases rapidly with its size. Beyond a certain critical point, the density at the periphery of glycogen particles becomes extremely high thus preventing any further growth, due to the inability of glycogen synthase to approach the macromolecule and bind to the active sites due to steric hindrance.[98,99] Madsen and Cori theoretically calculated the maximum number of tiers for glycogen and predicted that the area available for one glucose residue in the 13th tier would match the dimension of a glucose molecule, thus preventing access to much larger enzymes. [99] Goldsmith determined that the side chain of glycogen takes the form of a left-handed helix and studied the structure of glycogen with molecular modeling.[100] The thickness of a glycogen tier with side chains having a *CL* of 13 AGUs and a degree of branching of two would equal 1.9 nm according to that study. The average radius of a glycogen molecule, regardless of the source of glycogen, was determined to be about 21 nm corresponding to the size of a glycogen molecule made of 12 tiers, which was deemed to be the maximum number of tiers, that a glycogen particle could have. This conclusion was further supported by Meléndez-Heiva et al., who optimized the structure of glycogen mathematically.[101] The size (i.e. maximum number of tiers) of glycogen was simulated as a function of the number of AGUs in the side chains and the degree of branching. Glycogen with a degree of branching of 2 would maximize its glucose storing capability and have a total of 12 tiers with a radius of 21 nm. Glycogen with a degree of branching of 3 could only grow up to the 7th tier. The diameter of such a glycogen particle would be smaller than the diameter of glycogen molecules measured experimentally.

Although many studies have been conducted on glycogen, further evidence for the density-induced growth limit of glycogen has not been presented since the mathematical optimization of the glycogen structure by Meléndez-Heiva in 1993.[101] The most recent studies [102 - 104] and reviews[12,105,106] on glycogen have referred to Goldsmith's work published in 1982 for the self-limitation of size growth of glycogen. More detailed information about the interior of glycogen cannot be analyzed by X-ray crystallography due to its lack of crystallinity, despite the well-known ability of X-ray crystallography to probe the conformation of macromolecules in the solid state.[107] In fact, Kageyama et al. argued in a recent publication that *the internal structure of glycogen molecules is not fully understood*.[108] They suggested the use of fluorescence techniques, such as Fluorescence Resonance Energy Transfer (FRET), which are sensitive to the local density of a macromolecule over a length scale of a few nanometers, to get a deeper understanding of the structure of the interior of glycogen molecules.[12] These comments strongly suggest that further studies of the interior of glycogen would be of interest.

1.3.5. Multiply Branched Polyglucans – Amylopectin

Amylopectin is a major component of starch.[84] It is a branched polyglucan, whose branches are linear oligosaccharide segments, made of AGUs joined by $\alpha-(1,4)$ glycosidic bonds, linked to each other by $\alpha-(1,6)$ glycosidic bonds. Branching occurs every 20-25 AGUs, which results in the presence of 4-5 mol % of branching points per AGU in amylopectin.[84] As for glycogen, the spatial arrangement of the oligosaccharide side chains in the amylopectin interior has been the object of sustained research, which has led to several models.

1.3.5.1. The Cluster Model

The laminated and tree forms in Figures 1.6B and C were also considered as possible structural models for amylopectin. As for glycogen, enzyme treatment was instrumental in assigning the nature of the amylopectin interior. If amylopectin were in the laminated or tree form, the action of β-amylase on amylopectin would generate a very long chain or a more compact structure, respectively. In turn, if the β-limit dextrin took the form of a very long chain, acetylation of the β-limit dextrin followed by evaporation of the solvent would produce an elastic film, through the formation of entangled chains. Such an elastic film would not be achieved if the β-limit dextrin had a compact structure with side chains, that would be too short to entangle. In the end, the acetylated β-limit dextrin of amylopectin could not generate an elastic film, in the same manner that the acetylated β-limit dextrin of glycogen, which is a known branched polymer, could not form an elastic film. This result supported the notion that amylopectin is multiply branched and adopts a tree form as proposed by Meyer.[95] The tree form was further supported by a stepwise enzymatic degradation study.[95,109] The Cluster Model was proposed by French for amylopectin in 1972, based on experimental results that could not be rationalized by the tree form structure.[110] In particular, the viscosity of a KOH aqueous solution of an amylopectin sample with an M_n of 1.8×10^6 g/mol was much higher than a KOH aqueous solution of a glycogen sample with an M_n of 4.8×10^6 g/mol.[111] This result suggested that amylopectin does not have the same spherical shape as glycogen, and that its structure was thus better rationalized by the schematic representation shown in Figure 1.7A.[110]
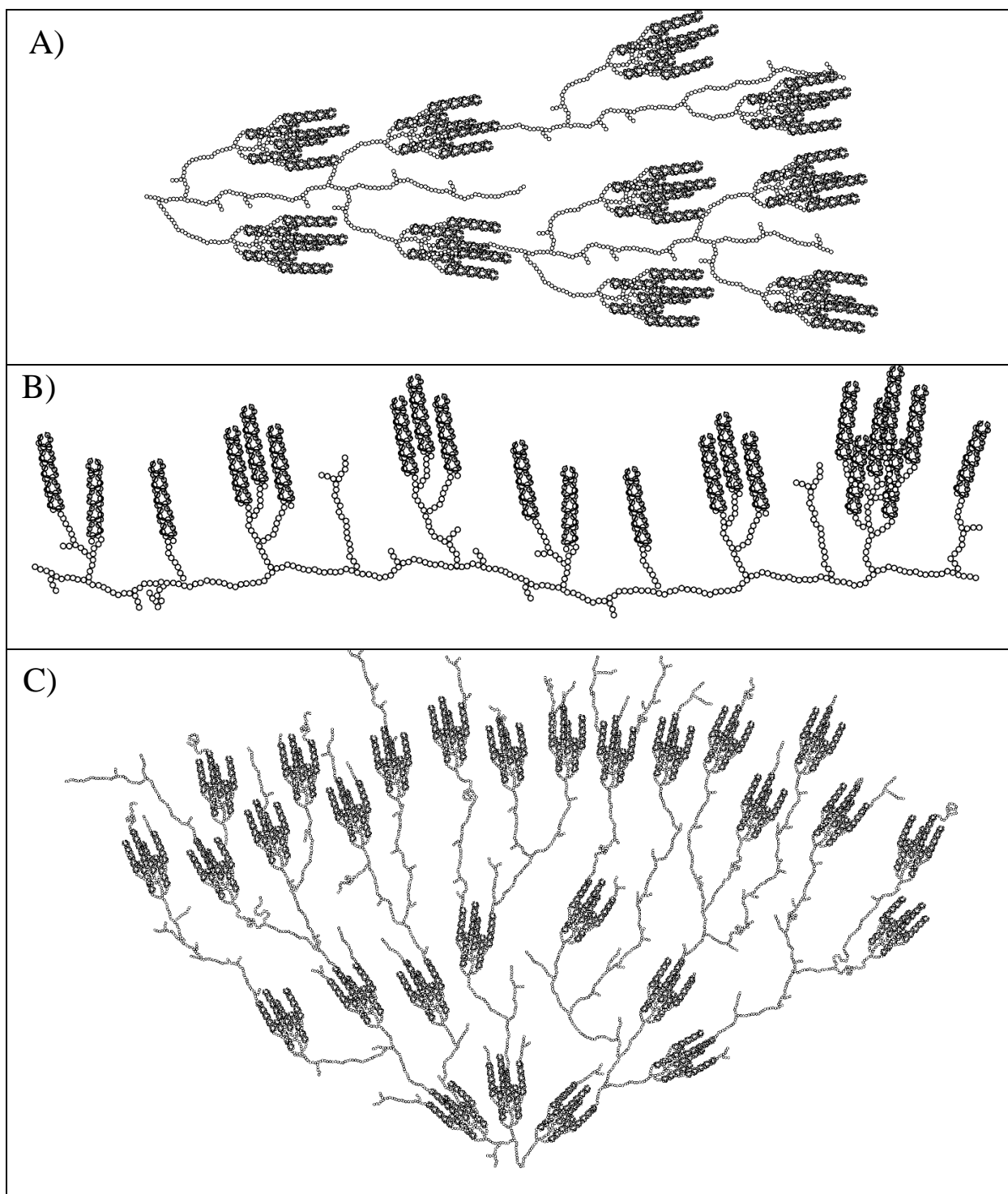
Figure 1.7. Illustration of the structure of amylopectin. (A) The traditional Cluster Model proposed by French for amylopectin in the solid state,[110] (B) the Building Block Backbone Model proposed by Bertoft,[118] and (C) the Solution Cluster Model proposed by Li et al. for amylopectin in solution.[19]

The incomplete acid hydrolysis of amylopectin suggested a heterogeneous environment made of amorphous and crystalline domains.[110] Later, SAXS experiments revealed that the periodic length of 9-10 nm found in the scattering pattern of amylopectin samples corresponded to lamellae generated in amylopectin by alternating amorphous and crystalline domains.[112] The structure of amylopectin was further investigated by characterizing the chain distribution profiles of the side chains obtained through the acid hydrolysis of amylopectin. Robin et al.[113] compared the chain distribution of native amylopectin from potato starch and its acid-resistant products. Since amorphous domains should be removed by the acid hydrolysis, the acid-resistant parts of amylopectin represented its crystalline domains. Debranching of a native amylopectin with pullulanase generated three groups of chains which had a *CL* of 15, 45, and > 60 AGUs.

The former two types of chains were also observed in the debranched acid-resistant part of amylopectin. The disappearance of the chain with a *CL* greater than 60 AGUs from the acid-resistant parts of amylopectin suggested that long chains with *CL* > 60 AGUs existed in the amorphous domains and were eliminated through the acid hydrolysis. The chains observed in both the native amylopectin sample and its acid-resistant parts were expected to be present in the crystalline domains. The chains, having a *CL* of ~15 AGUs corresponded to A-chains, which were involved into clusters of side chains and the chains having a *CL* of ~45 AGUs represented the chains connecting two clusters. Later on, Hizukuri reported that the *CL* profile for debranched amylopectin was not tri- but tetramodal by using HPSEC.[114] Chains were categorized into A-chains (DP = 12-16) and B-chains, which were subdivided into the three categories B1 (DP=20-24), B2 (DP=42-48), and B3 (DP=69-75). The definitions of the different chain types are provided schematically in Figure 1.8. The populations of A- and B1-chains represented 80-90 % of the total

side chains, while the remaining 10 % was mainly composed of B2-chains. Based on the *CL* profiles, the average *CL* would be ~ 24 – 27 AGUs, which would represent a repeating distance of 9-10 nm for the double helices formed by such side chains, matching the periodic length observed by SAXS of amylopectin in the solid-state.[112] The periodicity suggested that the B1-, B2-, and B3-chains interconnect one, two, and three clusters of side chains, respectively, with the clusters being oriented parallel to the B-chains.
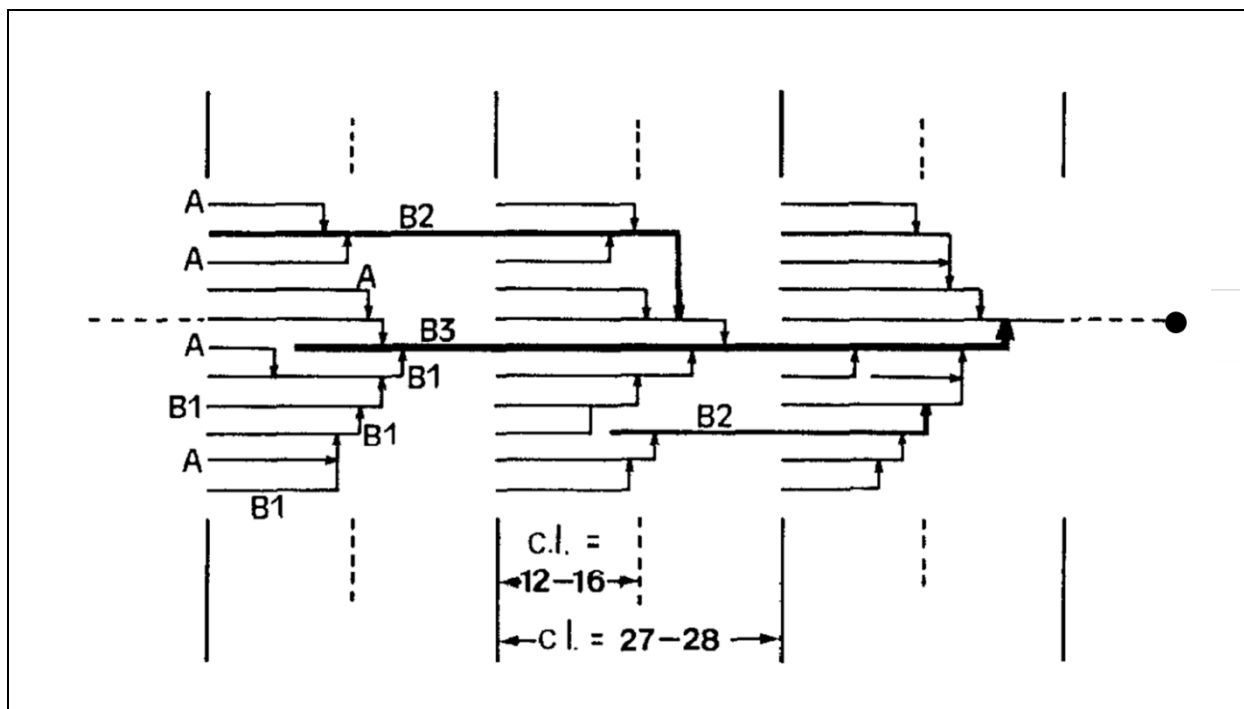
Figure 1.8. The Cluster Model for the structure of amylopectin illustrated by Hizukuri with (●) the reducing end, (—) side chains made of α-(1,4) glycosidic linkages, and (→) α-(1,6) glycosidic linkages. [Reprinted from *Carbohydr. Res.*, 147, Hizukuri, S. Polymodal Distribution of the Chain Lengths of Amylopectins, and its Significance. 342-347, Copyright (2021), with permission from Elsevier.]

Few studies have attempted to define the size of an amylopectin cluster of side chains. Gallant predicted that a single cluster contained 18-34 side chains based on microscopy images of amylopectin,[115] while Hizukuri predicted 22-25 side chains per cluster.[114] Amylopectin was treated with an endo-enzyme, which releases the side chains constituting the clusters by hydrolyzing the internal chain segments, as illustrated in Figure 1.4, in order to define the number of side chains per cluster. Their studies determined that the clusters were made of 4~12 side chains.[80,116,117] The discrepancy in the number of side chains per cluster found in these studies was attributed to the different modes of action or affinities of the endo-enzyme used in each study.[82]

1.3.5.2 Other Structural Models for Amylopectin

1.3.5.2.1 Building Block Backbone Model (BBBM)

The BBBM was proposed by Bertoft to explain some of the experimental results which could not be fully rationalized by the Cluster Model.[118] For instance, a much shorter periodicity of side chains estimated at 12 AGUs was observed for debranched amylopectin,[119] which could not be explained by the Cluster Model, which assumes that the chains interconnecting different clusters are embedded within the clusters. Molecular modelling conducted on amylopectin suggested that the interconnecting chains are arranged perpendicularly to the clusters and do not penetrate the crystalline domains, by arranging themselves parallel to the clusters.[120] Also, branched dextrins produced from α-amylolysis of amylopectin still contained long chains. The Cluster Model predicted that the interconnecting chains should be cleaved by the action of α-amylase, as illustrated in Figure 1.4, which was opposite to the experimental findings.[118] The BBBM was proposed to accommodate these later findings. In the BBBM, the building blocks are the branched structural units, which are distributed randomly and perpendicularly to the main chain, which is

29

embedded in the amorphous domains as shown in Figure 1.7B. Depending on the botanical source, the building blocks are separated by 5-8 AGUs on average.[121]

1.3.5.2.2 *Side Chain Liquid Crystalline Polymer (SCLCP) Model*

In the SCLCP model, amylopectin is viewed as a liquid crystalline polymer, where the helical side chains act as mesogens and the short segments connecting the helices to the backbone function as flexible spacers. The helical side chains of amylopectin can be in the nematic or smectic phase. The side chains are oriented parallel to the main connecting chains and arranged in undefined (nematic) or well-defined (smectic) planes. The smectic phase is entropy-driven, whereby the entropy of the main connecting chains and the spacers is maximized at the cost of the entropy of the mesogens.[122] The SCLCP model was proposed to explain several properties of amylopectin, such as its hydration, gelatinization, freezing etc. SAXS patterns of hydrated amylopectin exhibit a strong peak representing the lamellae of amylopectin corresponding to a repeating separation distance of 9 nm.[112] The peak disappeared and reappeared when cycles of dehydration and rehydration were applied to amylopectin, respectively.[123] The appearance of the peak in the SAXS patterns depends on the arrangement of the helices in the crystalline lamellae of amylopectin. In these experiments water acts as a plasticizer, which favors the formation of smectic planes in amylopectin by increasing the flexibility of the connecting chains and the spacers, thus allowing the alignment of the side chains. Dehydration leads to the formation of the nematic phase, where the helices form disordered lamellae as coupling between the backbone and helices is enhanced. Solid-state Cross-Polarization Magic Angle Spinning Carbon-13 Nuclear Magnetic Resonance (^{13}C CP MAS NMR) experiments have confirmed the enhanced mobility of the backbone and more ordered state of the double helices upon hydration.[123]

1.3.5.2.3   The Solution Cluster (Sol-CL) Model

The Sol-CL model was recently introduced by Li et al.[19] The density of amylopectin and nanosized

amylopectin fragments (NAFs) obtained by degradation of amylopectin and whose hydrodynamic

diameter ranged from 8 to 56 nm, was investigated in DMSO at the macromolecular and molecular

levels by intrinsic viscosity ($[\eta]$) and pyrene excimer formation (PEF) measurements, respectively.

The density of amylopectin (ρ) was predicted from the $[\eta]$ of amylopectin and the NAFs by

applying Equation 1.6, and was found to increase with decreasing sample size.

$$\rho = \frac{2.5}{[\eta]} \qquad (1.6)$$

PEF probes the local density of a macromolecule over a few nanometers, by monitoring the

formation of an excimer upon the encounter between an excited and a ground-state pyrene. The

volume probed by a pyrenyl label, while it remains excited, defines the space over which PEF

takes place. This volume, referred to as a *blob*, is used as a unit volume to compartmentalize a

macromolecule into a cluster of *blobs* among which the pyrenyl labels distribute themselves

randomly according to a Poisson distribution. Analysis of the PEF signal according to the

fluorescence *blob* model (FBM) yields the average number *<n>* of pyrenyl labels per *blob*, which

can be related to the experimental number N_{blob}^{exp} of structural units found inside a *blob*. Because

a polymer with a helical conformation is denser than a randomly coiled polymer, PEF between

pyrenyl labels covalently attached onto a polymer reflects the local concentration $[Py]_{loc}$ of ground-

state pyrenes and will yield a larger or smaller *<n>*, and thus a larger or smaller N_{blob}^{exp}, for a

helical or randomly coiled polymer, respectively. More detailed information about the

fluorescence of pyrene will be provided in the following section. The $N_{\text{blob}}^{\text{exp}}$ value determined by PEF can then be compared to the $N_{\text{blob}}^{\text{theo}}$ value determined by Molecular Mechanics Optimizations (MMOs) conducted on a pyrene-labeled construct adopting a specific conformation. A good match between $N_{\text{blob}}^{\text{exp}}$ and $N_{\text{blob}}^{\text{theo}}$ leads to the conclusion that the hypothesized conformation is that adopted by the polymer in solution. This methodology was applied to determine the conformation of amylose in DMSO. MMOs yielded $N_{\text{blob}}^{\text{theo}}$ values of 7 and 11 AGUs when amylose adopted random coil and helical conformations, respectively. Since $N_{\text{blob}}^{\text{exp}}$ for amylose in DMSO equaled 10 ($\pm$1) AGUs, the good agreement between $N_{\text{blob}}^{\text{theo}}$ and $N_{\text{blob}}^{\text{exp}}$ led to the conclusion that amylose must be a helix in DMSO. Since amylose is a linear polysaccharide, its $N_{\text{blob}}^{\text{exp}}$ of 11 AGUs reflected PEF occurring intra-helically. Since $N_{\text{blob}}^{\text{exp}}$ for amylopectin equaled 19 ($\pm$2) AGUs, this result suggested that PEF occurred intra- and inter-helically in amylopectin.

By conducting MMOs on pyrene-labeled oligosaccharide helices arranged in a hexagonal close packed lattice, $N_{\text{blob}}^{\text{theo}}$ could be determined as a function of the interhelical distance $d_{\text{h-h}}$ for PEF occurring intra- and inter-helically. Comparing the $N_{\text{blob}}^{\text{theo}}$ values obtained as a function of $d_{\text{h-h}}$ to the $N_{\text{blob}}^{\text{exp}}$ of 19 ($\pm$1) for amylopectin led to the conclusion that $d_{\text{h-h}}$ equaled 2.7 nm. This $d_{\text{h-h}}$ value implied that the local density (ρ_{fluo}) of amylopectin probed by PEF equaled 0.28 ($\pm$0.01) g/mL and was independent of the size of the polysaccharide, whether it was amylopectin with a D_{h} of 225 nm or the NAFs with D_{h}'s ranging from 8 to 56 nm. The constancy of ρ_{fluo} with the size of the particles suggested that ρ_{fluo} represented the density of the building blocks constituting amylopectin, namely the clusters of side chains, that were described in the Cluster Model for amylopectin. In contrast, the density (ρ) obtained from [η] measures the density of an entire particle, including its excluded volume. ρ was found to be one-to-two orders of magnitude smaller than ρ_{fluo} for a same polysaccharide sample. The discrepancy between ρ and ρ_{fluo} demonstrated the

32

heterogenous nature of the interior of amylopectin, which led to Sol-CL model proposed by Li et al. to describe the behavior of amylopectin in solution (see Figure 1.7C). According to this model the side chains of amylopectin retain their cluster arrangement in solution with helical side chains being separated by ~ 2.7 nm and the clusters being connected to each other by longer oligosaccharide segments, that generate the excluded volume probed by [η] measurements. More information about the pyrene fluorescence and how it can be analyzed to probe the conformation and internal dynamics of macromolecules is provided in the following section.

1.4 Pyrene Fluorescence

1.4.1 Pyrene Excimer Formation

Pyrene is a fluorophore with a large quantum yield ($\phi = 0.32$ in cyclohexane)[124] and a high molar absorbance coefficient ($\varepsilon_{py,336nm} = 45,000$ M$^{-1}\cdot$cm^{-1} in tetrahydrofuran),[125] thereby allowing a good absorption and emission of light. These features explain why pyrene exhibits a strong fluorescence response even at low concentration. Molecular pyrene absorbs strongly around 336 nm, while the absorbance of many pyrene derivatives is shifted to around 344 nm. Upon excitation, pyrene might relax by emitting a photon as a monomer, which results in the sharp bands observed between 370 and 410 nm in the fluorescence spectrum of pyrene (see Figure 1.9B). While the pyrene monomer remains excited, it might encounter a ground-state pyrene resulting in the formation of an excimer, which emits a broad structureless fluorescence centered around 480 nm as shown in Figure 1.9B. In a homogeneous solution of molecular pyrene, the process of excimer formation is well described by the Birks scheme shown in Figure 1.9A.[126] The association of pyrene moieties results in the formation of a stable excimer due to strong π-π stacking and the excimer decays more quickly than it dissociates. Consequently, the contribution of the dissociation process has been reported to be

negligible at temperatures below 35 °C.[127] Since one excited pyrene monomer is consumed during the formation of an excimer, the process results in the self-quenching of pyrene, which decreases the monomer fluorescence as the excimer emission appears in the fluorescence spectrum. The formation of an excimer depends on the local concentration and the diffusion coefficient of the pyrene monomer. As more pyrene moieties are present in a given volume and/or as pyrene moieties move faster, more excimer is generated. The effect of the local concentration of pyrene on the PEF efficiency is illustrated in Figure 1.9B.
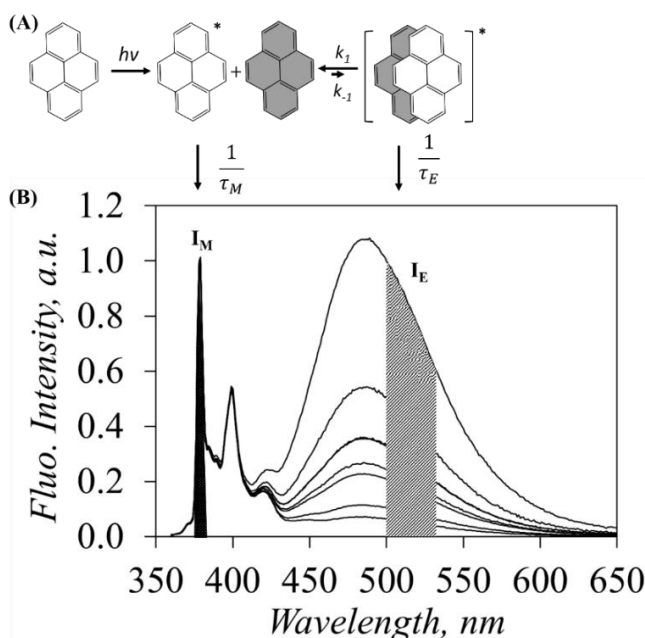
Figure 1.9. (A) Birks' scheme describing pyrene excimer formation. (B) Fluorescence emission spectra of a series of pyrene-labeled glycogen samples in DMSO, where the pyrene content increases from 1.5 mol % (bottom) to 13.6 mol % (top).

As the pyrene content of a series of pyrene-labeled glycogen samples increases, more excimer is generated, resulting in a stronger intensity of the excimer fluorescence. The fluorescence intensity of the pyrene excimer (I_E) and monomer (I_M) can be estimated by integrating

the fluorescence spectrum from 500 to 530 nm and from 376 to 383 nm, respectively. The I_E/I_M

ratio, which is a measure of the PEF efficiency, provides information about the local density of a

pyrene-labeled macromolecule. For example, pyrene-labeled amylopectin exhibited a higher I_E/I_M

ratio than pyrene-labeled amylose for a same pyrene content.[19] This result was attributed to the

different structures of the polysaccharides, amylose and amylopectin being mostly linear and

highly branched polysaccharides, respectively. Since the AGUs are targeted by the pyrene

derivatives during fluorescence labeling, the increased density of AGUs in the amylopectin interior

results in an increased local concentration of ground-state pyrenes ($[Py]_{loc}$). Since pyrenyl labels

on amylose can only interact intra-helically as amylose is linear, whereas pyrenyl labels on

amylopectin can interact intra and inter-helically due to the branched nature of amylopectin, $[Py]_{loc}$

is larger for amylopectin than for amylose, and the I_E/I_M ratio is likewise larger for amylopectin

than for amylose.[19]

1.4.2 The Fluorescence Blob Model

The Fluorescence Blob Model (FBM) was first introduced in 1993 as a mathematical tool to

retrieve quantitative information about the internal dynamics of polymers in solution through the

analysis of the PEF signal generated by the pyrenyl labels covalently attached to the polymer.[128]

Since then, it has been applied to numerous macromolecules.[16-19,129] The FBM was developed from

the observation that the fluorescence decays acquired with a pyrene-labeled polymer looked

surprisingly similar to those obtained with an aqueous solution of pyrene dissolved in polymeric

micelles. Assuming that an excited pyrene probed a finite volume referred to as a *blob*, the polymer

coil could be divided into a cluster of *blobs* of volume V_{blob} among which the pyrenyl labels would

distribute themselves randomly in the same manner as pyrene molecules distribute themselves among surfactant micelles. Application of the robust kinetics for PEF in micellar systems to PEF between pyrenyl labels distributed among the *blobs* used to compartmentalize a macromolecule led to the FBM, which is depicted in Figure 1.10 for a linear polymer randomly labeled with pyrene.

Within the framework of the FBM, four types of pyrene species contribute to PEF. No excimer can be formed inside a *blob* occupied by a single excited pyrene ($Py_{\text{free}}*$) without any ground-state pyrene. Consequently, $Py_{\text{free}}*$ relaxes back to the ground-state with its natural monomer lifetime, τ_M, and its contribution to the monomer fluorescence is defined by its molar fraction f_{free}. Excited pyrenes ($Py_{\text{diff}}*$) diffuse slowly inside a *blob* according to the motion of the structural units they are attached to. As a $Py_{\text{diff}}*$ species approaches a ground-state pyrene with a rate constant k_{blob}, it turns into the species $Py_{\text{k2}}*$, which undergoes a rapid rearrangement with the ground-state pyrene to form an excimer ($E0*$) with a rate constant k_2. Since the pyrene molecules are covalently attached onto the polymer, k_{blob} reflects the mobility of the structural units on the length scale of a *blob*. k_{blob} is equal to the product $k_{\text{diff}} \times (1/V_{\text{blob}})$, where k_{diff} is the bimolecular rate constant for diffusive encounters between AGUs bearing a pyrenyl label and $(1/V_{\text{blob}})$ is the local concentration equivalent to one ground-state pyrene inside the volume V_{blob} of a *blob*. Consequently, k_{blob} provides some qualitative information about V_{blob}.
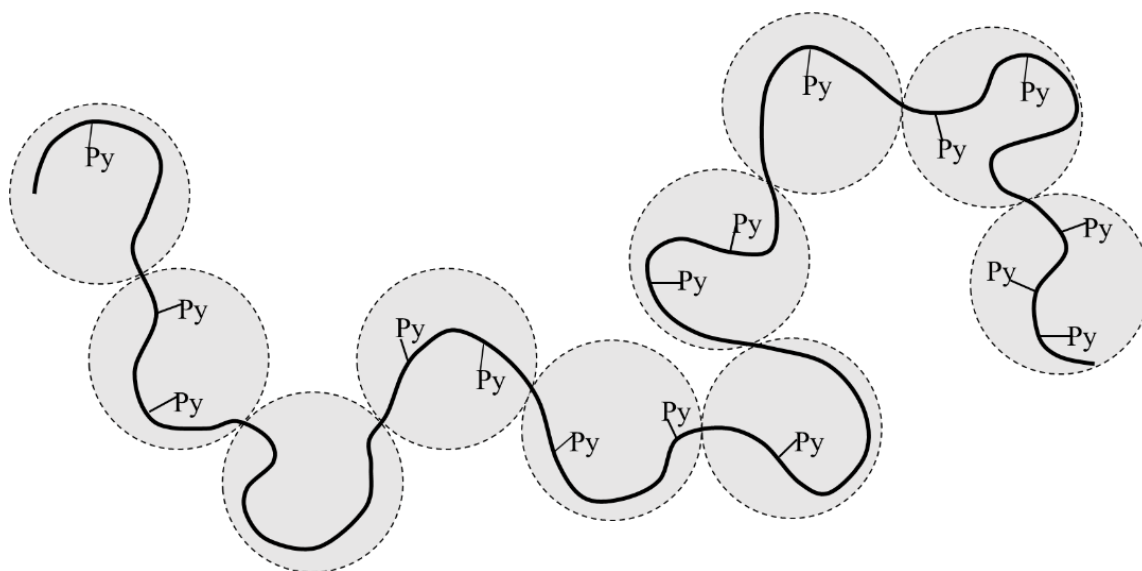
Figure 1.10. Illustration of the Fluorescence Blob Model, whereby the polymer was compartmentalized into a string of blobs and the pyrene labels are distributed along the polymer chain.

Pre-aggregated pyrenes ($Py_{agg}*$) can also form excimer upon direct excitation. Since PEF occurs instantaneously upon excitation of the species Py_{agg}, no dynamic information about this process is obtained. However, the molar fraction f_{agg} of the $Py_{agg}*$ species forming excimer instantaneously can yield valuable information about the conformation of a polymer. A higher f_{agg} value indicates that a polymer is adopting a conformation that is denser than that expected for a randomly coiled polymer, as the higher local polymer density promotes the formation of the $Py_{agg}*$ species. Another important parameter retrieved from the FBM analysis is the average number $<n>$ of ground-state pyrenes per *blob*, which reflects the local concentration of pyrene in a *blob*. The $<n>$ value depends on the pyrene content and the conformation of a polymer. As the number of pyrenyl labels attached on the polymer increases and the polymer adopts a denser conformation, the local concentration of pyrene increases and so does $<n>$. The parameter $<n>$ is then used to

37

determine the number N_{blob} of structural units comprising a *blob*. N_{blob} depends solely on the local conformation and internal dynamics of a polymer. For example, a large N_{blob} value is obtained for a dense and mobile chain, which allows a pyrenyl label to probe many structural units, while it remains excited. The product $k_{blob} \times N_{blob}$, expressed in s^{-1}, is another quantity of interest that is retrieved from the FBM analysis of fluorescence decays, because it has been found to describe the frequency of encounters between structural units, which is a measure of the internal backbone dynamics (IBD) of polymers.[14]

The combination of FBM analysis with MMOs has been shown to constitute an interesting experimental means for determining the conformation and IBD of various macromolecules such as polypeptides[17,129] and polysaccharides[18,19] in solution. The application of this methodology to confirm the helical conformation of amylose in DMSO has been discussed in the previous section. It has also been applied to a series of pyrene-labeled poly(*L*-glutamic acid)s (Py-P*L*GAs) to investigate the conformation of P*L*GA in DMSO.[17] MMOs were conducted to find that N_{blob}^{theo} equaled 10, 13, 19, and 23 if Py-P*L*GA was a random coil, a polyproline type II helix, a 3_{10}-helix, and an α-helix, respectively. The experimental N_{blob} value of 17.9 (±1.1) for Py-P*L*GA was taken as evidence that Py-P*L*GA adopts a 3_{10}-helix conformation in DMSO.[17]

In conclusion, the FBM is a powerful analytical tool to characterize macromolecules in solution. Thus, the FBM seems to be ideally suited to probe polysaccharides at the molecular level.

1.5 Research Goals and Thesis Outline

The overarching goal of this thesis was to investigate the applicability of PEF to the study of the conformation and IBD of polysaccharides. Chapters 2 and 3 focus on the characterization of the

interior of two highly branched polysaccharides, namely amylopectin and glycogen, while the linear polysaccharides dextran and pullulan are studied in Chapters 4 and 5, respectively. In Chapter 2, the PEF efficiency of pyrene-labeled amylopectin or nanosized amylopectin fragments (NAFs) derived from amylopectin was used to determine the size of the clusters of helices found in these polysaccharides, which represented the first example where PEF was applied for this purpose. The two possible density profiles describing the distribution of side chains in the interior of glycogen were investigated and optimized by monitoring the PEF efficiency of two series of pyrene-labeled glycogen molecules in Chapter 3. Both density distributions indicated that the density experienced by the side chains of glycogen is larger than that predicted from the Melendez-Hevia mathematical description of the Tier model for glycogen. The PEF study conducted in Chapter 4 on a series of pyrene-labeled dextran samples led to the conclusion that dextran was randomly coiled in DMSO. The conformation and IBD of dextran and pullulan, two linear polysaccharides, which were labeled with pyrene, were compared in Chapter 5. Although the two pyrene-labeled polysaccharides yielded small differences between the parameters retrieved from the FBM analysis of their fluorescence decays, these small differences indicated that dextran was more mobile and extended than pullulan in DMSO, a conclusion that agreed with the results published in the scientific literature. Finally, the main findings described in this thesis were summarized in Chapter 6, also including a list of experiments, which could be carried out as future work.

Chapter 2

Compressibility of Amylopectin and Nanosized Amylopectin Fragments Characterized by Pyrene Excimer Formation

2.1. Abstract

Amylopectin from waxy maize and three nanosized amylopectin fragments (NAFs) prepared from waxy corn starch, referred to as NAF(56), NAF(20), and NAF(8), with a hydrodynamic diameter of 227, 56, 20, and 8 nm, respectively, were randomly labeled with ~5.9 (±0.6) mol % of 1-pyrenebutyric acid. Their efficiency for pyrene excimer formation (PEF) upon diffusive encounters between an excited and a ground-state pyrene was assessed as the concentration of NAF(56) was increased in the DMSO dispersion of these polysaccharides (PSs). The fluorescence spectra of the pyrene-labeled PSs (Py-PSs) were acquired. A large increase in the ratio of the fluorescence intensity of the excimer over that of the monomer, namely the I_E/I_M ratio, was observed as a function of the [NAF(56)], indicating that increasing the [NAF(56)] promoted diffusive pyrene encounters by bringing the pyrenyl labels closer to each other. In other words, increasing the [NAF(56)] increased the osmotic pressure in the dispersion, which induced the shrinkage of the Py-PSs, resulting in stronger PEF. The fluorescence decays of the Py-PS dispersions in DMSO were acquired with increasing [NAF(56)] and analyzed with the fluorescence *blob* model (FBM) to yield the maximum number (N_{blob}^{exp}) of anhydroglucose units (AGUs) separating two AGUs bearing a pyrenyl label, while still allowing PEF. Comparison of N_{blob}^{exp} with N_{blob}^{theo}, obtained by conducting molecular mechanics optimizations (MMOs) on helical oligosaccharide constructs with HyperChem, led to a relationship between the interhelical distance (d_{h-h}) in a cluster of oligosaccharide helices and the [NAF(56)], that provided a means to determine the size of the cluster of helices constituting these PSs. Amylopectin, NAF(56), NAF(20), and NAF(8) were found to be composed of clusters made of 37, 37, 6, and 3 helices, respectively. Considering that clusters of oligosaccharide helices can be viewed as the building blocks of amylopectin and the NAFs derived from it, the ability of PEF-based experiments to yield the cluster size of these PSs should prove extremely helpful in their characterization.

2.2 Introduction

Amylopectin is a major energy source. Its functionality and structure have been studied over decades to extend its range of applications.[1-4] The structure of amylopectin has been characterized with a variety of techniques such as enzymatic treatment,[5,6] intrinsic viscosity,[7,8] nuclear magnetic resonance (NMR),[9,10] and X-ray scattering,[11] to name but a few. These studies have revealed that amylopectin is a highly branched polysaccharide constituted of linear oligosaccharide segments made of anhydroglucose units (AGUs) linked by $\alpha-(1,4)$ glycosidic bonds, which are connected to each other via α-(1,6) glycosidic bonds. Incomplete acid hydrolysis of amylopectin indicated that it is composed of both amorphous and crystalline domains.[12] X-ray diffraction experiments led to the conclusion that in the solid state, the side chains of amylopectin form double helices, that pack in a hexagonal array to form crystalline lamellae connected to each other by longer oligosaccharides.[13] These early studies resulted in several models that aimed to determine the spatial arrangement of the constituting parts of amylopectin. The Cluster Model (CLM), whereby a cluster is constituted of short oligosaccharides linked to other clusters by longer oligosaccharides, was introduced in 1972 and is well accepted.[12] The short and long oligosaccharide chains run parallel to each other and form crystalline lamellae in the dry state separated by amorphous lamellae, where the branching points are found. Further developments led to the Building Block Backbone Model (BBBM), which was introduced in 2004 by Bertoft.[14,15]Contrary to the CLM, the BBBM suggests that the short chains are oriented perpendicularly to the longer chains onto which they are linked. Other models such as the Side Chain Liquid Crystalline Polymer (SCLCP) model,[16-18] where the helical side chains are viewed as mesogens connected to the backbone via a flexible spacer, were introduced to better explain gelatinization resulting from the self-assembly

and hydration of the side chains of amylopectin. Similarly, the solution cluster model (Sol-CL) has been proposed to predict the internal arrangement of the side chains of amylopectin in solution.[19] The Sol-CL is based on the CLM for amylopectin and assumes that the helices generated by a cluster of short oligosaccharide chains hexagonally packed in a crystalline lamella remain clustered in solution.

Considering the importance of the clusters of helical oligosaccharide side chains in the composition, internal conformation, and properties (self-assembly, plasticization, hydration, gelatinization…) of amylopectin,[16-18] techniques capable of probing these clusters of side chains at the molecular level are particularly interesting, as they provide insights about their behavior in solution. One such technique, based on pyrene excimer formation (PEF), was recently applied to pyrene-labeled amylopectin and nanosized amylopectin fragments (NAFs). The results of this study led to the conclusion that the helical side chains inside a cluster were separated by 2.7 nm, and that different clusters were more than 3.2 nm apart inside the amylopectin interior. Compared to the diameter of a single helix with 7 AGUs per turn, which equals 1.5 nm,[20] the much larger $d_{\text{h–h}}$ found by PEF for amylopectin dispersed in dimethyl sulfoxide (DMSO) suggested that the helical oligosaccharide side chains constituting a cluster could undergo substantial lateral expansion when they transitioned from an ordered hexagonal array in a crystalline lamella to a more disordered cluster in solution. These early PEF experiments also suggested that the direct relationship between the PEF efficiency and the local concentration ($[Py]_{\text{loc}}$) of pyrenyl labels attached to amylopectin could be taken advantage of to monitor the $d_{\text{h-h}}$ for disordered side chains in a cluster of helices inside amylopectin dispersed in DMSO, as the side chains were brought closer to each other by increasing the osmotic pressure.

Preliminary PEF experiments have already been carried out by adding large quantities of poly(ethylene glycol) (PEG) samples with molecular weight ranging from 200 to 20,000 g/mol, to affect the osmotic pressure experienced by dispersions in DMSO of a sample of amylopectin from maize and three NAFs prepared from waxy corn starch, that had been labeled with pyrene.[19,21] The three NAF samples were referred to as NAF(8), NAF(20), and NAF(56) according to their hydrodynamic diameter (D_h) found by dynamic light scattering to equal 8, 20, and 56 nm, respectively. An increase in the concentration of the larger PEGs such as PEG(20K) resulted in an increase in PEF efficiency for the pyrene-labeled amylopectin and NAF(56) samples. However, the end-to-end distance (r_{EE}) of the largest PEG(20K) was only ~ 12 nm, suggesting that it could partially penetrate some parts of the interior of the polysaccharides. To minimize the possibility of penetration of the much larger polysaccharides by a smaller macromolecule, the present study describes the results obtained by increasing the osmotic pressure experienced by the dispersions of four pyrene-labeled polysaccharides (Py-PSs) in DMSO by adding NAF(56) to the Py-PS dispersions. The close to 5-fold larger D_h of NAF(56) compared to the r_{EE} of PEG(20K) reduced the possibility of partial penetration of the polysaccharides in DMSO, thus resulting in the observation of a substantial increase in PEF efficiency with increasing [NAF(56)], the magnitude of this PEF enhancement increasing with increasing PS size. This result was attributed to edge effects experienced by the finite clusters of helical side chains, as larger polysaccharides generated larger clusters of helices, which experienced smaller edge effects resulting in stronger PEF enhancement. Quantitative analysis of the fluorescence data by a combination of fluorescence *blob* model (FBM) and molecular mechanics optimizations (MMOs) yielded the average size of the clusters of helices constituting a given polysaccharide. Consequently, this procedure provides an

experimental means to probe the interior of highly branched macromolecules at the molecular level and assess the spatial arrangement of their interior. This information should prove most interesting to establish the structure-property correlations for these interesting macromolecules.

2.3 Experimental

*Materials***:** EcoSynthetix supplied three research-grade NAFs, that were prepared from waxy corn starch. The NAFs were purified by dialysis against water before being lyophilized. Amylopectin from waxy maize was purchased from Sigma Aldrich and precipitated in cold ethanol before use. All other chemicals were purchased from Sigma Aldrich and used without any further purification.

Preparation of pyrene-labeled nano-sized amylopectin fragments (Py-NAF): The procedure described earlier for the esterification of the polysaccharide hydroxyls with 1-pyrenebutyric acid (PyBA) to yield the Py-NAFs, their purification, and their characterization was followed to the letter.[19] The synthesis of amylopectin labeled with 5 mol% pyrene (Py(5)-Amylopectin) is described in detail hereafter. Amylopectin, that had been purified by precipitation in cold ethanol (1 g, 6.2 mmol of AGUs), was dispersed in 30 g of DMSO in a round bottom flask (RBF) by stirring at 95 °C. PyBA (0.63 g, 2.2 mmol) and 4-dimethylaminopyridine (DMAP) (42 mg, 0.3 mmol) were added into the RBF after the amylopectin was fully dispersed. Then, 10 mL of DMF was added into the mixture, to prevent DMSO from freezing in the ice bath used in the next step. The flask was sealed with a rubber septum and kept in an ice bath under nitrogen. *N,N'*-Diisopropylcarbodiimide (DIC) (0.5 mL, 3.3 mmol) was added to the mixture dropwise with a syringe. The flask was removed from the ice bath and covered with aluminum foil to prevent exposure of the pyrene derivative to light. The reaction was carried out at room temperature for 48 hours. The mixture was precipitated in ethanol at least four times for the complete removal of free

PyBA. The same procedure was followed for the NAFs, except that the NAF samples were dispersed in DMSO by stirring them at 60 °C instead of 95 °C, as was done earlier.[19]

Pyrene content determination: A stock dispersion with a known concentration of Py-PS in DMSO was prepared gravimetrically. The pyrene-labeled amylopectin (Py-Amylopectin) and Py-NAF stock dispersions were stirred overnight at 95 and 60 °C, respectively. The stock dispersions were diluted with different amounts of DMSO to change their concentration. The absorbance of all Py-PS samples was kept lower than 2.0. The absorption spectra of the Py-PSs were acquired with a quartz cuvette having a 1.00 cm path length (*L*) on a Cary 100 bio-UV-Vis spectrophotometer. A straight line was obtained by plotting the absorbance as a function of the mass concentration of the dispersions. The slope (*m*) of the line equaled $\varepsilon_{Py} \times L \times \lambda_{Py}$, where ε_{Py} was the molar absorption coefficient of the 1-pyrenebutyryl label equal to 41,400 $M^{-1} \cdot cm^{-1}$ at 346 nm in DMSO based on the ε_{Py} of PyBA,[19] *L* equaled 1.00 cm, and λ_{Py} was the pyrene content in moles of pyrene per gram of polysaccharide calculated according to Equation 2.1.

$$\lambda_{Py} = \frac{m}{\varepsilon_{Py} \times L} \tag{2.1}$$

The molar fraction (*x*) of pyrene-labeled AGUs in a given Py(*x*)-PS sample was determined by applying Equation 2.2, where M_{AGU} and M_{Py} are the molar mass of unlabeled and pyrene-labeled AGUs, equal to 162 g/mol and 432 g/mol, respectively.

$$x = \frac{M_{AGU}}{M_{AGU} - M_{Py} + \lambda_{Py}^{-1}} \tag{2.2}$$

Preparation of Py(0.004)-NAF(56) dispersions: Special care was applied to determine the natural lifetime (τ_M) of the pyrenyl monomer. To this end, the Py(0.004)-NAF(56) sample was prepared with an extremely low pyrene content, to minimize intramolecular PEF and measure the lifetime of isolated pyrene labels covalently attached onto NAF(56). Very little PEF was detected up to a Py(0.004)-NAF(56) concentration of 13 wt% in DMSO, corresponding to a 3.2 mM pyrene concentration. More significant PEF was observed at Py(0.004)-NAF(56) concentrations above 13 wt%. For this reason, unlabeled NAF(56) was mixed with Py(0.004)-NAF(56) to increase the starch concentration without inducing intermolecular PEF for dispersions with a NAF concentration higher than 13 wt%. In this concentration range, a stock solution was prepared by dispersing 4 wt% of Py(0.004)-NAF(56) in DMSO. Unlabeled NAF(56) (0.45-0.94 g) was added to 1.1-1.65 mL of the Py(0.004)-NAF(56) stock solution. The mixture was further diluted with DMSO to a final volume of 3.3 mL. At this stage, the mixture had a final concentration of less than 33 wt% of Py(0.004)-NAF(56) and NAF(56) combined. It contained enough solvent to disperse the solids. After a homogenous dispersion was obtained by stirring, the DMSO was evaporated by flowing N_2 over the dispersions. The dispersions were fluid enough to be transferred to a fluorescence cell to acquire their fluorescence spectra and decays. The dispersions were analyzed by steady-state (SSF) and time-resolved (TRF) fluorescence without degassing. The results from this study are reported as a function of the overall concentration of Py(0.004)-NAF(56) and NAF(56) combined.

Preparation of mixtures of pyrene-labeled polysaccharides and unlabeled NAF(56): Dispersions of naked NAF(56) with a concentration lower than 30 wt% were prepared by adding the required amount of unlabelled NAF(56) (0-30 wt %) to a Py-PS dispersion in DMSO with a pyrene concentration equal to 24 μM. The dispersions were stirred for two days at 60 °C, until they became

47

homogeneous. For dispersions with a NAF(56) content greater than 30 wt%, the proper mass of NAF(56) was added to a dilute Py-PS dispersion in DMSO. DMSO was then evaporated so that the final dispersion would contain about 24 µM pyrene of the Py-NAF sample and a large excess of NAF(56), that would result in the desired starch concentration (> 30 wt%).

Preparation of concentrated Py-NAF dispersions: Concentrated dispersions of Py(6.4)-NAF(56) were also prepared by stirring a 5 wt% Py(6.4)-NAF(56) dispersion at 60 $^{\circ}$C for two days. For dispersions with low or high Py(6.4)-NAF(56) concentrations, aliquots of the 5 wt% Py(6.4)-NAF(56) dispersion were either diluted with DMSO or subject to a gentle flow of N_2 to evaporate DMSO, respectively. Using this procedure, Py(6.4)-NAF(56) dispersions with concentrations ranging from 0.07 to 42 wt% were prepared and investigated.

Intrinsic viscosity of amylopectin in DMSO: The intrinsic viscosity of amylopectin was determined in DMSO at 25 $^{\circ}$C with an Ubbelohde viscometer. Amylopectin was dispersed in DMSO by stirring the dispersion at 95 $^{\circ}$C overnight. The dispersions were prepared with a concentration ranging from 0.61 to 2.82 mg/mL.

Characterization of NAFs by gel permeation chromatography: The NAF(20) or NAF(8) dispersions were prepared by stirring 10.0 mg of PS in 10.0 mL of DMSO at 60 $^{\circ}$C overnight. The clear homogeneous dispersion was filtered with a 0.22 µm syringe filter to remove dust particles. The molecular weight distribution (MWD) of the NAFs was determined with a TOSOH EcoSEC High Temperature gel permeation chromatography (GPC) equipped with a guard column and a 300 mm × 7.8 mm ID TSKgel Alpha-M column, a differential refractometer and a multi-angle laser light scattering detector. A pullulan standard with a M_n of 47.1 kg/mol and PDI of 1.07 was used to calibrate the GPC system. The mobile phase was run with a flow rate of 0.5 mL/min at 60 $^{\circ}$C.

Steady-state fluorescence measurements: The fluorescence emission spectra were acquired with a Photon Technology International LS-100 fluorometer equipped with a xenon arc lamp. The fluorescence spectra of pyrene were obtained by exciting the dispersion at 346 nm and collecting the fluorescence intensity from 360 to 670 nm. Excitation and emission slit widths of 1.0 nm were used for the fluorescence experiments. The contributions of the pyrene monomer (I_M) and excimer (I_E) to the fluorescence spectra were quantified by integrating the fluorescence spectra from 376 to 382 nm for the monomer and from 500 to 530 nm for the excimer, respectively. The I_M and I_E fluorescence intensities were used to calculate the I_E/I_M ratio, which provided a qualitative estimate of the PEF efficiency. The front-face geometry was applied when the concentration of the Py(6.4)-NAF(56) dispersion was higher than 24 μM (equivalent to an absorption of 1.0 at 346 nm) to avoid the inner filter effect at 379 nm, corresponding to the 0-0 transition of pyrene. Measurements conducted with the front face geometry were repeated three times.

Time-resolved fluorescence measurements: The time-resolved fluorescence decays were acquired with an IBH time-resolved fluorometer. The excitation wavelength was set at 346 nm with an excitation monochromator using a 340 nm nanoLED. A Ludox suspension was employed to obtain the instrument response function (IRF) by using a same excitation and emission wavelength of 346 nm. The fluorescence decays of the pyrene monomer and excimer were collected with a 1.02 ns/ch time-per-channel at 378 nm with a 370 nm cut-off filter, and at 510 nm with a 495 nm cut-off filter. The cut-off filters minimized the detection of light scattered by the PS dispersions. The fluorescence decays of two types of Py-PS dispersions were acquired. The short-lived emission of NAF(56) led to the appearance of a sharp spike at the beginning of the decays of the pyrenyl monomer in the Py(0.004)-NAF(56) dispersions (see Figure 2.1B). The decays were acquired with ~ 80,000 counts at the decay maximum to ensure that the decays would have at least 20,000 counts

just after the spike to obtain a good signal-to-noise ratio in the longer-lived section of the decay. The fluorescence decays were fitted with a biexponential, starting the analysis just after the spike. The exponential with the longest decay time had a pre-exponential contribution larger than 83% and its decay time was assigned to the natural lifetime of the pyrenyl monomer (τ_M). All the other dispersions of Py-PSs had a much stronger pyrene fluorescence, and the monomer and excimer decays of the pyrenyl labels were acquired with 20,000 counts at the decay maximum. These decays were fitted globally according to the fluorescence *blob* model (FBM).

Global fluorescence blob model analysis: The FBM is a mathematical tool that divides a macromolecule randomly labeled with the pyrene dye into identical unit volumes called *blobs*, that represent the volume probed by a pyrenyl label while it remains excited. Random labeling of the macromolecule ensures that the pyrenyl labels distribute themselves randomly among the *blobs* according to a Poisson distribution, defined by its average number <*n*> of pyrenyl labels per *blob*. Analysis of the fluorescence decays yields <*n*>, which can be related to the number of structural units, N_{blob}^{exp}, inside a *blob* according to Equation 2.3.

$$N_{blob}^{exp} = \frac{1}{1 - f_{Mfree}} \times \frac{<n>}{x} \qquad (2.3)$$

In Equation 2.3, x represents the molar fraction of AGUs bearing a pyrenyl label as defined by Equation 2.2 and f_{Mfree} represents the molar fraction of pyrenyl labels $Py_{free}*$ probed in the monomer decays, that cannot form excimer and emit, as if they were free in solution with their natural lifetime, τ_M. Beside $Py_{free}*$, the FBM also requires four other pyrenyl species. One is $Py_{diff}*$, whose slow diffusion in the solution, described by the rate constant k_{blob}, is controlled by the motion of the AGUs, that $Py_{diff}*$ is bound to, until $Py_{diff}*$ comes near a ground-state pyrene and

turns into the species Py_{k2}^*. Py_{k2}^* undergoes a rapid rearrangement with a rate constant k_2 to form an excimer $E0^*$ or D^*, depending on whether the two pyrenyl species are well- or poorly stacked, respectively. The pyrene species $E0^*$ and D^* can also be generated instantaneously upon direct excitation of a pyrene aggregate and they emit with their natural lifetimes τ_{E0} and τ_{EL}, respectively. Py_{free}^*, Py_{diff}^*, and Py_{k2}^* are detected in the monomer decays and their contributions to the decays are used to calculate their molar fractions f_{Mfree}, f_{Mdiff}, and f_{Mk2}, respectively. Py_{diff}^*, Py_{k2}^*, $E0^*$, and D^* are detected in the excimer fluorescence decays, whose analysis yields the molar fractions $f_{EdiffE0}$ and f_{Ek2E0} or f_{EdiffD} and f_{Ek2D}, representing the species Py_{diff}^* and Py_{k2}^* that lead to the formation of $E0^*$ or D^*, respectively, and the molar fractions f_{EE0} and f_{ED} for the instantaneous formation of $E0^*$ or D^* upon absorption of a photon, respectively. These molar fractions can be combined to yield the molar fractions f_{diff}, f_{k2}, f_{free}, and f_{agg}, that represent the species Py_{diff}^*, Py_{k2}^*, Py_{free}^*, and the combination of $E0^*$ and D^* referred to as Py_{agg}^*, respectively. In summary, the FBM provides a description of all the pyrenyl species contributing to PEF in a Py-PS dispersion. The monomer and excimer fluorescence decays were fitted globally according to Equations S2.1 and S2.2 provided as Supporting Information (SI). The parameters were optimized according to the Marquardt-Levenberg algorithm.[22] The fluorescence decay fits were deemed satisfactory when the χ^2 was smaller than 1.3 and the residuals and autocorrelation of the residuals were randomly distributed around zero, as shown in Figure S2.1 in the SI. The parameters retrieved from all the decay analyses were listed in Tables S2.1 – S2.9 in the SI.

2.4 Results

Size of amylopectin and of the nanosized amylopectin fragments: The size of three different NAFs in DMSO were determined earlier by dynamic light scattering. [23] The number-average

51

hydrodynamic diameters, D_h, of the three NAFs equaled 8, 20, and 56 nm and the particles were

referred to as NAF(8), NAF(20), and NAF(56), respectively. The D_h of amylopectin was estimated

from its intrinsic viscosity ($[\eta]$) = 122.5 ($\pm$0.3) mL/g) as shown in Figure S2.2 in the SI and the

relationship $D_h = 0.0258 \times [\eta]^{1.89}$, which was established earlier for a series of nanosized

amylopectin fragments (NAFs).[23] The D_h of amylopectin was found to equal 227 ($\pm$20) nm. Based

on these relationships, the viscosity average molecular weight (M_V) of amylopectin was estimated

from $[\eta]$ and D_h to equal 7.2×10^7 g/mol. The values of D_h, $[\eta]$, and M_v obtained for all PS are

listed in Table 2.1.

Table 2.1. Hydrodynamic diameter (D_h), intrinsic viscosity ($[\eta]$), viscosity (M_v), number (M_n),

and weight (M_w) average molecular weight, and polydispersity index (PDI) of the polysaccharide

samples, which were determined earlier.[19,24]

Sample	D_h (nm)	$[\eta]$ (mL/g)	M_v (g/mol)	M_n (g/mol)	M_w (g/mol)	PDI
Amylopectin	227	122.5	7.2×10^7	N/A	N/A	N/A
NAF(56) [a]	56	61	2.3×10^6	N/A	5.4×10^6	N/A
NAF(20)	20	40	N/A	1.0×10^6	1.9×10^6	1.9
NAF(8)	8	23	N/A	1.5×10^5	2.6×10^5	1.7

a. The M_w of NAF(56) was retrieved from reference [24]

Local viscosity experienced by a pyrenyl label: The natural lifetime of the pyrene monomer (τ_M)

was estimated from the analysis of the TRF decays of Py(0.004)-NAF(56) in DMSO. The very

low pyrene content of this sample ensured that no PEF occurred, as illustrated by the absence of a

broad structureless emission centered at 480 nm in Figure 2.1A, that would otherwise be characteristic of PEF. The residual emission past 450 nm in the fluorescence spectra belonged to NAF(56). The fluorescence spectra and decays of Py(0.004)-NAF(56) were acquired in DMSO with increasing concentration of non-fluorescently labeled NAF(56). While the fluorescence spectra showed similar spectral features for Py(0.004)-NAF(56) in DMSO without and with enough NAF(56) to generate an overall PS concentration of 42 wt%, the fluorescence decays shown in Figure 2.1B displayed some important differences. The spike observed at the beginning of the decay was attributed to the short- lived intrinsic fluorescence of NAF(56),[26,27] while the longer contribution was due to the emission of isolated pyrenyl labels. The decays past the spike were fitted with a biexponential, where the exponential having the longest lifetime contributed more than 83 % (Table S2.1) to the fluorescence decay and was attributed to τ_M. τ_M was plotted as a function of the overall concentration of Py(0.004)-NAF(56) and NAF(56) in Figure 2.1C. .
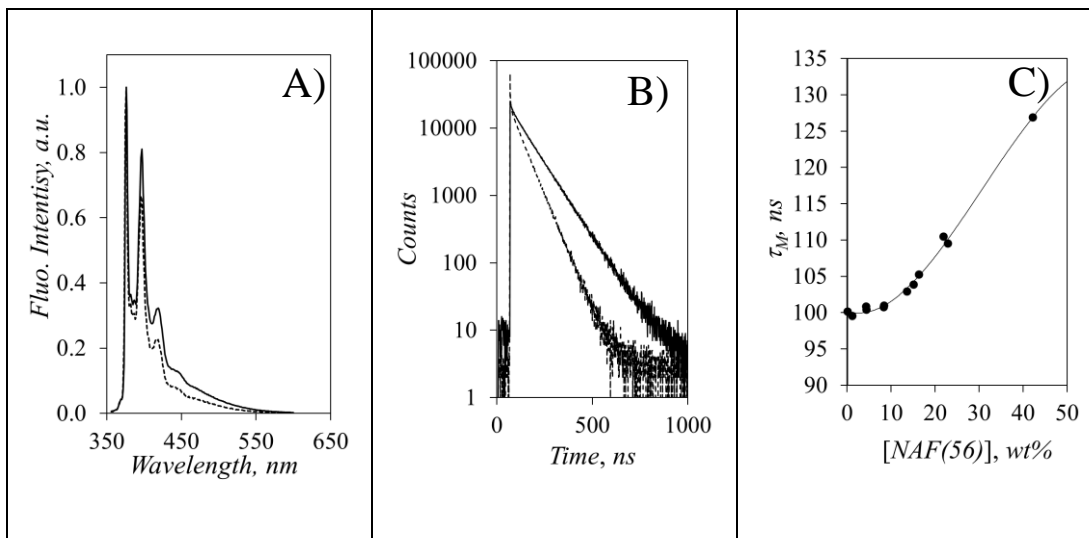
Figure 2.1. A) Fluorescence spectra and B) fluorescence decays of Py(0.004)-NAF(56) dispersions containing NAF(56) at an overall PS concentration of (---) 0.001 wt% and (—) 42.3 wt% in DMSO. C) Plot of the lifetime (τ_M) of Py(0.004)-NAF(56) as a function of PS concentration in DMSO.

τ_M was found to increase from 100.2 ($\pm$ 0.5) ns for NAF(56) concentrations lower than 13 wt%, before increasing progressively to 126.9 ns for a NAF(56) concentration of 42 wt%. τ_M for a pyrenyl label depends strongly on its accessibility to oxygen dissolved in the solvent. Based on the trend shown in Figure 2.1C, the increase in τ_M observed for a NAF(56) concentration larger than 13 wt% suggests that the diffusion of oxygen and the mobility of the pyrenyl labels are hindered at these large NAF(56) concentrations, resulting in the increase in τ_M. In fact, the lifetime of 126.9 ns obtained for 42 wt% PS approaches that of 135 ns obtained for a pyrenyl label in non-aerated DMSO, suggesting that at this NAF(56) concentration, the viscosity of the dispersion is so high that it prevents oxygen from reaching an excited pyrenyl label.

Intraparticle interactions: It was shown in earlier studies that the compression of Py-PSs can be induced by the addition of large quantities of poly(ethylene glycol) (PEG).[19,25] However, the largest PEG sample used had a molecular weight of 20K with an associated r_{EE} of ~12 nm, small enough to partially penetrate the PS interior. Addition of the much larger NAF(56) to a Py-PS dispersion should minimize the possibility of NAF(56) penetrating the interior of a Py-PS. By monitoring the compression of a dilute Py-PS dispersion by PEF as a function of the concentration of unlabeled NAF(56), any change in fluorescence would be the result of intraparticle interactions due to the compression of the particles induced by increased osmotic pressure. All the polysaccharides were labeled with about 5.9 ($\pm$0.6) mol % of pyrene, which resulted in a substantial amount of PEF even under dilute conditions. Since NAF(56) fluoresced, as reported earlier[26,27] and observed in Figures 2.1A and B, the concentration of the Py-PS samples was increased to prevent the detection of the NAF(56) fluorescence, but kept sufficiently low to avoid interactions between the Py-PSs. As can be seen in Figure S2.3 in SI, the I_E/I_M ratio of Py(6.7)-

NAF(56) remained constant for an absorbance of the pyrenyl labels in the Py-PS dispersion between 0.1 and 1.5. The constancy of I_E/I_M confirmed the absence of interactions between the Py(6.7)-NAF(56) samples over this range of absorbances. Consequently, fluorescence experiments were conducted with amylopectin, three NAFs, and amylose labeled with 5.9 (±0.6) mol% pyrene, using a pyrene absorbance for the Py-PS dispersions that was close to unity, in order to increase the fluorescence of the pyrenyl labels while preventing Py-PS interactions.

As shown in Figure 2.2A for the Py(6.7)-NAF(56) sample in DMSO, the fluorescence of the excimer centered at 480 nm increased substantially relatively to that of the pyrene monomer at 379 nm, as the NAF(56) concentration was increased from 0.0 to 36.0 wt%. Similar changes in the fluorescence spectra were observed for all Py-PS samples, but with different rates of PEF increase. These changes were better quantified by monitoring the I_E/I_M ratio of the Py-PS dispersions as a function of [NAF(56)] in Figure 2.2B. To account for the different pyrene contents for all the Py-PSs studied, the I_E/I_M-*vs*-pyrene content trends obtained in earlier publications[19,21,25] under dilute conditions were parametrized to predict the value of the I_E/I_M ratios of the Py-PS samples for an arbitrary pyrene content of 5.5 mol%, using an I_E/I_M ratio of 1.0 for Py-Amylopectin. After this normalization, the increase in I_E/I_M was found to be most pronounced for Py(4.2)-Amylopectin and Py(6.7)-NAF(56), modest for Py(5.8)-NAF(20), fairly small for Py(5.8)-NAF(8), and hardly noticeable for Py(5.5)-Amylose. The I_E/I_M ratio increased at a [NAF(56)] of 11 (±2) wt% for the Py-PS samples other than Py(5.5)-Amylose for which PEF remained almost unchanged. Changes in the I_E/I_M ratio of pyrene-labeled macromolecules are best described by referring to Equation 2.4, which states that the I_E/I_M ratio is proportional to the product between the rate constant (k_{diff}) for PEF by diffusive encounters between pyrenyl labels and the local concentration of ground-state pyrenes ($[Py]_{loc}$) experienced by an excited pyrenyl label. As discussed with Figure 2.1, the

increase in τ_M in Figure 2.1C reflected a decrease in the mobility of the pyrenyl groups at [NAF(56)] larger than 13 wt%, which prevented them from encountering oxygen molecules in the viscous dispersions. This decrease in mobility also implied that k_{diff} must have decreased for larger NAF(56) concentrations. Therefore, the increase in I_E/I_M observed in Figure 2.2B for several Py-PSs could only be due to an increase in $[Py]_{\text{loc}}$. As interpenetration of these highly branched polysaccharides was unlikely, the addition of NAF(56) must have led to an increase in osmotic pressure resulting in the compression of the Py-PSs, that brought the helical side chains of the PS closer to each other. In contrast, Py-Amylose being fully exposed to the solvent could not respond to the compression, $[Py]_{\text{loc}}$ was unaffected, and I_E/I_M remained constant within experimental error.

$$\frac{I_E}{I_M} \propto k_{diff} \times [Py]_{loc} \tag{2.4}$$

While the analysis of the I_E/I_M ratios demonstrated the compression of the Py(4.2)-Amylopectin and the Py-NAF samples, the retrieved information remained qualitative. Quantitative information about the Py-PSs could be obtained through the FBM analysis of their fluorescence decays. In particular, the FBM analysis yielded the molar fractions corresponding to the four pyrene species Py_{free}^*, Py_{diff}^*, Py_{k2}^*, and Py_{agg}^*, that are defined by the type of photophysical pathway that they underwent during PEF.[28,29] f_{free}, f_{diff}, f_{k2}, and f_{agg} are shown in Figure 2.2C for Py(6.7)-NAF(56). The most visible change in the molar fractions was observed for Py_{diff}^* and Py_{k2}^*. While the contributions from Py_{free}^* and Py_{agg}^* remained small and constant, less excimer formed by diffusion (f_{diff} decreased) and more excimer formed through a rapid rearrangement of the pyrene species (f_{k2} increased) as the [NAF(56)] increased. The trends shown

in Figure 2.2C suggest that compression of the Py-PS samples brought more excited pyrene molecules Py_{diff}^* close to a ground-state pyrene, which generated more Py_{k2}^* species, that formed excimer by rapid rearrangement.
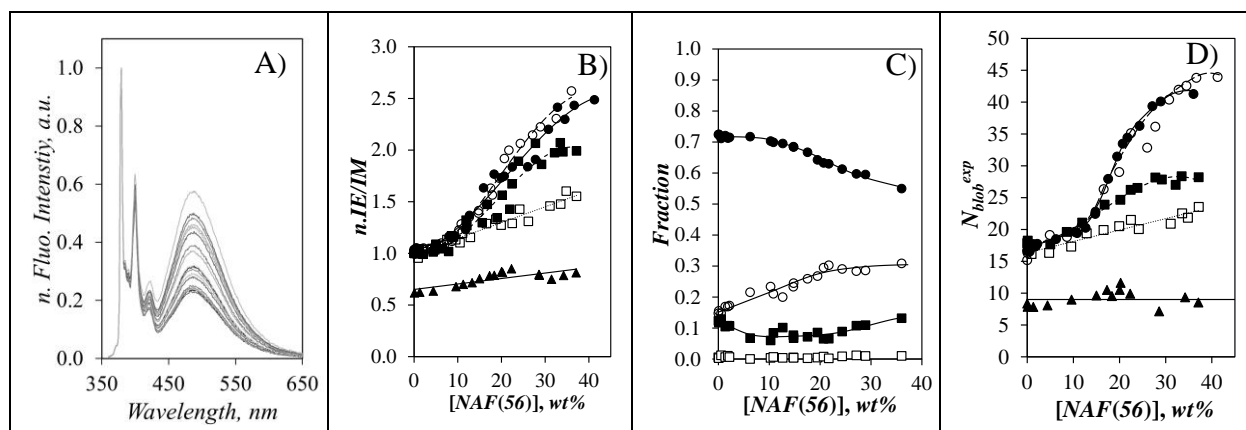
Figure 2.2. A) Fluorescence spectra of Py(6.7)-NAF(56) acquired with increasing [NAF(56)]. B) Plot of the normalized I_E/I_M ratios. C) Plot of the molar fractions for the pyrene species ($\bullet$) Py_{diff}, ($\circ$) Py_{k2}, ($\blacksquare$) Py_{agg}, and ($\square$) Py_{free} retrieved from the FBM analysis of the fluorescence decays of Py(6.7)-NAF(56) as a function of [NAF(56)]. D) Plot of N_{blob}^{exp} as a function of [NAF(56)]. Symbols in Figures 2.2B and D: ($\circ$) Py(4.2)-Amylopectin, ($\bullet$) Py(6.7)-NAF(56), ($\blacksquare$) Py(5.8)-NAF(20), ($\square$) Py(5.8)-NAF(8), and ($\blacktriangle$) Py(5.5)-amylose ($\blacktriangle$).

The FBM analysis also yielded N_{blob}^{exp}, which represents the maximum number of structural units separating two AGUs bearing a pyrenyl label, while still allowing PEF to occur. N_{blob}^{exp} was obtained by introducing the parameters $<n>$ and f_{Mfree} retrieved from the global FBM analysis of the monomer and excimer fluorescence decays into Equation 2.3. N_{blob}^{exp} increased with increasing [NAF(56)] for all the Py-PS samples except for Py(5.5)-Amylose in Figure 2.2D. After starting from a similar N_{blob}^{exp} value of 16.7 ($\pm$1.1) averaged over all the Py-PSs except Py-

Amylose at low [NAF(56)], N_{blob}^{exp} increased with increasing [NAF(56)], until it reached a maximum value in Figure 2.2D equal to 43, 40, 28, and 24 for Py(4.2)-Amylopectin, Py(6.5)-NAF(56), Py(5.8)-NAF(20), and Py(5.8)-NAF(8), respectively. Since the increase in N_{blob}^{exp} occurred at about the same [NAF(56)] as for the increase in I_E/I_M in Figure 2.2B, the increase in N_{blob}^{exp} was attributed to PEF occurring between oligosaccharide side chains, due to a reduction in the interhelical distance (d_{h-h}) induced by the increase in osmotic pressure. As a result, the changes in N_{blob}^{exp} should provide quantitative information about d_{h-h} and the arrangement of the side chains of amylopectin in its interior. A relationship between the theoretical N_{blob} (N_{blob}^{theo}) and the interhelical distance (d_{h-h}) was previously established by conducting molecular mechanics optimizations (MMOs) on a cluster of 7 helices, representative of an infinite array of helices.[19] In this earlier study, the interactions between the pyrenyl labels attached onto the central helix and the pyrenyl labels attached onto the six surrounding helices were quantified to determine N_{blob}^{theo} as a function of d_{h-h}.[19] The N_{blob}^{theo}-vs-d_{h-h} relationship represented the interactions experienced by the pyrenyl labels attached onto helices constituting an infinite array of hexagonally packed helices. This relationship predicted that N_{blob}^{theo} would increase with decreasing d_{h-h}. While this behavior could qualitatively rationalize the increase observed for the N_{blob}^{exp} values in Figure 2.2D with increasing [NAF(56)], it could not explain two features of the plots. First, the maximum N_{blob}^{theo} obtained by assuming an infinite array of helices was 37, a value that was lower than the N_{blob}^{exp} values of 41 ($\pm$2) obtained for the Py-Amylopectin and Py-NAF(56) samples in Figure 2.2D at high [NAF(56)]. Second, the maximum value taken by N_{blob}^{exp} in Figure 2.2D depended on the size of the PSs, something that could not be accounted for by the earlier N_{blob}^{theo}-vs-d_{h-h} relationship.[19] These discrepancies were attributed to the fact that the earlier N_{blob}^{theo}-vs-d_{h-h} relationship was derived by considering an infinite array of oligosaccharide helices with an

interhelical spacing equal to d_{h-h}. While this assumption might have been justified for large polysaccharides like the Amylopectin and NAF(56) samples, smaller polysaccharides like NAF(8) and NAF(20) might not contain enough helices to be well-represented by an infinite array of helices. These considerations led to the study of the effect that the size of a finite array of helices might have on the N_{blob}^{theo}-vs-d_{h-h} relationship.

Finite Array of helices: A hexagonal array of helices is depicted in Figure 2.3A, where the array expands outward from the central helix in a layer-by-layer fashion, with each layer being numbered from $n = 0$ for the central helix and increasing by one unit at a time for each additional concentric layer of helices. As an example, the array shown in Figure 2.3A would thus be a generation $n = 3$ array. The helices were classified into six different categories depending on their location and the associated number of adjacent helices with which they could interact (see Table 2.2). A complete array of generation n is comprised of a total number $H_{total} = 3n^2 + 3n + 1$ of helices, where $3n^2 - 3n + 1$ and $6n$ helices are internal and peripheral helices, respectively, as shown in Figure 2.3A. Since there are always 6 corner helices in the complete array, $(6n - 6)$ helices are present on the six sides at the periphery of the hexagonal array.

The earlier N_{blob}^{theo}-vs-d_{h-h} relationship[19] was established by considering that the reference pyrenyl label in Helix #0 in Figure 2.3B was aiming toward Helix #1 along the x-axis defined by the line linking the centers of Helices #0 and #1. The earlier N_{blob}^{theo}-vs-d_{h-h} relationship[19] was refined in the present study by considering that the reference pyrene could also be oriented along the bisector of the angle defined by Helices #1, 0, and 2 in Figure 2.3C, corresponding to an angle φ equal to 30° with respect to the horizontal axis x. This refinement allowed the study of the interhelical interactions for a reference pyrene on Helix #0 at 12 possible φ angles stemming from the central Helix #0 in 30° increments from 0° to 330°.
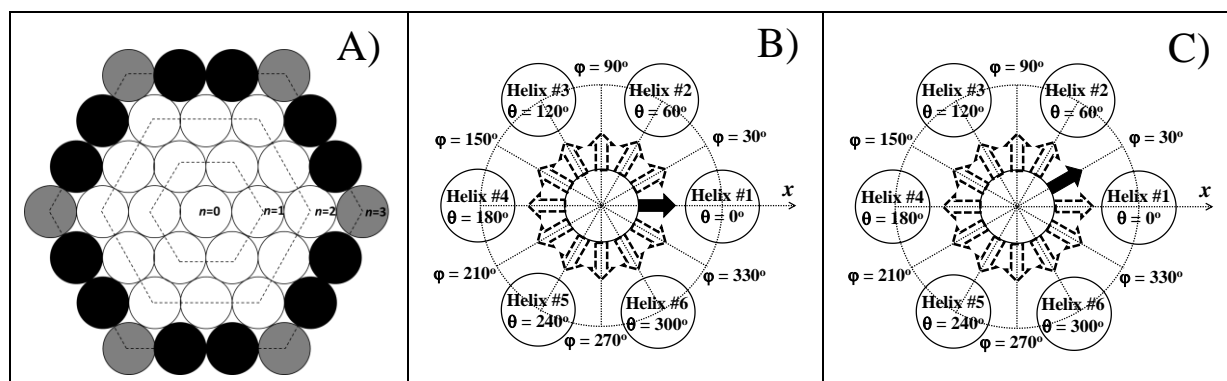
Figure 2.3. A) Illustration of an array of helices of generation n = 3, where the helices are defined according to their location as (●) side, (◉) corner, and (○) internal. The two configurations of pyrenyl labels considered in this study with the reference pyrenyl shown as a black arrow on the central Helix #0 located at (B) φ = 0° and (C) φ = 30° in a cluster of 7 helices.

Since the MMOs had already been conducted for a φ value of 0°, they were repeated herein for a reference pyrene having an orientation φ in Figure 2.3C equal to 30°. The secondary pyrenyl label was covalently attached to a second helix, separated from the central Helix #0 by a d_{h-h}, that was adjusted from 1.6 to 3.4 nm in 0.1 nm increments. The primary and secondary pyrenyl groups were induced to overlap by conducting MMOs with HyperChem in the same manner as what had been reported earlier.[19] In these MMOs, the pyrenyl moiety and its linker to the oxygen of the C2-hydroxyl of the AGU, to which the 1-pyrenebutyryl group was attached, was allowed to move, while the polysaccharide backbone of both helices was kept immobile. If the two frames of the overlapping pyrenyl labels retained a planar structure and resulted in 7 or more carbons of the reference pyrenyl overlapping the secondary pyrenyl, the overlap was considered suitable for successful PEF. N_{blob}^{theo} was then increased by one unit to account for the AGU bearing the secondary pyrenyl group leading to successful PEF. For a given d_{h-h}, the MMOs were repeated by changing the position of the secondary pyrenyl group along the backbone of the secondary helix, one AGU at a time, until the pyrenyl labels were too far apart to enable PEF. The MMOs were

60

then repeated by changing $d_{h\text{-}h}$ from 1.6 to 3.4 nm in 0.1 nm increments. N_{blob}^{theo} of each helix located at an angle $\theta = 0^o$ and 60° for φ equal to 0°, as depicted in Figure 2.3B, and at an angle $\theta = 60^o$ and 120° for φ equal to 30°, as depicted in Figure 2.3C, was plotted as a function of $d_{h\text{-}h}$ in Figure 2.4A, and the MMOs results are listed in Tables S2.10 and S2.11 in the SI. Over this range of $d_{h\text{-}h}$ values, no interactions could be detected between a reference pyrene attached on Helix #0 and a secondary pyrenyl label attached on a helix located at an angle θ greater than or equal to 90° or 120° in Figure 2.3B or C, where φ equaled 0 or 30°, respectively.
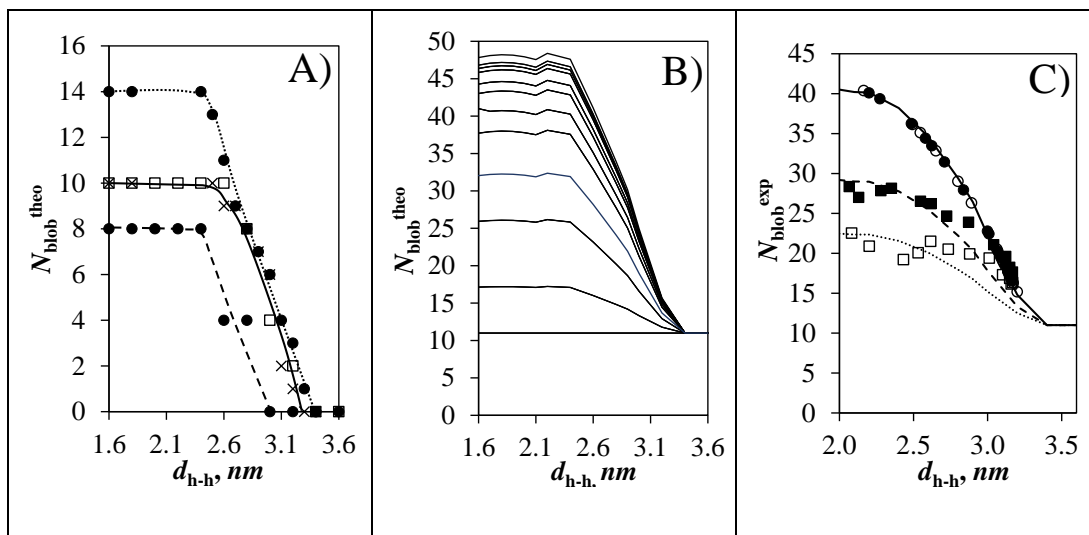
Figure 2.4. (A) Contributions to N_{blob} resulting from interhelical PEF when φ equals 0° and θ equals ($\square$) 0° and ($\bullet$) 60° and when φ equals 30° and θ equals ($\blacksquare$) 60° and ($\times$) 120° (see Figure 2.3B and C). (B) Plot of N_{blob}^{theo} with arrays constituted of different total numbers (H_{total}) of helices. From bottom to top: $H_{total} = 1, 2, 4, 7, 19, 37, 169, 547, 1027$, and ∞. (C) Plot of N_{blob}^{exp} of ($\bigcirc$) Py(4.2)-Amylopectin, ($\bullet$) Py(6.7)-NAF(56), ($\blacksquare$) Py(5.8)-NAF(20), and ($\square$) Py(5.8)-NAF(8) as a function of inter-helical distance. The lines represent the N_{blob}^{theo} predicted for an array with ($\cdots$) 3, (- - -) 6, and (—) 37 helices.

The effect of the position of the reference pyrene with different orientations in Helix #0 can be visualized in Figures 2.3B and C. In Figure 2.3B, the reference pyrene with $\varphi = 0°$ can interact with the three adjacent helices at $\theta = 0°$, $60°$, and $300°$, as reported earlier.[19] In Figure 2.3C, the reference pyrene with $\varphi = 30°$ can interact with the four adjacent helices located at $\theta = 0°$, $60°$, $120°$, and $300°$. The $N_{blob}^{theo}(\varphi{=}0°)$ or $N_{blob}^{theo}(\varphi{=}30°)$ values obtained for a primary pyrene located on Helix #0 with an orientation φ of $0°$ or $30°$ would thus equal $[N_{blob}^{intra}+N_{blob}(\theta{=}0°)+2{\times}N_{blob}(\theta{=}60°)]$ or $[N_{blob}^{intra}+2{\times}N_{blob}(\theta{=}30°)+2{\times}N_{blob}(\theta{=}90°)]$, respectively. In these expressions, N_{blob}^{intra} represents the maximum number of AGUs that would allow PEF between a reference and a secondary pyrenyl label both attached onto Helix #0. N_{blob}^{intra} was determined earlier and found to equal 11 for a single helix with 7 AGUs per turn.[21] In turn, $N_{blob}^{theo}(\varphi{=}0°)$ and $N_{blob}^{theo}(\varphi{=}30°)$ could be used to determine $N_{blob,\text{internal}}^{theo}$ for an internal helix, like Helix #0 in Figures 2.3B and C, surrounded by 6 helices in the hexagonal array. The expression for $N_{blob,\text{internal}}^{theo}$ is provided in Table 2.2. A similar methodology was applied to determine the expressions for $N_{blob,\text{side}}^{theo}$ and $N_{blob,\text{corner}}^{theo}$ for helices located at a side or a corner in the hexagonal array shown in Figure 2.3A and their expressions were also listed in Table 2.2. Using the same procedure, N_{blob}^{theo} for a complete n^{th} generation array of helices could be determined with Equation 2.5.

$$N_{blob}^{theo} = \frac{(3n^2 - 3n + 1)N_{blob,\text{internal}}^{theo} + (6n - 6)N_{blob,\text{side}}^{theo} + 6N_{blob,\text{corner}}^{theo}}{3n^2 + 3n + 1} \qquad (2.5)$$

The trends given in Figure 2.4A for $N_{blob}^{theo}(\varphi=0^o,\theta=0^o)$, $N_{blob}^{theo}(\varphi=0^o,\theta=60^o)$, $N_{blob}^{theo}(\varphi=30^o,\theta=60^o)$, and $N_{blob}^{theo}(\varphi=30^o,\theta=90^o)$ as a function of d_{h-h} could then be applied to determine how N_{blob}^{theo} would vary as a function of d_{h-h} and the number of helices included in a given array, as shown in Figure 2.4B. The N_{blob}^{theo} values merged into a single value equal to N_{blob}^{intra} for d_{h-h} values larger than 3.6 nm, where PEF occurred between two pyrenyl labels attached on a same helix. Since considering the angle $\varphi = 30^o$ in the MMOs led to an increase in N_{blob}^{theo}, the cut off where PEF could only occur intra-helically was increased from 3.2 nm, when only $\varphi = 0^o$ was considered,[19] to 3.6 nm with the present upgraded version of MMOs. As d_{h-h} decreased, N_{blob}^{theo} increased and spread more widely with increasing number of helices in an array, reaching a maximum spread for a d_{h-h} value of 2.4 nm. Interestingly, the plot of N_{blob}^{theo}-vs-d_{h-h} in Figure 2.4B could be viewed as being the mirror image of the plot of N_{blob}^{exp}-vs-[NAF(56)] obtained for the pyrene-labeled NAF(8), NAF(20), NAF(56) and Amylopectin samples in Figure 2.2D. This striking resemblance suggested that d_{h-h} and [NAF(56)] must be related to each other.

To find the relationship between d_{h-h} and [NAF(56)], the following procedure was applied. Since N_{blob}^{exp} for Py-Amylopectin and Py-NAF(56) seemed to plateau at a value of 41 (± 2), which corresponded to a hexagonal array of 37 helices in Figure 2.4B, the N_{blob}^{exp}-vs-[NAF(56)] plot in Figure 2.2D was attributed to that of a 37-helix array. The N_{blob}^{theo}-vs-d_{h-h} plot for a 37-helix array in Figure 2.4B was parametrized to find an empirical expression of d_{h-h} as a function of N_{blob}^{theo} with Equation 2.6. Replacing N_{blob}^{theo} for 37 helices in Equation 2.6 by the N_{blob}^{exp} values obtained for Py-Amylopectin and Py-NAF(56) as a function of [NAF(56)] yielded a plot of d_{h-h} as a function of [NAF(56)], which could be parametrized according to Equation 2.7.

$$d_{h-h} = \frac{62.08 + \sqrt{3854.3 - 64.43 \times [18.52 + N_{blob}^{theo}(37\ helices)]}}{32.22} \tag{2.6}$$

$$d_{\text{h-h}} = 2.82 \times 10^{-5} \times [\text{NAF}(56)]^3 - 2.36 \times 10^{-3} \times [\text{NAF}(56)]^2 + 1.52 \times 10^{-2} \times [\text{NAF}(56)] + 3.15 \quad (2.7)$$

Assuming that the osmotic pressure generated by high concentrations of NAF(56) onto the oligosaccharide helices was the same for Py-NAF(8) and Py-NAF(20) as for Py-NAF(56) and Py-Amylopectin, Equation 2.7 could be applied to plot $N_{\text{blob}}^{\text{exp}}$ of Py-NAF(8) and Py-NAF(20) as a function of $d_{\text{h-h}}$ in Figure 2.4C. Comparison of the $N_{\text{blob}}^{\text{exp}}$-vs-$d_{\text{h-h}}$ trends obtained for Py-NAF(8) and Py-NAF(20) in Figure 2.4C with the $N_{\text{blob}}^{\text{theo}}$-vs-$d_{\text{h-h}}$ trends obtained in Figure 2.4B led to the conclusion that the $N_{\text{blob}}^{\text{exp}}$ values were best represented by a subsection of an hexagonal array composed of 3 and 6 helices, respectively. Equation 2.7 also implied that in dilute dispersions, where $N_{\text{blob}}^{\text{exp}}$ equaled 17, 18, 16, and 15 for, respectively, Py(4.2)-Amylopectin, Py(6.7)-NAF(56), Py(5.8)-NAF(20), and Py(5.8)-NAF(8), $d_{\text{h-h}}$ equaled 3.2 nm, which was 0.3 nm larger than the $d_{\text{h-h}}$ of 2.9 nm found earlier[19] assuming that the array of oligosaccharide helices could be viewed as being infinite.

The reduction in the number of helices constituting arrays of 37, 37, 6, and 3 helices for Py-Amylopectin, Py-NAF(56), Py-NAF(20), and Py-NAF(8) was reasonable, when considering the reduction in D_{h} from 227 to 56, 20, and 8 nm, respectively. Indeed, a 37-helix array such as the one depicted in Figure 2.3A would have a diameter of ~21 nm assuming a $d_{\text{h-h}}$ of 3.2 nm under dilute conditions and a single helix diameter of 1.5 nm. NAF(8), with a D_{h} of 8 nm, would be much too small to accommodate such a large array of helices. It is also important to note that if the $N_{\text{blob}}^{\text{exp}}$-vs-$d_{\text{h-h}}$ trend for Py-NAF(8) in Figure 2.4C was best represented by an array of 3 helices, it did not mean that NAF(8) contained only three helices. Since the side chains of amylopectin from waxy corn are made of 19 AGUs on average,[30,31] 3 helices of 19 AGUs each would represent

a molar mass of 9.2×10^3 g/mol, much lower than the M_n of 1.5×10^5 g/mol reported for NAF(8) in Table 2.1. For NAF(20), NAF(56), and Amylopectin, the molar mass of clusters made of 6, 37, and 37 helices would equal 18.5, 114, and 114 kg/mol, which would be much lower than the M_n value of 1.0×10^6 g/mol and the M_v values of 2.3×10^6 and 7.2×10^7 g/mol of the corresponding PSs, respectively. Instead, these PSs should rather be viewed as groups of clusters of helices, where the clusters do not appear to interact with each other, since the trends described in Figure 2.4C assume a constant number of helices per cluster.

The similarity of the I_E/I_M-vs-[NAF(56)] plots in Figure 2.2B and the $N_{\text{blob}}^{\text{exp}}$-vs-[NAF(56)] plots in Figure 2.2D suggested that a similar procedure could be applied to the trends observed in Figure 2.2B for the I_E/I_M ratios in order to predict the size of the arrays of helices present in the Py-PSs. Consequently, the response of the I_E/I_M ratio to the number of helices constituting a hexagonal array was investigated as well by applying the following procedure. Each helix was divided into 12 sectors representing 30° each. A single helix, like amylose, could only form excimer intra-helically, resulting in an equivalent I_E/I_M(intra) ratio equal to β in each sector. Since each helix is composed of 12 sectors, the intra-helical I_E/I_M(intra) ratio would equal $12\times\beta$. A helix surrounded by six other helices as in Figures 2.3B and C could form excimer inter-helically, if d_{h-h} was small enough. Each sector capable of forming excimer inter-helically could do so with an I_E/I_M ratio equal to α. MMOs have established that a reference pyrenyl at $\varphi=0^o$ on Helix #0 in Figure 2.3B can contact 3 helices, which would represent six 30° sectors, and would thus yield an I_E/I_M ratio of $6\alpha+12\beta$. Similarly, since the reference pyrene at $\varphi=30^o$ in Figure 2.3C can interact with 4 helices, it would generate an I_E/I_M ratio of $8\alpha+12\beta$, respectively. Thus, the I_E/I_M (internal) ratio generated by a pyrenyl label attached on an internal helix would be $7\alpha+12\beta$ on average. The I_E/I_M(side) and I_E/I_M(corner) ratios of pyrenyl labels attached on helices located at, respectively

the sides or corners of a hexagonal array of helices were determined and the corresponding expressions are listed in Table 2.2. The I_E/I_M ratio of an nth generation array of helices would then be predicted by Equation 2.8.

$$\frac{I_E}{I_M} = \frac{(3n^2 - 3n + 1) \times I_E/I_M \text{(internal)} + (6n - 6) \times I_E/I_M \text{(side)} + 6 \times I_E/I_M \text{(corner)}}{(3n^2 + 3n + 1)} \quad (2.8)$$

The parameter β was determined with the I_E/I_M ratio of amylose at a given [NAF(56)]. The parameter α was determined by assuming that the I_E/I_M ratios obtained for Py-NAF(56) and Py-Amylopectin reflected those of a hexagonal array made of 37 helices, as was determined from the analysis of the N_{blob}^{exp}-vs-[NAF(56)] trends. α was found to increase sharply with increasing [NAF(56)], as compared to the modest increase in β, as shown in Figure 2.5A.

The α and β values at a given [NAF(56)] were applied to calculate the I_E/I_M ratio as a function of [NAF(56)] for hexagonal arrays composed of different numbers of helices. The I_E/I_M ratio increased with increasing [NAF(56)] as well as the number of helices, as shown in Figure 2.5B. The I_E/I_M profiles of Py-NAF(8) and Py-NAF(20) showed good agreement with the I_E/I_M ratios predicted for arrays of 4 and 7 helices. The estimates based on the I_E/I_M ratios, that NAF(8) and NAF(20) were constituted of arrays of 4 and 7 helices, matched fairly well the N_{blob}^{exp}-based predictions of 3 and 6 helices constituting the arrays of NAF(8) and NAF(20), respectively. The agreement found between the trends obtained with the I_E/I_M ratios and N_{blob}^{exp} suggests that these two sets of data obtained by SSF and TRF experiments and their analysis are internally consistent.
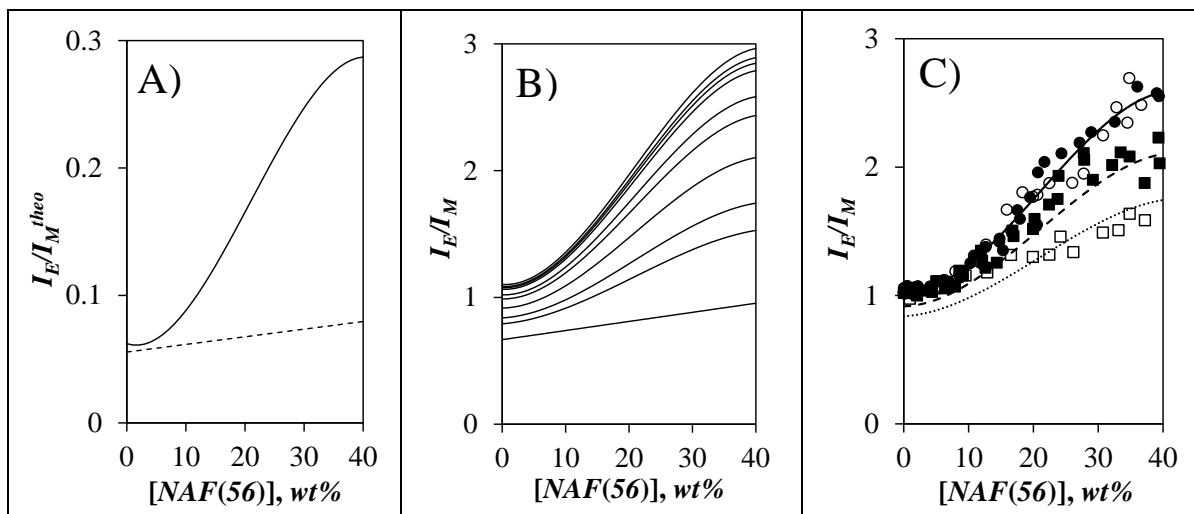
Figure 2.5. Plots of the predicted I_E/I_M ratio for (A) (—) α and (---) β, (B) for hexagonal arrays constituted of (from bottom to top) 1, 3, 4, 7, 19, 37, 168, 397, 1027, and ∞ helices, and (C) I_E/I_M ratio for hexagonal arrays of (⋯) 4, (---) 7, and (—) 37 helices compared with the experimental I_E/I_M ratios obtained for (◯) Py(4.2)-Amylopectin, (●) Py(6.7)-NAF(56), (■) Py(5.8)-NAF(20) and (☐) Py(5.8)-NAF(8).

Interparticle interactions: Interparticle interactions were identified by plotting I_E/I_M and N_{blob}^{exp} obtained for dispersions of Py-NAF(56) as a function of [Py-NAF(56)] in Figures 2.6A and B, and comparing the profiles to those obtained as a function of [NAF(56)] in Figures 2.2B and D. The I_E/I_M ratio and N_{blob}^{exp} obtained for Py-NAF(56) as a function of [NAF(56)] and [Py-NAF(56)] showed similar profiles, except that the increase in I_E/I_M and N_{blob}^{exp} occurred at a lower [Py-NAF(56)] in Figures 2.6A and B. The onset of the increase in I_E/I_M and N_{blob}^{exp} was observed at a [Py-NAF(56)] of 6.5 wt%, compared to 12 ($\pm$1) wt%, when NAF(56) was added to the Py-NAF(56) dispersion. Since an increase in I_E/I_M or N_{blob}^{exp} such as the one observed in Figures 2.6A and B suggested an increase in interparticle interactions, the fraction due to interparticle interactions (f_{inter}) was calculated by applying Equation 2.9. In Equation 2.9, I_E/I_M(high) was obtained with

dispersions of Py-NAF(56) only, whereas I_E/I_M(low) was obtained with 0.0059 wt% of Py-NAF(56) and a large excess of unlabeled NAF(56). f_{inter} was plotted as a function of [NAF(56)] in Figure 2.6C.

$$f_{\text{inter}} = \frac{I_E/I_M(high) - I_E/I_M(low)}{I_E/I_M(high)} = \frac{N_{blob}^{\exp}(high) - N_{blob}^{\exp}(low)}{N_{blob}^{\exp}(high)} \qquad (2.9)$$
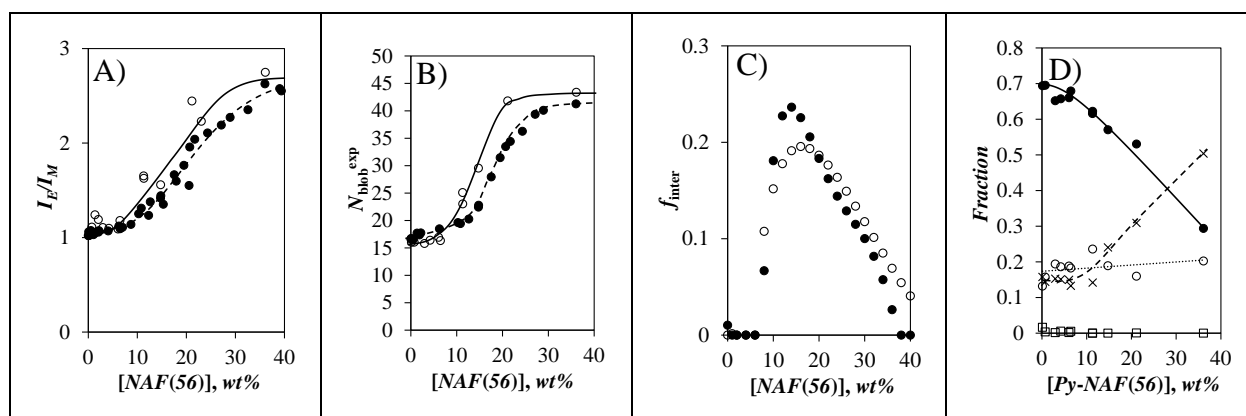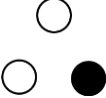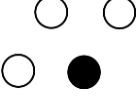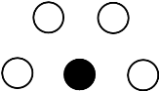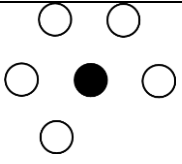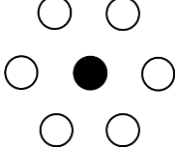
Figure 2.6. Plots of (A) I_E/I_M and (B) N_{blob}^{exp} for Py(6.7)-NAF(56) as a function of the concentration of (●) unlabelled NAF(56) and (○) Py(6.7)-NAF(56). (C) Plot of the fraction of interparticle interactions (f_{inter}) obtained with (●) N_{blob}^{exp} and (○) the I_E/I_M ratio. (D) Plot of the molar fractions of (●) Py$_{diff}$, (○) Py$_{k2}$, (×) Py$_{agg}$, and (□) Py$_{free}$ for Py(6.7)-NAF(56) as a function of [Py(6.7)-NAF(56)].

The f_{inter} trends obtained in Figure 2.6C with the I_E/I_M ratio and N_{blob}^{exp} were similar. f_{inter} increased sharply from a value of 0.0 at a [NAF(56)] of 6.5 wt%, reached its maximum value of 0.22 (±0.03) at a [NAF(56)] of 15 (±1) wt%, and decreased thereafter. Due to its branched structure, amylopectin is expected to exhibit a behavior intermediate between that of a hard sphere and a

flexible chain, as illustrated by a study based on the osmotic modulus. [32] The interparticle interactions observed for amylopectin in Figure 2.6C might occur via partial interpenetration of the NAF(56) particles and the association of their side chains, particularly for those helices located at the periphery of the particles. The penetration of helical side chains in the outermost layer of NAF(56) would increase the number of helices inside a cluster and decrease the d_{h-h}. These changes would lead to an increase in I_E/I_M and N_{blob}^{exp} as $[Py]_{loc}$ increases. On the other hand, I_E/I_M and N_{blob}^{exp} remained constant up to a [NAF(56)] of 12 ($\pm$1) wt% in Figures 2.4B and D, above which compression of Py-NAF(56) was observed. This observation suggests that the penetration of helices from NAF(56) into the peripheral voids of Py-NAF(56) did not affect d_{h-h} up to a [NAF(56)] of 12 ($\pm$1) wt%. Once the compression of the clusters of helices was triggered, I_E/I_M, N_{blob}^{exp}, and f_{inter} increased up to a [NAF(56)] of 15 wt%. Above this [NAF(56)], f_{inter} decreased indicating that the particles dissociated from each other to adopt a more compact conformation. I_E/I_M and N_{blob}^{exp} continued to increase as the helices were brought closer to each other and d_{h-h} was reduced. As the helices were brought ever closer to each other, $[Py]_{loc}$ increased and the major pathway for PEF changed from a diffusive pathway to a direct excitation of pyrene aggregates as f_{diff} was found to decrease and f_{k2} increase for [NAF(56)] greater than 12 wt%.

Table 2.2. Illustration of a helix surrounded by different number of adjacent helices and its corresponding N_{blob} and I_E/I_M ratio

Name (# adjacent helices)	Illustration	Expressions of $N_{\text{blob}}^{\text{theo}}$ for different arrays of helices	I_E/I_M
Single (1)	○ ●	$\dfrac{12N_{blob}^{\text{intra}} + N_{blob}(0,0) + 2N_{blob}(30,60) + 2N_{blob}(0,60) + 2N_{blob}(30,90)}{12}$	$\left(\dfrac{14}{12}\right)\alpha + 12\beta$
Vertex (2)	○ ○ ●	$\dfrac{12N_{blob}^{\text{intra}} + 2N_{blob}(0,0) + 4N_{blob}(30,60) + 4N_{blob}(0,60) + 3N_{blob}(30,90)}{12}$	$\left(\dfrac{28}{12}\right)\alpha + 12\beta$
Corner (3)	○ ○ ○ ●	$\dfrac{12N_{blob}^{\text{intra}} + 3N_{blob}(0,0) + 6N_{blob}(30,60) + 6N_{blob}(0,60) + 6N_{blob}(30,90)}{12}$	$\left(\dfrac{42}{12}\right)\alpha + 12\beta$
Side (4)	○ ○ ○ ● ○	$\dfrac{12N_{blob}^{\text{intra}} + 4N_{blob}(0,0) + 8N_{blob}(30,60) + 6N_{blob}(0,60) + 8N_{blob}(30,90)}{12}$	$\left(\dfrac{56}{12}\right)\alpha + 12\beta$
Quasi-Internal (5)	○ ○ ○ ● ○ ○	$\dfrac{12N_{blob}^{\text{intra}} + 5N_{blob}(0,0) + 10N_{blob}(30,60) + 10N_{blob}(0,60) + 10N_{blob}(30,90)}{12}$	$\left(\dfrac{70}{12}\right)\alpha + 12\beta$
Internal (6)	○ ○ ○ ● ○ ○ ○	$N_{blob}^{\text{intra}} + \dfrac{N_{blob}(0,0)}{2} + N_{blob}(30,60) + N_{blob}(0,60) + N_{blob}(30,90)$	$7\alpha + 12\beta$

70

2.5 Discussion

Following the proposal of the CL model, amylopectin was treated with different enzymes to determine the size of a cluster of helices.[12] Endoenzymes cleave long internal chains connecting clusters and thereby release the clusters, whose composition has been determined by light scattering,[33] microscopy,[34] chromatography,[31] and exo-enzymatic treatment followed by ^{1}H NMR analysis.[35] The number of helices constituting a cluster in amylopectin has been reported to range from 4.2 single helices[33] to 17 double helices.[34] The array of helices predicted by the PEF experiments are expected to represent a single cluster, and it is thus noticeable that the latter estimate of 17 double helices in a crystalline cluster[34] would translate into a 34 single helices cluster in an amylopectin dispersion, remarkably close to the PEF-based estimate of 37 helices made in this study. The changes in I_E/I_M and N_{blob}^{exp} for a particular Py-PS could be rationalized by assuming that the fluorescence response of the Py-PSs was the result of a constant number of helices in the clusters for [NAF(56)] ranging from 0 to 40 wt%. These PEF experiments were expected to probe the changes that occur in a single cluster rather than changes resulting from interactions between clusters. The number of helices constituting a cluster depended on the size of the PS studied. This was reasonable as the NAFs were obtained through degradation of amylopectin from waxy corn starch, where random parts of amylopectin, including clusters of helices, must have been cleaved off during the process. Since amylopectin from waxy maize is constituted of oligosaccharides that are about 19 AGUs in length, [30, 31] a cluster with 37 helices 19 AGU-long would have an M_n of 1.1×10^5 g/mol. The M_w of NAF(56),[19] NAF(20), and NAF(8) were determined to equal 5.4×10^6, 1.9×10^6, and 2.6×10^5 g/mol, respectively. NAF(8) and NAF(20), constituted of clusters containing 3 and 6 helices, respectively, would be expected to contain

degraded clusters where some helices were removed through debranching taking place during the degradation of amylopectin to produce the NAFs. Considering that the helices inside a cluster are expected to be separated by ~ 3.2 nm in dilute dispersions, such a cluster of 3 or 6 helices would have a size of ~ 5 or 9 nm, which would fit within the internal volume defined by the D_h of 8 and 20 nm for NAF(8) and NAF(20), respectively.

The Side Chain Liquid Crystalline Polymer (SCLCP)[16,17,18] has been proposed to rationalize the hydration and gelatinization of amylopectin. Amylopectin behaves like a liquid crystalline polymer, where the helical side chains can be viewed as mesogens and the short chains connecting the helix to the polysaccharide backbone act as a flexible spacer. In the SCLCP model, the helices can be either oriented in loose parallel lines or arranged in a lamella with their axis perpendicular to the plane of the lamella, in a process that generates nematic or smectic phases, respectively. The smectic orientation of amylopectin has been observed in the presence of water, which acts as a plasticizer and which facilitates the decoupling of the helices from the backbone.[16] The assumption made to predict N_{blob}^{theo} and I_E/I_M^{theo} was that all the helices were ordered laterally as expected in a smectic orientation. The good agreement between the theoretical and experimental results shown in Figures 2.4C and 2.5C with, respectively, N_{blob}^{theo} and I_E/I_M^{theo} suggests that this assumption is valid. It is possible that DMSO might function as a plasticizer, in the same manner as water does, which would allow the helices to take the smectic orientation. Consequently, the PEF results appear to agree with the SCLCP model, assuming that the helical side chains adopt a smectic phase in DMSO.

The Building Block Backbone Model (BBBM) was proposed based on the experimental results of the enzymatic treatment of amylopectin.[14,15] From its design, the BBBM refutes the notion of cluster. The building block consists of the ultimate branching units, whose degree of

branching varies from 2 to 10 for waxy maize amylopectin.[36] The building blocks are randomly distributed along the backbone and separated by 6 AGUs on average in waxy maize amylopectin.[37] MMOs conducted with HyperChem showed that an AGU spans 0.78 nm. In this case, two adjacent building blocks or side chains would be separated by 4.7 nm, and it has been suggested that these side chains might adopt a single helix conformation, which would lead to the formation of microcrystallites upon bringing the building blocks closer.[38] First, if the side chains were so far apart, no interhelical PEF would occur, since the MMO results shown in Figure 2.4B require two helices to be separated by less than 3.6 nm for PEF to occur. The experimental results indicate a substantial increase in PEF for dilute dispersions, which requires that the helices be within ~ 3.0 nm from one another, much closer than expected from the BBBM. Furthermore, the BBBM suggests that the number of helices involved in PEF would be expected to increase as the $d_{\text{h-h}}$ gets smaller. However, the PEF results were well represented by assuming that the number of helices involved in PEF remained constant inside a cluster upon compressing the pyrene-labeled amylopectin and NAF samples. Consequently, the PEF results presented in this report were better explained by the recently suggested Solution-Cluster model[19] than the BBBM.

2.6 Conclusion

The compressibility of amylopectin and three NAFs was studied by monitoring the $I_{\text{E}}/I_{\text{M}}$ ratio and $N_{\text{blob}}^{\text{exp}}$ as a function of [NAF(56)]. The increase in NAF concentration above C* increased the osmotic pressure in the dispersions, which triggered the shrinkage of these branched PSs. The compression reduced the $d_{\text{h-h}}$ resulting in an increase in $[Py]_{\text{loc}}$, which translated into larger $I_{\text{E}}/I_{\text{M}}$ and $N_{\text{blob}}^{\text{exp}}$ values as [NAF(56)] increased. Amylopectin and the three NAFs showed evidence of

compression at 12 ($\pm$1) wt% regardless of their size. The maximum values reached by the I_E/I_M ratio and N_{blob}^{exp} upon increasing [NAF(56)] showed a dependency with the size of the PSs. Amylopectin and NAF(56) showed the largest increase, followed by NAF(20) and NAF(8). These observations suggested that PEF between pyrenyl labels was generated in finite domains, assumed to be clusters of helices, whose size increased with the size of the corresponding PS. MMOs were conducted to predict how the I_E/I_M^{theo} ratio and N_{blob}^{theo} values would vary as a function of the number of helices in a cluster and as a function of d_{h-h}. Comparison of the I_E/I_M^{theo} ratio and N_{blob}^{theo} values with the I_E/I_M^{exp} ratio and N_{blob}^{exp} values led to the conclusion that a cluster of helices in amylopectin, NAF(56), NAF(20), and NAF(8) consisted of 37, 37, 6, and 3 helices, respectively. The number of 37 single helices in a cluster of amylopectin in a DMSO dispersion was in surprisingly good agreement with reports stating that clusters of up to 17 double helices (i.e. 34 single helices), had been observed in the unit cell of amylopectin.[34] Considering how important the notion of clusters of helices is in amylopectin and PSs derived from it, the ability to probe the size of these clusters by PEF experiments is expected to find numerous applications for the characterization of amylopectin extracted from different organisms.

Chapter 3

Interior of Glycogen Probed by Pyrene Excimer Fluorescence

3.1 Abstract

A glycogen sample from oyster (O) and another from corn (C) were fluorescently labeled with 1-pyrenebutyric acid to yield two series of pyrene-labeled glycogen samples (Py-Glycogen(O/C)). The glycogen samples were characterized at the macroscopic level by applying gel permeation chromatography (GPC) and viscosity measurements to determine their number average molecular weight (M_n) and intrinsic viscosity ($[\eta]$). The internal structure of the glycogen samples was investigated further by conducting time-resolved fluorescence (TRF) measurements to probe the process of excimer formation between an excited and a ground-state pyrene with the Py-Glycogen(O/C) samples. Global analysis of the TRF decays of the pyrene monomer and excimer with the fluorescence *blob* model (FBM) yielded the maximum number ($<N_{\text{blob}}^{\text{exp}}>$) of anhydroglucose units (AGUs), that could separate two pyrene-labeled AGUs and still allow efficient pyrene excimer formation (PEF). Assuming that interhelical PEF occurred in the denser parts of the Py-Glycogen(O/C) samples, where the helical oligosaccharide side chains labeled with pyrene were assumed to form a hexagonal close packed (HCP) lattice, molecular mechanics optimizations (MMOs) were conducted on this lattice to determine the theoretical $<N_{\text{blob}}^{\text{theo}}>$ value representing the entire glycogen molecule. $<N_{\text{blob}}^{\text{exp}}>$ was compared to $<N_{\text{blob}}^{\text{theo}}>$ obtained with two local density profiles across the glycogen particles, where the local density of glycogen took its maximum value either at the center or at the periphery of the particles. The local density profiles found to yield a good agreement between $<N_{\text{blob}}^{\text{exp}}>$ and $<N_{\text{blob}}^{\text{theo}}>$ suggested that the internal side chains of glycogen experienced a dense environment. This study further illustrates the ability of PEF to characterize the interior of complex polysaccharide particles.

3.2 Introduction

Glycogen is a major carbohydrate, that animals and humans alike use for energy storage. The structure of glycogen has been investigated for many years.[123456-7]Glycogen is made of linear segments of anhydroglucose units (AGUs) joined by α-(1,4) glycosidic bonds connected to each other by α-(1,6) glycosidic bonds.[1,2] The general structure of glycogen is similar to that of amylopectin, the major carbohydrate used for energy storage by plants. However, the degree of branching of glycogen is twice larger than for amylopectin. Over the years, several models involving single[1,3] or multiple branches[10] have been proposed to describe the structure of glycogen. The application of enzymatic treatments to glycogen demonstrated that the internal structure of glycogen involved multiple branches, where the branching points were arranged in "tiers" with the number of branching points increasing from the inner tier to the outer tier.[4,5,11]Since the volume of a glycogen molecule increases less quickly than the number of branches in each tier, the Tier Model implied that a limit had to be reached, where steric congestion at the periphery would block further glycogen growth.[6,12]Theoretical calculations led to the prediction, that glycogen was constituted of a maximum of 12 tiers.[6,1314]This prediction was further supported by more recent studies aiming to better understand the glycogen turnover in the brain,[15]the oxidation of glycogen in various solvents,[16]and the distribution of glycogen molecules in the liver[17]and in resting, human skeletal muscle.[18,19]The Tier Model has also been acknowledged in more recent reviews.[20-22]However, recent Monte-Carlo simulation of glycogen have led to the suggestion that the density profile inside glycogen particles is opposite to that predicted by the Tier Model.[23]The simulation results show that the density of glycogen reaches its maximum near the center of mass and not at the periphery as predicted by the Tier Model. These predictions have been supported by small

angle neutron scattering experiments, that provide support to a dense core decorated with short chains at its periphery.[24]

To date, glycogen has been characterized at the macroscopic level by determining the size distribution of a population of glycogen molecules, typically by microscopy,[17,19,25] size exclusion chromatography,[17,26]or scattering techniques.[24]In contrast, a recent publication[27]has argued that *the internal structure of glycogen molecules is not fully understood*. To address this issue, this study uses the fluorescence of an excimer generated through the encounter between an excited and a ground-state pyrene to examine the internal structure of glycogen. To this end, two glycogen samples from oyster (O) and corn (C) were randomly labeled with different amounts of 1-pyrenebutyric acid (PyBA) to yield two series of Py(x)-Glycogen(O/C) constructs, where x represents the molar percentage of pyrene-labeled AGUs, that ranged from 0.02 to 7.8 mol%. The fluorescence decays of the Py(x)-Glycogen(O/C) samples were analyzed according to the fluorescence *blob* model (FBM), which arbitrarily compartmentalizes the volume of a macromolecule into identical *blobs* representing the volume probed by an excited pyrenyl label. In turn, the FBM analysis yielded the number (N_{blob}^{exp}) of AGUs encompassed in a *blob*. In the case of polysaccharides labeled with a PyBA derivative, a *blob* can be viewed as a monodisperse sphere of diameter 4.6 nm[28] or 5.1 nm (see Supporting Information (SI)) depending on whether PyBA is attached on a C2- or C6-hydroxyl, respectively.

The short length scale, over which an excimer between an excited and a ground-state pyrene is formed, implies that fluorescence only senses the space occupied by the polymeric segments inside the macromolecular interior, where the pyrenyl labels are sufficiently close to interact with each other and form an excimer. Consequently, pyrene excimer

fluorescence/formation (PEF) offers a means to probe the spacing between the oligosaccharide branches of the Py(x)-Glycogen(O/C) samples, an information, which can be applied to predict the local density (ρ) of glycogen. This is accomplished in the present study by comparing $<N_{\text{blob}}^{\text{exp}}>$, obtained after averaging over all pyrene contents x of a given Py(x)-Glycogen series, with the theoretical $<N_{\text{blob}}^{\text{theo}}>$ value, obtained by conducting molecular mechanics optimizations (MMOs) on pyrene-labeled oligosaccharide helices arranged in a hexagonal close packed (HCP) lattice. These MMOs were carried out to determine the number $N_{\text{blob}}^{\text{theo}}$ of AGUs on different helices, that could be labeled with pyrene and would lead to PEF, as a function of the interhelical distance ($d_{\text{h–h}}$) in the HCP lattice. The $d_{\text{h-h}}$ was converted into the local density ρ. The $N_{\text{blob}}^{\text{theo}}$-$vs$-$\rho$ relationship allowed the calculation of $<N_{\text{blob}}^{\text{theo}}>$ taken as the weighed average of all the $N_{\text{blob}}^{\text{theo}}(\rho)$ values obtained by considering two $\rho(r)$ profiles as a function of the distance r from the center of the Glycogen(O/C) molecules. The $\rho(r)$ distributions assumed that ρ either increases or decreases from the center to the periphery. The former distribution is that predicted from a mathematical representation of the Tier Model by Meléndez-Hevia et al.,[13] referred to as the Meléndez-Hevia model, and the latter distribution was assumed to obey a $\rho_{\text{max}} \times \exp(-ar^b)$ function, which was referred to as the Gilbert model.[23] The $\rho(r)$ distribution based on the Meléndez-Hevia model underestimated $<N_{\text{blob}}^{\text{theo}}>$ compared to $<N_{\text{blob}}^{\text{exp}}>$, which led to the suggestion that the side chains in the interior of glycogen must experience a much larger local density than that predicted from the Meléndez-Hevia model. Assuming a $\rho_{\text{max}} \times \exp(-ar^b)$ profile for the $\rho(r)$ distribution, the ρ_{max}, a, and b parameters could be determined from M_n and the hydrodynamic radius (R_h) of the glycogen particles, that yielded an $<N_{\text{blob}}^{\text{theo}}>$ value, that matched $<N_{\text{blob}}^{\text{exp}}>$. Consequently, the PEF-based methodology described in this study suggests that the side chains of glycogen located

in the interior of the particles experience a high density, in agreement with the Gilbert model[23] and a recent SANS study.[24]

3.3 Experimental

Materials: Glycogen from oyster (Type II) was purchased from Sigma Aldrich and phytoglycogen from corn was generously donated by Mirexus (Guelph, ON, Canada). Dextran (M_w= 1.07×10^4 g/mol; PDI=1.5) was purchased from Biosynth Carbosynth. All polysaccharides were first dispersed in dimethylsulfoxide (DMSO) before being precipitated in ethanol. The precipitate was collected through suction filtration, rinsed with a large amount of ethanol to wash away any remaining DMSO, and finally air dried. All other chemicals were purchased from Sigma Aldrich and used without purification.

Characterization of Glycogen by Gel Permeation Chromatography: The number (M_n) and weight (M_w) average molecular weight of the glycogen samples were determined with a TOSOH EcoSEC high temperature gel permeation chromatography (GPC) instrument equipped with a triple detection system, a guard column, and a 300 mm×7.8 mm ID TSKgel Alpha-M column. This column had an upper theoretical cut off of 10^7 Da based on the hydrodynamic volume of linear PEGs in water. The triple detection system included an in-line differential refractometer, a multi-angle laser light scattering detector, and a viscometer. A flow rate of 0.6 mL/min of DMSO at 60 °C was used. The system was calibrated with a 1.0 g/L solution of a pullulan standard in DMSO with an M_n of 47.1 kg/mol and PDI of 1.07. The Glycogen(O/C) samples were dispersed in DMSO at a concentration of 1.0 g/L. They were kept at 80 °C until the dispersions were clear, before being left to cool to room temperature. The dispersions were gently filtered through a 0.22 μm syringe filter twice before injection into the GPC instrument.

Intrinsic Viscosity of Glycogen Samples in DMSO: The intrinsic viscosity of the glycogen samples was determined in DMSO at 25 °C with an Ubbelohde viscometer. The glycogen samples were dispersed in DMSO by stirring the dispersions at 80 °C for two hours. The dispersions were prepared with polysaccharide concentrations ranging from 0.02 to 0.05 g/mL.

Labeling of Glycogen with 1-Pyrenebutyric Acid/1-Naphthelene Acetic Acid: The esterification, purification, and characterization of the pyrene- or naphthalene-labeled samples of glycogen from oyster or corn (Py/Np(x)-Glycogen(O/C)) or dextran (Py/Np(x)-Detran) were conducted in the same manner as presented in an earlier publication, where nanosized amylopectin fragments were labeled with 1-pyrenebutyric acid (PyBA).[29] The synthesis of glycogen from oyster labeled with 8 mol% pyrene (Py(8)-Glycogen(O)) is described in detail hereafter. The purified glycogen (1.00 g, 6.2 mmol of AGU) was dispersed in 30 mL of DMSO at 80 °C and the solution was placed in a three-neck round bottom flask (RBF). PyBA (1.0 g, 3.5 mmol) and 4-dimethylaminopyridine (DMAP) (67 mg, 0.5 mmol) were added into the RBF, after glycogen was fully dispersed. Then, 10 mL of DMF was added to the mixture. The flask was sealed with a rubber septum. The purpose of DMF was to prevent the mixture from freezing in the next step, where the mixture was kept in an ice bath under nitrogen. After 15 minutes, *N,N'*-diisopropylcarbodiimide (DIC) (0.8 mL, 5.3 mmol) was added dropwise into the solution with a syringe. The flask was then removed from the ice bath and covered with aluminum foil to minimize degradation of pyrene from exposure to light and the mixture was left to react at room temperature for 48 hours. Afterwards, the reaction mixture was precipitated four times into THF to remove unreacted free PyBA.

Dye Content Determination: A stock dispersion of the Py/Np(x)-Glycogen(O/C) samples was prepared in DMSO with a known mass concentration. The dispersion was stirred at 80 °C for about

two hours. The stock dispersion was diluted with DMSO to yield a minimum of five diluted dispersions, whose absorbance at 346 nm for the Py(x)-Glycogen(O/C) samples or at 284 nm for the Np(x)-Glycogen(O/C) samples were selected to be lower than 2.0 to not saturate the detector. The absorption spectra of the Py/Np(x)-Glycogen(O/C) dispersions were acquired with a 1.00 cm path length (L) quartz cuvette using a Cary 100 bio-UV-Vis spectrophotometer. Plotting the absorbance at 346 nm or 284 nm of the dispersions as a function of their mass concentration yielded a straight line, whose slope (m) equaled $\varepsilon_{Py/Np} \times L \times \lambda_{Py/Np}$, where $\varepsilon_{Py/Np}$ is the molar absorption coefficient equal to 41,400 $M^{-1}.cm^{-1}$ at 346 nm and 6,140 $M^{-1}.cm^{-1}$ at 284 nm for 1-pyrenebutyric acid[30] and 1-napthalene acetic acid[29] in DMSO, respectively, and $\lambda_{Py/Np}$ is the pyrene/naphthalene content, expressed in moles of pyrene per gram of polysaccharide. $\lambda_{Py/Np}$ was determined from Equation 1 after re-arranging the expression of m.

$$\lambda_{Py/Np} = \frac{m}{\varepsilon_{Py/Np} \times L} \tag{3.1}$$

The molar fraction x of AGUs labeled with pyrene or naphthalene in a given Py/Np(x)-Glycogen(O/C) sample was calculated by applying Equation 3.2, where M_{AGU} is the molar mass of an unlabeled AGU (162 g/mol), M_X (with X = Py or Np) represents the molar mass of pyrene-labeled (432 g/mol) or naphthalene-labeled (330 g/mol) AGUs, respectively, and λ_X is the pyrene or naphthalene content of the Py/Np(x)-Glyogen(O/C) samples determined with Equation 3.1.

$$x = \frac{M_{AGU}}{M_{AGU} - M_X + \lambda_X^{-1}} \tag{3.2}$$

The dye contents of the Py/Np(*x*)-Dextran samples were determined in the same manner as described for Py/Np(*x*)-Glycogen(O/C), except that the solutions of Py/Np(*x*)-Dextran in DMSO were prepared by stirring at room temperature instead of 80 $^{\circ}$C.

Preparation of Samples for Fluorescence Resonance Energy Transfer Experiments: All Py/Np-Glycogen dispersions and Py/Np-Dextran solutions in DMSO were prepared in a similar manner as described in more detail hereafter for the glycogen sample. Np(126)-Glycogen and Py(6.8)-Glycogen were dispersed separately in DMSO at 80 $^{\circ}$C to obtain the same absorbance of 0.5 at 284 nm for the Np(126)-Glycogen dispersion and at 346 nm for the Py(6.8)-Glycogen dispersion, corresponding to a concentration of 31.8 and 24.3 mg/L for the Py(6.8)-Glycogen and Np(126)-Glycogen, respectively. A mixture of the two dispersions was prepared by mixing 0.3 g of the Py(6.8)-Glycogen dispersion with 2.7 g of the Nap(126)-Glycogen dispersion. Two 1 g aliquots of the mixture were placed in two vials. In one vial, 9 g of water was added, whereas 9 g of DMSO was added to the other vial, to generate two dispersions of Np(126)-Glycogen and Py(6.8)-Glycogen mixture in a 10:90 DMSO:water mixture and in pure DMSO, respectively. Dispersions of 2.2 mg/L Np(126)-Glycogen and 0.3 mg/L Py(6.8)-Glycogen were prepared with different water contents by mixing different ratios of the two stock dispersions prepared in a 10:90 DMSO:water mixture and in pure DMSO. The emission spectra were excited at 293 nm by exciting the naphthalene labels for the FRET measurements and at 346 nm to solely excite the pyrenyl labels for the PEF measurements. The same procedure was applied to prepare solutions for the FRET and PEF measurements with 2.1 mg/L and 0.2 mg/L of the Np(130)-Dextran and Py(12.8)-Dextran samples, respectively, the only differences between the glycogen dispersions and dextran solutions being that the dextran solutions were stirred at room temperature for two hours and that

the Py(12.8)-Dextran concentration was smaller than that of the Py(6.8)-Glycogen dispersion, since its pyrene content was twice larger.

Deformability of the Polysaccharides: The sample of Py(5.5)-Amylopectin, which had been prepared in Chapter 2, and the Py(5.3)-Glycogen(O) sample were dispersed in DMSO by stirring overnight at 95 °C and 80 °C, respectively. The polysaccharide dispersions were prepared so that the final concentration of pyrene was about 2.4×10^{-6} M, which corresponded to an absorbance of ~0.1. Samples of poly(ethylene glycol) (PEG(X), where X represents an M_n value of 0.2, 0.4, 2.0, and 10 K), were added to the polysaccharide dispersions. The PEG concentration ranged from 0 to 36 wt% for PEG(0.2K), PEG(0.4K), and PEG(2K) and to 22 wt% for PEG(10K). The polysaccharide dispersions in DMSO with PEG were stirred at 60 °C for an hour. The steady-state fluorescence spectra of the dispersions were acquired immediately after cooling the samples to room temperature. The samples were visually inspected to check for any possible crystallization of PEG at high concentration before acquiring the spectra.

Steady-State Fluorescence Measurements: The steady-state fluorescence spectra were acquired on a Horiba QM-400 spectrofluorometer equipped with a xenon arc lamp. Dispersions of the Py(x)-Glycogen(O/C) samples in DMSO were prepared with a pyrene concentration of 2.4 μM (equivalent to an absorption of 0.1) to avoid inter-macromolecular interactions as well as the inner-filter effect. The fluorescence spectra were acquired by scanning the fluorescence intensity from 360 to 650 nm and using an excitation wavelength of 346 nm. The width of the excitation and emission slits was set at 1.0 nm for the fluorescence experiments. The contributions of the pyrene monomer (I_M) and excimer (I_E) to the fluorescence spectra were quantified by integrating the fluorescence spectra from 376 to 382 nm for the pyrene monomer and from 500 to 530 nm for the pyrene excimer. They were used to determine the I_E/I_M ratio to assess the PEF efficiency of a given

Py(x)-Glycogen sample. An excitation wavelength of 293 nm was selected for the FRET measurements, where the glycogen and dextran solutions had an absorption smaller than 0.1 for wavelengths greater than 290 nm. The fluorescence spectra were acquired from 310 to 570 nm.

Time-Resolved Fluorescence Measurements: The fluorescence decays of the pyrene monomer and excimer were acquired with a time-resolved fluorometer from IBH. The excitation wavelength was set at 346 nm with an excitation monochromator using a 340 nm nanoLED. A Ludox suspension was employed to obtain the instrument response function (IRF) by exciting and collecting the scattering response at the same wavelength of 346 nm as for the excitation. The fluorescence decays of the pyrene monomer and excimer were collected at 375 nm with a 370 nm cut-off filter and 510 nm with a 470 nm cut-off filter, respectively. The cut off filters prevented stray light from reaching the detector. Fluorescence decays were obtained with a time-per-channel of 1.02 ns/ch and at least 20,000 counts at the decay maximum.

Analysis of the Fluorescence Decays with the Fluorescence Blob Model (FBM): The FBM was applied to fit the fluorescence decays of the Py(x)-Glycogen dispersions in DMSO. Details of the FBM analysis can be found in earlier publications.[31,-33] A brief summary of the FBM is provided hereafter. The FBM acknowledges that an excited pyrenyl label covalently attached onto a macromolecule can only probe a subvolume of the macromolecule, while it remains excited. This unit volume referred to as a *blob* can be used to compartmentalize the macromolecular volume into a cluster of *blobs*. Random labeling of the macromolecule with pyrene derivatives ensures that the pyrenyl labels are randomly distributed among the *blobs* according to a Poisson distribution. Four excited pyrene species are considered for the FBM analysis. *Py*$_{free}$* represents the excited pyrenes, that cannot form excimer, because they are isolated in the macromolecule and

relax back to their ground state by emitting a photon with their natural lifetime, τ_M. Excited pyrenes, that are aggregated with ground-state pyrenes, are referred to as $Py_{agg}*$ and form excimer quasi-instantaneously upon direct excitation. The $Py_{agg}*$ pyrenes can generate two types of excimer, namely $E0*$ and $D*$, which are dimers made of two pyrenyl units, that are well or poorly stacked and emit with their lifetime τ_{E0} and τ_D, respectively.

The two other excited pyrene species lead to PEF according to a sequential process. First, an excited pyrene $Py_{diff}*$ bound to an AGU diffuses in solution based on the internal dynamics experienced by the macromolecule. The diffusive motions of the AGUs are captured by the rate constant k_{blob}, which describes the rate of encounters between two AGUs. Upon encounter of one AGU bearing $Py_{diff}*$ with another AGU bearing a ground-state pyrenyl label, $Py_{diff}*$ turns into the species $Py_{k2}*$, which rearranges rapidly with the ground-state pyrene to form an excimer with a rate constant k_2, that is ~10 times larger than k_{blob}. Finally, a short decay time of ~3.5 ns was detected in the pyrene excimer decays. Such a contribution has often been observed, when PEF occurs in hindered environments such as those experienced in rigid macromolecules. This short decay time was accounted for by adding an exponential to the excimer equation and fixing its decay time to 3.5 ns in the analysis.

The pyrene monomer and excimer fluorescence decays were fitted globally according to the FBM with Equations S3.1 and S3.2 given in Supporting Information (SI) with the *globmis90lbg* and *globmis90rbg* programs, depending on whether one ($E0*$) or two ($E0*$ and $D*$) excimer species were required for the decay fits. Both $E0*$ and $D*$ are viewed as aggregated pyrene species and their combined contribution is referred to as $Py_{agg}*$. The fluorescence decays were fitted first by allowing the rate constant (k_2) to float. The k_2 values obtained from the decay fits were then averaged and fixed in a second global analysis of the fluorescence decays with the

86

programs *globmis90obg* or *globmis90sbg* to handle one or two excimer types, respectively. The decay fits yielded the average number ($<n>$) of pyrenyl labels in a *blob* and k_{blob}. $<n>$ was used to calculate the number (N_{blob}^{exp}) of AGUs in a *blob* according to Equation 3.3. f_{Mfree} in Equation 3.3 represents the molar fraction of Py_{free}* species in the monomer decays.

$$N_{blob}^{exp} = \frac{1 - f_{Mfree}}{x} < n >$$ (3.3)

Among other parameters, the global FBM analysis of the monomer and excimer fluorescence decays acquired with the Py-Glycogen(O/C) samples also yielded the molar fractions f_{free}, f_{agg}, f_{diff}, and f_{k2} of the pyrene species Py_{free}*, Py_{agg}*, Py_{diff}*, and Py_{k2}*, respectively. Optimization of the parameters used in Equations S3.1 and S3.2 for the decay fit was conducted according to the Marquardt-Levenberg algorithm.[34] The decay fits were deemed satisfactory when the χ^2 was less than 1.3 and the residuals and autocorrelation of the residuals were randomly distributed around zero as shown in Figure S3.1 in SI.

3.4 Results and Discussion

Mathematical representation of the Tier model by Meléndez-Hevia et al. - Intrinsic Viscosity ($[\eta]$) and Gel Permeation Chromatography (GPC): The mathematical representation of the Tier model for glycogen by Meléndez-Hevia et al., referred to from here on as the Meléndez-Hevia model, provides several relationships, that can be applied to relate a number of experimental parameters to the properties of glycogen.[13] For instance, the molecular weight of a glycogen molecule is expected to be well described by Equation 3.4, where 162 g/mol, *r*, and *t* represent the molar mass

of an AGU, the degree of branching, and the number of tiers, respectively. Based on Equation 3.4, degrees of branching greater than 2 would result in impossibly large densities for glycogen. In contrast, a degree of branching of 2 (i.e. $r = 2$ in Equation 3.4) yields an optimum structure for glycogen, that maximizes storage of AGUs in the smallest possible volume.[13]

$$M_n = 162 \times \left(\frac{1 - r^t}{1 - r} \times CL \right) \tag{3.4}$$

Considering that each AGU in an oligosaccharide helix increases the tier thickness (tt) by 0.126 nm, that the side chains of glycogen from oyster[9,35] and corn[7,8] are constituted of 10 and 12 AGUs, respectively, and that the branching point generated by an α-(1,6) glycosidic bond adds 0.35 nm to the tier thickness tt,[14] tt could be calculated according to Equation 3.5.

$$tt = 0.126 \times SCL + 0.35 \tag{3.5}$$

The density (ρ) of glycogen could be calculated by combining Equation 3.4 and Equation 3.6, which defines the volume of a glycogen molecule based on its number of tiers (t) and the thickness of each tier (tt), into the ratio $\rho = M_n/volume$.

$$volume = \frac{4}{3}\pi(t - 0.5)^3(tt)^3 \tag{3.6}$$

In turn, ρ and M_n predicted from the Meléndez-Hevia model could be related to the intrinsic viscosity ($[\eta] = 2.5/\rho$, determined in Figure S3.2 in SI) and the M_n values of the glycogen molecules in DMSO obtained experimentally by viscometry and GPC experiments, respectively, which were reported in Table 3.1. It is worth noting that the Glycogen(O/C) particles have a polydispersity index (PDI), that is close to unity, so that the PDI should not affect the results much, when different types of molecular weights are being used. The experimental M_n and $2.5/[\eta]$ values were compared in Figure 3.1 and Figure S3.3 for glycogen from oyster and corn, respectively, to their predicted values based on Equations 3.4 – 3.6. Based on this analysis, the glycogen from oyster and corn consisted of 11.3 and 12.2 tiers, respectively. Taking advantage of the fact that V_h can be approximated as $[\eta] \times M_w/(2.5 N_A)$, where N_A is the Avogadro number and M_w is the weight average molecular weight of a glycogen molecule, 11.8 and 12.8 tiers were obtained for the oyster and corn glycogen molecules, respectively, by equating the hydrodynamic radius (R_h) to the product $t \times tt$. The numbers of tiers obtained for the glycogen samples from the experimentally determined M_n, M_w, $[\eta]$, and R_h values are listed in Table 3.1. The good agreement found for the number of tiers pertaining to one type of glycogen molecules obtained from different experimental parameters suggests that the glycogen molecules from oyster and corn were made of 11.5 (± 0.3) and 12.3 (± 0.4) tiers, respectively.
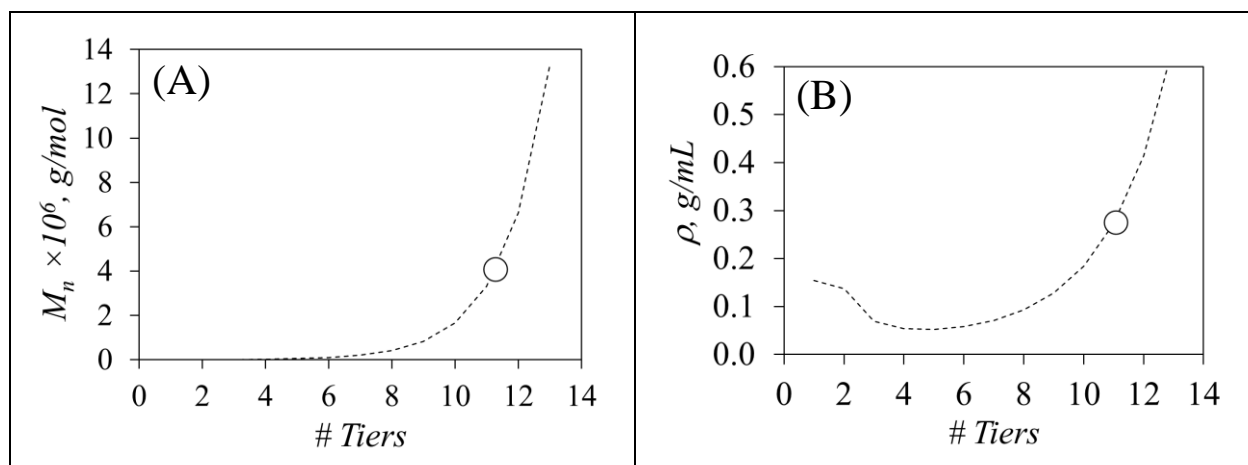
Figure 3.1. Plots of *A)* M_n and B) ρ (= 2.5/[η]) obtained *(.......)* theoretically based on Equations 3.4 – 3.6 and experimentally for glycogen from oyster.

Table 3. 1. Molecular weight, polydispersity index (PDI), intrinsic viscosity, hydrodynamic radius (R_h), number of tiers, side chain length (SCL), tier thickness (*tt*), and glycogen molecule radius (*R*) taken from the center of the outer tier.

Glycogen origin	Oyster			Corn		
SCL (# of AGUs per side chain)	10			12		
tt (nm)	1.61			1.86		
	M_n=4.1×10^6 g/mol (PDI=1.02)	$[\eta]$ = 9.1 mL/g	R_h = 18.1 nm	M_n=8.5×10^6 g/mol (PDI=1.15)	$[\eta]$ = 7.8 mL/g	R_h = 23.5 nm
# of tiers	11.3	11.3	11.8	12.0	12.2	12.8
$R = (t - 0.5) \times tt$ (nm)	17.4	17.4	18.1	21.4	21.8	23.5

Dye Distribution in Fluorescently Labeled Glycogen molecules: Fluorescence resonance energy transfer (FRET) experiments were conducted to assess the distribution of the dyes resulting from the labeling of Glycogen(O) by 1-pyrenebutyric acid or 1-napthalene acetic acid. Since the

fluorescence emission of naphthalene overlaps the absorption of pyrene, naphthalene and pyrene are often paired up as a FRET donor and acceptor, respectively, to study intermacromolecular interactions.[29,36] The efficiency of FRET (E_{FRET}) increases strongly, when the distance separating the acceptor from the donor decreases. FRET was applied to investigate how naphthalene and pyrene covalently attached to glycogen were distributed in the glycogen molecules. Since glycogen molecules are known to be very dense, dye labeling might not occur throughout the interior of glycogen but might be limited instead to the periphery of glycogen due to its compact nature. To assess whether the dyes were confined to the surface of glycogen, a mixture of pyrene-labeled (Py-Glycogen) and naphthalene-labeled (Np-Glycogen) glycogen molecules were dispersed in DMSO and induced to aggregate by addition of water, which is a poor solvent for naphthalene and pyrene. Upon aggregation of the particles, a low and high E_{FRET} was expected, if the dyes were distributed throughout the interior or confined to the surface of glycogen molecules, respectively.

Dextran was selected as a control for the FRET experiments, since dextran adopts a random coil conformation in DMSO,[37] where all AGUs should be accessible for esterification. A dextran sample was labeled with 1-pyrenebutyric acid or 1-naphthaleneacetic acid to yield the Py-Dextran and Np-Dextran samples, respectively. Aggregation of the fluorescently labeled dextran samples induced by adding water to the dextran solutions in DMSO should result in a large E_{FRET}, since all dyes should be able to interact with each other, thus providing a benchmark against which the E_{FRET} of the glycogen samples could be compared.

Solutions of 2.2 (±0.1) mg/L naphthalene-labeled polysaccharides (Np-PS) and 0.3 (±0.1) mg/L pyrene-labeled polysaccharide (Py-PS) were prepared in DMSO and the solvent quality was

adjusted by progressively changing the solvent composition of DMSO:water mixtures from a 100:0 to a 10:90 ratio. The seven-fold larger concentration of Np-PS compared to Py-PS was meant to maximize interactions between Np-PS and Py-PS, while minimizing inter-particular interactions between Py-PS. In pure DMSO, where both dyes and PSs were soluble, the macromolecules were solvated and were not expected to show any interactions at the minuscule mass concentrations used for the FRET experiments. The fluorescence spectra obtained for two separate dispersions of 0.3 mg/L Py(6.8)-Glycogen(O) and 2.2 mg/L Np(126)-Glycogen(O) in DMSO excited at 293 nm are shown in Figure 3.2A.
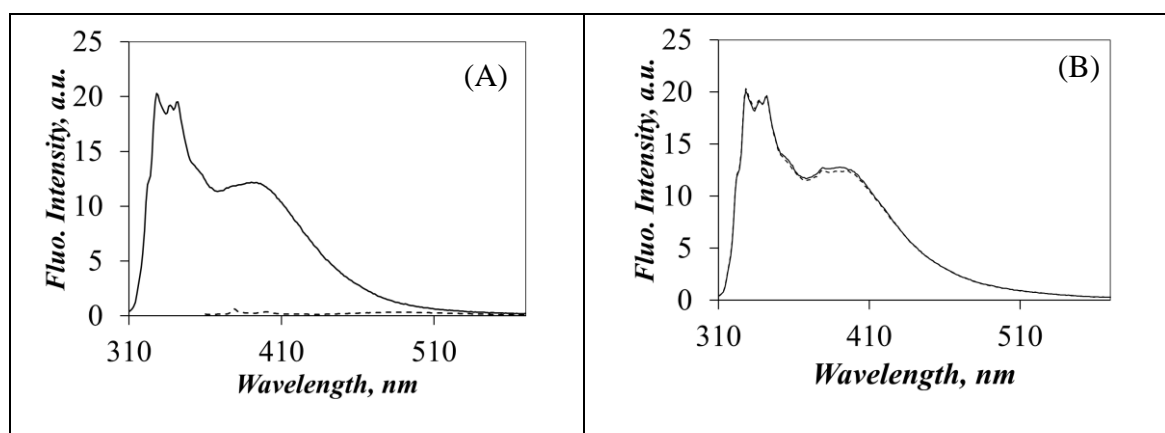
Figure 3. 2. A) Fluorescence spectra of the individual dispersion of (——) Np(126)-Glycogen(O) and (---) Py(6.8)-Glycogen(O) in DMSO and B) (——) the fluorescence spectra of the mixture of 2.2 mg/L Np(126)-Glycogen(O) and 0.3 mg/L Py(6.8)-Glycogen(O) in DMSO with (---) the sum of the two individual spectra shown in Figure 3.2A. λ_{ex} = 293 nm.

The very low pyrene content of Py(6.7)-Glycogen(O) and its seven-fold lower concentration compared to Np(126)-Glycogen(O) with a much higher naphthalene content and concentration resulted in the very weak fluorescence observed for the Py(6.8)-Glycogen(O) sample in Figure 3.2A. Summing the individual fluorescence spectra of Np(126)-Glycogen(O) and Py(6.8)-

Glycogen(O) shown in Figure 3.2A resulted in the same fluorescence spectrum as that obtained for a mixture of 2.2 mg/L Np(126)-Glycogen(O) and 0.3 mg/L Py(6.8)-Glycogen(O), confirming the absence of FRET between the two samples. Similar results were obtained for the fluorescently labeled dextran samples as shown in Figure S3.4 in the SI.

As water was added to the Np-PS and Py-PS mixtures, the hydrophobic naphthyl and pyrenyl labels became less soluble leading to the aggregation of the Np-PS and Py-PS samples, which promoted interactions between the naphthyl and pyrenyl labels, that resulted in FRET. This was indeed observed in Figures 3.3A and B for the dextran and glycogen samples, respectively, where the strong decrease in the fluorescence of naphthalene between 330 and 345 nm was accompanied by a strong increase in the fluorescence of pyrene between 370 and 410 nm as water was added to DMSO. It is worth noting that the concentration used for the Np-PS and Py-PS samples, whose spectra are shown in Figures 3.3A and B, were the same as those used in Figures 3.2 and S3.3, where the fluorescence of Py-PS was hardly visible. In order to assess the efficiency of FRET (E_{FRET}), the intensity at 340 nm (I_{340}) and 379 nm (I_{379}) were selected to represent the fluorescence of the naphthalene and pyrene monomer, respectively. The 340 nm wavelength was chosen for naphthalene, so that it would not interfere with the Raman scattering peak of water at 330 nm. Upon aggregation of the fluorescently labeled polysaccharides, I_{340} of the Np-PS decreased with increasing water content, while I_{379} increased as shown in Figures 3.3A and B.
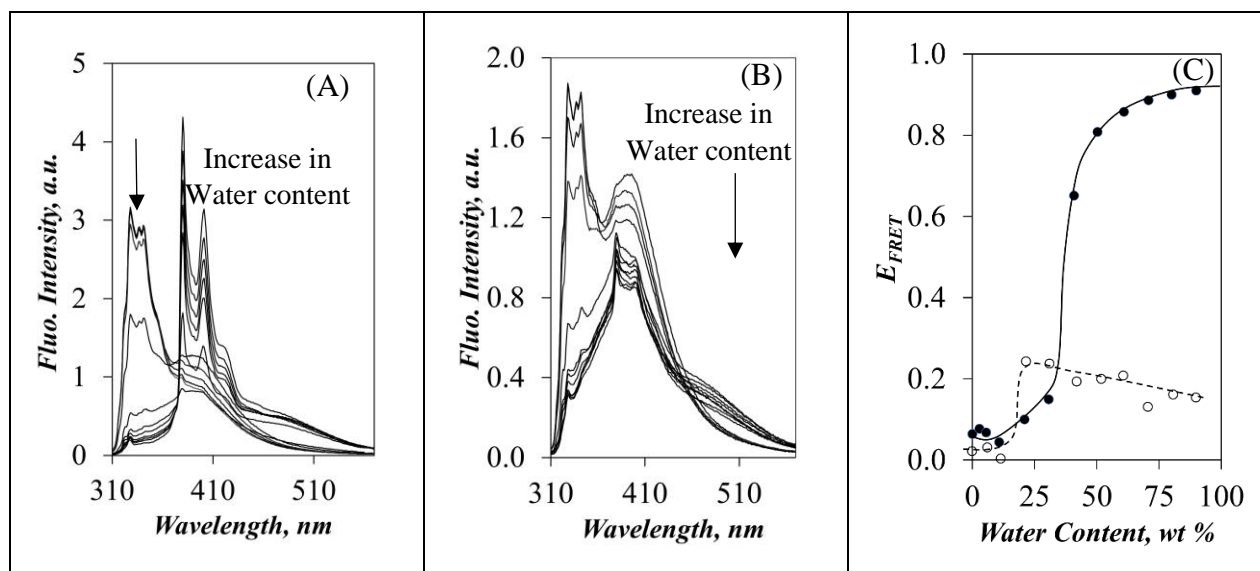
Figure 3.3. Fluorescence spectra of A) the mixture of 2.1 mg/L of Np(130)-Dextran and 0.2 mg/mL Py(12.8)-Dextran and B) the mixture of 2.2 mg/L Np(126)-Glycogen(O) and 0.3 mg/L Py(6.8)-Glycogen(O) in different DMSO:water mixtures. C) Plots of FRET efficiency for the (●) dextran and (○) glycogen samples as a function of the water content. The lines were drawn to guide the eyes. $\lambda_{ex} = 293$ nm.

Like pyrene, naphthalene can also form an excimer, whose fluorescence centered at 390 nm is broad and structureless (see Figure 3.2A). Upon addition of water to the DMSO solutions, aggregation of the Np-PS led to increased excimer formation, which overlapped the emission of the pyrene monomer. Consequently, the emission of the naphthalene excimer interfered with the emission of the pyrene monomer at 379 nm. Equation 3.7 was introduced in an effort to account for this interference, where the ratio $[I_{379}/I_{340}]^{Np}$ is obtained for the Np-PS solutions and the ratio $[I_{379}/I_{340}]^{FRET}$ is obtained for solutions of the Np-PS and Py-PS mixtures. Due to the much lower absorption of the Py-PS samples, I_{340} takes a same value for solutions with or without Py-PS and is used to normalize the fluorescence intensity at 379 nm after accounting for small experimental variation in the absorbance of the solutions. If no FRET occurs, $[I_{379}/I_{340}]^{FRET}$ equals $[I_{379}/I_{340}]^{Np}$

94

and E_{FRET} equals 0, whereas strong FRET yields ratios $[I_{379}/I_{340}]^{FRET} \gg [I_{379}/I_{340}]^{Np}$ resulting in $E_{FRET} \sim 1$. The results of this calculation are shown in Figure 3.3C.

$$E_{FRET} = 1 - \frac{\left[\dfrac{I_{379}}{I_{340}}\right]^{Np}}{\left[\dfrac{I_{379}}{I_{340}}\right]^{FRET}} \times \frac{Abs_{293}^{FRET}}{Abs_{293}^{Np}} \qquad (7)$$

A large increase in E_{FRET} was observed in Figure 3.3C, when the water content increased past 20 and 30 wt% in the dextran solutions and glycogen dispersions, respectively. E_{FRET} approached 90 % for dextran in a 10:90 DMSO:water mixture, while it remained at $\sim$ 20 % for glycogen. The much lower E_{FRET} obtained for glycogen reflects the structural difference between the two polysaccharides. Since dextran is randomly coiled in DMSO and water,[37] all dyes from the fluorescently labeled dextran samples could undergo hydrophobic associations with each other upon addition of water, resulting in strong FRET. On the other hand, only the fluorophores located at the periphery of the glycogen molecules were expected to undergo hydrophobic associations, while the fluorophores inside the glycogen molecules could not. This explains the lower E_{FRET} obtained for the glycogen dispersions compared to the dextran solutions.

The much weaker FRET observed for glycogen could also be the result of having glycogen undergoing some large-scale rearrangement to bury some of its peripheral hydrophobic dyes into its interior, where they would be inaccessible for FRET. While these large-scale rearrangements would reduce E_{FRET}, they would also suggest a fairly mobile peripheral tier, that would easily allow penetration of the glycogen interior by the much smaller dye derivatives used for the fluorescence labeling. Consequently, the E_{FRET} results shown in Figure 3.3C suggest that the fluorescent labels of dextran are fully accessible resulting in a 90 % E_{FRET} for a 10:90 DMSO:water mixture, whereas the same solvent composition results in a 20 % E_{FRET} for the glycogen samples, indicating that a

substantial fraction of the dyes are located in the interior of glycogen and that the glycogen molecules were fluorescently labeled throughout their interior.

Steady-State Fluorescence of Py-Glycogen Samples: After having established that the pyrene labels of the Py-Glycogen(O/C) samples were randomly distributed throughout the interior of the particles, their fluorescence spectra were acquired. The normalized fluorescence spectra of the Py-Glycogen(O) and Py-Glycogen(C) dispersions in DMSO are shown in Figures 3.4A and S3.4 in SI, respectively. The typical spectral features expected from the fluorescence of a pyrene-labeled macromolecule in solution are observed for the Py-Glycogen(O/C) dispersions. The pyrene monomer emitted sharp bands between 370 and 420 nm, while the excimer showed a broad structureless fluorescence centered at 480 nm. The emission of the excimer relative to that of the monomer increased with increasing pyrene content in Figure 3.4A due to increased pyrene-pyrene encounters. These effects could be quantified by plotting the I_E/I_M ratio obtained for both glycogen samples as a function of pyrene content in Figure 3.4B.

The I_E/I_M ratios for the Py-Glycogen(O/C) samples overlapped suggesting that both glycogen samples generated excimer with the same efficiency. The increase in I_E/I_M with increasing pyrene content has already been reported for other pyrene-labeled α-(1,4) polyglucans such as amylose[30] and amylopectin[28] and the I_E/I_M ratios of these samples are also shown in Figure 3.4B. For a same pyrene content, the PEF efficiency increased in the order of amylose, amylopectin, and glycogen. Interestingly, this trend parallels the known degree of branching of these polysaccharides, with linear amylose having the lowest PEF efficiency, amylopectin with a branching frequency of one branch point per ~20 AGUs[38] yielding an intermediate PEF efficiency, and glycogen with a branching frequency of one branch point per ~10 AGUs[8] generating excimer

96

most efficiently. The trends shown in Figure 3.4B for the different Py-PSs suggest that PEF is sensitive to the internal structure of a given polysaccharide, which could be a valuable feature to assess the nature of polysaccharides from their PEF response after pyrene labeling. However, PEF appears to not be sensitive enough to distinguish between two polysaccharide samples of different origin such as the glycogen samples obtained from corn and oyster.
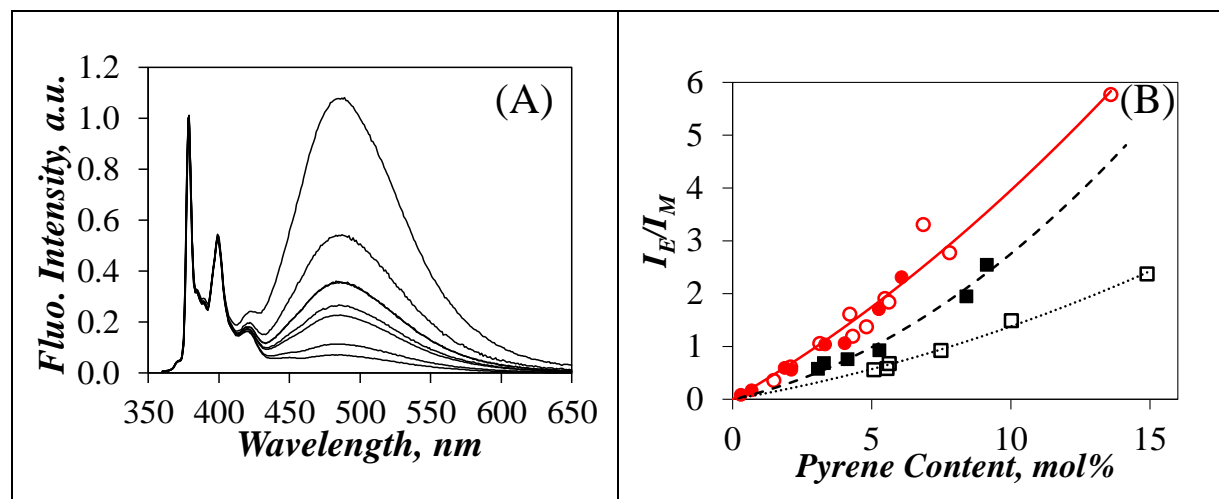
Figure 3. 4. A) Fluorescence spectra of Py-Glycogen(O) in DMSO and B) plot of the I_E/I_M ratios of (solid line) Py-Glycogen from (●) oyster and (○) corn, (■, dashed line) Py-Amylopectin, and (□, dotted line) Py-Amylose in DMSO as a function of pyrene content. Lines were added to guide the eyes. [Py] = 2.5×10^{-6} M, λ_{ex} = 346 nm.

All I_E/I_M-*vs*-pyrene content profiles showed substantial curvature, when extrapolated to the origin. This curvature reflects the fact that PEF is a localized process, that requires that two pyrenyl labels be within ~ 2.5 nm from each other. At low pyrene content, many pyrenyl groups are isolated, do not form excimer, and the resulting I_E/I_M ratio is lower than expected. Consequently, a minimum pyrene content must be reached to allow all pyrenyl labels to undergo PEF. Above this critical pyrene content, a more linear increase in the I_E/I_M ratio is obtained as a function of pyrene content. This behavior is a direct consequence of the Poisson distribution of the pyrene labels among the

blobs defining the macromolecule, which is better handled by analyzing the fluorescence decays of the Py-PS samples as described in the following section.

Time-resolved fluorescence: The analysis of the fluorescence spectra shown in Figure 3.4 provided some valuable, although qualitative, information on the PEF efficiency for the different polysaccharides. However, quantitative structural and dynamic information about pyrene-labeled glycogen molecules can only be obtained by applying the FBM to the analysis of the fluorescence decays acquired with dispersions of the Py-Glycogen(O/C) samples in DMSO. The global FBM analysis of the decays resulted in good fits as can be seen in Figure S3.1 in SI. As described in the Experimental section, the FBM analysis of the decays yielded N_{blob}^{exp} and f_{agg}, which were plotted as a function of pyrene content in Figures 3.5A and B, respectively, for the Py-Glycogen(O/C), Py-Amylose, and Py-Amylopectin samples in DMSO.
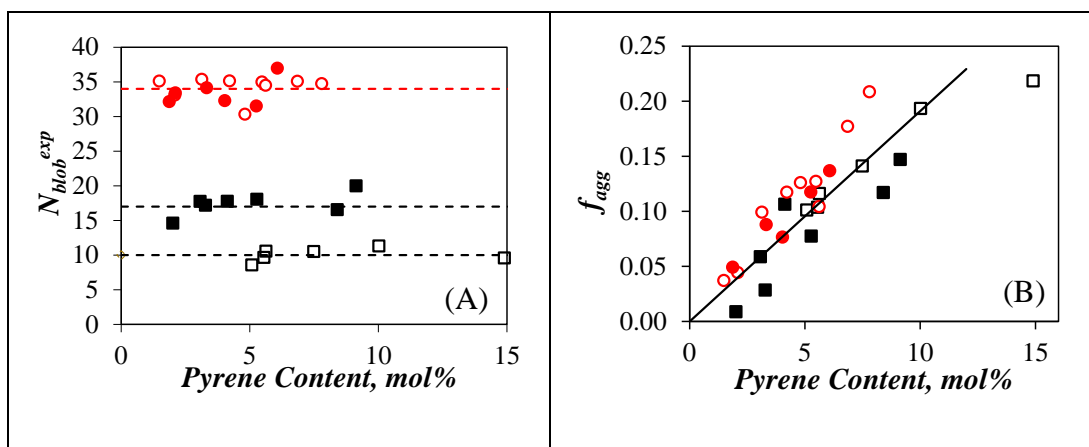
Figure 3.5 Plots of A) N_{blob}^{exp} and B) f_{agg} as a function of pyrene content. Py-Glycogen samples from (○) oyster and (●) corn, (■) Py-Amylopectin and (□) Py-Amylose.

Within experimental error, N_{blob}^{exp} remained constant as a function of pyrene content for the four polysaccharides, yielding a value $<N_{blob}^{exp}>$, after averaging over all pyrene contents of a given Py-PS series, equal to 34 (±2), 33 (±2), 18 (±2), and 10 (±1) for Py-Glycogen(O), Py-

Glycogen(C), Py-Amylopectin,[28] and Py-Amylose,[30] respectively. As earlier studies have indicated,[28,30,39] $<N_{blob}^{exp}>$ represents the maximum number of AGUs separating two pyrenyl labels, while still allowing PEF. The $<N_{blob}^{exp}>$ value of 10 AGUs found for the Py-Amylose constructs demonstrated that linear amylose adopted a helical conformation in DMSO and represented the number of AGUs, that were involved for intrahelical PEF.[30] The larger $<N_{blob}^{exp}>$ value of 18 found for amylopectin was attributed to interhelical encounters between pyrenyl labels attached on different oligosaccharide helices close enough to enable PEF. This observation led to the proposal, that the arrangement of the oligosaccharide side chains of amylopectin in solution obeyed the Solution-Cluster model, whereby clusters of short oligosaccharide side chains were connected to each other by longer oligosaccharide segments.[28] These conclusions were drawn by conducting molecular mechanics optimizations (MMOs) with HyperChem to determine *in silico* the number (N_{blob}^{theo}) of AGUs separating two pyrene-labeled AGUs, that would result in good pyrene-pyrene overlap, and thus efficient PEF. Assuming that the single helices generated by amylopectin would form clusters in solution corresponding to an array of 37 helices arranged in a HCP lattice, an interhelical distance (d_{h-h}) of 3.2 nm was determined in Chapter 2. Based on these early results, the much larger $<N_{blob}^{exp}>$ value of 34 (±2) found for both glycogen samples in dilute dispersions suggested that their helical oligosaccharide side chains would be even closer than for amylopectin with $<N_{blob}^{exp}>$ equal to 18 (±2), thus resulting in stronger PEF between pyrenyl labels located on different helices. This conclusion agrees with the trends obtained with the I_E/I_M ratios in Figure 3.4B, which indicated that the most efficient PEF was obtained for the glycogen samples.

The higher degree of branching in glycogen results in a denser interior for glycogen compared to amylopectin. Using the MHS parameters K = 0.22 mL/g and a = 0.34 found for

amylopectin in DMSO,[28] an amylopectin sample having the same M_n of 4.1×10^6 g/mol as Glycogen(O) would have an $[\eta]$ value of 39 mL/g compared to that of 9.1 mL/g found for Glycogen(O). The much larger $[\eta]$ value found for amylopectin illustrates how much denser glycogen is compared to amylopectin and rationalizes why $<N_{blob}^{exp}>$ takes a much higher value for the glycogen samples. Furthermore, macromolecules, that adopt a helical conformation like amylose in DMSO, have been shown to produce more pyrene aggregates upon pyrene-labeling due to the more compact substrate provided by the polysaccharide helix.[30] The Py-Glycogen(O/C) samples were found to generate pyrene aggregates in the same manner as amylose and amylopectin in DMSO as illustrated by the molar fraction f_{agg} of aggregated pyrenes plotted as a function of pyrene content in Figure 3.5B, which was similar to that of amylopectin and amylose. This result was attributed to the compact helical nature of the side chains of glycogen, which brought pyrenyl labels closer to each other.

Molecular Mechanic Optimizations: In order to relate the $<N_{blob}^{exp}>$ values obtained experimentally for the Py-Glycogen(O/C) samples to the conformation of their interior, MMOs were performed with HyperChem on short dodecaglucose oligomers, that were labeled with two PyBAs. The published structure of a single maltoheptaose helix with 6-7 residues per turn complexed with glycogen phosphorylase a[14] was imported in HyperChem and was used to build oligosaccharide helices with 10 and 12 AGUs to match the side chain length (SCL) of the glycogen from oyster and corn, respectively. The side chains of glycogen are unlikely to form double helices in solution as they are considered to be too short.[40] Since the primary C6-hydroxyl was less sterically hindered and is more nucleophilic than the C2-hydroxyl,[41] PyBA was covalently attached to the C6-hydroxyl of the AGUs, when it was accessible in the oligosaccharide helix.

When the C6-hydroxyl was not accessible for pyrene-labeling, the C2-hydroxyl of the AGUs was labeled with PyBA, since it has been found to be more reactive than the C3-hydroxyl.[42] These MMOs differed from those conducted earlier with amylose[30] or with the side chains of amylopectin,[28] where the PyBA label was solely attached to the C2-hydroxyl of the AGUs, as the C6-hydroxyl was found to point toward the center of these long helices. In the much shorter oligosaccharide side chains of glycogen, the C6-hydroxyls of the top 8 AGUs in these short helices were accessible, which justified the selection of the C6-hydroxyl for PyBA labeling.

Intramolecular PEF was first considered with an oligosaccharide helix made of 12 AGUs. The reference pyrene was attached to the C6-hydroxyl of the first AGU located at the top of the helix. The secondary pyrene was attached onto the next AGU on the same helix. The two pyrenes were induced to come within 0.34 nm from each other and overlap and the number of carbons of one pyrene overlapping the frame of the second pyrene was determined to equal 8 and was reported in Figure 3.6A for residue #2. As mentioned earlier, successful PEF occurs when 7 or more overlapping carbons are obtained.[30,39] The largest number of AGUs separating two pyrene labels, while still allowing PEF, was taken as $N_{\text{blob,intra}}^{\text{theo}}$. Based on the plot shown in Figure 3.6A, where the reference pyrene was attached to the C6-hydroxyl of the first AGU, the reference pyrene could form excimer successfully with a number $N_{\text{o}} = 8$ AGUs located on the same side of the reference pyrene. In this case, $N_{\text{blob,intra}}^{\text{theo}}$ was therefore $N_0+1 = 9$, where one AGU was added to N_{o} to account for the AGU bearing the reference pyrene. The MMOs were repeated by changing the position of the reference pyrenyl from the first to the last AGU along the helix, one AGU at a time and $N_{\text{intra,blob}}^{\text{theo}}$ was determined for all the residues along the oligosaccharide helix and plotted in Figure 3.6B. This plot indicated that the location of the reference pyrene did not have much impact

on the N_{blob} value. Consequently, the $N_{blob,intra}^{theo}$ values were averaged for all the positions of the reference pyrene to yield $\langle N_{blob,intra}^{theo}\rangle$, whose value depended on the SCL of the oligosaccharide helix as shown in Figure 3.6C. $\langle N_{blob,intra}^{theo}\rangle$ did not change much with helix SCL, taking values of 8.3 ($\pm$1.3) and 9.1 ($\pm$1.5) AGUs for SCLs made of 10 and 12 AGUs corresponding to the side chains of glycogen obtained from oyster[9,35] and corn,[7,8] respectively.

The $\langle N_{blob,intra}^{theo}\rangle$ values of 8.3 and 9.1 AGUs for SCLs made of 10 and 12 AGUs, respectively, were shorter than those obtained for an infinitely long helix such as for amylose, where PyBA was attached onto the C2-hydroxyl for which $N_{blob,intra}^{theo}$ equaled 11.[30] This difference in $N_{blob,intra}^{theo}$ is substantial, since PyBA was mostly attached onto the C6-hydroxyl of the short helices used for glycogen, and thus had a longer 5.1 nm reach compared to the 4.6 nm reach for PyBA attached onto the C2-hydroxyl for the longer helices used for amylopectin (see Figure S3.6). This difference in $N_{blob,intra}^{theo}$ also illustrates how end effects affect N_{blob} for shorter oligosaccharide helices, where a pyrenyl label located at one end of the helix senses fewer pyrenes than a pyrenyl label located at the helix center, thus resulting in a smaller $N_{blob,intra}^{theo}$ value. Since intrahelical PEF resulted in $N_{blob,intra}^{theo}$ of ~8.7 AGUs, interhelical PEF must be substantial in glycogen for $\langle N_{blob}^{exp}\rangle$ to equal 34 AGUs.

Additional MMOs were conducted to assess the contribution of interhelical PEF. To this end, an hexagonal array of 7 oligosaccharide helices was created as shown in Figure 3.7A with a primary helix (O) at the center surrounded by six adjacent helices (I – VI). The position of the six adjacent helices was defined by the angles θ and ϕ and the distance d_{h-h} as shown in Figure 3.7A. θ represented the angle between the x-axis defined by the line joining the centers of Helices IV – O – I and the line joining the centers of Helix O and Helix II. ϕ represented the relative orientation of an helix with respect to the the x-axis and d_{h-h} was the interhelical distance separating two helix

centers. The six helices were placed at an angle $\theta = 0, 60, 120, 180, 240,$ and $300\,^\circ$ and at a distance $d_{\text{h-h}}$ from each other.
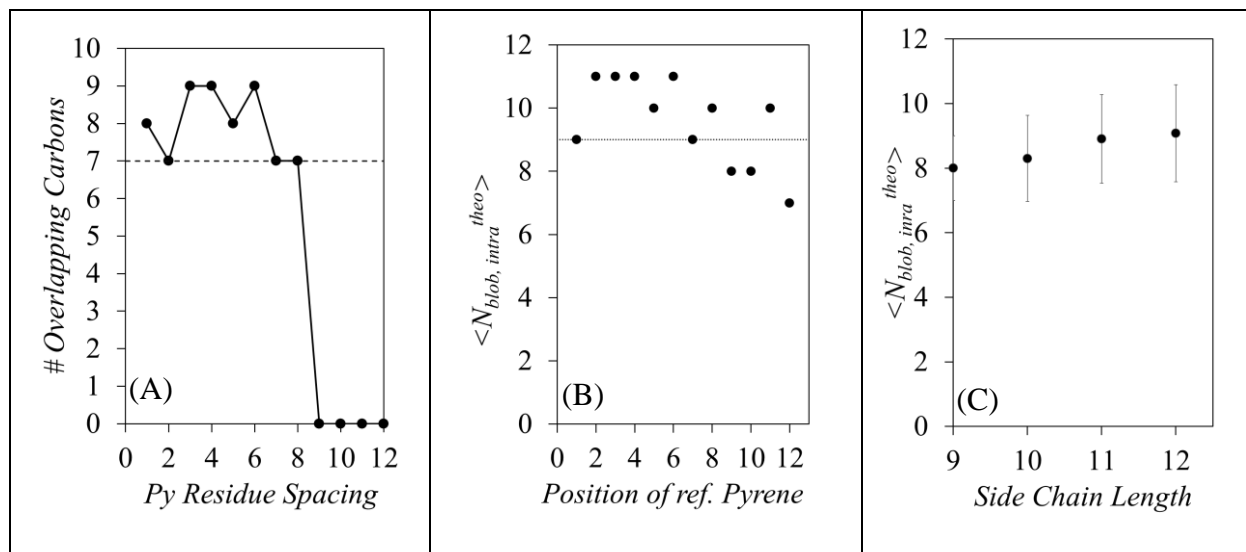
Figure 3.6. A) Plot of the number of overlapping carbons as a function of the position of the AGU bearing the secondary pyrene label away from the reference pyrene attached on a single oligosaccharide helix made of 12 AGUs. The dash line (---) indicates 7 overlapping carbons reflecting successful PEF. Plot of $<N_{\text{blob,intra}}^{\text{theo}}>$ as a function of B) the position of the reference pyrene when SCL=12, where the dotted line indicates the $<N_{\text{blob,intra}}^{\text{theo}}>$ values after averaging over all positions taken by the reference pyrene, and C) the SCL of an oligosaccharide helix.

$N_{\text{blob,inter}}^{\text{theo}}$ was determined as a function of $d_{\text{h-h}}$ by considering that PEF occurred between two pyrenyl labels attached on two different helices. The reference pyrene was attached on Helix O of the hexagonal array and the second pyrene was attached on one of the adjacent helices. The first series of MMOs was conducted at $\phi = 0^\circ$ with a $d_{\text{h-h}}$ of 1.8 nm. The position of the reference pyrene was changed from the first to the twelfth AGU of the helix, one residue at the time. For each reference pyrene attached on Helix O, the secondary pyrene was attached on all the AGUs of one of the six adjacent helices, one AGU at a time. The primary and secondary pyrenes were

induced to overlap and the extent of overlap between the two pyrenyl labels was determined. Those

pyrene pairs, that would yield seven or more overlapping carbons, were included in the calculation

of $N_{\text{blob,inter}}^{\text{theo}}$. $N_{\text{blob}}^{\text{theo}}$ was calculated by adding $<N_{\text{blob,intra}}^{\text{theo}}>$ provided in Figure 3.6C for a given

SCL and $N_{\text{blob,inter}}^{\text{theo}}$, after averaging the $N_{\text{blob,inter}}^{\text{theo}}$ values obtained for all reference pyrenyl

labels. As long as the reference pyrene was attached to a same C6- or C2-hydroxyl, $N_{\text{blob}}^{\text{theo}}$(C2/C6)

remained more or less constant regardless of the location of the reference pyrene as shown in

Figure 3.7B.

The results obtained in Figure 3.7B had the following implication. If the 1-pyrenebutyroyl

group was attached onto a C6-hydroxyl for the first 8 AGUs and the 11th AGU, $N_{\text{blob}}^{\text{theo}}$(C6) took

a similar value of 39.6 ($\pm$2.5) regardless of the reference AGU. Similarly, if the 1-pyrenebutyroyl

group was attached onto the C2-hydroxyl of the 9th, 10th, or 12th AGU, $N_{\text{blob}}^{\text{theo}}$(C2) equaled 25.3

($\pm$3.1) regardless of the reference AGU. Consequently, MMOs were conducted as a function of

$d_{\text{h–h}}$ where the reference 1-pyrenebutyroyl group was attached on the C6-hydroxyl of the first AGU

at the top of the oligosaccharide helix and on the C2-hydroxyl of the 9th AGU on the middle of the

oligosaccharide helix. As shown in Figures 3.7C and S3.7A in SI, $N_{\text{blob}}^{\text{theo}}$(C2) was substantially

lower when the reference pyrene was attached on the C2-hydroxyl of the 9th AGU compared to

$N_{\text{blob}}^{\text{theo}}$(C6) when the reference pyrene was attached on the C6-hydroxyl of the 1st AGU at the

lower $d_{\text{h-h}}$ values for SLC = 10 and 12, respectively. The $N_{\text{blob}}^{\text{theo}}$(C2/C6) value was affected by

the nature of the hydroxyl used to attach the pyrenyl label, since attachment on the C2-hydroxyl

resulted in a shorter reach for the pyrenyl label than attachment on the C6-hydroxyl. Furthermore,

shorter $d_{\text{h-h}}$ led to the segregation of the pyrene labels, attached to the C2-hydroxyls of the short

oligosaccharide helices, between the interhelical voids of the lattice, which prevented $N_{\text{blob}}^{\text{theo}}$(C2)

from increasing past 30 AGUs. In contrast, the pyrenyl labels attached to a C6-hydroxyl at the end

of the helices could not be segregated and smaller $d_{\text{h-h}}$ favored interhelical pyrene-pyrene encounters, thus resulting in the continuous increase in $N_{\text{blob}}{}^{\text{theo}}(C6)$ with decreasing $d_{\text{h-h}}$ shown in Figure 3.7C. In fact, a reference pyrenyl label located at the tip of a short oligosaccharide helix could interact with secondary pyrenyl labels attached on all six adjacent helices. In contrast, a reference pyrenyl label attached to the C2-hydroxyl of the 9$^{\text{th}}$ AGU of the O-helix experienced a limited number of inter-helical interactions, as it could only interact with pyrenyl labels attached to four neighboring helices at the shorter $d_{\text{h-h}}$. Figure 3.8 illustrates these considerations by comparing the enhanced reach of a pyrenyl label located at the end of a helix with that of a pyrenyl label located in the middle of a helix. Attaching the reference pyrenyl at any of the C6-hydroxyls of the 8 accessible AGUs at the top of the helix in Figure 3.8A favors its encounter with secondary pyrenyl groups located on the other helices. A good overlap between two pyrenyl labels is more difficult to achieve in Figure 3.8B, when the pyrenyl labels are attached on a C2-hydroxyl, as they meander their way around the oligosaccharide helices. $N_{\text{blob}}{}^{\text{theo}}$ of glycogen was calculated by averaging the $N_{\text{blob}}{}^{\text{theo}}(C2/C6)$ values in Figures 3.7C and S3.7A over the contributions of the C2- and C6-hydroxyls generated by the AGUs in a short oligosaccharide helix. Since the side chain of Glycogen(O) particles were made of 10 AGUs, with two C2-hydroxyls on the 9$^{\text{th}}$ and 10$^{\text{th}}$ AGUs and eight C6-hydroxyls on the 8 other AGUs, $N_{\text{blob}}{}^{\text{theo}}$ reflected the contribution of the C6-hydroxyls more than that of the C2-hydroxyls in Figure 3.7C.
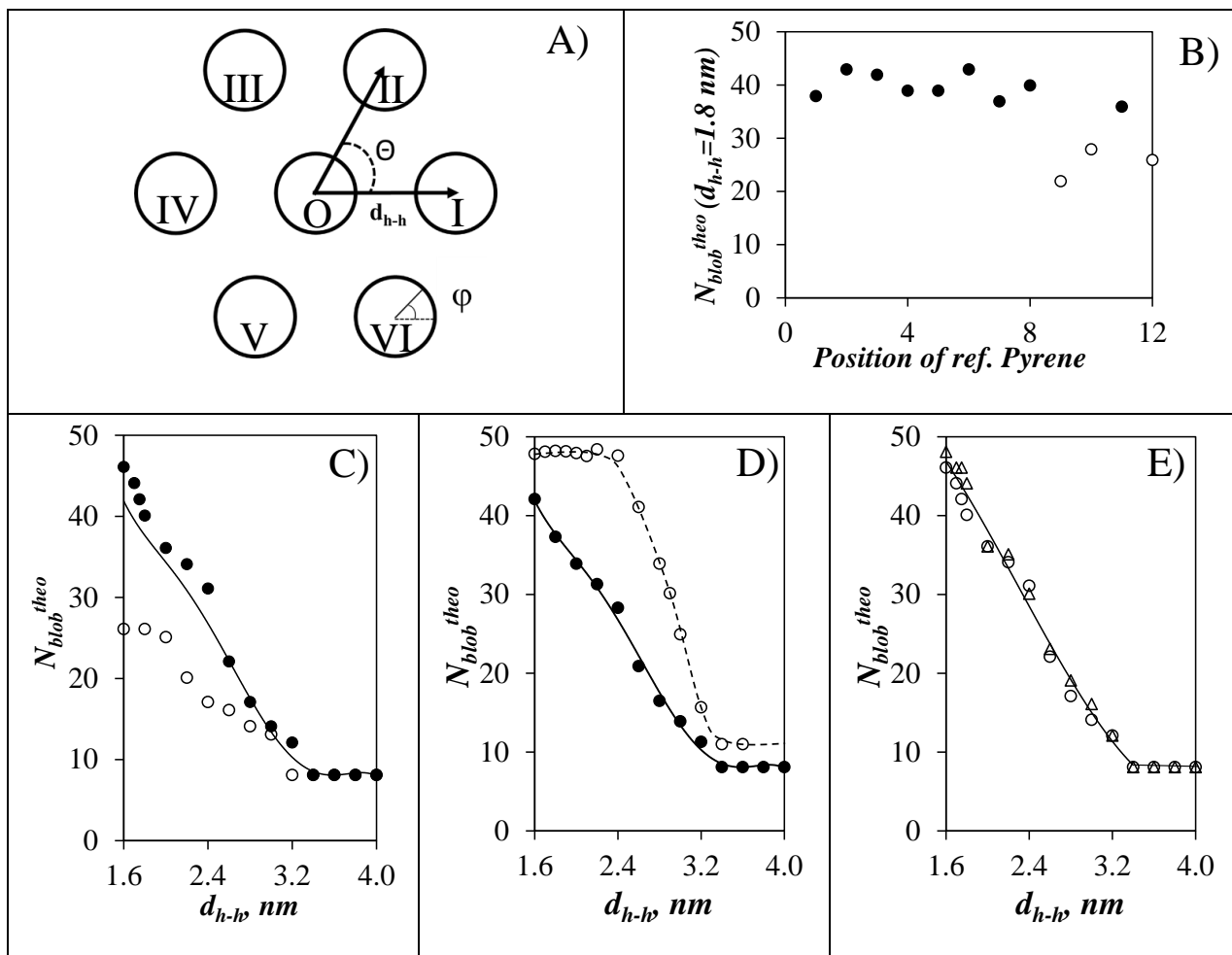
Figure 3.7. A) Illustration of an array of 7 hexagonal close packed helices. B) Plot of N_{blob}^{theo} at φ = 0° as a function of the position of the reference pyrene attached on the (○) C2- and (●) C6-hydroxyls for d_{h-h}=1.8 nm. C) Plot of (○) N_{blob}^{theo}(C2), (●) N_{blob}^{theo}(C6), where the reference pyrene is attached at the C2-hydroxyl of the 9th AGU and at the C6-hydroxyl of the 1st AGU, respectively, and (solid line) N_{blob}^{theo} averaged over the eight N_{blob}^{theo}(C6) and two N_{blob}^{theo}(C2), for glycogen with SCL=10, as a function of d_{h-h} D) Plot of N_{blob}^{theo} as a function of d_{h-h} for glycogen with SCL=10 (●, solid line) and (○, dashed line) amylopectin obtained for an infinite array of helices. Lines were added to guide the eye. E) Plot of N_{blob}^{theo}(C6) as a function of d_{h-h} for glycogen with SCL=10 at (○) $\varphi = 0°$ and (△) $\varphi = 30°$. The line represents the N_{blob}^{theo} averaged for the N_{blob}^{theo}(C6) values obtained with the Helix #0 oriented at $\varphi = 0°$ and 30°.

The MMOs for amylopectin were conducted with pyrenyl labels attached on the C2-hydroxyl of the AGUs as the C2-hydroxyl is more accessible for labeling with PyBA than the C6-hydroxyl, which pointed toward the helix interior. A consequence of dealing with a HCP lattice of infinitely long helices, as was used for amylopectin, was that the reference pyrene could only interact with a secondary pyrene attached on 3~4 helices. Although interhelical interactions involved a smaller number of helices for the MMOs conducted for amylopectin compared to glycogen, the twice longer helical side chains of amylopectin compared to those of glycogen[8,9] implied that end-effects were more prominent for glycogen than for amylopectin. Since end-effect reduce the number of interactions between pyrenyl labels, it explains why N_{blob}^{theo} was smaller for glycogen than for amylopectin in Figure 3.7D.

The influence of the angle ϕ on N_{blob}^{theo} was investigated for values of 0° and 30°, while keeping the reference pyrene on the C6-hydroxyl of the first AGU of Helix O. N_{blob}^{theo} was determined for the Glycogen(O) sample with a SCL=10 using ϕ values equal to 0 and 30° and it was plotted as a function of d_{h-h} in Figure 3.7E. The plot of N_{blob}^{theo} representative of the Glycogen(C) sample with a SCL=12 was also determined at $\phi=0$ and 30° and was plotted in Figure S3.7B in SI. The N_{blob}^{theo} values obtained for $\phi = 0$ and 30° were similar suggesting that N_{blob}^{theo} did not depend much on the ϕ angle for these short oligosaccharide helices.

107
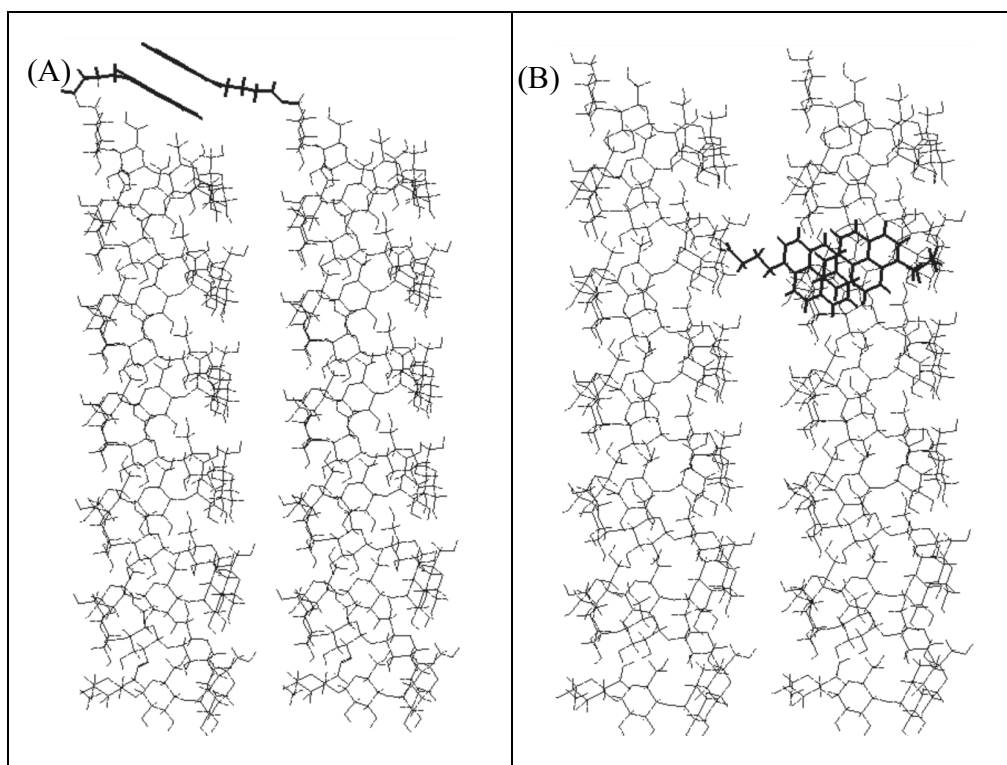
Figure 3.8. Illustration of the ability of two pyrenyl derivatives to overlap when they are attached on one AGU located in A) the 1st turn or B) the middle of an oligosaccharide helix.

Density Distribution of the Glycogen Interior: As confirmed by the FRET experiments, the pyrene labels were most likely distributed throughout the glycogen interior. Consequently, the PEF experiments were expected to probe the entire glycogen molecules. The average number of ground-state pyrenes per *blob*, <*n*>, which was retrieved from the FBM analysis to determine <N_{blob}^{exp}>, reflects the local concentration $[Py]_{loc}$ of ground-state pyrenes experienced by an excited pyrene throughout the entire glycogen molecule. However, since the local density (ρ) changes substantially with the distance from the center to the periphery of the glycogen particles whether one uses the Meléndez-Hevia model[13] or the Gilbert[23] model, $[Py]_{loc}$ changed also with the distance (r) from the centre of mass. As a result, <N_{blob}^{exp}> represents the N_{blob} value averaged throughout a glycogen molecule for the different $\rho(r)$ values obtained at different distances from

108

the center of mass of the glycogen particle. To relate $<N_{blob}^{exp}>$ to $N_{blob}^{theo}(d_{h-h})$ in Figures 3.7E and S3.7B in the SI, $N_{blob}^{theo}(d_{h-h})$ had to be first converted to the function $N_{blob}^{theo}(\rho)$. This was accomplished by changing d_{h-h} into ρ by using Equation 3.8, derived for a HCP lattice of oligosaccharide helices resulting in the function $N_{blob}^{theo}(\rho)$ shown in Figures 3.9A and S3.8A for glycogen with SCL=10 and 12 AGUs, respectively. The empirical Equations S3.14 and S3.15 were then applied to express the function $N_{blob}^{theo}(\rho)$ for glycogen with SCL=10 and SLC=12 AGUs, respectively. A single helix with 7 AGUs per turn was used to represent a side chain of glycogen and the height, h, increased by 0.88 nm per turn, as determined by the MMOs.

$$\rho = \frac{n_{AGU} \times M_o}{\sin(60^o) \times h \times N_A} \times \left(\frac{1}{d_{h-h}}\right)^2 \qquad (3.8)$$

$<N_{blob}^{exp}>$ could then be compared to $<N_{blob}^{theo}>$ after integrating $N_{blob}^{theo}(\rho)$ over the entire glycogen particle volume according to Equation 3.9.

$$<N_{blob}^{theo}> = \frac{\int_0^R \rho(r) \times N_{blob}^{theo}(\rho) \times 4\pi r^2 dr}{\int_0^R \rho(r) \times 4\pi r^2 dr} \qquad (3.9)$$

Two possible $\rho(r)$ profiles were considered in Figure 3.9B. The first profile was based on the Meléndez-Hevia model, whereby $\rho(r)$ increased continuously from the center to the pheriphery of the glycogen particles.
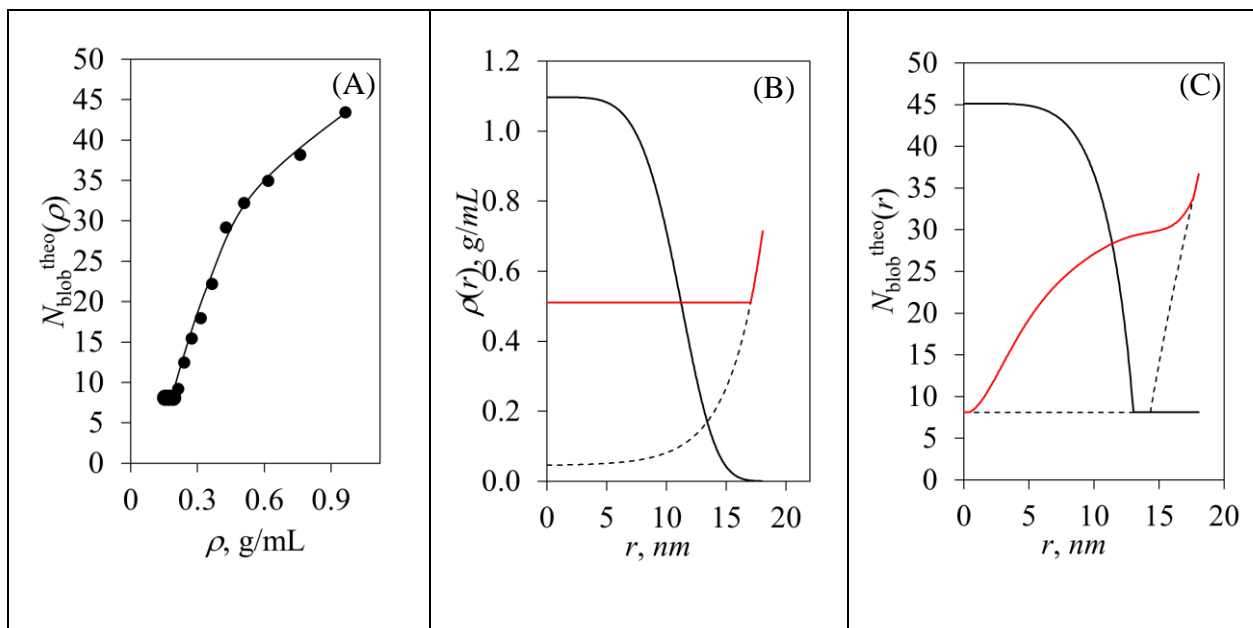
Figure 3.9. Plots of (A) $N_{\text{blob}}^{\text{theo}}(\rho)$ as a function of local density (ρ) when SLC=10 and (B) ρ profiles and (C) $N_{\text{blob}}^{\text{theo}}$ of a glycogen molecule as a function of ρ according to (▬ ▬) the Meléndez-Hevia model, (▬▬) the modified Meléndez-Hevia model, and (▬▬) the function $\rho_{\text{max}} \times \exp(-ar^b)$ with $r_{\text{max}} = 1.1$ g/mL, a= 4.3×10^{-6}, and b=5 in Equation 3.10.

The Meléndez-Hevia model is a mathematical representation of the Tier model, which predicts an increase in $\rho(r)$ from the core to the periphery of a glycogen particle, and provides a theoretical means to describe $\rho(r)$ with r representing the distance from the center of the glycogen particle assumed to adopt a spherical geometry.[10-13] The local density in each tier t was calculated by taking the mass in each tier and dividing it by the volume of the tier. Taking r for each tier as $t \times tt$, where tt is the tier thickness defined in Equation 3.5 and equal to 1.61 and 1.86 nm for glycogen from oyster and corn, respectively, the function $\rho(r)$ could be determined, which led to the $\rho(r)$ profiles shown in Figures 3.9B and S3.8B, which were plotted according to the empirical Equations S3.14 and S3.15 in the SI for the glycogen particles with SCL=10 and SCL=12 AGUs, respectively.

According to the $\rho(r)$ profiles in Figures 3.9A and S3.8A, $\rho(r)$ values lower than 0.2 g/mL would result in a $d_{h\text{-}h}$ larger than 3.4 nm, where interhelical PEF could not occur and N_{blob}^{theo} took a value of 8.1 and 9.1 for glycogen from oyster and corn, respectively, which corresponded to intramolecular PEF.

Now that $N_{blob}^{theo}(\rho)$ and $\rho(r)$ had been determined for the Meléndez-Hevia model, the radius (R) of the glycogen particles needed to be estimated in order to calculate $<N_{blob}^{theo}>$ with Equation 3.9. The determination of R required special care due to the exponential growth of ρ with increasing r. Although R_h was reported in Table 3.1 to equal 18.1 and 23.5 nm for glycogen from oyster and corn respectively, an error of 1.61 or 1.86 nm in these R_h values, equivalent to a tier thickness (tt) and representing less than 10 % of R_h, could be viewed as reasonable at first glance. Yet it would represent a much more significant 100 % error in M_n, since half of the mass of a glycogen molecule is located in the outer tier according to the Meléndez-Hevia model. Instead, R was determined with Equation 3.10, where M_n equaled 4.1 and 8.5×10^6 g/mol for the particles of glycogen from oyster and corn, respectively. According to the function $\rho(r)$ shown in Figures 3.9B and S3.8B, R was found to equal 18.1 nm and 22.1 nm for glycogen from oyster and corn, respectively. These values were close to the R_h of 18.1 and 23.5 nm calculated with $[\eta]$ and M_n for glycogen from oyster and corn and reported in Table 1, respectively.

$$M_n = \int_{r=0}^{r=R} \rho(r) \times 4\pi r^2 dr \qquad (3.10)$$

With $N_{blob}^{theo}(\rho)$, $\rho(r)$, and R known, $<N_{blob}^{theo}>$ could be calculated with Equation 3.9 and was found to equal 24 and 27 for glycogen from oyster and corn, which was significantly lower than

$<N_{blob}^{exp}>$ equal to 34 ($\pm$2) and 33 ($\pm$2), respectively. While this analysis according to the Tier model yields $<N_{blob}^{theo}>$, that is significantly lower than $<N_{blob}^{exp}>$, a number of other factors would need to be taken into further consideration before concluding that the Meléndez-Hevia model cannot rationalize the PEF measurements.

One possible reason for the discrepancy between $<N_{blob}^{theo}>$ and $<N_{blob}^{exp}>$ could be that $\rho(r)$ predicted by the Meléndez-Hevia model in Figure 3.9B represents an apparent density in the lower tiers, that underestimates the actual density experienced by the branched oligosaccharide side chains, and thus $[Py]_{loc}$, since the pyrenyl labels are attached onto the side chains, and finally N_{blob}^{theo}. For instance, Figure 3.9B shows that as $\rho(r)$ approaches 0.2 g/mL at $r \sim 15$ nm, $N_{blob}^{theo}(r)$ for $r < 15$ nm in Figure 3.9C equals 8.1 corresponding to intrahelical PEF. However, an $N_{blob}^{theo}(r)$ of 8.1 when $\rho(r) < 0.2$ g/mL for a given tier is based on the assumption, that the side chains in that tier are homogeneously distributed throughout the volume of the tier. Unfortunately, this assumption is unlikely to be obeyed since all the side chains are connected to each other via multiple branching points and the d_{h-h} experienced by the side chains is likely to be shorter than the d_{h-h} predicted by Equation 3.9 for an apparent $\rho(r)$ being less than 0.2 g/mL. Instead, the side chains in the inner tiers of a glycogen molecule are clustered with a d_{h-h}, that is shorter than 3.4 nm, and result in a larger $N_{blob}^{theo}(\rho)$ in these tiers due to interhelical PEF. A larger $N_{blob}^{theo}(\rho)$ in the inner tiers, than that represented in Figure 3.9C, would result in a larger $<N_{blob}^{theo}>$ for glycogen.

While the density experienced by the clusters of side chains in the inner tiers of a glycogen molecule might be larger than the apparent $\rho(r)$, which would lead to larger $<N_{blob}^{theo}>$ values, the clusters will also create edge effects, whereby the pyrenyl labels located on the peripheral side chains of a cluster will not be able to undergo interhelical PEF, thus reducing $N_{blob}^{theo}(\rho)$ in that tier. The decrease in $N_{blob}^{theo}(\rho)$ due to edge effects can be accounted for by applying a reduction

factor, that would decrease with decreasing number of side chains in a cluster, by considering the edge effects identified earlier in Chapter 2 for clusters of side chains in amylopectin.

In an attempt to assess how the clustering of side chains and the the edge effects generated by these clusters in the inner tiers of glycogen molecules might affect $<N_{blob}^{theo}>$, the following procedure was applied. The clusters were assumed to be constituted of a number ($n_{SC}(t)$ calculated with Equation S3.18 in each tier t) of oligosaccharide helices with a fixed d_{h-h}, whose values are listed in Table 3.2. These d_{h-h} were associated with an N_{blob}^{theo} obtained for an infinite array of oligosaccharide helices in Figure 3.7E. In turn, N_{blob}^{theo} decreased with decreasing tier number due to the edge effects of the clusters, which became more important as $n_{SC}(t)$ decreased toward the center of the glycogen particles. Plots of the corresponding $N_{blob}^{theo}(r)$ functions obtained by assuming different d_{h-h} in the clusters are provided in Figures S3.10A and B in SI for glycogen from oyster and corn, respectively.

Decreasing d_{h-h} in Table 3.2 led to increasing $<N_{blob}^{theo}>$ values approaching $<N_{blob}^{exp}>$ for d_{h-h} equal to 2.2 nm, which would correspond to a density of 0.51 g/mL, that would be experienced by the side chains in the inner tiers of the glycogen particles. The $\rho(r)$ predicted with a d_{h-h} of 2.2 nm in the lower tiers, referred to as $\rho_o(r)$ and plotted in red in Figure 3.9B, is significantly higher than the $\rho(r)$ of the Meléndez-Hevia model in Figure 3.9B for r values smaller than 15 nm. While $\rho_o(r<15$ nm) would equal 0. 51 g/mL for a d_{h-h} equal to 2.2 nm and would be larger than the density of 0.28 g/mL found earlier for clusters made of 37 oligosaccharide helical side chains in amylopectin,[28] the density of 0.51 g/mL found for glycogen particles is reasonable considering that the degree of branching of glycogen is twice that of amylopectin.[8] In fact, the plot of the density $\rho_o(r)$ predicted from a combination of PEF measurements and the Meléndez-Hevia model

113

suggests that the density experienced by the side chains in the interior of the glycogen particles is significantly larger than the predicted $\rho(r)$ at the center of the glycogen particles.

Table 3. 2. The $<N_{\text{blob}}^{\text{theo}}>$ resulted with different $d_{\text{h-h}}$.

$d_{\text{h\_h}}$, nm	ρ, g/mL	glycogen from oyster (SCL=10 AGUs)		Phytoglycogen (SCL=12 AGUs)	
		$N_{\text{blob}, \rho}$	$<N_{\text{blob}}^{\text{theo}}>$	$N_{\text{blob}, \rho}$	$<N_{\text{blob}}^{\text{theo}}>$
3.4	0.21	8	24	9	27
3.2	0.24	11	25	12	26
3.0	0.27	14	25	15	27
2.8	0.32	17	26	18	28
2.6	0.37	21	27	22	29
2.4	0.43	28	30	29	32
2.2	0.51	31	32	32	33
2.0	0.62	34	34	35	35
1.8	0.76	37	36	38	37
1.6	0.97	42	40	43	41

Contrary to the Meléndez-Hevia model, recent Monte-Carlo simulations have suggested that $\rho(r)$ for glycogen reaches its maximum at $r \sim 0$ nm near the center of the glycogen particle.[23] This representation of the glycogen particles is referred to as the Gilbert model. Equation 3.11 was considered to represent this different $\rho(r)$ profile, that would decrease from the center to the periphery of a glycogen particle. Assuming a ρ_{max} value of 0.8, 0.9, 1.0, and 1.1 g/mL led to a set of a and b parameters, that would satisfy the condition given by Equation 3.10, where M_{n} and R_{h} took the values listed in Table 3.1 for the Glycogen(O/C) particles. Errors on R_{h} are much less critical with the Gilbert model, where $\rho(r)$ takes its smallest value close to the periphery of the particles. The boundaries of 0.8 and 1.1 g/mL were set for ρ_{max}, since ρ_{max} values lower than 0.8 g/mL would fail to yield $<N_{\text{blob}}^{\text{theo}}>$ values that would match $<N_{\text{blob}}^{\text{exp}}>$, and a ρ_{max} of 1.1 g/mL represents a $d_{\text{h-h}}$ of 1.5 nm, which is the closest distance, that single oligosaccharide helices can

reach before distorting each other. For the different (ρ_{max},a,b) combinations tried with a given ρ_{max}, only one combination would result in $<N_{blob}{}^{theo}>$ calculated with Equation 3.9, that would match the $<N_{blob}{}^{exp}>$ values as shown in Figures S3.11B and S3.12B. These unique (ρ_{max},a,b) combinations are listed in Table 3.3.

$$\rho(r)=\rho_{max} \times \exp(-ar^{b}) \qquad\qquad (3.11)$$

The optimized $\rho(r)$ profiles obtained for these (ρ_{max},a,b) combinations were plotted in Figures S3.11C and S3.12C, of which the profile obtained with a ρ_{max} of 1.1 g/mL for Glycogen(O) is shown in Figure 3.9B. The corresponding $N_{blob}{}^{theo}(r)$ obtained by combining Figures 3.9A and B is shown in Figure 3.9C. The $\rho(r)$ profiles shown in Figure 3.9B and S3.8B describe the glycogen particles as having a dense core with a much lesser dense corona as suggested by the Gilbert model[23] and found by SANS experiments.[24]

Table 3.3. (ρ_{max},a,b) combinations yielding $<N_{blob}{}^{theo}>$ matching $<N_{blob}{}^{exp}>$.

		Glycogen from Oyster $M_n=4.1\times10^6$ g/mol	Phytoglycogen $M_n=8.5\times10^6$ g/mol
ρ_{max}, g/mL	b	a	a
0.8	12	4.00E-14	2.15E-15
0.9	8	1.51E-09	2.17E-10
1.0	6	3.00E-07	7.00E-08
1.1	5	4.30E-06	1.29E-06

In summary, two density distributions for the interior of glycogen particles were considered and optimized to yield $<N_{blob}{}^{theo}>$ values, that would match $<N_{blob}{}^{exp}>$. The two optimized density distributions are similar with both suggesting that the density experienced by the side chains

located at the center of the glycogen particles should be much higher than the density inferred from the Meléndez-Hevia model.

Effect of osmotic pressure: As mentioned earlier, the [η] value of 9.1 reported in Table 3.1 for the Glycogen(O) particles was much lower than the [η] value of 39 mL/g expected for an amylopectin sample of similar molar mass.[28] This observation suggested that the glycogen molecules were much denser in DMSO than amylopectin. The glycogen molecules would be expected to exhibit much less free volume than amylopectin, and consequently, to be much less deformable compared to amylopectin. As it turns out, PEF has been successfully applied to probe the deformability of polymeric particles such as amylopectin.[28] This was accomplished by monitoring the I_E/I_M ratio of a sample of Py-Amylopectin as poly(ethylene glycol)s (PEGs) of different molar masses were added to the dispersion and by relating I_E/I_M to the product $k_{diff} \times [Py]_{loc}$ as described in Equation 3.12. Whereas the addition of PEGs to the dispersion increased the dispersion viscosity and thus decreased k_{diff}, only the shorter PEGs induced a reduction in I_E/I_M as would be expected from a diffusion-controlled PEF process. The larger PEGs were unable to enter the amylopectin interior and applied osmotic pressure to amylopectin, which brought the pyrenyl labels closer, thus increasing $[Py]_{loc}$ and resulting in an increase in I_E/I_M with increasing PEG concentration. These experiments have been duplicated in Figure 3.10A with a Py(5.3)-Amylopectin sample, which was labeled with 5.3 mol% PyBA. The I_E/I_M ratio in Figure 3.10A decreased with increasing PEG(0.2K) and PEG(0.4K) concentration due to an increase in dispersion viscosity, but it increased with increasing PEG(10K) concentration due to an increase in osmotic pressure.

$$I_E/I_M \propto k_{diff} \times [Py]_{loc} \tag{3.12}$$
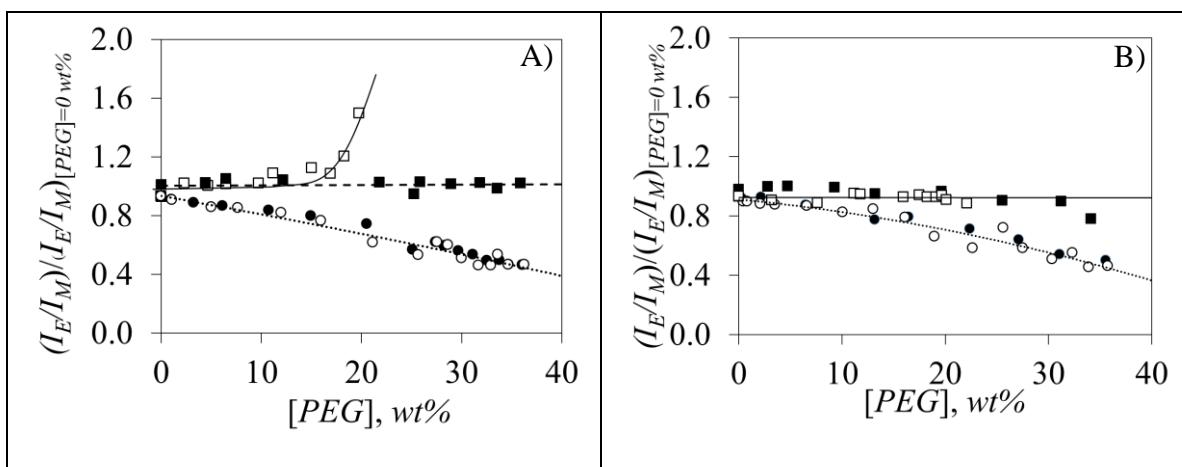
Figure 3.10. Plots of I_E/I_M as a function of PEG concentration for A) Py(5.3)-Amylopectin, B) Py(5.5)-Glycogen(O). PEGs with M_n of (●) 0.2, (○) 0.4, (■) 2.0, and (□) 10 K.

These experiments were repeated with a Py(5.5)-Glycogen(O) sample. As for Py(5.1)-Amylopectin, I_E/I_M decreased with increasing PEG(0.2K) and PEG(0.4K) concentration. On the other hand, I_E/I_M remained constant upon the addition of PEG(2K) and PEG(10K) over the same PEG(10K) concentration range, where Py(5.1)-Amylopectin had shown a sharp increase in I_E/I_M. This result strongly suggested the glycogen(O) particles were much less deformable than amylopectin, since the osmotic pressure generated by 20 wt% PEG(10K) could bring the pyrenyl labels, and thus the oligosaccharide side chains, closer to each other in Py(5.1)-Amylopectin but not in Py(5.5)-Glycogen(O). The end-to-end distance (r_{EE}) of PEG(2K) and PEG(10K) in water equal 3.8 nm and 8.4 nm, respectively, based on the relationship $r_{EE} = 0.119 \times M_n^{0.5} \times 0.707$ reported earlier.[43] Since the 12th outer tier of a Glycogen(O) particle would be populated by oligosaccharide helices separated by $d_{h-h} = 1.6$ nm (see Figure 3.9A), it is reasonable that PEG(2K) and PEG(10K) with their relatively large hydrodynamic sizes could not penetrate the interior of glycogen(O), thus fully excluded from the interior of the glycogen molecules and maintained the same I_E/I_M ratio. On the other hand, the peripheral chains of glycogen, with the maximum density near the core,

117

would expose to the network of PEG(20K) and PEG(10K). The high viscous environment decreases the k_{diff} of pyrene labels on the peripheral chains, thus slightly lowers the I_E/I_M. The constant I_E/I_M can be explained better with Tier Model.

3.5 Conclusions

This study represents the first example in the literature, where a combination of PEF, FBM, and MMOs was applied to probe the interior of two glycogen molecules at the molecular level. The FBM was taken advantage of to determine the maximum number $<N_{\text{blob}}^{\text{exp}}>$ of AGUs separating two pyrene-labeled AGUs, while still enabling PEF to occur in two series of Py-Glycogen(O/C) samples. The large $<N_{\text{blob}}^{\text{exp}}>$ values found for both glycogen particles indicated that the side chains of glycogen experienced a much denser environment than that of amylopectin. This insight led to the idea that $<N_{\text{blob}}^{\text{exp}}>$ could be used to characterize the density profile experienced by the side chains across the glycogen particles. To this end, two density profiles for the interior of glycogen were considered, one based on the Meléndez-Hevia model[13] and the other on the Gilbert model.[23] Optimization of both density profiles led to the conclusion that the density experienced by the side chains inside the glycogen particles must be much higher than that suggested by the Meléndez-Hevia model[13] in agreement with the simulations on which the Gilbert model[23] is based and results from SANS experiments.[24] Consequently, this study has illustrated how PEF measurements can be applied to predict the density of complex polysaccharide particles in solution.

Chapter 4

Random Coil Conformation of Pyrene-Labeled Dextran in DMSO Characterized by Pyrene Excimer Fluorescence

4.1 Abstract

Dextran was randomly labeled with 1-pyrenebutyric acid to yield a series of Py-Dextran samples, whose ability to form an excimer from the encounter between an excited and a ground-state pyrene was applied to characterize the conformation and internal backbone dynamics (IBD) of dextran in solution. The efficiency of pyrene excimer formation (PEF) in the Py-Dextran samples was assessed from the fluorescence intensity ratio I_E/I_M of the pyrene excimer over that of the monomer, and it was compared to that of Py-Amylose and Py-Amylopectin. I_E/I_M took the highest, intermediate, and lowest values for Py-Amylopectin, Py-Amylose, and Py-Dextran in DMSO, respectively. This trend agreed with the known conformation of these pyrene-labeled polysaccharides (Py-PSs) in DMSO, since randomly coiled Py-Dextran is the least dense, helical Py-Amylose is denser, and highly branched Py-Amylopectin has the highest internal density. The fluorescence decays of Py-Dextran were analyzed with the Fluorescence Blob Model (FBM) to yield the number N_{blob}^{exp} of anhydroglucose units (AGUs) found in a *blob*, which is the volume probed by an excited pyrene attached onto dextran, and k_{blob}, which is the rate constant for the diffusive encounters between two AGUs bearing an excited and a ground-state pyrenyl label located inside a *blob*. Comparison of N_{blob}^{exp} obtained by PEF and N_{blob}^{theo} obtained from molecular mechanics optimizations (MMOs) for Py-Dextran demonstrated that a dextran segment located inside a *blob* was extended. Comparison of the products $N_{blob}^{exp} \times l_{SU}$ and $k_{blob} \times N_{blob}^{exp} \times l_{SU}$, where l_{SU} is the length of a structural unit (SU) obtained for dextran and a series of pyrene-labeled poly(oligo(ethylene glycol) methyl ether methacrylate)s (PEG$_n$MA) in DMSO, showed that dextran was more extended and stiffer than a PEG$_n$MA sample having a hypothetical SU of similar molar mass as dextran. In summary, this PEF-based study provides a methodology for gauging the conformation and IBD of linear polysaccharides like dextran in solution.

4.2 Introduction

Over the past five years, the fluorescence of the dye pyrene and its ability to form an excimer have been applied to monitor the interactions between pyrene-labeled amylopectin and surfactants in water,[1] probe the compressibility of amylopectin in dimethyl sulfoxide (DMSO),[2,3] characterize the helical conformation of amylose in DMSO,[4] and quantify the extent of hydrophobicity of nanosized amylopectin fragments (NAFs), modified with propionyl and hexanoyl groups.[5,6] The fluorescence *blob* model (FBM) analysis of the fluorescence decays acquired with the pyrene-labeled polysaccharides (Py-PSs) has proved instrumental in probing the interior of highly branched amylopectin and NAFs[45] and the conformation of amylose[47] in DMSO. The FBM works by dividing the macromolecular volume into identical *blobs*, where each *blob* represents the volume probed by an excited pyrene. The randomly attached pyrenyl labels distribute themselves among the *blobs* according to a Poisson distribution. The FBM analysis of the fluorescence decays yields k_{blob}, the rate constant for encounters between two anhydroglucose units (AGUs) bearing one excited and one ground-state pyrene, and the average number $<n>$ of pyrenyl labels per *blob*, which is used to determine the parameter N_{blob}^{exp}, representing the number of structural units encompassed in the volume of a *blob*. Comparison of N_{blob}^{exp} to its theoretical counterpart (N_{blob}^{theo}), obtained by conducting molecular mechanics optimizations (MMOs) with HyperChem on the assumed conformation of the pyrene-labeled macromolecule, enables one to assign the conformation of the macromolecule in solution. Beside its application to PSs in solution, the random coil,[7,8] α-helical,[51,9] and 3_{10}-helical[10] conformation of several polypeptides randomly labeled with pyrene was also characterized in solution with FBM analysis. These studies on PSs and polypeptides confirmed that the FBM is a valuable experimental tool to characterize the

conformation and internal backbone dynamics (IBD) of macromolecules in solution. Since amylose, amylopectin, and a series of NAFs are the only PSs to have been examined with the FBM to date, the present study was conducted to widen the ability of the FBM to probe PSs in solution, by characterizing the IBD and conformation of pyrene-labeled dextran (Py-Dextran) in DMSO.

Dextran is a bacterial homoglycan, whose main chain is constituted of AGUs joined by α-(1,6) glycosidic bonds, with some branches generated at various hydroxyls of the AGUs.[11–13] The degree of branching of dextran has been reported to increase with increasing molecular weight.[14,15] The side chains are usually reported to be fairly short and often made of one or two AGUs.[16] The extra chain mobility afforded by the α-(1,6) glycosidic bond increases the solubility of dextran in a variety of solvents like water or DMSO.[17] The good water solubility of dextran has resulted in its use in the pharmaceutical industry as a blood plasma expander.[18] Its applicability for drug delivery is being actively researched[19] and it is used in cosmetics and bakery products.[20] Measurements conducted by calorimetry,[21] intrinsic viscosity,[22] nuclear magnetic resonance (NMR),[23] and dynamic light scattering (DLS)[24] suggest that dextran adopts a random coil conformation in DMSO or water. Compared to the earlier PEF-based studies on highly branched amylopectin[45,46] and helical amylose,[47] probing the conformation of dextran in DMSO by PEF would represent the first example of a PEF-based study on a linear unstructured polysaccharide.

As a result, this report describes the study of the IBD and conformation of a low molecular weight dextran sample. The random coil conformation of this dextran sample in DMSO was confirmed by intrinsic viscosity measurements. A series of Py-Dextran samples were prepared and their fluorescence decays were acquired in DMSO and analyzed with the FBM. The FBM parameters obtained for the Py-Dextran samples were different from those obtained earlier for

122

pyrene-labeled amylose (Py-Amylose) and amylopectin (Py-Amylopectin).[45-47] The FBM parameters indicated that dextran adopts an extended conformation and has a stiff backbone in DMSO, as would be expected from this polysaccharide. The FBM parameters were also compared to a calibration curve established with a series of pyrene-labeled poly(oligo(ethylene glycol) methyl ether methacrylate)s (Py-PEG$_n$MAs), that supported the extended and stiff nature of dextran. Together, these experiments confirmed that PEF can be used to probe the conformation and IBD of polysaccharides in solution, and that it is sensitive enough to distinguish between the conformations and IBD of different Py-PSs in solution.

4.3 Experimental

Materials: Dextran from *Leuconostoc mesenteroides* was purchased from Biosynth Carbosynth and was precipitated in cold ethanol from DMSO before use. All the other chemicals were purchased from Sigma Aldrich and used without purification.

Characterization of dextran by gel permeation chromatography: A TOSOH EcoSEC High Temperature gel permeation chromatography (GPC) instrument was equipped with a guard column, a 300 mm × 7.8 mm ID TSKgel Alpha-M column, and a triple detection system including a differential refractometer, viscosity, and Wyatt DAWN HELEOS multiangle laser light scattering (MALLS, λ= 660 nm) detectors. The lower and upper theoretical cut-offs for the GPC column corresponded to macromolecules having a hydrodynamic diameter equivalent to that of linear PEGs in water with a molecular weight of 10^3 and 10^7 Da, respectively. The instrument was operated with a flow rate of 0.5 mL/min of DMSO at 60 °C. A pullulan standard with a M_n of 47.1 kg/mol and PDI of 1.07 was used to calibrate the instrument. A dextran solution with a concentration of 1.0 mg/mL in DMSO was prepared by stirring at room temperature until a

transparent and homogeneous solution was obtained. The solution was gently filtered through a 0.22 μm syringe filter before injecting it into the GPC instrument.

Labeling of dextran with 1-pyrenebutyric acid: The dextran sample was labeled with 1-pyrenebutyric acid (PyBA) in the same manner as previously described for the preparation of pyrene-labeled amylopectin (Py-Amylopectin).[45] The reaction for the preparation of a dextran sample labeled with 8.0 mol % pyrene (Py(8.0)-Dextran) is described in detail. A 3 wt% dextran solution in DMSO was prepared gravimetrically and left to stir at room temperature until a homogenous solution was obtained. PyBA (0.64 g, 2.22 mmol) and 4-dimethylaminopyridine (47 mg, 0.38 mmol) were added to the solution. *N,N*-Dimethylformamide (10 mL) was added to the mixture to prevent the dextran solution in DMSO from freezing, when it was placed in an ice bath and capped with a rubber septum. The reaction mixture was purged with nitrogen gas (N_2, Praxair) for 30 min and kept under a N_2 atmosphere. *N,N′*-Diisopropylcarbodiimide (0.59 mL, 3.81 mmol) was added dropwise into the solution with a syringe under N_2. After 20 min, the solution was removed from the ice bath and covered with aluminium foil to prevent degradation of the pyrenyl labels by exposure to light. The reaction was left to stir at room temperature for 48 hours. The product was precipitated in cold ethanol more than three times to remove the remaining reagents, especially unreacted PyBA.

Pyrene content determination: The molar fraction (*x*) of AGUs bearing a pyrenyl label was determined by absorption measurements conducted with a Cary 100 bio-UV-Vis spectrophotometer. A stock solution of Py-Dextran was prepared with a known concentration. It was diluted with DMSO to generate five dilute Py-Dextran solutions. The absorption spectra of the five diluted samples were acquired with a 1.0 cm path length (*L*) quartz cuvette. The absorbance was kept lower than 1.5 to prevent the instrument from saturating. A plot of absorbance as a

function of the mass concentration of the Py-Dextran solutions yielded a straight line, whose slope (m) equaled $\varepsilon_{Py} \times L \times \lambda_{Py}$, with ε_{Py} being the molar extinction coefficient of PyBA equal to 41,400 $M^{-1} \cdot cm^{-1}$ at 346 nm, and λ_{Py} being the pyrene content of the Py-Dextran sample expressed in mole of pyrene per gram of sample. Equation 4.1 was then applied to determine λ_{Py}.

$$\lambda_{Py} = \frac{m}{\varepsilon_{Py} \times L} \tag{4.1}$$

The molar fraction (x) was calculated with Equation 4.2, where M_{AGU} (= 162 g/mol) and M_{Py} (= 432 g/mol) were the molar mass of unlabeled and pyrene-labeled AGU, respectively.

$$x = \frac{M_{AGU}}{\lambda_{Py}^{-1} + M_{AGU} - M_{Py}} \tag{4.2}$$

Steady-state fluorescence: Steady-state fluorescence (SSF) spectra of Py-Dextran solutions with a 2.5 μM concentration of pyrenyl labels, equivalent to a 0.1 absorption at 346 nm in DMSO, were acquired with the right-angle geometry on a Horiba QM-400 spectrofluorometer equipped with an Ushio UXL-75 xenon arc lamp. The excitation wavelength was set at 346 nm and the fluorescence of the solution was collected from 350 to 650 nm. The excitation and emission slit widths were set at 1.0 nm. The emission spectra were integrated from 376 nm to 382 nm and from 500 nm to 530 nm to yield the fluorescence intensity of the pyrene monomer (I_M) and of the pyrene excimer (I_E), respectively. The I_E/I_M ratio was calculated with these integrated values as a qualitative measure of the PEF efficiency for the Py-Dextran samples.

Time-resolved fluorescence: The monomer and excimer fluorescence decays of the Py-Dextran solutions prepared for the SSF experiments were acquired with an IBH Ltd time-resolved fluorometer fitted with an IBH 340 nm NanoLED excitation source. The excitation wavelength was set at 346 nm, and the monomer and excimer fluorescence was collected at 378 and 510 nm, respectively. A 370 or 470 nm cut-off filter was placed before the emission monochromator to suppress stray light from reaching the detector during the acquisition of the monomer or excimer fluorescence decays, respectively. The fluorescence decays of the pyrene monomer and excimer were obtained with 40,000 counts at the decay maximum using a time-per-channel of 1.02 ns/ch. The decay of a ludox suspension was acquired with a same 346 nm excitation and emission wavelength to collect the instrument response function (IRF).

Fluorescence blob model (FBM) analysis of the fluorescence decays: Four excited pyrene species have been identified in the PEF generated by pyrene-labeled macromolecules. They are the species Py_{free}^*, which are isolated from other pyrenyl labels, cannot form excimer, and relax back to the ground-state with their natural lifetime (τ_M), Py_{diff}^*, which diffuse slowly in solution with a rate constant k_{blob} reflecting the slow diffusive motion of the AGUs, to which they are covalently attached Py_{k2}^*, which represents an excited pyrene close to a ground-state pyrene, rearranging rapidly with a large rate constant k_2 ($\sim 10 \times k_{blob}$) to form an excimer, and $E0^*$, D^*, and ES^*, which are the pre-associated pyrene species collectively referred to as Py_{agg}^*, which generate an excimer instantaneously upon absorption of a photon with a lifetime that is short ($\tau_{ES} \sim 3.5$ ns), intermediate ($\tau_{E0} \sim 30\text{-}50$ ns), and long ($\tau_D \sim 60\text{-}90$ ns), respectively. The species $E0^*$, D^*, and ES^* are typically encountered in more rigid environments induced by a high solvent viscosity or stiff polymeric backbones, where re-arrangement of an excited and a ground-state pyrene to form an excimer is more hindered. PEF occurs in a sequential manner through slow diffusive motions that bring

together the AGUs bearing an excited (Py_{diff}*) and a ground-state pyrenyl label close to each other with a rate constant k_{blob}, with Py_{diff}* turning into the species Py_{k2}*, that re-arranges rapidly to form an excimer with the nearby ground-state pyrene with the rate constant k_2. Fitting the monomer and excimer fluorescence decays of the Py-Dextran samples with Equations S4.1 and S4.2, whose expressions are given in the Supporting Information (SI), yielded the molar fractions f_{diff}, f_{k2}, f_{free}, f_{E0}, and f_D of the pyrene species Py_{diff}*, Py_{k2}*, Py_{free}*, $E0$*, D*, k_{blob}, k_2, and the average number $<n>$ of ground-state pyrene per *blob*. ES* is typically omitted from the calculation of the molar fractions of the different pyrenyl species, as it only appears in the excimer decay and its contribution is much shorter-lived than all the other species in solution. The species $E0$* and D* are often combined into the aggregated pyrenyl labels (Py_{agg}*) with a molar fraction f_{agg} (= f_{E0} + f_D). $<n>$ was used to determine the number N_{blob}^{exp} of AGUs encompassed inside a *blob* according to Equation 4.3, where x is the molar fraction of AGUs bearing a pyrenyl label according to Equation 4.2, and f_{Mfree} is the molar fraction of Py_{free}* detected in the fluorescence decay of the pyrene monomer.

$$N_{blob}^{exp} = \frac{<n>}{x}\left(1 - f_{Mfree}\right) \qquad (4.3)$$

The parameters were optimized with the Marquardt-Levenberg algorithm during the decay analysis.[25] The decay fits were deemed satisfactory if the χ^2 was lower than 1.3, and the residuals and autocorrelation of the residuals were randomly distributed around zero as shown in Figure S4.1 in the SI.

4.4 Results and Discussion

As determined by GPC analysis in DMSO, the dextran sample used in this study had a number- (M_n) and weight- (M_w) average molecular weight of 7.32×10^3 g/mol and 1.07×10^4 g/mol, respectively. Since M_n was larger than 2.0×10^3 g/mol, this dextran sample could be viewed as being in a random coil conformation.[64] This M_n value corresponded to a number-average degree of polymerization DP_n of 45 AGUs, which was substantially larger than N_{blob}^{exp} found to equal 9.1 (± 0.4) AGUs in DMSO. The smaller N_{blob}^{exp} value compared to DP_n meant that the randomly coiled dextran sample could be represented by a cluster of several *blobs*, which could be characterized by applying the FBM. Furthermore, the relatively low M_n value ensured that this dextran sample should have less than one branching point per chain on average.[57,59] Since branches are mostly made of one or two AGUs for dextran,[59] this dextran sample could thus be viewed as a mostly linear chain adopting a random coil conformation in solution. Its study by PEF is described hereafter.

Fluorescence study of the Py-Dextran samples: The fluorescence spectra of the Py-Dextran samples acquired in aerated DMSO are shown in Figure 4.1A. The intensity of the spectra was normalized at 379 nm, which corresponds to the 0-0 electronic transition of pyrene. The broad band centered at 480 nm corresponds to the pyrene excimer, and its intensity relatively to that of the pyrene monomer increased with increasing pyrene content, as more pyrene-pyrene encounters took place along the PS backbone. Similar fluorescence spectra were obtained for the Py-Dextran samples in ethylene glycol and they are shown in Figure S4.2 in the SI.
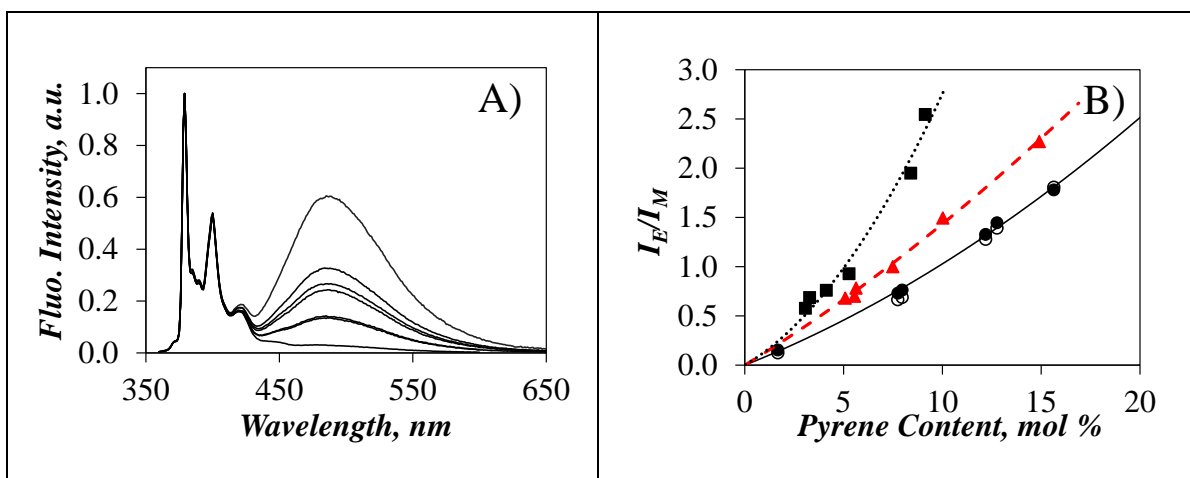
Figure 4.1. A) Fluorescence spectra of Py-Dextran in DMSO and B) plot of the I_E/I_M ratios of (■, dotted line) Py-Amylopectin, (▲, red dashed line) Py-Amylose, and (●,○ solid line) Py-Dextran in DMSO (filled symbol) and ethylene glycol (empty symbol) as a function of the pyrene content. Lines were added to guide the eye.

The efficiency of PEF between Py-Amylopectin,[46] Py-Amylose,[47] and Py-Dextran could be better compared by plotting the I_E/I_M ratio of these three Py-PSs as a function of pyrene content as shown in Figure 4.1B. In DMSO, each Py-PS yielded a different trend, with the Py-Amylopectin, Py-Amylose, and Py-Dextran samples exhibiting a large, intermediate, and low PEF efficiency, respectively. These trends could be rationalized by considering Equation 4.4, which indicates that the I_E/I_M ratio is proportional to the product $k_{diff} \times [Py]_{loc}$, where k_{diff} is the bimolecular rate constant for PEF by diffusion and $[Py]_{loc}$ is the local concentration of ground-state pyrenyl labels experienced by an excited pyrene bound to the PSs. In turn, Equation 4.5 provides the expression for k_{diff}. In Equation 4.5, N_A is the Avogadro number, σ is the encounter radius, D is the diffusion coefficient of the pyrenyl labels, which is inversely proportional to the solution viscosity and depends on the IBD of the macromolecule, and p is the probability of forming an excimer upon

encounter between an excited and a ground-state pyrene. Since the same pyrene derivative (PyBA) was used to prepare all the Py-PSs, and since the Py-PSs were constituted of the same AGUs and were all studied in DMSO, they shared similar k_{diff} values and the I_E/I_M ratio was expected to respond mainly to $[Py]_{\text{loc}}$. This was indeed observed in Figure 4.1B, where the trends followed the local density of the different PSs, which is reflected by $[Py]_{\text{loc}}$, with highly branched amylopectin being denser than helical amylose, itself being denser than the randomly coiled dextran sample. Since the pyrenyl labels were covalently attached onto the PSs, $[Py]_{\text{loc}}$ nicely tracked their local density. The different responses in I_E/I_M observed for each PS suggested that PEF could provide a relatively easy experimental means to distinguish between different PSs based on their relative internal density.

$$\frac{I_E}{I_M} \propto k_{\textit{diff}} \times [Py]_{\textit{loc}} \tag{4.4}$$

$$k_{\textit{diff}} = 4\pi N_A \sigma Dp \tag{4.5}$$

The fluorescence spectra of the Py-Dextran samples were also acquired in ethylene glycol. Surprisingly, considering that the viscosity of ethylene glycol equals 14.8 mPa·s at 25 $^{\circ}$C, which is about 7 times larger than that of 1.99 mPa·s for DMSO at 25 $^{\circ}$C, the I_E/I_M ratios were the same regardless of whether the Py-Dextran samples were dissolved in DMSO or ethylene glycol. Since PEF is expected to be diffusion-controlled in these organic solvents, where the pyrenyl labels are relatively well-solvated, Equations 4.4 and 4.5 would suggest that the I_E/I_M ratios obtained in ethylene glycol should be substantially lower than in DMSO, even after accounting for differences

in p, which is known to depend on the solvent.[26] Since PEF is also a localized phenomenon that occurs over $3 - 5$ nm, depending on the nature of the pyrene derivative,[45] effects due to solvent quality are usually not very important over this length scale, and are not expected to affect the I_E/I_M ratio much. The fact that the I_E/I_M ratios are so close in DMSO and ethylene glycol could suggest that these higher viscosity solvents have halted the IBD of dextran, and that PEF occurs mainly between pyrenyl labels located so close to each other that they can always encounter and form an excimer regardless of solvent viscosity.

While the trends obtained with the I_E/I_M ratio of the different Py-PSs in DMSO are interesting, they are the result of a delicate balance between the contributions to PEF from the different pyrene species $Py_{diff}*$, $Py_{k2}*$, $Py_{free}*$, and $Py_{agg}*$, which could be affected differently depending on the different conformations of the PSs. Similarly, increasing the solvent viscosity 7-fold could affect the balance of the pyrene species, which could result in the similar I_E/I_M ratios obtained in DMSO and ethylene glycol for the Py-Dextran samples. The contribution of each pyrene species could be determined by applying the global FBM analysis of the fluorescence decays acquired with the pyrene monomer and excimer of the Py-Dextran samples, which were acquired in DMSO and ethylene glycol and were fitted globally with Equations S4.1 and S4.2 in the SI. The fits were good with χ^2 lower than 1.25, and residuals and autocorrelation of the residuals randomly distributed around zero, as seen in Figure S4.1 in the SI as a representative example of a fluorescence decay fit. The parameters retrieved from the FBM analysis are now discussed.

The number N_{blob}^{exp} of AGUs found in a *blob* was plotted as a function of pyrene content in Figure 4.2A for the three Py-PSs in DMSO, and for Py-Dextran in ethylene glycol. Within

experimental error, the N_{blob}^{exp} values did not depend on the pyrene content, indicating that N_{blob}^{exp} was unaffected by changes in pyrene content. Contrary to the I_E/I_M ratios, that showed marked differences between the Py-PSs studied in DMSO, the N_{blob}^{exp} value of 18 ($\pm$1) obtained for Py-Amylopectin in DMSO was significantly larger than those of 10 ($\pm$1) and 9.1 ($\pm$0.4) obtained for Py-Amylose and Py-Dextran in DMSO, respectively, with the two latter sets of N_{blob}^{exp} values being close to each other. The N_{blob}^{exp} values obtained for Py-Dextran in DMSO and ethylene glycol were similar and equal to 9.1 ($\pm$0.4) and 8.1 ($\pm$0.3), respectively.

The molar fractions of the pyrenyl species shown in Figures 4.3B and C indicate that PEF occurred mainly by diffusive encounters between the pyrenyl pendants, since f_{diff} took the largest value of all the molar fractions. Increasing the pyrene content of the Py-Dextran samples resulted in a decrease in the number of isolated pyrenyl groups (f_{free} decreased in Figure 4.2C), and an increase in the number of aggregated pyrenyl labels (f_{agg} and f_{k2} increased in Figures 4.2B and 4.2C, respectively). An increase in solvent viscosity reduced f_{diff}, since the higher solvent viscosity hindered the mobility of the pyrenyl labels. This led to an increase in the contribution of the pyrenyl labels that were isolated (f_{free} increased in Figure 4.2C) or already aggregated (f_{agg} and f_{k2} increased in Figure 4.2B). Somehow, the combination of the increase in f_{free} for the pyrenyls Py_{free}^*, which do not form excimer, with the increase in f_{agg} and f_{k2} for the pyrenyls Py_{agg}^* and Py_{k2}^*, which form excimer efficiently, must have balanced out, resulting in the same I_E/I_M ratios observed for Py-Dextran in DMSO and ethylene glycol in Figure 4.1B. Interestingly, the 7-fold increase in solvent viscosity between DMSO and ethylene glycol had only a minor effect on N_{blob}^{exp} in Figure 4.2A. This result suggests that the IBD must be strongly attenuated in these solvents, so that PEF reports mainly on the conformation of the polysaccharide backbone. This conclusion will be confirmed later by conducting molecular mechanics optimizations (MMOs) on the Py-Dextran constructs.
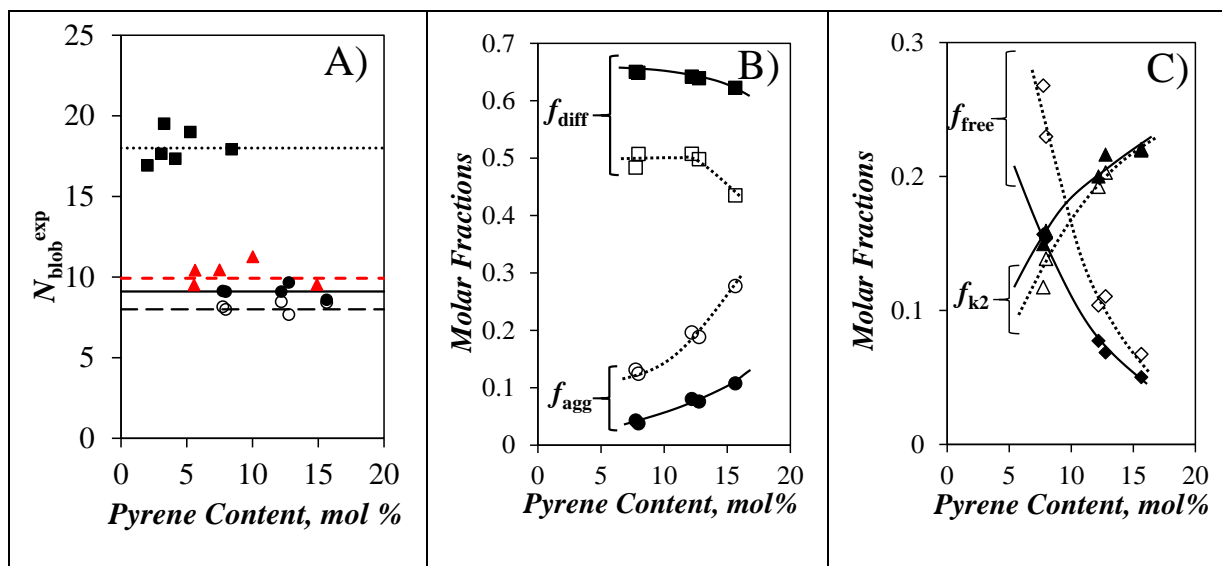
Figure 4.2. Plots as a function of pyrene content of A) N_{blob}^{exp} for (●,○) Py-Dextran, (▲) Py-Amylose, and (■) Py-Amylopectin in DMSO (filled symbol) and ethylene glycol (empty symbol), B) (●,○) f_{agg} and (■,□) f_{diff} for Py-Dextran, and C) (▲,△) f_{k2} and (◆,◇) f_{free} for Py-Dextran in DMSO (filled symbols) and ethylene glycol (empty symbols).

The larger N_{blob}^{exp} found for Py-Amylopectin was rationalized by noting that PEF could occur between different side chains in amylopectin, in a process that increased $[Py]_{loc}$ and N_{blob} compared to amylose, where PEF occurred only between pyrenyl labels along a same helix.[47] Yet amylose forming a helix in DMSO should have a denser conformation than randomly coiled dextran, which should result in a larger N_{blob} value for amylose than for dextran, contrary to what was observed in Figure 4.2A, where both dextran and amylose yielded similar N_{blob}^{exp} values. One possible reason for this unexpected result might be the conformation of the dextran backbone, where all the hydroxyls providing attachment points for the 1-pyrenebutyryl derivatives are held away from the main chain by the width of the sugar ring, thus enhancing the reach of the pyrenyl

labels, which resulted in an increase in $N_{\text{blob}}^{\text{exp}}$ for the Py-Dextran samples. In contrast, the C6-hydroxyl points toward the center of the amylose helix and is thus inaccessible for pyrene labeling. Labeling occurs at the C2- and C3-hydroxyls of amylose, where the sugar ring is locked in the helix, thus hindering the mobility of the pyrenyl label and reducing its reach to form an excimer. The special geometry of the polysaccharide backbone of dextran will be discussed in more detail later, in Figure 4.7.

Considering that Py-Amylose and Py-Dextran shared similar $N_{\text{blob}}^{\text{exp}}$ values in DMSO in Figure 4.2A, the marked difference observed in Figure 4.1 between the I_E/I_M ratios of Py-Amylose and Py-Dextran in DMSO might seem surprising at first. This result can be explained by considering the molar fraction f_{agg} of aggregated pyrenes for the three Py-PSs in DMSO. Py-Amylopectin and Py-Amylose shared similarly large f_{agg} values. Larger than expected f_{agg} values are typically found with structured macromolecules such as α–helical polypeptides[51,52,53,27] or helical PSs such as amylose[47], or the side chains of amylopectin.[45,46] If a linear polymer adopts a helical conformation, two pyrenyl labels attached onto two structural units (SUs) that are far apart along the chain might end up being next to each other after a helical turn, leading to the formation of a pyrene dimer and increased f_{agg}. The f_{agg} values obtained for dextran in Figure 4.3A are indeed much smaller than those obtained for amylose and amylopectin. Since dimers can form excimer more efficiently, the larger f_{agg} values obtained for amylose and amylopectin compared to dextran are thus expected to yield larger I_E/I_M ratios for the two former constructs, as observed experimentally in Figure 4.1A.
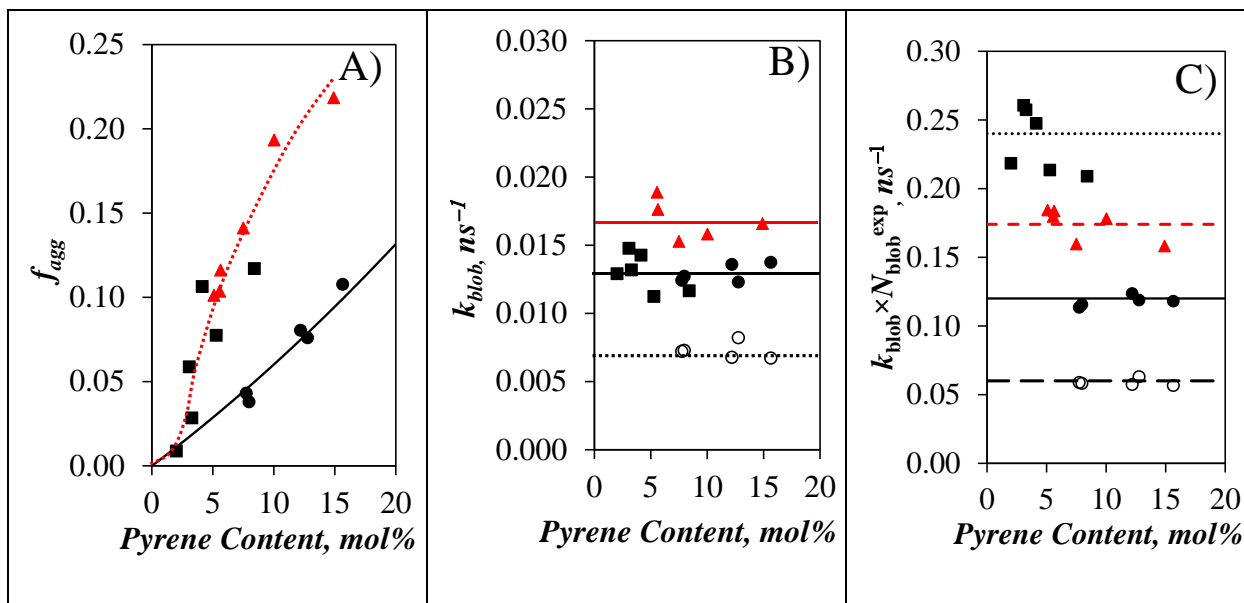
Figure 4.3. Plots of A) f_{agg}, B) k_{blob}, and C) $k_{blob} \times N_{blob}^{exp}$ for (●,○) Py-Dextran, (▲) Py-Amylose, and (■) Py-Amylopectin in DMSO (filled symbol) and ethylene glycol (empty symbol) as a function of pyrene content.

Another parameter retrieved from FBM analysis of the fluorescence decays acquired with the Py-PSs is k_{blob}, whose expression is given in Equation 4.6. k_{blob} is the product of the bimolecular rate constant k_{diff}, whose expression was given in Equation 4.5, and $1/V_{blob}$, which represents the concentration equivalent to one ground-state pyrene inside the volume V_{blob} of a *blob*. In DMSO, helical amylose restricts the mobility of the pyrenyl labels, which results in a relatively small V_{blob} and a large k_{blob}. Despite the fact that the pyrenyl labels are attached onto helical oligosaccharide side chains inside amylopectin, the highly branched interior of amylopectin is expected to hinder the mobility of the pyrenyl labels, which reduces k_{diff} and thus k_{blob} with respect to amylose, as shown in Figure 4.3B.

$$k_{blob} = k_{diff} \times \frac{1}{V_{blob}} \tag{4.6}$$

Although dextran and amylose in DMSO share a similar N_{blob}^{exp} value in Figure 4.2A, which would suggest a similar V_{blob}, the configuration of the AGUs in dextran implies that the pyrenyl labels are located further away from the effective dextran backbone, thus enhancing the reach of the pyrenyl labels compared to those attached to helical amylose, and resulting in a larger V_{blob} and a smaller k_{blob} for dextran compared to amylose in DMSO. That k_{blob} for dextran and amylopectin in DMSO are similar would just be mere coincidence. Changing the solvent from DMSO to much more viscous ethylene glycol reduces k_{diff}, and thus k_{blob} in Figure 4.3B. However, the ~50% decrease in k_{blob} observed when changing the solvent for dextran from DMSO to ethylene glycol in Figure 4.3B did not match the 7-fold increase in viscosity of the solvent at 25 °C, from 1.99 mPa.s for DMSO to 14.8 mPa.s for ethylene glycol. The reason for this discrepancy was that the diffusion coefficient in Equation 4.5 depends not only on the solvent viscosity but also on the rigidity of the polysaccharide backbone. Consequently, although k_{blob} does respond to the solvent viscosity, as shown in Figure 4.3B for dextran in DMSO and ethylene glycol, the change is not as pronounced as expected, since PEF is controlled by the internal backbone dynamics (IBD) of the PS backbone.

A much better representation of the IBD experienced by a macromolecule is obtained from the product $k_{blob} \times N_{blob}^{exp}$, which was plotted as a function of pyrene content in Figure 4.3C. $k_{blob} \times N_{blob}^{exp}$ represents the frequency of encounters between pyrenyl labels. Within experimental error, $k_{blob} \times N_{blob}^{exp}$ remained constant with the pyrene content, demonstrating that a change in the number of pyrenyl labels attached to the PSs did not affect their IBD. As it turns out, $k_{blob} \times N_{blob}^{exp}$ appears to be the perfect means to differentiate between the different PSs in different solvents,

since each set of Py-PS constructs yielded $k_{blob} \times N_{blob}^{exp}$ values that clustered around a distinct value in Figure 4.3C. Based on the trends shown in Figure 4.3C, the pyrene-pyrene encounter frequency in DMSO was highest for amylopectin, with its dense highly branched interior, intermediate for helical amylose, where the pyrenyl labels can only form excimer along a single helix, and lowest for randomly coiled dextran, where the pyrenyl labels are held farther away from the polysaccharide backbone, thus yielding a large V_{blob} and a small k_{blob}. An increase in solvent viscosity reduces the frequency of pyrene-pyrene encounters for dextran when the solvent is changed from DMSO to ethylene glycol.

In summary, the FBM analysis of the fluorescence decays acquired with the Py-PSs provides a much more detailed description of the IBD experienced by the PSs through k_{blob} and the product $k_{blob} \times N_{blob}^{exp}$, and the conformation of the PSs through N_{blob}^{exp}, compared to the cruder interpretation of the fluorescence trends obtained from the analysis of the fluorescence spectra through the I_E/I_M ratio. Comparison of the parameters k_{blob}, N_{blob}^{exp}, $k_{blob} \times N_{blob}^{exp}$, and the molar fraction f_{agg} obtained for amylopectin, amylose, and dextran led to conclusions that agreed with the known conformations of the respective PSs. Stronger support for the notion that dextran is randomly coiled in DMSO is obtained by comparing the N_{blob}^{exp} values obtained from FBM analysis to the theoretical N_{blob}^{theo} values obtained by conducting molecular mechanics optimizations (MMOs), as described in the following section.

Molecular Mechanic Optimizations: The first step in the MMOs consisted in building a dextran construct adopting an extended random coil conformation with the HyperChem software (version 7). The sugar builder function was applied to generate a dextran construct with 35 AGUs without any torsion restrictions. The chain ends of the oligosaccharide were pulled apart to generate the extended conformation expected for randomly coiled dextran, in a manner similar to the MMOs

conducted in the past on polypeptides.[50,53] In contrast to polypeptides however, special care needed to be applied during the stretching of the chain, as pulling the oligosaccharide ends too far apart induced a chair-to-boat conformational change of the AGUs. Consequently, the oligosaccharide was stretched by an amount that was increased gradually to minimize any possible distortion of the chair conformation of the AGUs. The extended chain was relaxed back to obtain a configuration of the polysaccharide backbone that was expected to locally mimic the extended random coil conformation of dextran, as shown in Figure 4.4.
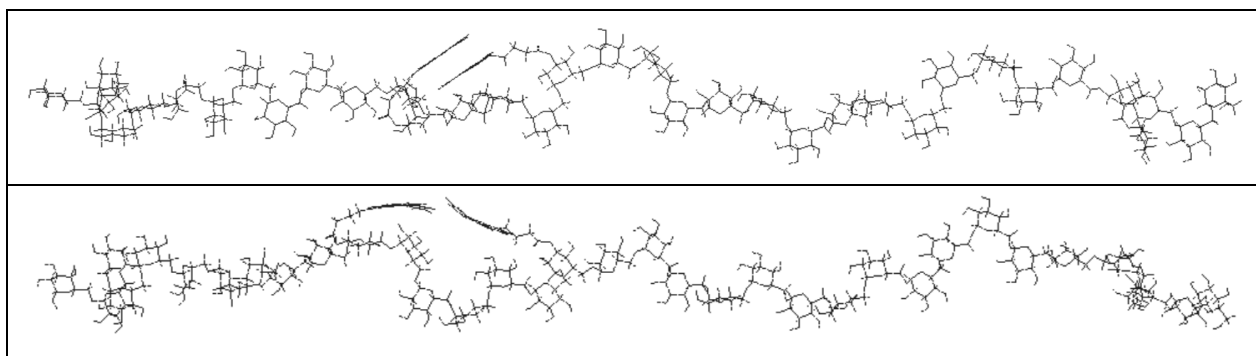
Figure 4.4. Illustration of the ability of two pyrenyl derivatives to overlap when separated by 4 AGUs (top: good overlap) and 6 AGUs (down: poor overlap).

The N_{blob}^{exp} of 9.1 (±0.4) and 8.1 (±0.3) AGUs found from FBM analysis of the fluorescence decays for dextran in DMSO and ethylene glycol, respectively, implied that two pyrenyl labels located within a 9 AGU-long segment of the oligosaccharide should be able to form an excimer. In other words, if one pyrenyl label referred to as the primary pyrene was located at the center of a *blob*, successful PEF would be achieved with another pyrene located as far as 4 AGUs away from either side of the primary pyrene. To assess whether this was indeed the case, the following procedure was applied to determine the theoretical N_{blob} value (N_{blob}^{theo}). A first

MMO was conducted by attaching the primary pyrene onto the 12th AGU of the oligomer, and a secondary pyrenyl label onto the 13th AGU. Esterification of dextran with PyBA can take place at the C2-, C3-, or C4-hydroxyl of each AGU. The reactivity of the three hydroxyls of dextran toward PyBA was estimated from the known reactivity of these hydroxyls for the acetylation of dextran (Table 4.1).[28,29] The reactivity of the three hydroxyl groups toward acetylation in organic solvents increases in the order C2 > C3 > C4. Consequently, the position of a 1-pyrenebutyroyl label on an AGU was determined with the random number generator in MS Excel, based on the probabilities listed in Table 4.1 of reacting the C2-, C3-, or C4-hydroxyl with PyBA according to the following formula. If the random number generator gave a value between 0 and 0.49, 0.50 and 0.76, or 0.77 and 1.00, PyBA was attached on the C2-, C3-, or C4-hydroxyl of the AGU, respectively.

Table 4.1. The reactivity of each hydroxyl group of dextran on acetylation.

Reaction	DS	percentage of substitution at the position		
		C2	C3	C4
acetylation with acetyl anhydride[71]	0.73	0.55	0.23	0.22
acetylation with acetyl anhydride[72]	0.45	0.45	0.29	0.26
acetylation with acetyl chloride[72]	0.41	0.51	0.29	0.20
	average	0.50	0.26	0.24

The two pyrene molecules were then induced to come within 0.34 nm from each other, while the position of the PS backbone atoms was fixed in place during the MMO, which was conducted with the Fletcher-Reeves Conjugate gradient. If the frame of the primary pyrenyl label had 7 or more carbons overlapping with the frame of the secondary pyrene, while maintaining a planar conformation (Figure 4.4 top), the overlap between the two pyrenes was considered

sufficient for successful PEF, and the AGU with the secondary pyrene was counted toward the $N_{blob}{}^{theo}$. Successive MMOs were carried out by moving the position of the secondary pyrenyl label along the backbone, while maintaining the position of the primary pyrenyl label on the 12th AGU. Each MMO resulting in 7 or more carbon atoms of the primary pyrene overlapping with the frame of the secondary pyrene was counted toward $N_{blob}{}^{theo}$, until the position of the secondary pyrene was too far from that of the primary pyrene to result in a satisfactory overlap to form an excimer (Figure 4.4 bottom). The MMOs were repeated with five different positions for the primary pyrenyl label, to account for possible differences in the local conformation of the dextran oligomer. The results of these MMOs are shown in Figure 4.5, where the number of overlapping carbons was plotted as a function of the number of AGUs separating the primary and the secondary pyrenes.
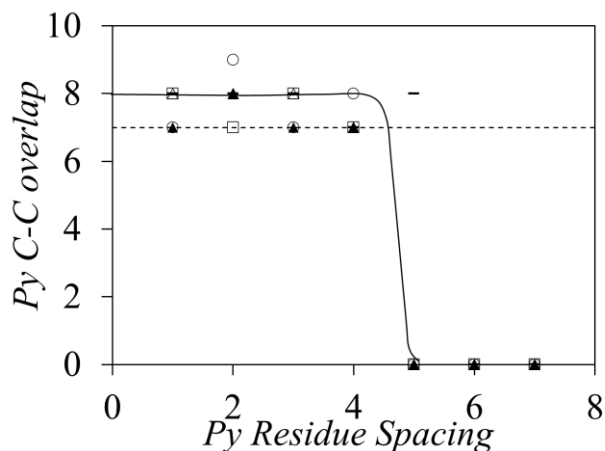
Figure 4.5. Pyrene carbon overlap as a function of the number of AGUs separating the pyrenyl groups obtained with four different positions of the reference pyrene via molecular mechanics optimization of dextran in a random coil conformation.

Based on the trends shown in Figure 4.5, the primary pyrene was unable to reach the secondary pyrene when the latter was attached on an AGU located ~5 or more AGUs away from the primary pyrene. The primary pyrene could thus reach a secondary pyrene located up to a number N_o of 4.2 AGUs away, resulting in an N_{blob}^{theo} equal to $2 \times N_o + 1 = 9.4$ (± 0.9). One AGU is added in the expression of N_{blob}^{theo} to account for the primary pyrene in the MMOs. The good agreement obtained between N_{blob}^{theo} (= 9.4 (± 0.9)) and N_{blob}^{exp} (= 9.1 (± 0.4) in DMSO and 8.1 (± 0.3) in ethylene glycol) further confirmed that dextran adopted an extended random coil conformation in DMSO and ethylene glycol.

Internal backbone dynamics of dextran: Since the $k_{blob} \times N_{blob}^{exp}$ values shown in Figure 4.3C did not depend on the pyrene content, they were averaged over all the pyrene contents for the Py-Dextran samples to yield $<k_{blob} \times N_{blob}^{exp}>$. $<k_{blob} \times N_{blob}^{exp}>$ has been shown to faithfully describe the IBD of different linear polymers.[30,74] In particular, $<k_{blob} \times N_{blob}^{exp}>$ obtained for a series of pyrene-labeled poly(alkyl methacrylate)s (Py-PAMAs) was shown to decrease with increasing side chain length, as would be expected, since a longer side chain decreases the backbone mobility.[74] Most importantly, a plot of $<k_{blob} \times N_{blob}^{exp}>$ as a function of the molecular weight of the structural unit (MW$_{SU}$) could be viewed as a calibration curve against which the IBD of other macromolecules could be gauged. For instance, the IBD of the Py-PAMAs were compared to those of poly(isobutylene-*alt*-maleic anhydride) copolymers by applying PEF.[73] Unfortunately, the calibration curve based on $<k_{blob} \times N_{blob}^{exp}>$ was obtained from Py-PAMA solutions in tetrahydrofuran (THF), where dextran is not soluble, making a comparison of the IBD of dextran and PAMAs more challenging.

Fortunately, Hunter Little, a graduate student in the Duhamel laboratory, has prepared a series of pyrene-labeled poly(oligo(ethylene glycol) methyl ether methacrylate)s (Py-PEG$_n$MA), where the number of ethylene glycols unit n ranged from 0 for poly(methyl methacrylate) to 19. The more polar oligo(ethylene glycol) side chains ensured that these polymers would dissolve in DMSO. $<N_{blob}^{exp}>$ and $<k_{blob} \times N_{blob}^{exp}>$ of the Py-PEG$_n$MA samples were determined in DMSO and they showed a decreasing trend as a function of the molar mass of a structural unit (MW_{SU}). Py-PEG$_0$MA had a lower $<N_{blob}^{exp}>$ and $<k_{blob} \times N_{blob}^{exp}>$ than pyrene labelled poly(methyl acrylate) (Py-PMA).[4] The presence of the methyl group on Py-PEG$_0$MA slows IBD which resulted in the lower $<N_{blob}^{exp}>$ and $<k_{blob} \times N_{blob}^{exp}>$ than the Py-PMA. This trend could be employed to compare $<N_{blob}^{exp}>$ and $<k_{blob} \times N_{blob}^{exp}>$ obtained for Py-Dextran. But such a comparison required the different parameters to be normalized, mainly because a methacrylate unit contributes a number n_{bb} of 2 backbone atoms, whereas an AGU contributes either 5 or 7 atoms to the backbone (see Figure 4.6). Due to the PEF dependency on the contour length of a polymer, the shortest contour length shown in Figure 4.6A was selected with n_{bb} equal to 5 atoms for dextran. Since PEF depends on the mobility of a polymeric backbone in solution, which is affected by MW_{SU},[31] and the average contour length between two pyrenyl labels depends on n_{bb}, equal to 2 and 5 for PEG$_n$MA and dextran, respectively, the ratio MW_{SU}/n_{bb}, representing the equivalent molar mass of a structural unit per backbone atom for a given polymer, was expected to be a good indicator of the effect that MW_{SU} would have on the IBD of a polymer. Furthermore, the dependency of PEF on contour length meant that $<N_{blob}^{exp}>$ obtained for the Py-PMA, Py-PEG$_n$MA and Py-Dextran samples needed to be multiplied by the length l_{SU} of a structural unit to account for the different l_{SU} of the two polymeric backbone. Using HyperChem, l_{SU} was determined to equal 0.24 and 0.47 nm for a

methacrylate unit and an AGU, respectively, and these values were used to adjust $<N_{blob}^{exp}>$ and $<k_{blob} \times N_{blob}^{exp}>$. Finally, since the length of the spacer connecting the pyrenyl label to the main chain affects both $<N_{blob}^{exp}>$ and $<k_{blob} \times N_{blob}^{exp}>$,[74] the length of the linker connecting the pyrenyl labels to the main chain, expressed in terms of the number n_L of atoms in the linker, needed to be taken in account. As shown in Figure 4.7A, n_L equals 6, 7, and 6, when the 1-pyrenebutyroyl group is attached on the C2-, C3-, and C4-hydroxyl of an AGU. After accounting for the probability of attaching the 1-pyrenebutyroyl pendant to each hydroxyl group listed in Table 4.1, an n_L value of 6.23 atoms was obtained, which is essentially the same as the n_L value of 6 for the Py-PMA and Py-PEG$_n$MA samples. Consequently, no correction was applied for these slight changes in linker length. At this stage, the quantities $<N_{blob}^{exp}> \times l_{SU}$ and $<k_{blob} \times N_{blob}> \times l_{SU}$ obtained for the Py-Dextran, Py-PMA and Py-PEG$_n$MA samples could be compared as a function of MW_{SU} in Figure 4.8A, B and C, respectively.
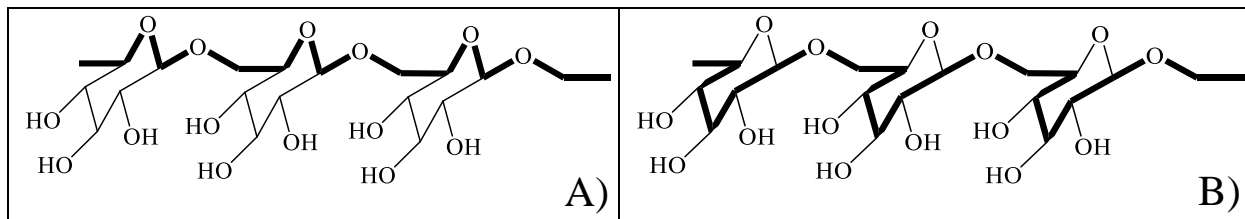
Figure 4.6. Chemical structure of dextran with the bold line highlighting different paths that can be followed to define the contour length of the polysaccharide A) $n_{bb} = 5$; B) $n_{bb} = 7$.
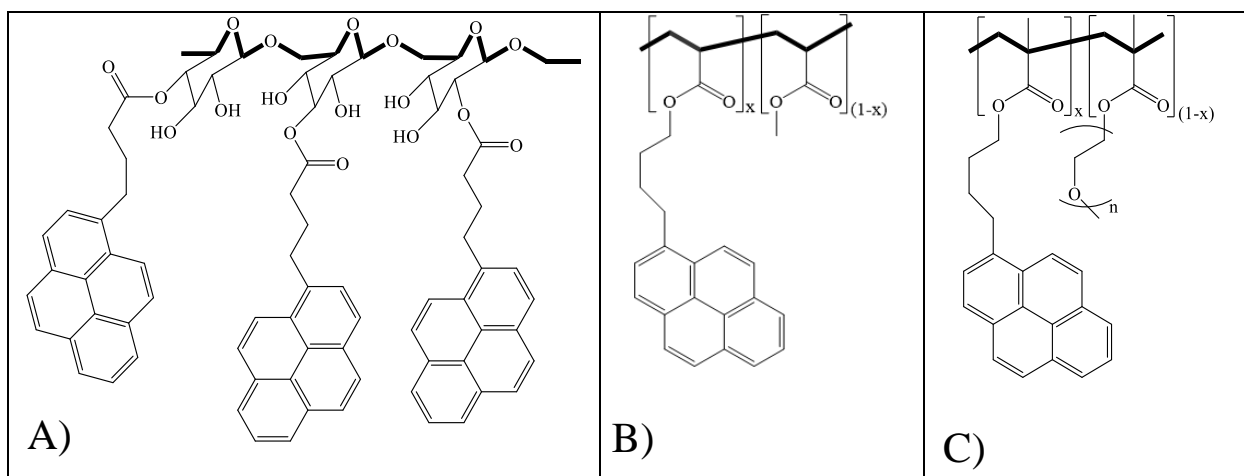
Figure 4.7. Chemical structures of A) Py-Dextran B) Py-PMA and C) Py-PEG$_n$MAs, to compare the number of atoms separating the pyrenyl label from the main chain.

Dextran took a much lower $<N_{blob}^{exp}>\times l_{SU}$ value compared to the PMA sample, which shares a similar MW_{SU}/n_{bb}. This indicated that within the volume V_{blob} of a *blob*, which should be similar for the Py-Dextran, Py-PMA and Py-PEG$_n$MA samples, since the samples shared a same n_L value, dextran contained fewer structural units than PMA. This result was probably a consequence of the cyclic nature of the AGU, whose inherent rigidity made the oligosaccharide segment more extended over the length scale of a *blob*, and whose bulkier nature prevented the backbone from folding onto itself.

After having established that dextran adopts a conformation that is more extended than a PMA having a similar MW_{SU}/n_{bb}, the IBD of dextran were now considered by comparing the product $<k_{blob}\times N_{blob}^{exp}>\times l_{SU}$ of the Py-Dextran, Py-PMA and Py-PEG$_n$MA samples. As for $<N_{blob}^{exp}>\times l_{SU}$, $<k_{blob}\times N_{blob}^{exp}>\times l_{SU}$ for dextran was also much smaller than for Py-PMA, which had a similar MW_{SU}/n_{bb} value. This result suggested that the more extended dextran sample exhibits slower IBD than a PMA sample. This conclusion was reasonable, as dextran is constituted of cyclic AGUs, which are expected to reduce the IBD of this PS.

144
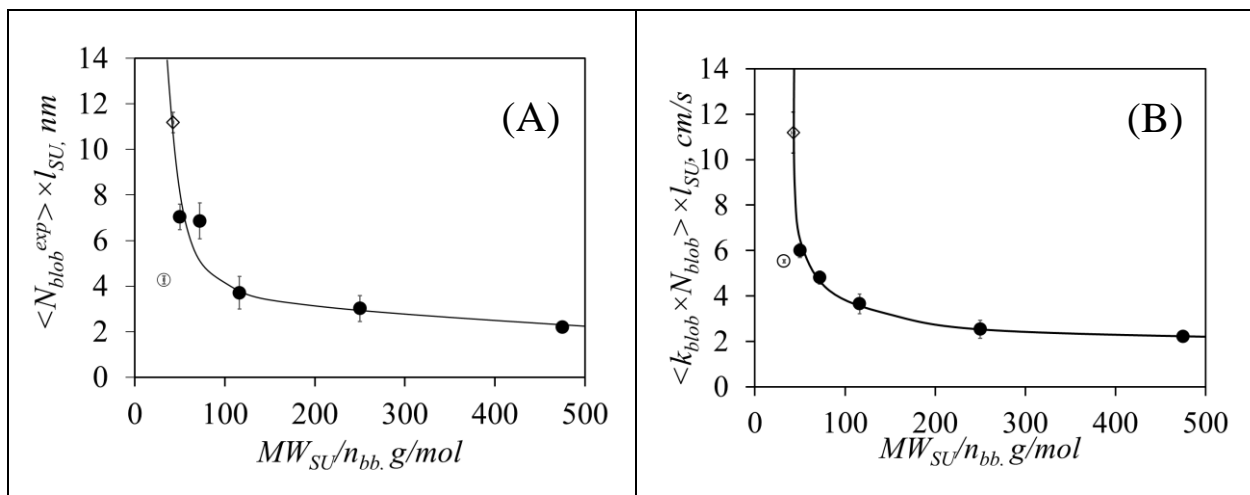
Figure 4.8. Plot of A) $<N_{blob}{}^{exp}>\times l_{SU}$ and B) $<k_{blob}\times N_{blob}{}^{exp}>\times l_{SU}$ as a function of MW_{SU}/n_{bb} for the

($\diamondsuit$) Py-PMA,[4] ($\bullet$) Py-PEG$_n$MAs and ($\circ$) Py-Dextran samples in DMSO.

4.5 Conclusion

The conformation and IBD of dextran were probed by applying PEF. The dextran sample was labeled with 1-pyrenebutyric acid, and the fluorescence spectra and decays of the Py-Dextran samples were acquired in DMSO. Their analysis indicated that PEF responds to the conformation and IBD of three different PSs, namely amylopectin, amylose, and dextran, which suggests that it could be applied to assess the nature of a given PS. Samples of amylopectin, amylose, and dextran, that had been randomly labeled with 1-pyrenebutyric acid, yielded different trends when the ratio I_E/I_M obtained from the analysis of SSF spectra and the product $<k_{blob}\times N_{blob}{}^{exp}>$ obtained from the FBM analysis of the TRF decays were plotted against the pyrene content of the Py-PSs. In DMSO, I_E/I_M and $<k_{blob}\times N_{blob}{}^{exp}>$ took their largest values for amylopectin, intermediate values for amylose, and their lowest values for dextran. These trends were in good agreement with the known conformation of these PSs in solution. The internal density and dynamics of dextran were also compared to those of MA and a series of PEG$_n$MA samples, whose $<N_{blob}{}^{exp}>$ and $<k_{blob}\times N_{blob}{}^{exp}>$ were used to establish a calibration curve. After multiplying the $<N_{blob}{}^{exp}>$ and $<k_{blob}\times N_{blob}{}^{exp}>$

values by the average length l_{SU} of a structural unit, the $<N_{blob}^{exp}> \times l_{SU}$ and $<k_{blob} \times N_{blob}^{exp}> \times l_{SU}$ values obtained for the Py-Dextran, Py-PMA and the Py-PEG$_n$MA samples could be compared by plotting them against MW_{SU}/n_{bb}. The $<N_{blob}^{exp}> \times l_{SU}$ and $<k_{blob} \times N_{blob}^{exp}> \times l_{SU}$ values obtained for dextran in DMSO suggested that it is more extended, less dense and has slower IBD than a MA sample with a similar MW_{SU}/n_{bb} value. These conclusions are reasonable, considering the respective chemical compositions of the MA and dextran backbones, with dextran expected to have a much stiffer backbone than a polymethacrylate sample, due to the cyclic AGUs constituting its backbone. In summary, this study represents the first example in the literature where PEF has been applied to characterize the internal density and dynamics of a dextran sample in solution. The results suggest that the combination of PEF, FBM analysis of fluorescence decays, and MMOs can be viewed as a reliable methodology for probing the conformation and IBD of PSs in solution.

Chapter 5

Conformation and Internal Backbone Dynamics of Pullulan in DMSO Characterized by a Combination of Pyrene Excimer Fluorescence, Fluorescence Blob Model, and Molecular Mechanics Optimizations

5.1 Abstract

A sample of the linear polysaccharide pullulan was randomly labeled with the dye pyrene to yield a series of Py-Pullulan constructs, whose ability to form an excimer upon encounter between an excited and a ground-state pyrene was examined in DMSO to probe the conformation and internal backbone dynamics (IBD) of pullulan. The efficiency of pyrene excimer formation (PEF) was characterized qualitatively from the ratio of the fluorescence intensity of the excimer over that of the monomer, namely the I_E/I_M ratio. The I_E/I_M ratios of the Py-Pullulan samples were compared with those of two other pyrene-labeled linear polysaccharides, namely a series of Py-Amylose and Py-Dextran samples, that had been previously studied. The PEF efficiency of Py-Pullulan was larger and lower than that of Py-Dextran and Py-Amylose, respectively. The difference was attributed to the different conformations and types of glycosidic bonds joining the anhydroglucose units (AGUs) in the different polysaccharides. The fluorescence decays of the Py-Pullulan samples were then analyzed with the Fluorescence Blob Model (FBM) to retrieve the parameters N_{blob}^{exp} and k_{blob}, which provide information about the internal density and dynamics of macromolecules, respectively. The N_{blob}^{exp} value of 11 (± 1) AGUs was identical with the theoretical N_{blob}^{theo} value of 11 AGUs obtained by molecular mechanics optimizations (MMOs) conducted on an extended pullulan segment used to mimic a conformation analogous to that of randomly coiled pullulan. The perfect agreement found between N_{blob}^{exp} and N_{blob}^{theo} was taken as confirmation that the Py-Pullulan samples are randomly coiled in DMSO. The N_{blob}^{exp} value of 11 (± 1) AGUs was larger than that of 9.1 (± 0.4) found for dextran, suggesting that pullulan is a bit more compact than dextran in DMSO. Analysis of the product $k_{blob} \times N_{blob}$, which represents the frequency of encounters between AGUs and provides a measure of the IBD of a polymer, led to the conclusion that dextran experiences faster IBD than pullulan.

5.2 Introduction

Pullulan is a homoglucan made of maltotriose units, which are three anhydroglucose units (AGUs) connected by two α-(1,4) glycosidic bonds, joined to each other by α-(1,6) glycosidic bonds. The α-(1,6) glycosidic bond gives additional conformational freedom to pullulan,[1] making it a more flexible and water-soluble polyglucan than amylose, whose AGUs are joined by α-(1,4) glycosidic bonds. The properties of pullulan are often compared to those of amylose and dextran, the latter polyglucan having its AGUs joined by α-(1,6) glycosidic bonds.[2-5] The properties of pullulan have been characterized by several techniques that include single-molecule atomic force microscopy (SAFM),[2] nuclear magnetic resonance (NMR),[3,4] and differential scanning calorimetry (DSC).[5] The flexibility of polyglucans has been characterized by their persistence length, determined from computational simulations[6,7] and small angle X-ray scattering.[8,9] Even though α-(1,6) glycosidic bonds are more flexible than α-(1,4) glycosidic bonds, which imparts greater motional freedom to the dextran chain compared to pullulan,[4] the persistence length of dextran, which contains only α-(1,6) glycosidic bonds, has been reported in one example to be greater than 2.0 nm in water,[9] which is larger than the less than 2.0 nm persistence length reported for pullulan,[6-8,10] which contains a mixture of more flexible α-(1,6) glycosidic bonds and less flexible α-(1,4) glycosidic bonds, and should thus be less extended than dextran. In another work, dextran and pullulan were found to share a similar persistence length of 1.3 nm.[6] These somewhat contradicting conclusions[6-10] raised the question as to whether the conformation of pullulan could be investigated by applying another technique to compare the conformation of pullulan to that of dextran in solution.

Earlier studies, conducted with macromolecules randomly labeled with the dye pyrene have established that the process of excimer formation between an excited and a ground-state pyrenyl

label can be used to characterize the conformation[11,13] and internal backbone dynamics (IBD)[14,15] of macromolecules in solution. Information on the conformation and IBD of pyrene-labeled macromolecules was obtained by applying the fluorescence *blob* model (FBM)[16] to the analysis of their fluorescence decays. Within the framework of the FBM, an excited pyrenyl label covalently bound to a macromolecule can only probe a finite subvolume of the macromolecular volume. This subvolume, called a *blob*, can be used to compartmentalize the macromolecular volume into a cluster of *blobs,* among which the pyrenyl labels are randomly distributed according to a Poisson distribution. The FBM yields the average number <n> of pyrenes per *blob*, which is used to determine the number N_{blob} of structural units (SUs) comprising a *blob*, and the rate constant k_{blob} for encounters between two SUs bearing one excited and one ground-state pyrenyl label. The product $k_{blob} \times N_{blob}$ represents the frequency of encounters between SUs and provides a quantitative measure of the IBD of a macromolecule.[14]

The properties of a few polysaccharides have been characterized with the FBM. In the case of amylose, whose conformation in DMSO is still being debated,[17,18] the FBM analysis of the fluorescence decays acquired with pyrene-labeled amylose (Py-Amylose) samples led to the conclusion that amylose adopts a helical conformation in DMSO.[13] The FBM was also applied to probe the internal density of amylopectin, which was found to be one-to-two orders of magnitude larger than that determined from intrinsic viscosity measurements.[19] The difference was attributed to the fact that intrinsic viscosity probes the density of the whole macromolecule, including its excluded volume, while the short length scale over which PEF operates enables PEF to probe the denser parts of a macromolecule, represented by clusters of helices in the case of amylopectin. The internal density of glycogen was also probed with the FBM in Chapter 3 of this thesis. It was found

to match the density that would be expected from the application of the Tier Model.[20] Finally, dextran was found in Chapter 4 to be randomly coiled in DMSO according to the FBM. Consequently, these earlier studies have demonstrated that the FBM is a suitable tool to determine the conformation of polysaccharides, whether they are randomly coiled like dextran (see Chapter 4), helical like amylose in DMSO,[13] or composed of clusters of helices like amylopectin[19] and glycogen in Chapter 3. Like dextran, pullulan is expected to be randomly coiled in solution.[21,22] Dextran and pullulan, however, should exhibit different internal densities and backbone dynamics due to the different configurations of their AGUs.

In the present study, pullulan was characterized by gel permeation chromatography (GPC), intrinsic viscosity, and PEF. Pyrene-labeled pullulan (Py-Pullulan) samples were prepared by reacting pullulan with different amounts of 1-pyrenebutyric acid, and their fluorescence response was characterized by steady-state and time-resolved fluorescence. The results obtained by fluorescence confirmed that pullulan is randomly coiled in DMSO and support the notion that the polysaccharide backbone of pullulan might be slightly less extended than that of dextran, as was inferred earlier based on the measured persistence length of these polysaccharides.[6-10] Consequently, this study confirms that a combination of PEF and FBM can probe the internal density and backbone dynamics of polysaccharides, and can thus be applied to polysaccharides having more complex compositions and/or architectures.

5.3 Experimental

Material: Pullulan was purchased from Tokyo Chemical Industry America. It was dissolved in DMSO and precipitated in acetone for intrinsic viscosity and gel permeation chromatography

(GPC) measurements. All the other chemicals were purchased from Sigma Aldrich and used without any purification.

Characterization of the pullulan sample by GPC: A 1.00 mg/mL pullulan solution was prepared in DMSO by stirring at 25 °C overnight. The solution was then filtered through a 0.22 μm syringe filter and analyzed with a TOSOH EcoSEC High Temperature gel permeation chromatography (GPC) instrument. The GPC instrument was equipped with a guard column, a 300 mm × 7.8 mm ID TSKgel Alpha-M column, and a differential refractive index (DRI) and multi-angle laser light scattering (MALLS) detector. The GPC system was calibrated with a pullulan standard having a number-average molecular weight (M_n) of 47.1 kg/mol and a polydispersity index (PDI) of 1.07. The instrument was operated with a flow rate of 0.4 mL/min at 60 °C. The number- (M_n) and weight- (M_w) average molecular weight of pullulan equaled 1.8×10^5 g/mol and 3.6×10^5 g/mol, respectively, resulting in a PDI of 2.0. The GPC trace of the pullulan sample acquired with the DRI detector can be found in Figure S5.1 in the Supporting Information (SI).

Intrinsic viscosity of pullulan in DMSO: A 0.01 g/mL pullulan stock solution was prepared in DMSO by stirring at 25 °C overnight. The stock solution was diluted with different amounts of DMSO to prepare 6 samples, whose concentration ranged from 0.9 to 7.8 mg/mL. The inherent (η_{inh}) and reduced (η_{red}) viscosity of each solution in DMSO were measured with an Ubbelohde viscometer at 25 °C. Extrapolating the straight lines obtained for η_{inh} and η_{red} to the *y*-intercept yielded the intrinsic viscosity, found to equal 148 (±2) g/mL.

Labeling of pullulan with 1-pyrenebutyric acid (PyBA): The pyrene-labeled pullulan (Py-Pullulan) samples were prepared via Steglich esterification as described for the preparation of pyrene-labeled amylopectin.[19] The protocol used to prepare a Py-Pullulan sample labeled with 6.6 mol% of 1-pyrenebutyric acid (PyBA) is described hereafter. A 3 wt% pullulan solution (1.0 g, 6.2 mmol

AGUs) was prepared in DMSO by stirring at room temperature until a transparent and homogenous solution was obtained. PyBA (0.6 g, 2.0 mmol) and 4-dimethylaminopyridine (DMAP) (54.3 mg, 0.44 mmol) were added to the solution. After the complete dissolution of PyBA and DMAP, 10 mL of dimethylformamide was added to the solution to prevent it from freezing, when its temperature was brought to 0 °C in the following step. The solution was capped with a rubber septum, transferred to an ice bath, and kept under N_2 atmosphere by purging with N_2 gas. While the solution was kept under N_2 atmosphere at 0 °C, N,N'-diisopropylcarbodiimide (DIC) (0.34 mL, 2.2 mmol) was added dropwise. About 20 minutes after DIC addition, the solution was removed from the ice bath and covered with aluminum foil to prevent the degradation of pyrene by exposure to light. The reaction was continued for 48 hours at room temperature before being quenched by letting air in. The product was purified by several precipitations in cold acetone. Since the precipitations were aimed at removing unreacted PyBA, which emits as a monomer in the fluorescence spectra, the purity of the Py-Pullulan samples was verified by monitoring changes in the fluorescence spectra between two precipitations. The removal of unreacted PyBA was deemed complete when two successive precipitations resulted in two identical fluorescence spectra.

Pyrene content determination: The molar fraction x of AGUs labeled with pyrene in a Py-Pullulan sample was determined with a Cary 100 bio-UV-Vis spectrophotometer. A DMSO solution of a Py-Pullulan sample with a known mass concentration in DMSO was prepared and stirred at 25 °C overnight. The stock solution was diluted with different amounts of DMSO to prepare at least 5 solutions with an absorbance at 346 nm that was lower than 2, to avoid saturating the UV-Vis spectrophotometer. The absorbance at 346 nm was plotted as a function of the mass concentration based on the Beer-Lambert law. Linear plots were obtained with the slope (m) being equal to $\varepsilon_{Py} \times L \times \lambda_{Py}$, where ε_{Py} is the molar extinction coefficient of pyrene at 346 nm equal to 41,400

$M^{-1} \cdot cm^{-1}$ for PyBA,[13] L is the path length of an absorption cell equal to 1 cm, and λ_{Py} is the pyrene content in moles of pyrene per gram of pullulan. λ_{Py} was obtained by applying Equation 5.1.

$$\lambda_{Py} = \frac{m}{\varepsilon_{Py} \times L} \tag{5.1}$$

The molar fraction x of pyrene-labeled AGUs in a Py-Pullulan sample was determined by applying Equation 5.2, where the molar mass of unlabeled (M_{AGU}) and pyrene-labeled (M_{Py}) AGU equaled 162 g/mol and 432 g/mol, respectively.

$$x = \frac{M_{AGU}}{M_{AGU} - M_{Py} + \lambda_{Py}^{-1}} \tag{5.2}$$

Steady-state fluorescence: A Horiba QM-400 spectrofluorometer equipped with an Ushio UXL-75 xenon arc lamp was used to acquire the fluorescence emission spectra of the Py-Pullulan samples with the right-angle geometry. The absorbance of the Py-Pullulan solutions was kept at 0.1, equivalent to a 2.5 μM concentration of pyrenyl labels, a concentration low enough to avoid the inner filter effect and prevent intermolecular interactions. The slit width of the excitation and emission monochromators were set at 1.0 nm. The Py-Pullulan solutions were excited at 346 nm and their emission was collected from 360 to 650 nm. The fluorescence intensity of the pyrene monomer (I_M) and pyrene excimer (I_E) were determined by integrating the emission spectrum from 376 to 382 nm and from 500 to 530 nm, respectively. The I_E/I_M ratio was used to gauge the PEF efficiency of the Py-Pullulan samples.

Time-resolved fluorescence: An IBH Ltd. time-resolved fluorometer was used with an IBH 340 nm NanoLED as an excitation source to acquire the fluorescence decays of the Py-Pullulan samples. The Py-Pullulan solutions were excited at 346 nm, while their fluorescence was collected at 378 and 510 nm, respectively. Cut-off filters at 370 and 470 nm were placed before the emission monochromator to minimize stray light from hitting the detector during the acquisition of the monomer and excimer fluorescence decay, respectively. Both fluorescence decays were collected with 20,000 counts at the decay maximum and with a time-per-channel of 1.02 ns/ch. The instrument response function (IRF) was obtained by acquiring the decay of a Ludox suspension with the same excitation and emission wavelength of 346 nm.

Fluorescence blob model (FBM) analysis of the fluorescence decays: The dynamics experienced by the pyrenyl groups attached onto pullulan were probed by analyzing the fluorescence decays of the Py-Pullulan samples according to the FBM. Upon absorption of a photon, the excited pyrene can decay according to several pathways. An isolated pyrene (Py_{free}*), that cannot form an excimer, will decay back to the ground state with its own lifetime (τ_M). The pyrenyl groups Py_{diff}* diffuse slowly according to the motion of the AGUs, to which they are attached. Diffusive motions of two AGUs bearing an excited Py_{diff}* and a ground-state pyrene are described by the rate constant k_{blob}. As the species Py_{diff}* approaches a ground-state pyrene, it transforms into the species Py_{k2}*, that rearranges quickly with a rate constant k_2 to form an excimer with the nearby ground-state pyrene. k_2 is ~10 times larger than k_{blob}. PEF is enhanced by increasing the average number $<n>$ of ground-state pyrenyl groups present in a *blob*. Direct excitation of pyrenyl labels involved in pyrene aggregates (Py_{agg}*) can result in a poorly (D*) or well- ($E0$*) stacked pyrene excimer, which emits with its natural lifetime τ_D or τ_{E0}, respectively. The FBM analysis of the fluorescence decays retrieves $k_{blob}, k_2, <n>$, and the molar fractions $f_{free}, f_{diff}, f_{k2}, f_{E0}$, and f_D of the pyrene species Py_{free}*,

*Py*diff*, *Py*k2*, *E0**, and *D**, respectively. The molar fraction f_{agg} of aggregated pyrenes (*Py*agg*) is taken as the sum $f_{E0} + f_D$. $<n>$ can be used to calculate the number N_{blob} of AGUs constituting a *blob* as shown in Equation 5.3, where f_{Mfree} is the molar fraction of *Py*free* species being detected in the monomer decays and x is the molar fraction of AGUs, that are labeled with PyBA.

$$N_{blob}^{exp} = \frac{1 - f_{Mfree}}{x} \times <n>$$ (5.3)

The fluorescence decays of the pyrene monomer and excimer for the Py-Pullulan samples were fitted globally according to the FBM with Equations S5.1 and S5.2 given in the SI, respectively. All the parameters retrieved from the fluorescence decay fits were optimized with the Marquardt-Levenberg algorithm.[23] The quality of the fits of the fluorescence decays with the FBM was gauged from a χ^2 value that was lower than 1.3, and a random distribution around zero of the residuals and of the autocorrelation of the residuals.

5.4 Results and Discussion

Conformation of Py-Pullulan: Five Py-Pullulan samples were prepared whose molar fraction x of pyrene-labeled AGUs ranged from 2.5 to 13.1 mol %. The fluorescence spectra of the Py-Pullulan samples were normalized at 379 nm, which corresponds to the 0-0 transition of pyrene. They are shown in Figure 5.1A. They illustrate how PEF increases with increasing pyrene content as a result of increased pyrene-pyrene encounters. The I_E/I_M ratios of the Py-Pullulan samples were calculated and compared in Figure 5.1B with the I_E/I_M ratios of Py-Dextran obtained in Chapter 2, and those

of Py-Amylose.[13] Within experimental error, Py-Pullulan and Py-Amylose yielded similar I_E/I_M ratios in Figure 5.1B, with Py-Dextran showing the smallest I_E/I_M ratios in DMSO.

The analysis of the I_E/I_M trends is complicated by the interplay, described in Equation 5.4, that exists between the internal backbone dynamics (IBD) of the polysaccharides, reflected by the rate constant k_{diff} for PEF by diffusive encounters between two pyrenyl labels, and the conformation of the polysaccharide, reflected by the local concentration $[Py]_{loc}$ of ground-state pyrenes experienced by an excited pyrene. For instance, a collapsed chain in a poor solvent will have a high $[Py]_{loc}$ but k_{diff} might be small due to steric hindrance generated by the collapsed polymer coil. In contrast, a polymer in a good solvent will generate a lower $[Py]_{loc}$ with a larger k_{diff}. Consequently, since both k_{diff} and $[Py]_{loc}$ contribute to the I_E/I_M ratio in often opposite manners, interpretation of the I_E/I_M trends is usually more subtle, particularly in cases where the I_E/I_M trends show little differences, as found in Figure 5.1B for the Py-Amylose, Py-Pullulan, and Py-Dextran samples.
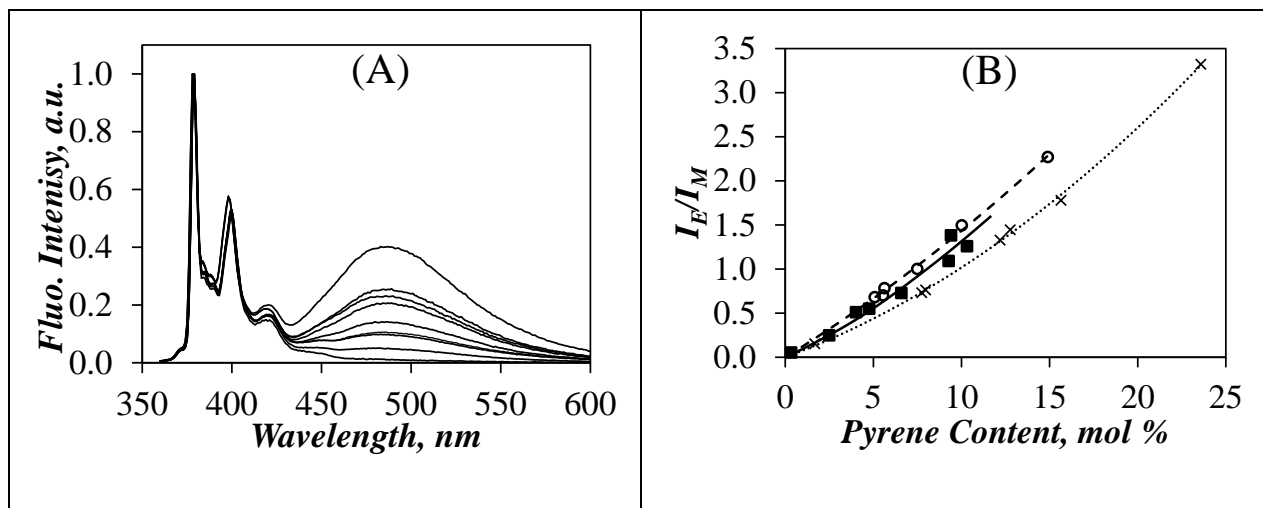
Figure 5.1. Fluorescence spectra of Py-Pullulan in DMSO and B) plot of the I_E/I_M ratio for (■, solid line) Py-Pullulan, (×, dotted line) Py-Dextran, and (O, dotted line) Py-Amylose in DMSO as a function of pyrene content. Lines were added to guide the eyes.

$$\frac{I_E}{I_M} \propto k_{diff} \times [Py]_{loc} \qquad\qquad (5.4)$$

Fortunately, the contributions from the IBD and conformation of a pyrene-labeled polysaccharide reflected by the PEF signal and given by, respectively, k_{diff} and $[Py]_{loc}$ can often be differentiated through the global FBM analysis of its pyrene monomer and excimer fluorescence decays. The FBM analysis of the Py-Pullulan samples was conducted to obtain the parameters k_{blob} and $<n>$, and the molar fractions f_{diff}, f_{k2}, f_{free}, f_{E0}, and f_D of the pyrenyl species $Py_{diff}*$, $Py_{k2}*$, $Py_{free}*$, $E0*$, and $D*$, respectively, with the molar fraction f_{agg} of aggregated pyrenyl species being equal to the sum $f_{E0} + f_D$. The behavior of the parameter k_{blob} is discussed first in Figure 5.2A, that shows a plot of k_{blob} as a function of pyrene content for the Py-Pullulan, Py-Dextran, and Py-Amylose samples. Within experimental error, k_{blob} remained constant for all the polysaccharides over all pyrene contents and equalled 12 ($\pm$1), 13 ($\pm$1), and 17 ($\pm$1) μs^{-1} for pullulan, dextran, and amylose, respectively. The constancy of k_{blob} with the pyrene content indicates that pyrene-labeling did not affect the conformation and dynamics of the polysaccharides in solution. Based on the trends obtained for the k_{blob} values, k_{blob} was larger for Py-Amylose than for the Py-Dextran and Py-Pullulan samples. The difference in k_{blob} was attributed to differences in both the conformation of the polysaccharides in DMSO, with amylose adopting a helical conformation[13] and dextran and pullulan being randomly coiled, and the length of the linker connecting the pyrenyl group to the backbone of the polysaccharides.
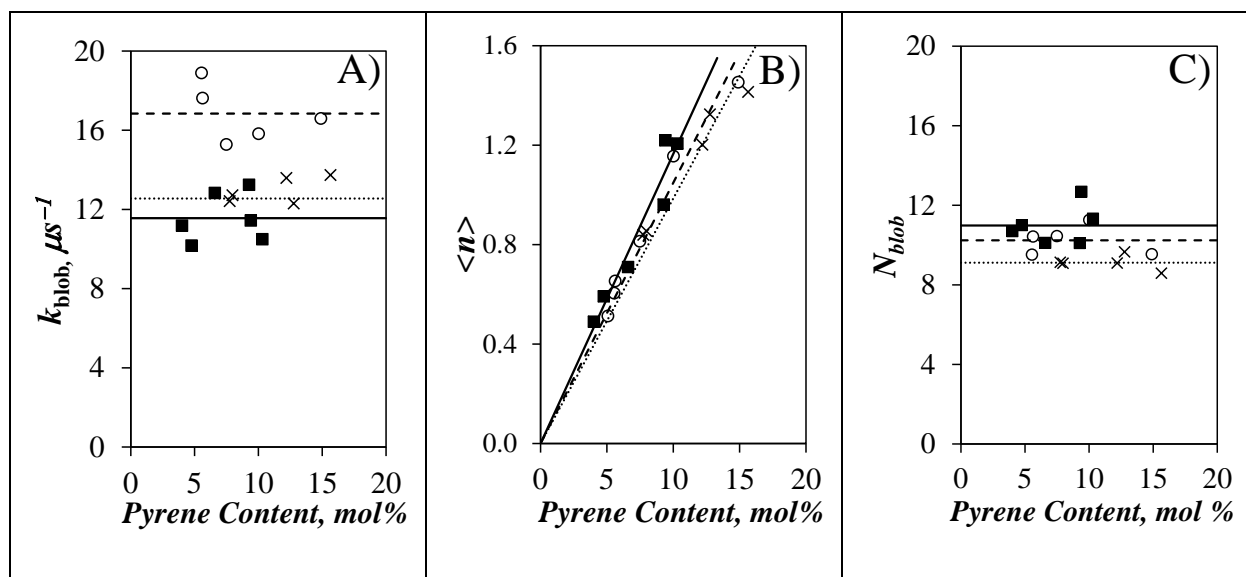
Figure 5.2. Plots of A) k_{blob}, B) $<n>$, and C) N_{blob}^{exp} as a function of pyrene content. (solid line, ■) Py-Pullulan, (dotted line, ×) Py-Dextran, and (dashed line, ○) Py-Amylose. The lines in Figures 5.2A and C represent the average values, while the lines in Figure 5.2B represent the line of best fit.

Within the framework of the FBM, k_{blob}, whose expression is given in Equation 5.5, equals the product of k_{diff} by ($1/V_{blob}$), where $1/V_{blob}$ is the concentration equivalent to one ground-state pyrene inside a *blob*. Consequently, k_{blob} is affected by the size of a *blob*, which is defined in part by the size of the linker used to attach pyrene to the polysaccharide. In the present study, the pyrene-labeling of a polysaccharide involves the reaction of PyBA with the different hydroxyl groups of the AGUs in the polysaccharide. The AGUs in dextran are joined by α-(1,6) glycosidic bonds. Only the secondary C2-, C3-, and C4-hydroxyls can react with PyBA. In contrast, pullulan is made of maltotriose repeating units, whose three AGUs are joined by two α-(1,4) glycosidic bonds. The maltotriose units are then joined by α-(1,6) glycosidic bonds. Consequently, some C6-hydroxyls are available in pullulan and they are expected to represent the main type of hydroxyls

to primarily undergo esterification with PyBA, due to their higher nucleophilicity.[24] The position

of the pyrenyl labels along dextran and pullulan is illustrated in Figure 5.3.

$$k_{blob} = k_{diff} \times \frac{1}{V_{blob}} \tag{5.5}$$

Although the pyrenyl labels attached to the C6-hydroxyl of a pullulan AGU is separated

from the AGU by a 6 atom-long linker, that has one more carbon than the 5 atom-long linker

connecting pyrene to dextran at the C2-hydroxyl of its AGUs, the linker length must be referenced

with respect to the atom defining the branching point along the contour length of the

polysaccharide. As discussed in Chapter 4, the pyrenyl labels and the polysaccharide contour

length are separated by 6.2 atoms in Py-Dextran (see Chapter 4 and Figure 5.3B) versus 6.0 atoms

in Py-Pullulan (see Figure 5.3A). The similar number of atoms constituting both linkers suggests

that both polysaccharides share a similar V_{blob}. Since both Py-Pullulan and Py-Dextran also yield

a similar k_{blob} value, they must also share a similar k_{diff} according to Equation 5.5. However, sharing

a same k_{diff} value does not mean that dextran and pullulan also share similar IBD, because k_{diff}

reflects the IBD and linker dynamics of these pyrene-labeled polysaccharides. Since part of the

linker joining the pyrenyl label of Py-Dextran to its contour length includes the rigid sugar ring in

Figure 5.3B, the linker dynamics of Py-Dextran must be slower compared to the linker dynamics

of Py-Pullulan, implying that the IBD of dextran are faster than the IBD of pullulan, if dextran and

pullulan share a same k_{blob} value as indicated in Figure 5.2A. This conclusion is reasonable since

the polysaccharide backbone of dextran contains more $\alpha-(1,6)$ glycosidic bonds, which are known

to be flexible than $\alpha-(1,4)$ glycosidic bonds.[4]
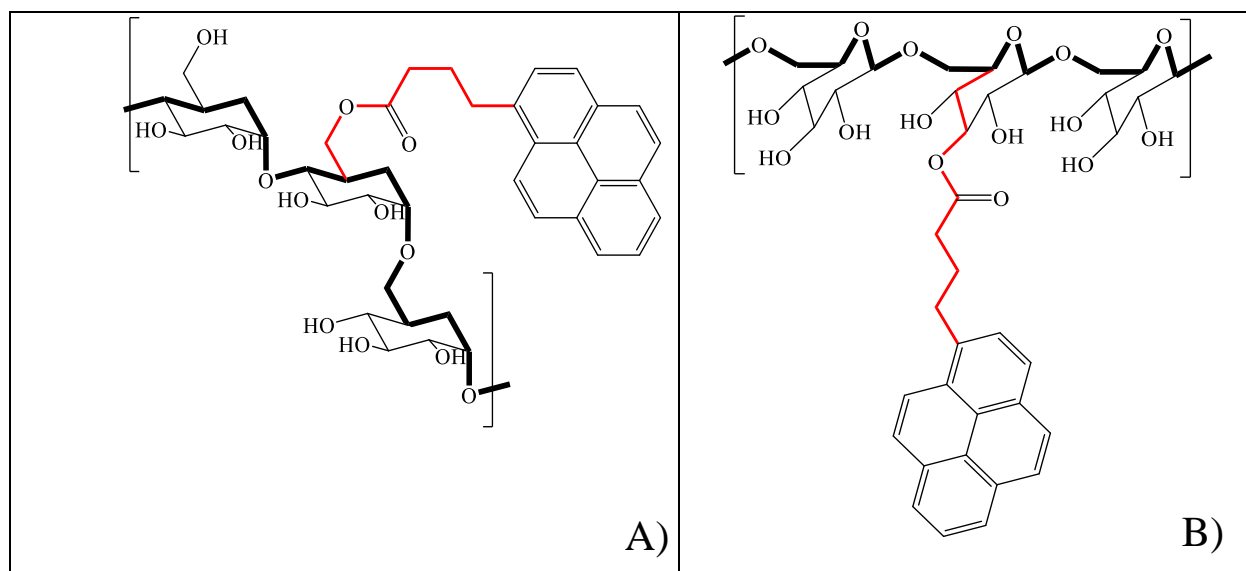
Figure 5.3. Chemical structure of A) Py-Pullulan and B) Py-Dextran. The contour length of the polysaccharide backbone and the linker length are indicated by thick black and red chemical bonds, respectively.

The significant difference in k_{blob} obtained for Py-Amylose compared to both the Py-Dextran and Py-Pullulan series was attributed to the different conformations between helical amylose[13] and randomly coiled dextran and pullulan.[21,22] The helical backbone of amylose holds the pyrenyl labels closer to the envelop of the helix via a short 5-atom long linker connected to the C2-hydroxyl, which reduces V_{blob} in Equation 5.5 and results in a larger k_{blob} value.

The FBM yielded the average number *<n>* of ground-state pyrenes inside a *blob* for Py-Pullulan, which was compared to that of Py-Amylose and Py-Dextran in Figure 5.2B. Similar *<n>* values were obtained, that translated into similar N_{blob}^{exp} values calculated according to Equation 5.3. Within experimental error, the N_{blob}^{exp} values in Figure 5.2C remained constant with the pyrene content, indicating that the level of pyrene labeling did not affect the parameters retrieved from the FBM analysis. After averaging over all the pyrene contents of a same polysaccharide series,

$<N_{\mathrm{blob}}^{\mathrm{exp}}>$ was found to equal 11 ($\pm$1), 9.1 ($\pm$0.3), and 10.2 ($\pm$0.7), for Py-Pullulan, Py-Dextran, and Py-Amylose, respectively. Since Py-Pullulan and Py-Dextran share a similar linker length based on the chemical structure of the polysaccharides provided in Figure 5.3 and since the AGUs contribute 5 bonds to the contour length of both polysaccharides, the slightly larger $<N_{\mathrm{blob}}^{\mathrm{exp}}>$ obtained for Py-Pullulan compared to Py-Dextran suggests that dextran is more extended than pullulan in DMSO. Comparison of the $<N_{\mathrm{blob}}^{\mathrm{exp}}>$ values between helical amylose and the two other polysaccharides is more complicated due to their different conformations.

More information about the conformation of the polysaccharides can be obtained from the analysis of the molar fractions of pyrenyl labels shown in Figure 5.4. The molar fraction f_{diff} shown in Figure 5.4A was largest. It equalled 0.64 ($\pm$0.06) for the three polysaccharides. This indicated that PEF occurred mainly by diffusive encounters between two pyrenyl labels. The molar fraction f_{agg} of aggregated pyrenes reflects the density of a polymer in solution, with a denser polymer yielding larger f_{agg} values. Py-Amylose yielded the largest f_{agg} values in Figure 5.4B, followed by Py-Pullulan, and Py-Dextran. This trend agreed with the expected helical conformation of amylose and supported the notion that dextran is more extended in DMSO than pullulan, thus resulting in less aggregation for the pyrenyl labels of Py-Dextran. The molar fraction f_{free} of isolated pyrenes in Figure 5.4C also suggested that dextran is the most extended polysaccharide, since it yielded the largest f_{free} value. The more coiled conformation of pullulan brought the pyrenyl labels of Py-Pullulan closer to each other, resulting in fewer isolated pyrenyl labels and lower f_{free} values compared to Py-Dextran. In fact, it shared the same f_{free} values as amylose, whose helical conformation in DMSO brought the pyrenyl labels closer to each other, resulting in larger f_{agg} values. Further information about the conformation of pullulan in DMSO can be obtained by comparing $<N_{\mathrm{blob}}^{\mathrm{exp}}>$ of pullulan to the $<N_{\mathrm{blob}}^{\mathrm{theo}}>$ value determined from molecular mechanics

optimizations (MMOs) on pyrene-labeled polysaccharide constructs mimicking the conformation of randomly coiled pullulan.
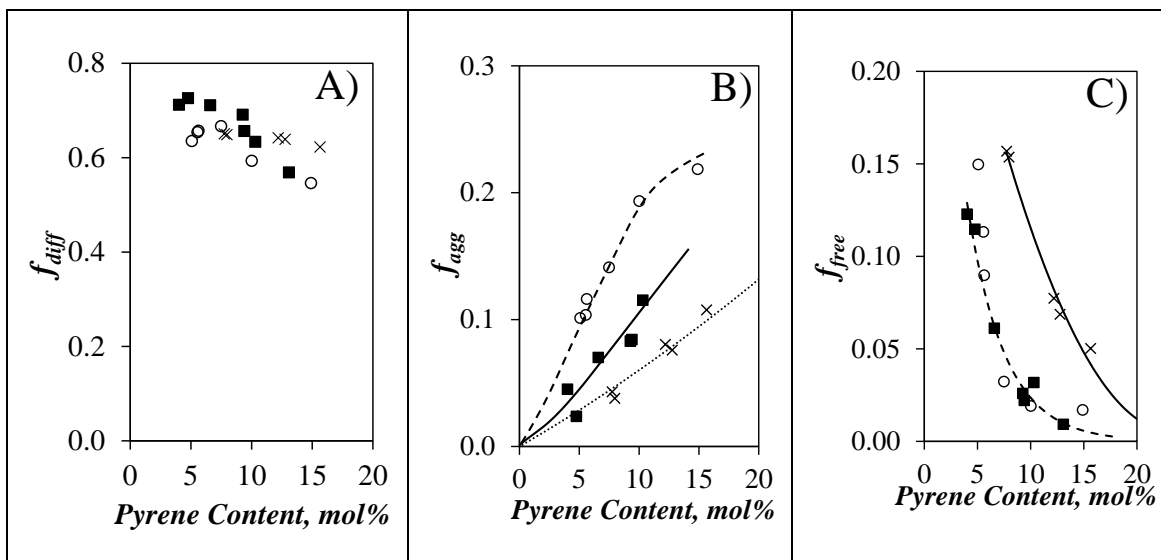
Figure 5.4. Plots of A) f_{diff}, B) f_{agg}, and C) f_{free} as a function of pyrene content. (■) Py-Pullulan, (×) Py-Dextran, and (○) Py-Amylose. Lines were added to guide the eye.

Molecular Mechanics Optimizations: A pullulan construct with 43 AGUs was built with the sugar builder function in the program HyperChem. The three torsion angles ϕ, ψ, and ω were not restricted. The chain was stretched by imposing a distance between the chain ends, that was increased step by step to minimize any distortion of the AGUs from a chair to another, mainly boat, conformation.[2] Once the chain was as extended as possible without showing any distortions induced by chair-to-boat transitions, the constraint imposing an extended distance between the chain ends was lifted and the polysaccharide backbone was allowed to relax into a conformation representative of an extended random coil for pullulan, as shown in Figure 5.5. The pyrenyl groups were covalently attached to pullulan by creating ester bonds with the C6-hydroxyl, since it has the

highest reactivity for esterification.[24, 25] The first pyrene was referred to as the reference pyrene and was attached on five different locations on pullulan, to account for any potential differences arising from the random coil conformation of the backbone. A second pyrenyl group was attached on the C6-hydroxyl of the AGU next to the reference AGU. If the C6-hydroxyl of an AGU was involved in an α-(1,6) glycosidic bond with another AGU, the C2-hydroxyl of the AGU was selected to attach PyBA, since it is known to have a better reactivity than the other secondary alcohol.[26] The two pyrenyl groups were induced to come within 0.34 nm from each other after fixing all atoms of the polysaccharide backbone. The overlap between the two pyrenyl groups was considered to be conducive of PEF when the frame of the primary pyrene remained planar and had 7 or more carbons overlapping the frame of the secondary pyrene as in the top panel of Figure 5.5. If a good overlap was obtained, the AGU for the secondary pyrenyl label was counted as one unit for the number N_0 of AGUs on one side of the reference pyrenyl label that would generate a good pyrene-pyrene overlap. The secondary pyrenyl label was then attached to the next AGU and the MMO was repeated. A good overlap indicated that this secondary AGU should be counted toward N_0, whose value was increased by one unit. The process was repeated until the reference and secondary pyrenyl labels were too far apart to ensure satisfactory overlap, as shown in the bottom panel of Figure 5.5. A few positions past the AGU, where a poor overlap had been obtained for the first time, were also tried and after confirmation of poor or no overlap, the series of MMOs was ended and the N_0 value was recorded. A different AGU was selected for the reference pyrene and a new series of MMOs was conducted to generate another N_0 value. In all, five different reference AGUs were tried and the number of overlapping carbons were plotted as a function of the number of AGUs separating the reference and secondary pyrenyls in Figure 5.6.
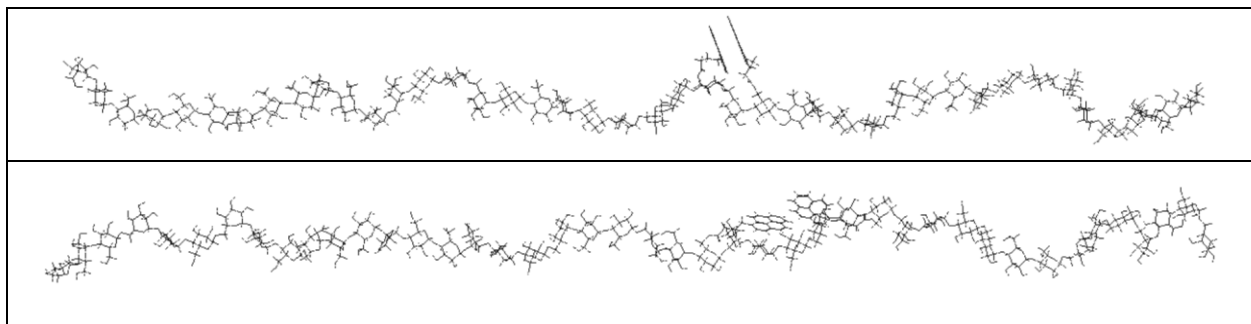
Figure 5.5. Illustration of the ability of two pyrenyl derivatives to overlap when separated by 3 AGUs (top: good overlap) and 6 AGUs (down: poor overlap) for an extended conformation of pullulan.

According to Figure 5.6, a good overlap was obtained between the reference and secondary pyrene if N_0 equaled 5. Since the same N_0 would have been obtained on both sides of the reference pyrene, N_{blob}^{theo} was taken as $2 \times N_0 + 1 = 11$ AGUs, where 1 accounted for the reference pyrene. N_{blob}^{theo} was thus in perfect agreement with the N_{blob}^{exp} value of 11 (± 1) determined with the FBM. The good agreement between N_{blob}^{theo} and N_{blob}^{exp} supported the fact that pullulan is randomly coiled in DMSO.
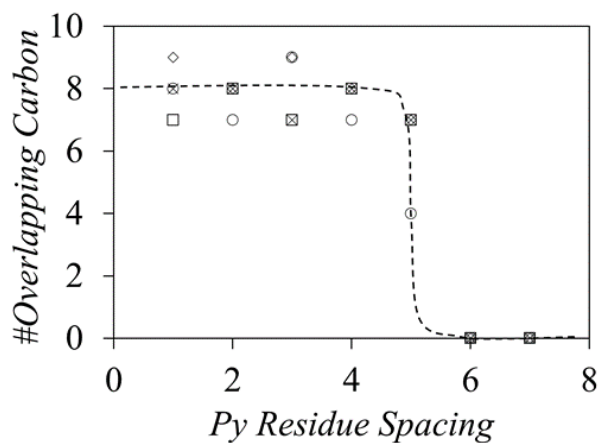
Figure 5.6. Pyrene carbon overlap as a function of the number of AGUs separating the reference and secondary pyrenyl groups obtained with five different reference positions, by conducting MMOs with the pullulan construct shown in Figure 5.5.

Stiffness of the backbone of pullulan: Having determined the parameters $N_{\text{blob}}^{\text{exp}}$ and k_{blob} for dextran in Chapter 4, $<N_{\text{blob}}^{\text{exp}}>$ and the product $<k_{\text{blob}} \times N_{\text{blob}}^{\text{exp}}>$, representing the frequency of AGU encounters inside a *blob*, were compared to the same parameters obtained for pyrene-labeled poly(methyl acrylate) (Py-PMA)[13] and a series of pyrene-labeled poly(oligo(ethylene glycol) methyl ether methacrylate)s (Py-PEG$_n$MAs with n = 0, 1, 3, 9, and 19). This comparison took advantage of an earlier study conducted with a series of pyrene-labeled poly(alkyl methacrylate)s (Py-PAMAs) in tetrahydrofuran (THF), which had established that $<N_{\text{blob}}^{\text{exp}}>$ and the product $<k_{\text{blob}} \times N_{\text{blob}}^{\text{exp}}>$ were representative of the conformation and IBD of a macromolecule, respectively.[14] Unfortunately, the Py-PAMA series being insoluble in polar solvents like DMSO prevented its use for comparison purposes for the study of many biological macromolecules like dextran and pullulan, which are soluble in DMSO. This explains why the fluorescence experiments originally conducted with the Py-PAMAs were repeated by graduate student Hunter Little, who prepared a series of Py-PEG$_n$MA samples, which were soluble in DMSO. However, comparisons between different polymer backbones must account for the structural parameters that were illustrated in Figures 5.3 and 5.8, such as the number of atoms n_{bb} involved in each structural unit (2 and 5 for a methacrylate and AGU, respectively), the length of the linker connecting the pyrenyl label to the polymer backbone (~ 6 for the Py-Dextran, Py-Pullulan, Py-PMA and Py-PEG$_n$MA samples), and the average length l_{bb} per atom constituting the contour length of the polymer (1.2, 1.2, 0.94, and 0.89 Å for PEG$_n$MA, MA, dextran, and pullulan, respectively). Since PEF depends on the contour length, both $<N_{\text{blob}}^{\text{exp}}>$ and $<k_{\text{blob}} \times N_{\text{blob}}^{\text{exp}}>$ were corrected by multiplying them by the length l_{SU} ($= n_{\text{bb}} \times l_{\text{bb}}$) of a structural unit equal to 0.24, 0.47, 0.45 and 0.45 nm for the Py-Dextran, Py-Pullulan, Py-PMA and Py-PEG$_n$MA samples, respectively. Since the four polymers have a similar linker length, as discussed earlier in Figure 5.3, the linker length was not accounted

for in the discussion for $<N_{blob}^{exp}>$ and $<k_{blob} \times N_{blob}^{exp}>$. A plot of $<N_{blob}^{exp}> \times l_{SU}$ is shown in Figure 5.8 as a function of MW_{SU}/n_{bb}, which represents the molar mass of the structural unit per atom contributing to the contour length. The plot shows that as the oligo(ethylene glycol) side chain of the Py-PEG$_n$MA samples increased, the quantity $<N_{blob}^{exp}> \times l_{SU}$ decreased, since steric hindrance generated by the side chains stiffened the polymethacrylate backbone, forcing it to adopt an increasingly extended conformation. This also explains why Py-PMA took a higher $<N_{blob}^{exp}> \times l_{SU}$ and $<k_{blob} \times N_{blob}^{exp}> \times l_{SU}$ value than Py-PEG$_0$MA because the absence of methyl group increases the IBD of Py-PMA. Py-Pullulan and Py-Dextran yielded similar $<N_{blob}^{exp}> \times l_{SU}$ values, but their value was much lower than that expected for a Py-PMA sample of similar MW_{SU}/n_{bb}, indicating that dextran and pullulan are quite extended in DMSO. The $<N_{blob}^{exp}> \times l_{SU}$ value for Py-Pullulan appeared to be slightly larger than that for Py-Dextran, suggesting that dextran is slightly more extended than pullulan in DMSO, in agreement with earlier reports.[8,9]
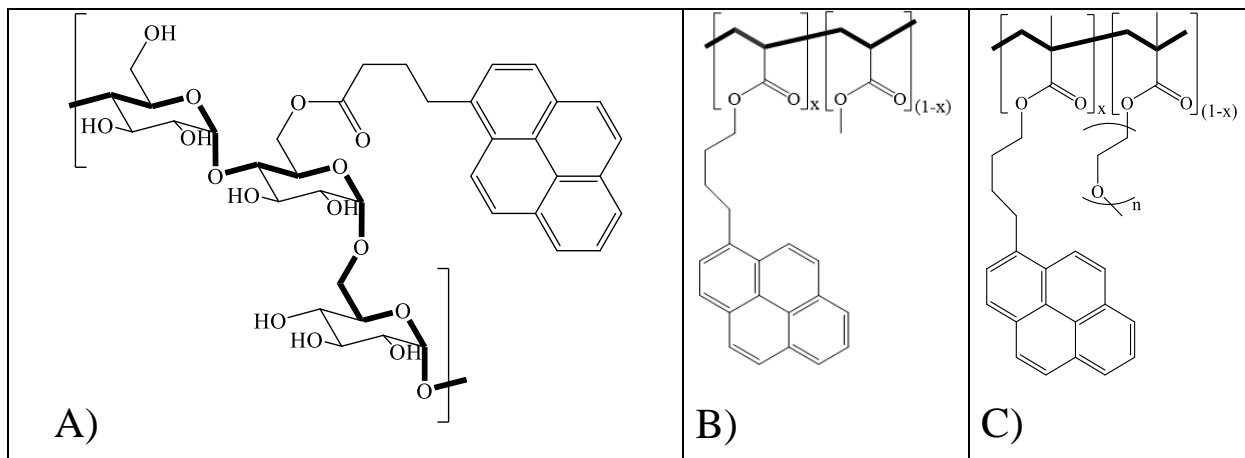
Figure 5.7. Chemical structures of A) Py-Pullulan, B) Py-PMA and C) Py-PEG$_n$MA samples. The bold line on the structure represents the contour length of the polymer.
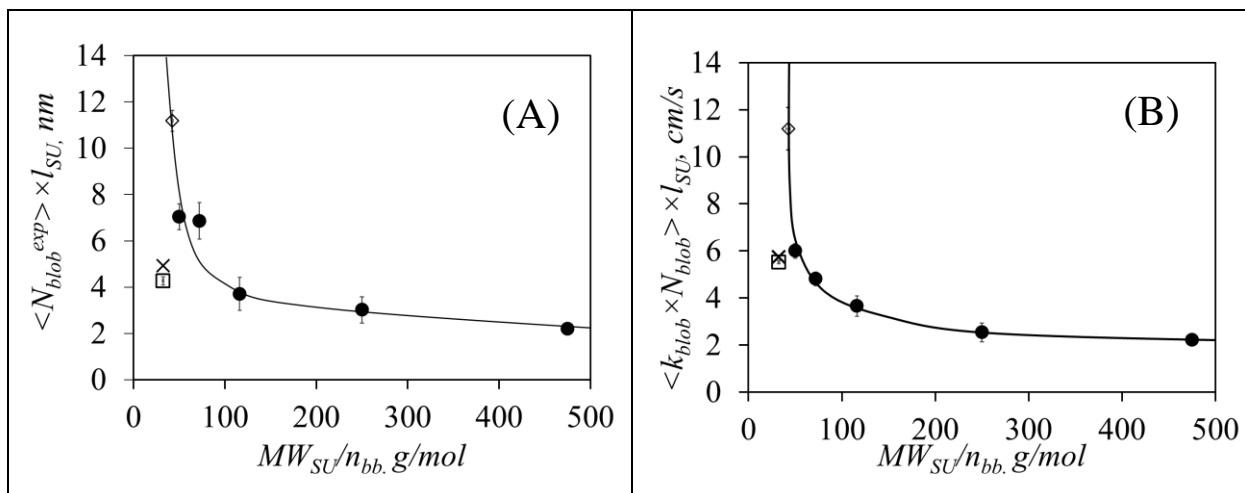
Figure 5.8. Plot of A) $N_{blob}^{exp} \times l_{SU}$ and B) $k_{blob} \times N_{blob}^{exp} \times l_{SU}$ as a function of the corrected molar mass of a repeating unit for ($\diamond$) Py-PMAs,[13] ($\bullet$) Py-PEG$_n$MAs, ($\times$) Py-Pullulan, and ($\square$) Py-Dextran.

Figure 5.8B compares the product $<k_{blob} \times N_{blob}^{exp}> \times l_{SU}$, which represents the frequency of encounters between the atoms constituting the polymeric backbone located inside a *blob*, for the pullulan and dextran constructs. The $<k_{blob} \times N_{blob}^{exp}> \times l_{SU}$ values obtained for pullulan and dextran were similar and took a value that was smaller than the $<k_{blob} \times N_{blob}^{exp}> \times l_{SU}$ value of the Py-PMA having a similar MW_{SU}/n_{bb} ratio. This comparison led to the conclusion that dextran and pullulan exhibit slower IBD compared to the Py-PMA constructs, due to the cyclic nature of their repeating units which stiffen the polysaccharide backbone. Although the linkers separating the pyrenyl label from the contour length of the Py-Pullulan and Py-Dextran samples share a same number of atoms, the linker of the Py-Dextran samples include the rigid sugar ring (see Figure 5.3B). Since the product $<k_{blob} \times N_{blob}^{exp}>$ combines the backbone and linker dynamics, where the linker dynamics of the Py-Dextran samples must be slower than the linker dynamics of the Py-Pullulan samples, the IBD of pullulan must be slower than those of dextran if a same $<k_{blob} \times N_{blob}^{exp}> \times l_{SU}$ value is obtained in Figure 5.8B. These considerations suggest that dextran exhibits increased mobility

compared to pullulan, a reasonable conclusion considering that the dextran backbone contains more mobile α-(1,6) glycosidic bonds compared to pullulan.[4]

The flexibility of polysaccharides in water has been examined by computational simulations,[6,7] small-angle x-ray scattering (SAXS),[8,9] and intrinsic viscosity measurements.[10] In water values between 1.0 and 1.9 nm have been reported for the experimentally determined persistence length of pullulan,[8] while the persistence length of dextran has been found to decrease from 2.8 to 2.0 nm when the molecular weight of dextran increased from 11.2 to 253 kg/mol.[9] The persistence length of 2.8 nm reported for a 11.2 kg/mol dextran, short enough to minimize branching,[27] should be similar to that of the dextran sample studied by PEF in Chapter 4, which had an M_n value of 7.3 kg/mol and a PDI of 1.5. The larger persistence length found in the literature for dextran would suggest that dextran is a stiffer polymer compared to pullulan. Despite the small difference between the product $<N_{blob}^{exp}> \times l_{SU}$ of 4.3 ($\pm$0.2) nm for dextran and 4.9 ($\pm$0.4) nm for pullulan, the larger value obtained for pullulan suggests that dextran is more extended than pullulan in DMSO, as expected from the persistence length values reported in the scientific literature.[8,9]

5.5 Conclusion

PEF was applied to examine the conformation and flexibility of pullulan in solution. A series of Py-Pullulan samples was prepared and their ability to form excimer in DMSO was characterized by steady-state and time-resolved fluorescence. The I_E/I_M ratio and FBM parameters such as N_{blob}^{exp} and f_{agg} were determined for the Py-Pullulan samples and compared to the values obtained earlier with other polysaccharides. $<N_{blob}^{exp}>$ for Py-Pullulan equaled 11 ($\pm$1) and matched exactly the N_{blob}^{theo} value found by MMOs for Py-Pullulan adopting a random coil conformation. Although this finding might not be surprising, since the random coil conformation of pullulan in DMSO has

already been established by intrinsic viscosity measurements,[21,22] it still demonstrates that the combination of FBM, PEF, and MMOs applied in the present study constitutes a useful and robust methodology to examine the conformation of polysaccharides in solution. The larger $<N_{\text{blob}}^{\text{exp}}>$ value of 11 ($\pm$1) for pullulan compared to that of 9.1 ($\pm$0.4) found for dextran suggested that pullulan is more coiled than dextran, in agreement with published persistence lengths of the two polysaccharides.[8,9] The same $<k_{\text{blob}}>$ value found for dextran and pullulan, which reflected the IBD of the polysaccharides and the dynamics of their linker with pyrene, also suggested that the backbone of dextran is more mobile than that of pullulan, since the dynamics of the Py-Dextran linker are hindered by the cyclic AGU compared to the dynamics of the Py-Pullulan linker. The conclusion that the backbone of dextran is more mobile than that of pullulan was reasonable based on the ratio of the less mobile $\alpha-(1,4)$ to the more flexible $\alpha-(1,6)$ glycosidic bonds, equal to 0 and $0.3\bar{3}$ for dextran and pullulan, respectively. In summary, the parameters retrieved in this comparative study of Py-Pullulan, Py-Dextran, and Py-Amylose agree with the general understanding in the literature about these polysaccharides, with pullulan being a slightly more flexible but less dynamic polysaccharide than dextran.

Chapter 6

Conclusions and Future Work

6.1. Thesis Summary

In this thesis, the conformations and internal backbone dynamics (IBD) of several α-polyglucans ranging from linear to highly branched polysaccharides were successfully characterized in solution and at the molecular level by a combination of pyrene excimer formation (PEF), Fluorescence Blob Model (FBM), and Molecular Mechanics Optimizations (MMOs). The combination of PEF, FBM, and MMOs had been applied earlier to probe the conformation[1-3] and IBD of a variety of macromolecules in solution, but this thesis represents the first example where such a large set of polysaccharides has been studied by using this methodology.

The successful application of the combination of PEF, FBM, and MMOs to study the interior of highly branched amylopectin and glycogen in solution was certainly an important achievement of this thesis. The inter-helical distance (d_{h-h}) between the side chains arranged into clusters inside amylopectin in dilute dispersion and in the crystalline form had been examined earlier by PEF and X-ray crystallography,[6] respectively. Since d_{h-h} between single amylose helices with 7 AGUs per turn equals 1.5 nm in a crystal lattice,[7] the larger d_{h-h} of ~ 2.7 nm found for the side chains of amylopectin dispersed in DMSO suggested the existence of free volume between the side chains of amylopectin in DMSO.[5] This assumption was tested in Chapter 2, where the compressibility of amylopectin and three Nanosized Amylopectin Fragments (NAFs) with a hydrodynamic diameter (D_h) of 227, 56, 20, and 8 nm was probed. The four particles were labeled with 1-pyrene butyric acid to yield Py-Amylopectin and Py-NAF(D_h) samples, where the number in parenthesis indicated the hydrodynamic diameter of the NAFs expressed in nanometer. Non-fluorescently labeled NAF(56) was added to the Py-Amylopectin and Py-NAF(D_h) dispersions in DMSO to increase the osmotic pressure. Increasing the NAF(56) concentration from 0.001 to 40 wt% triggered the

compression of the polysaccharide particles and the $d_{\text{h-h}}$ between the helical side chains decreased. At a NAF(56) concentration of 12 wt%, the fluorescence intensity ratio of the excimer over the monomer (I_E/I_M) and the number of anhydroglucose units (AGUs) inside a *blob* ($N_{\text{blob}}^{\text{exp}}$) begun to increase, which indicated enhanced PEF. As the side chains became closer, inter-helical interactions between the pyrenyl labels were enhanced. While both the I_E/I_M ratio and $N_{\text{blob}}^{\text{exp}}$ increased with increasing NAF(56) concentration, the magnitude of their increase depended on the size of the polysaccharide under study. Py-Amylopectin and the smallest Py-NAF(8) showed the largest and smallest increase in I_E/I_M and $N_{\text{blob}}^{\text{exp}}$, respectively. To better understand the origin of this effect, MMOs were conducted with 7 helices arranged in a hexagonal closed packed lattice to determine $N_{\text{blob}}^{\text{theo}}$ as a function of $d_{\text{h-h}}$ and the number of helices constituting a cluster. The trends of $N_{\text{blob}}^{\text{exp}}$ obtained for Py-Amylopectin and the Py-NAFs as a function of the NAF(56) concentration were compared with the trends obtained for $N_{\text{blob}}^{\text{theo}}$ as a function of $d_{\text{h-h}}$ and cluster size. By noting that the $N_{\text{blob}}^{\text{exp}}$ trend obtained for Py-Amylopectin and Py-NAF(56) were similar and seemed to match the trend obtained for $N_{\text{blob}}^{\text{theo}}$ with a cluster of 37 helices, a relationship could be established between $d_{\text{h-h}}$ and [NAF(56)], that led to the finding that $d_{\text{h-h}}$ for Py-Amylopectin and the Py-NAFs decreased from 3.2 to 2.0 nm as the concentration of the naked NAF(56) sample increased from 0.001 to 40 wt%. The finding that the increase in the I_E/I_M ratio and $N_{\text{blob}}^{\text{exp}}$ for Py-Amylopectin and Py-NAF(56) could be attributed to the existence of clusters made of 37 helices was similar to the cluster size reported in the literature determined by microscopy imaging of amylopectin.[8] The fluorescence response of the Py-NAF(20) and Py-NAF(8) samples, when NAF(56) was added to the dispersions, was well described if they were made of clusters consisting of 6 and 3 helices, respectively. A smaller cluster size might have been

a consequence of the stronger degradation, that was applied to produce the smaller NAF samples. These PEF experiments demonstrated how detailed structural information about the size of clusters of helical side chains could be obtained for highly branched amylopectin and NAFs.

Chapter 3 described how PEF can be applied to study the interior of glycogen at the molecular level. The internal structure of glycogen can be represented by the Tier Model, which assumes that the side chains are arranged in concentric tiers with the number of side chains increasing from the inner to the outer tier.[9-11] Since the number of AGUs in a tier increases more quickly than the tier volume, the density of glycogen increases rapidly with increasing tier number. In fact, glycogen particles cannot grow past the 12th tier as the density of a hypothetical 13th tier would be so high that the enzymes, responsible for the synthesis of glycogen, would no longer have access to the glycogen binding sites due to steric hinderance.[12] The structure of glycogen has been investigated at the macroscopic level by microscopy,[13,14] size exclusion chromatography,[13,15] or scattering techniques.[16] Recently, the density distribution with a higher density at and near the core was suggested by Gilbert based on the SAXS experiment of glycogen.[17]

To this end, two density distributions were considered to examine the internal structure of glycogen from oyster and corn in Chapter 3. The number average molecular weight (M_n), intrinsic viscosity ($[\eta]$), and hydrodynamic radius (R_h) of the glycogen particles were determined by gel permeation chromatography (GPC) analysis and viscosity measurements. The parameters describing the macroscopic properties of glycogen indicated that these glycogen particles were made of 12 tiers based on the mathematic rendering of the Tier Model by Meléndez-Hevia.[18] The glycogen samples from oyster and corn were labeled with 1-pyrenebutyric acid or 1-naphthaleneacetic acid to yield the samples Py-Glycogen(O/C) and Np-Glycogen(O/C),

respectively. The efficiency of Fluorescence Resonance Energy Transfer (FRET) between the Np- and Py-Glycogen(O) samples was examined and compared to the FRET efficiency (E_{FRET}) obtained for Py/Np-Dextran solutions. The E_{FRET} of the Py/Np-glycogen dispersions was significantly lower than that of the Py/Np-Dextran solutions. The different E_{FRET} values were attributed to the different structures of these polysaccharides. All pyrene pendants of the linear Py-Dextran samples could interact with the naphthalene pendants to induce FRET. In contrast, only the peripheral pyrenyl labels of the Py-Glycogen samples could induce FRET. Consequently, a significantly lower E_{FRET} was obtained for the Py/Np-Glycogen dispersions compared to the E_{FRET} obtained for the Py/Np-Dextran solutions. This result was taken as evidence that the pyrenyl labels were distributed throughout the entire glycogen particles and not concentrated at their periphery.

The Py-Glycogen(O/C) samples yielded similar I_E/I_M ratios and N_{blob}^{exp} values, but these values were higher than those obtained for Py-Amylopectin. Since glycogen is twice more densely branched than Py-Amylopectin,[19] the higher local density experienced by the pyrenyl labels of Py-Glycogen yielded a much higher I_E/I_M ratio and $<N_{blob}^{exp}>$ than the values obtained for Py-Amylopectin. MMOs were conducted with 7 shorter oligosaccharide helices, that would be more representative of the glycogen helices, arranged in a hexagonal closed packed lattice to build a N_{blob}^{theo}-vs-d_{h-h} plot that could be used to estimate the relationship between N_{blob}^{theo} and ρ. Two density distributions based on Meléndez-Hevia model[18] and Gilbert model[17] were considered and the parameters used to represent them were optimized to yield an $<N_{blob}^{theo}>$ value that would best match $<N_{blob}^{exp}>$. Good agreement between $<N_{blob}^{theo}>$ and $<N_{blob}^{exp}>$ was obtained only if the side chains of glycogen were more densely packed toward the center of the glycogen particles than predicted by the Melendez-Hevia model. Consequently, the study described in Chapter 3

established a PEF-based methodology where $<N_{blob}^{exp}>$ can be employed to characterize the internal density of complex polysaccharide particles like glycogen.

Up to this point, the combination of PEF, FBM, and MMOs had been applied to probe the interior of highly branched amylopectin and glycogen and helical amylose in DMSO. The PEF-FBM-MMO combination was applied to probe the conformation of two randomly coiled polyglucans, namely dextran in Chapter 4 and pullulan in Chapter 5.[20,21] The dextran and pullulan samples were labeled with 1-pyrenebutyric acid to yield two series of Py-Dextran and Py-Pullulan constructs, respectively, and their fluorescence response was compared to that of the other polysaccharides studied to date. A summary of this comparison is provided in Figure 6.1A and its main conclusions are discussed hereafter. The main metrics that were used to gauge the PEF efficiency were the I_E/I_M ratio, N_{blob}^{exp}, the product $k_{blob} \times N_{blob}^{exp}$, and f_{agg}, which were plotted as a function of pyrene content in Figures 6.1A, B, C, and D, respectively. The I_E/I_M ratio in Figure 6.1A reflected the local concentration of ground-state pyrene ($[Py]_{loc}$), and since the pyrenyl labels were covalently attached to the polysaccharides, the I_E/I_M ratio reflected the local density of the polysaccharides. Since the local density generated by the different polysaccharides were expected to follow the sequence glycogen > amylopectin > amylose ~ pullulan ~ dextran, the trends shown in Figure 6.1A provided a good representation of the local density of the polysaccharides. A similar sequence was found for N_{blob}^{exp} in Figure 6.1B, where N_{blob}^{exp} was largest for the two glycogen samples, followed by amylopectin and the linear amylose, pullulan, and dextran yielding similar N_{blob}^{exp} values. This trend was reasonable, based on the known density of these polysaccharides, with glycogen and amylopectin allowing inter-helical PEF, while PEF occurred along a single polysaccharide chain in the case of amylose, pullulan and dextran. A better resolution was obtained

176

for the product $k_{blob} \times N_{blob}^{exp}$, which showed the largest frequency of pyrene-pyrene encounters for glycogen, followed by amylopectin, amylose, and with pullulan and dextran yielding the same $k_{blob} \times N_{blob}^{exp}$ product. The only parameters, that resulted in a clear separation between pullulan and dextran was the molar fraction f_{agg} of aggregated pyrenes. Since PEF occurred along helices in glycogen, amylopectin, and amylose,[3] that promote the formation of pyrene aggregates, similar trends were observed for the f_{agg} values obtained for these three polysaccharides. However, dextran, which is expected to be more extended than pullulan, resulted in substantially lower f_{agg} values compared to pullulan, which itself yielded lower values than for glycogen, amylopectin, and amylose. The conclusion that pullulan was more coiled than dextran agreed with the published persistence lengths of dextran and pullulan.[22,23]
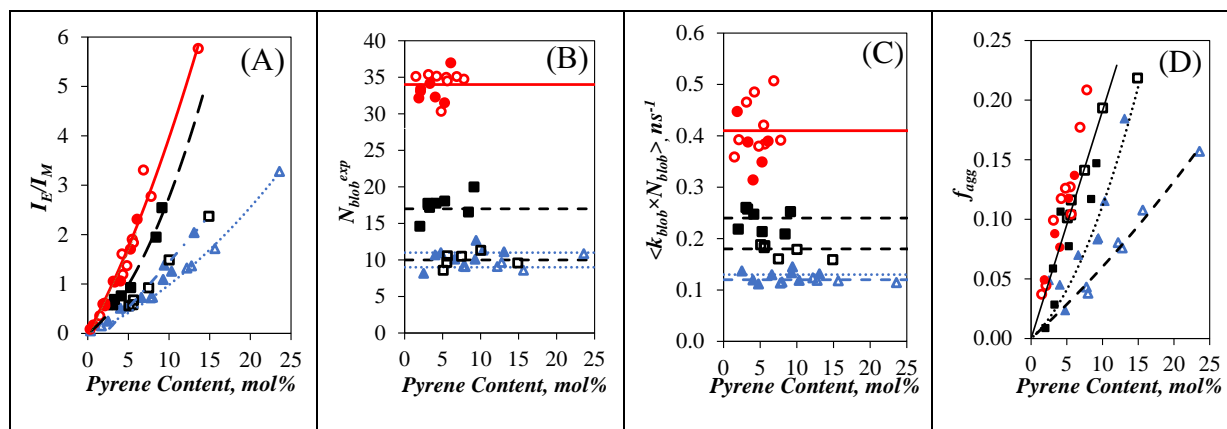
Figure 6. 1. Plots of (A) the I_E/I_M ratio, (B) N_{blob}^{exp}, (C) $<k_{blob} \times N_{blob}^{exp}>$ and (D) f_{agg} of Py-Glycogen from (○) oyster and (●) corn, (■) Py-Amylopectin, (□) Py-Amylose, (▲) Py-Pullulan, and (△) Py-Dextran in DMSO.

At this point, the PEF-FBM-MMO combination has been applied to a wide variety of polysaccharides to probe their conformation and IBD. The conclusions drawn from the application of this PEF-based methodology are supportive of the conclusions reported in the literature for the

polysaccharides studied in this thesis. It suggests that the PEF-FBM-MMO combination represents a robust analytical tool to probe polysaccharides in solution at the molecular level.

6.2 Future Work

The study of the compression of amylopectin and NAFs in Chapter 2 showed that the PEF response reflected the size of clusters of helical side chains found in amylopectin and the NAFs. In the specific case of amylopectin, the clusters of Py-Amylopectin were found to be made of 37 helical side chains. The clusters in the smaller NAFs were found to be made of fewer side chains, a consequence of the destructive procedure applied to prepare the NAFs. In contrast, partial hydrolysis of amylopectin with an endo-enzyme such as α-amylase would be expected to produce amylopectin fragments of different sizes but with conserved clusters. The α-limit dextrin of amylopectin could be labeled with 1-pyrenebutyric acid and the same PEF experiments conducted in Chapter 2 could be carried out to estimate the size of the clusters of helical side chains. A similar PEF response as that found for amylopectin would be expected from the α-limit dextrin if the clusters were conserved regardless of the size of the α-limit dextrin of amylopectin.

Chapter 3 demonstrated that a combination of PEF, FBM, and MMOs could be applied to provide a concrete answer to the density distribution of glycogen. This study suggested that the stepwise enzymatic treatment of glycogen with exo-enzymes followed by debranching enzymes could be applied to generate glycogen particles with different overall density. The structural properties of the degraded glycogen particles could be examined with $[\eta]$, M_n, and R_h determined by conducting viscosity, GPC, and dynamic light scattering measurements, respectively. The degraded glycogen particles could then be labeled with 1-pyrenebutyric acid. Their fluorescence decays could be acquired and fitted according to the FBM to yield $\langle N_{blob}^{exp} \rangle$. The $\langle N_{blob}^{exp} \rangle$ of the

degraded glycogen should be compared with the $\langle N_{\text{blob}}^{\text{exp}} \rangle$ value of the non-degraded glycogen. The β-amylolysis of glycogen would remove the most/least dense part of glycogen based on Tier Model[18] and Gilbert model,[17] respectively. The hydrolysis of the densest part should result in a lower $\langle N_{\text{blob}}^{\text{exp}} \rangle$ than the $\langle N_{\text{blob}}^{\text{exp}} \rangle$ of the non-degraded glycogen observed in this study while the hydrolysis of the least dense part would cause of increase in the $\langle N_{\text{blob}}^{\text{exp}} \rangle$. Such a study on top of the experimental results presented in Chapter 3 would answer regarding to the density distributions of glycogen which is debatable in the literature and demonstrate the usefulness of the combination of PEF, FBM, and MMOs for characterizing macromolecules in solution at the molecular level.

Four major α-polyglucans have been studied in this thesis, but several others remain to be characterized and the combination of PEF, FBM, and MMOs could be applied for this purpose. Dextran, which was studied in Chapter 4 of this thesis, is one of four classifications of α-D-glucans produced from lactic acid bacteria.[24] The other three classifications are mutan, reuteran, and alternan. Mutan is constituted of AGUs joined by α-(1,3) glycosidic linkages and forms an extended helix, which makes it water-insoluble like cellulose.[25] However, mutans are soluble in 9:1 DMSO:water mixtures,[26] which should be suitable for PEF experiments. Reuteran is made of AGUs linked by α-(1,4) and α-(1,6) glycosidic bonds in a 1:1 ratio. The structure of alternan is unique as its AGUs are joined via alternating α-(1,3) and α-(1,6) glycosidic linkages with a 7-11% branching frequency. Considering that pullulan does not adopt a helical conformation as it possesses heterogeneous glycosidic linkages,[27] it would be interesting to apply PEF measurements to assess whether alternan might adopt a random coil or helical conformation in solution. If randomly coiled, the PEF study could characterize the chain mobility of randomly coiled alternan and compare it to that of dextran, whose AGUs are connected solely by α-(1,6) glycosidic bonds,

and pullulan, whose AGUs are linked by a 1:2 mixture of α-(1,6) and α-(1,4) glycosidic bonds, as was done for the comparison conducted in Chapter 5 between dextran and pullulan.

Finally, regioselective esterification of pullulan with vinyl 1-pyrenebutyrate would be an interesting control study. The transesterification of starch with vinyl acetate in the presence of NaCl yielded acetylated starch, where all acetates were formed at the C2-hydroxyl.[28] The transesterification of pullulan with vinyl 1-pyrenebutyrate in the presence of NaCl should produce a Py-Pullulan sample, where all the pyrenyl labels would be attached on the C2-hydroxyls. The PEF response should be substantially different from that presented in Chapter 5, where all the pyrene pendants were expected to be attached on the C6-hydroxyls of pullulan. The difference in PEF response would be attributed to the difference in linker length, since the length of the linker separating the pyrene moiety from the polysaccharide backbone would be different if 1-pyrenebutyric acid were attached to the C2- or C6-hydroxyl of the AGUs.

Letter of Copyright Permission

Permissions for reproduction of Figure 1.4.

Permissions for reproduction of Figure 1.5.

Permissions for reproduction of Figure 1.6.

Permissions for reproduction of Figure 1.8.

References

Chapter 1

1. Teegarden, D. M. Polymer Chemistry: Introduction to an Indispensable Science. National Science Teachers Association Press, Virginia, 2004.

2. Synytsya, A.; Novak, M. Structural Analysis of Glucans. *Ann. Transl. Med*. **2014**, *2*, 17-30.

3. Kulicke, W. M.; Heinze, T. Improvements in Polysaccharides for Use as Blood Plasma Expanders. *Macromol. Symp*. **2006**, *231*, 47–59.

4. Marszalek, P. E.; Oberhauser, A. F.; Pang, Y. P.; Fernandez, J. M. Polysaccharide Elasticity Governed by Chair-Boat Transitions of the Glucopyranose Ring. *Nature* **1998**, *396*, 661-664.

5. Brant, D.; Burton, B. A. The Configurational Statistics of Pullulan and Some Related Glucans. In *Solution Properties of Polysaccharide*, Brant, E. A. Ed.; ACS Book:1981; pp. 81-99.

6. Burton, B. A.; Brant, D. A. Comparative Flexibility, Extension, and Conformation of Some Simple Polysaccharide Chains. *Biopolymers* **1983**, *22*, 1769-1792.

7. Nishinari, K.; Tsutsumi, A. Studies on Molecular Motion of Polysaccharides in the Solid State by Broad-Line Nuclear Magnetic Resonance. *J. Polym. Sci., Polym. Phys. Ed.* **1984**, *22*, 95-99.

8. Manners, D. J. Recent Developments in our Understanding of Glycogen Structure. *Carbohydr. Polym*, **1991**, *16*, 37-82.

   (8.b. Staudinger, H., and Husemann, E., <u>Über hochpolymere Verbindungen. 150. Mitteilung. Über die Konstitution der Stärke</u>. *Ann. Chem*. **1937**, *627*, 195-236. (in German))
   Gidely, M. J.; Bulpin, P. V. Crystallisation of Malto-Oligosaccharides as Models of the

Crystalline Forms of Starch: Minimum Chain Length Requirement for the Formation of Double Helices. *Carbohydr. Res.* **1987**, *161*, 291-300.

9. Sullivan, M. A.; Nitschke, S.; Skwara, E. P.; Wang, P.; Zhao, X.; Pan, X. S.; Chown, E. E.; Wang, T.; Perri, A. M.; Lee, J. P. Y.; Vilaplana, F.; Minassian, B. A.; Nitschke, F. Skeletal Muscle Glycogen Chain Length Correlates with Insolubility in Mouse Models of Polyglucosan-Associated Neurodegenerative Diseases. *Cell Rep.* **2019**, *27*, 1334–1344.

10. Imberty, A.; Tran, V.; Perez, S. Recent Advances in Knowledge of Starch Structure. *Starch/Stärke* **1991**, *43*, 375-384

11. Bezborodkina, N. N.; Chestnova1, A. Y.; Vorobev, M. L.; Kudryavtsev, B., N. Spatial Structure of Glycogen Molecules in Cells. *Biochemistry (Moscow)* **2018**, *83*, 627-644.

12. Vilaplana, F.; Gilbert, R. G. Characterization of Branched Polysaccharides Using Multiple-Detection Size Separation Techniques. *J. Sep. Sci.* **2010**, *33*, 3537-3554.

13. Farhangi, S.; Weiss, H.; Duhamel, J. Effect of Side-Chain Length on the Polymer Chain

14. Dynamics of Poly(alkyl methacrylate)s in Solution. *Macromolecules* **2013**, *46*, 9738-9747.

15. Casier, R.; Duhamel, J. The Effect of Amino Acid Size on the Internal Dynamics and Conformational Freedom of Polypeptides. *Macromolecules* **2020**, *53*, 9811-9822.

16. Casier, R.; Duhamel, J. Pyrene Excimer Fluorescence as a Direct and Easy Experimental Means to Characterize the Length Scale and Internal Dynamics of Polypeptide Foldons. *Macromolecules* **2018**, *51*, 3450−3457.

17. Casier, R.; Duhamel, J. Effect of Like Charges on the Conformation and Internal Dynamics of Polypeptides Probed by Pyrene Excimer Fluorescence. *Macromolecules* **2020**, *53*, 5147−5157.

18. Li, L.; Duhamel, J. Conformation of Pyrene-Labeled Amylose in DMSO Characterized with the Fluorescence Blob Model. *Macromolecules* **2016**, *49*, 7965-7974.

19. Li, L.; Kim, D.; Zhai, X.; Duhamel, J. A Pyrene Excimer Fluorescence (PEF) Study of the Interior of Amylopectin in Dilute Solution. *Macromolecules* **2020**, *53*, 6850-6860.

20. Adams. G. A. Complete Acid Hydrolysis. In *Methods in Carbohydrate Chemistry V. General Polysaccharide*, Whistler, R. L. Ed.; Academic Press: New York,1965; pp.269-276.

21. Basedow, A. M.; Ebert, K. H.; Ederer, H. J. Kinetic Studies on the Acid Hydrolysis of Dextran. *Macromolecules* **1978**, *11*, 774-781.

22. Wolfrom, M. L.; Franks, N. E. Partial Acid Hydrolysis of Amylopectin. In *Methods in Carbohydrate Chemistry IV. Starch.* Whistler, R. L. Ed.; Academic Press: New York, 1964; pp.250-252.

23. Dean. G. R. Acid Hydrolysis of Starch to D-Glucose. In *Methods in Carbohydrate Chemistry IV. Starch*. Whistler, R., L., Ed.; Academic Press: New York,1964; pp.249-250.

24. Hassid, W. Z.; Barker, H. A. The Structure of Dextran Synthesized from Sucrose by Betacoccus Arabinosaceus, Orla-Jensen. *J. Biol. Chem.* **1940**, *134*, 163-170.

25. Faithfull, N. T. Acid Hydrolysis Prior to Automatic Analysis for Starch. *J. Sci. Food. Agric.* **1990**, *50,* 419-421.

26. Taguchi, R.; Kikuchi, Y.; Sakano, Y.; Kobayashi, T. Structural Uniformity of Pullulan Produced by Several Strains of Pullularia pullulans. *Agr. Biol. Chem.* **1973**, *37*, 1583-1588.

27. Drake, E. N.; Brown, C. Application of NMR to Biochemical Kinetics. A Laboratory Experiment in Physical Biochemistry. *J. Chem. Ed.* **1977**, *54*, 124-127.

28. Spedding, H. Infrared Spectroscopy. In *Methods in Carbohydrate Chemistry I. Analysis and Preparation of Sugars*., Whistler, R. L. Ed.; Academic Press: New York, 1962; pp.539-550.

29. Hirst, E. L.; Percival, E. Methylation of Polysaccharides and Fractionation of the Methylated Product. In *Methods in Carbohydrate Chemistry V. General Polysaccharide*, Whistler, R. L. Ed.; Academic Press: New York, 1965; pp.287-296.

30. Van Cleve, J. W., Schaefer, W. C.; Rist, C. E. The Structure of NRRL B-512 Dextran. Methylation Studies 2, *J. Am. Chem. Soc*. **1956**, *78*, 4435-4438.

31. Jones, J. K. N.; Wilkie, K. C. B. Structural Studies on Clinical Dextrans Part 1. Methylation and Periodate Oxidation Studies1. *Can. J. Biochem. Physiol*. **1959**, *37*, 377-390.

32. Hay, G. W.; Lewis, B. A.; Smith, F. Methylation. In *Methods in Carbohydrate Chemistry IV. Starch*, Whistler, R. L. Ed.; Academic Press: New York,1964; pp.306-310.

33. Wu, S.; Chen, H.; Tong, Q.; Xu, X.; Jin, Z. Preparation of Maltotriose by Hydrolyzing of Pullulan with Pullulanase. *Eur. Food Res. Technol.* **2009**, *229*, 821-824.

34. Wallenfels, K.; Bechteler, G.; Kuhn, R.; Trischmann, H.; Egge, H. Permethylation of Oligomeric and Polymeric Carbohydrates and Quantitative Analysis of the Cleavage Products. *Angew. Chem. Int. Ed. Engl*. **1963**, *2*, 515-523.

35. Abdullah, M.; French, D. Reversible Action of Pullulanase. *Nature* **1966**, *210*, 200.

36. Carolan, G.; Catley, B. J.; McDougal, F. J. The Location of Tetrasaccharide Units in Pullulan. *Carbohydr. Res*. **1983**, *114*, 237-243.

37. Singh, R. S.; Saini, G. K.; Kennedy, J. F. Pullulan: Microbial Sources, Production and Applications. *Carbohydr. Polym.* **2008**, *73*, 515-531.

38. Heinze, T.; Libert, T.; Heublein, B.; Schubert, S. Functional Polymers Based on Dextran. *Adv. Polym. Sci.* **2006**, *205*,199-291.

39. Jeanes, A.; Havnes, W. C.; Wilham, C. A.; Rankin, J. C.; Melvin, E. H.; Austin, M. J.; Cluskey, J. E.; Fisher, B. E.; Tsuchiya, M.; Rist, C. E. Characterization and Classification of Dextrans from Ninety-six Strains of Bacteria. *J. Am. Chem. Soc.* **1954**, *76*, 5041–5052.

40. Seymore, F. D.; Soldki, M. E.; Plattner, R. D.; Jeanes, A. Six Unusual Dextrans: Methylation Structural Analysis by Combined G.L.C.-M.S. of Per-O-Acetyl-Aldononitriles. *Carbohydr. Res*. **1977**, *53*, 153-166.

41. Vettori, M. H. P.; Franchetti, S. M. M.; Contiero, J. Structural Characterization of a New Dextran with a Low Degree of Branching Produced by Leuconostoc Mesenteroides FT045B Dextransucrase. *Carbohydr. Polym*. **2012**, *88*, 1440-1444.

42. Jeanes, A.; Wilham, C. A. Periodate Oxidation of Dextran. *J. Am. Chem. Soc.* **1950**, *72*, 2655–2657.

43. Remaud-Simeon, M.; Wilemont, R.-M.; Sarçabal, P.; Montalk, G. P. D.; Monsan, P. Glucansucrases: Molecular Engineering and Oligosaccharide Synthesis. *J. Mol. Catal. B: Enzym*. **2000**, *10*, 117-128.

44. Côte, G. L.; Robyt, J. F. The Formation of α-D-(1→3) Branch Linkages by an Exocellular Glucansurase from NRRL B-742*. *Carbohydr. Res.* **1983**, *119*, 141-156.

45. Larm, O.; Lindberg, B.; Svensson, S. Studies on the Length of the Side Chains of the Dextran Elaborated by Leuconostoc Mesenteroides NRRL B-512*. *Carbohydr. Res*. **1970**, *20*, 39-48.

46. Antonini, E.; Bellelli, L.; Bruzzesi, M. R; Caputo, A.; Chiancone, E.; Rossi-Fanelli, A. Studies on Dextran and Dextran Derivatives. I. Properties of Native Dextran in Different Solvents. *Biopolymers* **1964**, *2*, 27-34.

47. Kothari, D.; Das, D.; Patel, S.; Goyla, A. Dextran and Food Application. In *Polysaccharides: Bioacitivity and Biotechnology*. Ramawat, K. G.; Merillon, J-M. Eds.; Springer: Switzerland, 2015, pp 735- 752.

48. Naessens, M.; Cerdobbel, A.; Soetaert, W.; Vandamme, E. J. Leuconostoc Dextransucrase and Dextran: Production, Properties and Applications. *J. Chem. Technol. Biotechnol*. **2005**, *80*, 845–860.

49. Sarbini, S. R.; Kolida, S.; Naeye, T.; Einerhand, A. W.; Gibons, G. R.; Rastall, R. A. The Prebiotic Effect of a-1,2 Branched, Low Molecular Weight Dextran in the Batch and Continuous Faecal Fermentation System. *J. Funct. Foods*. **2013**, *5*, 1938-1946.

50. Cheetham, N. W. H.; Tao, L. Amylose Conformational Transitions in Binary DMSO/Water Mixtures. *Carbohydr. Polym*. **1998**, *35,* 287-295.

51. Çatiker, E.; Güner, G. Unperturbed Molecular Dimensions and the Theta Temperature of Dextran in Dimethylsulfoxide (DMSO) solutions. *Polym. Bull*. **1998**, *41*, 223-230.

52. Garg, S. K.; Stivala, S. S. Assessment of Branching in Polymers from Small Angle X-Ray Scattering (SAXS). *J. Polym. Sci. Polym. Phys. Ed.* **1978**, *16*, 1419-1434.

53. Striegel, A. M. Viscometric Detection in Size-Exclusion Chromatography: Principles and Select Applications. *Chromatographia* **2016**, *79*, 945-960.

54. Senti, F. R.; Hellman, N. N.; Ludwig, N. H.; Babcock, G. E.; Tobin, R.; Glass, C. A.; Lamberts, B. L. Viscosity, Sedimentation, and Light-Scattering Properties of Fractions of an Acid-Hydrolyzed Dextran. *J. Polym. Sci.* **1955**, *17*, 527-546.

55. Gekko, K. Physicochemical Studies of Oligodextran II. Intrinsic Viscosity-Molecular Weight Relationship. *Macromol. Chem. Phys.* **1971**, *148*, 229-238.

56. Granath, K. A. Solution Properties of Branched Dextrans. *J. Colloid Sci.* **1958**, *13*, 308-328.

57. Zimm, B. H.; Stockmayer W. H. The Dimensions of Chain Molecules Containing Branches and Rings. *J. Chem. Phys.* **1949**, *17*, 1301-1314.

58. Prajapati, V. D.; Jani, G. K.; Khanda, S. M. Pullulan: An Exopolysaccharide and its Various Applications. *Carbohydr. Polym.* **2013**, *95,* 540-549.
(The original article, "Wallenfels, K.; Bender, H.; Keilich, G.; Bechtler, G. On pullulan, the glucan of the slime coat of Pullularia pullulans. *Angew Chem.* **1961**, *73*, 245–246." could not be found)

59. Nishinari, K.; Kohyama, K.; Williams, P. A.; Phillips, G. O.; Burchard, W.; Ogino, K. Solution Properties of Pullulan. *Macromolecules* **1991**, *24*, 5590-5593.

60. Kawahara, K.; Ohta, K. Preparation and Solution Properties of Pullulan Fractions as Standard Samples for Water-soluble Polymers. *Carbohydr. Polym*. **1984**, *4*, 335-356.

61. Kato, T.; Okamoto, T.; Tokuya, T.; Takahashi, A. Solution Properties and Chain Flexibility of Pullulan in Aqueous Solution. *Biopolymers* **1982**, *21*, 1623-1633.

62. Kato, T.; Katsuki, T.; Takahash, A. Static and Dynamic Solution Properties of Pullulan in a Dilute Solution. *Macromolecules* **1984**, *17*, 1726-1730.

63. Pavlov, G. M.; Yevlampieva, N. P.; Korneeva, E. V. Flow Birefringence of Pullulan Molecules in Solutions. *Polymer* **1998**, *39*, 235-239.

64. Isenberg, S. L.; Brewer, A. K.; Côte, G. L.; Striegel, A. M.; Hydrodynamic versus Size Exclusion Chromatography Characterization of Alternan and Comparison to Off-Line MALS. *Biomacromolecules* **2010**, *11*, 2505–2511.

65. Sullivan, M.; Powell, P. O.; Witt, T.; Vilaplana, F.; Roura, E.; Gilbert, R. G. Improving Size-Exclusion Chromatography Separation for Glycogen. *J. Chromatogr. A* **2014**, *1332*, 21-29.

66. Liu, J. H. Y.; Brameld, K. A.; Brant, D. A.; Goddard III, W. A. Conformational Analysis of Aqueous Pullulan Oligomers: An Effective Computational Approach. *Polymer* **2002**, *43*, 509-516.

67. Stjacques, M.; Sundararajan, P. R.; Taylor, K. J.; Marchessault, R. H. Nuclear Magnetic-Resonance and Conformational Studies on Amylose and Model Compounds in Dimethyl-Sulfoxide Solution. *J. Am. Chem. Soc.* **1976**, *98*, 4386-4391.

68. Fujii, M.; Honda, K.; Fujita, H. Dilute-Solution of Amylose in Dimethylsulfoxide. *Biopolymers* **1973**, *12*, 1177-1195.

69. Yang, J.; Sato, T. Conformation of Pullulan in Aqueous Solution Studied by Small-Angle X-ray Scattering. *Polymers* **2020**, *12*, 1266-1276.

70. Dais P.; Vlachou, S.; Taravel, F. R. 13C Nuclear Magnetic Relaxation Study of Segmental Dynamics of the Heteropolysaccharide Pullulan in Dilute Solutions. *Biomacromolecules* **2001**, *2*, 1137-1147.

71. Kitamura, S.; Tanahashi, H.; Kuge, T. The Fluorescence Method. III. Chain Length Dependence of the Micro-Brownian Motion of Amylose in Aqueous Solution. *Biopolymers.* **1984**, *23*, 1043-1056.

72. Muroga, Y.; Yamada, Y.; Noda, I.; Nagasawa, M. Local Conformation of Polysaccharides in Solution Investigated by Small-Angle X-ray Scattering. *Macromolecules* **1987**, *20*, 3003-3006.

73. Pavlov, G. M.; Korneeva, E. V.; Yevlampieva, N. P. Hydrodynamic Characteristics and Equilibrium Rigidity of Pullulan Molecules. *Int. J. Biol. Macromol.* **1994**, *16*, 318–323.

74. Ioan, C. E.; Aberle, T.; Burchard, W. Structure Properties of Dextran. 2. Dilute Solution. *Macromolecules* **2000**, *33*, 5730-5739.

75. Meyer, K. H.; Bernfeld, P.; Biossonnas, R. A.; Gutler, P.; Noelting, G. Starch Solutions and Pastes and their Molecular Interpretation. *J. Phys. Chem.* **1949**, *56*, 319-334.

76. Whelan, W. J. Hydrolysis with α-Amylase. In *Methods in Carbohydrate Chemistry IV. Starch*, Whistler, R. L. Ed.; Academic Press: New York, 1964; pp.252-260.

77. Manners, D. J. The Enzymic Degradation of Polysaccharides. *Q. Rev. Chem. Soc.* **1955**, *9*, 73-99.

78. Bertoft, E. Partial Characterization of Amylopectin Alpha-Dextrins. *Carbohydr. Res*. **1989**, *189,* 181-193.

79. Harada, T. Isoamylase and its Industrial Significance in the Production of Sugars from Starch. *Biotechnol. Genet. Eng. Rev.* **1984**, *1*, 39-64.

80. Thurn, A.; Burchard, W. Heterogeneity in Branching of Amylopectin. *Carbohydr. Polym.* **1985**, *5*, 441-460.

81. Harada, T.; Misaki, A.; Akai, H.; Yokobayahi, K.; Sugimoto, K. Characterization of Pseudomonas Isoamylase by its Actions on Amylopectin and Glycogen: Comparison with Aerobacter Pullulanase. *Biochim. Biophys. Acta.* **1972**, *268*, 497-505.

82. Bertoft, E. Analysing starch structure. In *Starch in Food: Structure, Function and Applications*. Eliasson, A. C. Ed.; CBC Press: 2004; pp. 57-96.

83. Bender, H.; Wallenfels K. [95] Pullulanase (an Amylopectin and Glycogen Debranching Enzyme) from Aerobacter Aerogenes. *Methods Enzymol.* **1966**, *8*, 555-559.

84. Manners, D. J. Recent Developments in our Understanding of Amylopectin Structure. *Carbohydr. Polym.* **1989**, *11*, 87-112.

85. Nilsson, G. S.; Bergquist, K.-E., Nilsson, U.; Gorton, L. Determination of the Degree of Branching in Normal and Amylopectin Type Potato Starch with H-NMR Spectroscopy. Improved Resolution and Two-Dimensional Spectroscopy. *Starch/Stärke* **1996**, *48*, 352-357.

86. Ingle, T. R.; Whistler, R. L. End-Group Analysis by Methylation. In *Methods in Carbohydrate Chemistry IV. Starch*, Whistler, R. L. Ed.; Academic Press: New York, 1964; pp.83-86.

87. Shasha, B.; Whistler, R. L. End-group Analysis by Periodate Oxidation. In *Methods in Carbohydrate Chemistry IV. Starch*. Whistler, R. L. Ed.; Academic Press: New York, 1964; pp.86-88.

88. Whelan, W. J. Enzymatic Exploration of the Structures of Starch and Glycogen. *Biochem. J.,* **1971**, *122*, 609–622.

89. Young, F. G. Claude Bernard and the Discovery of Glycogen. *Br. Med. J.* **1957**, *1*, 1431-1437.

90. Haworth, W. N.; Percival, E. G. V. Polysaccharides. Part X I. Molecular Structure of Glycogen. *J. Chem. Soc*. **1932**, 2277-2282.

91. Bell, D. J. CCXI. Glycogen VI. The Molecular Structure of Horse Muscle Glycogen. *Biochem. J.* **1937**, *31*, 1683–1691.

92. Dutta, S.; Wade, M. A.; Walsh, D. J.; Guironnet, D.; Rogers, S. A.; Sing, C. E. Dilute Solution Structure of Bottlebrush Polymers. *Soft Matter* **2019**, *15*, 2928-2941.

93. Meyer, K. H. The Chemistry of Glycogen. *Adv. Enzymol. Relat. Areas Mol. Biol.* **1943**, *3*, 109-135.

94. Cori, G. T.; Cori, C. F. Crystalline Muscle Phosphorylase IV. Formation of Glycogen. *J. Biol. Chem*. **1943**, *151*, 57-63.

95. Larner, J.; Illingworth, B.; Cori, G. T.; Cori, C. F. Structure of Glycogens and Amylopectins: II. Analysis by Stepwise Enzymatic Degradation. *J. Biol. Chem*. **1952**, *199*, 641-651.

96. De Gennes, P. G.; Hervet, H. Statistics of « Starburst » Polymers. *J. Phys. Lett.* **1983**, *44*, 351-360.

97. Gunja-Smith, Z.; Marshall, J. J.; Mercier, C.; Smith, E. E.; Whelan, W. J. A Revision of the Meyer-Bernfeld Model of Glycogen and Amylopectin. *FEBS Lett*. **1970**, *12*, 101-104.

98. French, D. Structure of Glycogen and its Amylolytic Degradation. In *Control of Glycogen Metabolism*, Whelan, W. J.; Cameron, M. P. Eds.; Wiley Book:1964; pp.7-28.

99. Madsen, N. B.; Cori, C. F. The Binding of Glycogen and Phosphorylase. *J. Biol. Chem*. **1958**, *233*, 1251-1256.

100. Goldsmith, E.; Sprang, S.; Fletterick, R. Structure of Maltoheptaose by Different Fourier Methods and a Model for Glycogen. *J. Mol. Biol.* **1982**, *156*, 411-427.

101. Meléndez-Heiva, E.; Waddell, T. G.; Shelton, E. D. Optimization of Molecular Design in the Evolution of Metabolism: The Glycogen Molecule. *Biochem. J*. **1993**, *295*, 477-483.

102. DiNuzzo, D. Kinetic Analysis of Glycogen Turnover: Relevance to Human Brain 13C-NMR Spectroscopy. *J. Cereb. Blood Flow Metab*. **2013**, *33*, 1540-1548.

103. Sullivan, M. A.; O'Connor, M. J.; Umana, F.; Roura, E.; Jack, K.; Stapleton, D. I.; Gilbert, R. G. Molecular Insights into Glycogen α-Particle Formation. *Biomacromolecules* **2012**, *13*, 3805−3813.

104. Shearer. J.; Graham, T. E. Novel Aspects of Skeletal Muscle Glycogen and Its Regulation During Rest and Exercise. *Exercise Sport Sci. Rev*. **2004**, *32*, 120-126.

105. Roach, P. J.; Depaoli-Roach, A. A.; Hurley, T. D.; Tagliabracci, V. S. Glycogen and Its Metabolism: Some New Developments and Old Themes. *Biochem. J*. **2012**, *441*, 763–787.

106. Prats, C.; Graham, T. E.; Shearer, J. The Dynamic Life of the Glycogen Granule. *J. Biol. Chem*. **2018**, *293*, 7089- 7098.

107. Perez, S.; Bertoft, E. The Molecular Structures of Starch Components and Their Contribution to the Architecture of Starch Granules: A Comprehensive Review. *Starch/Stärke* **2010**, *62*, 389-420.

108. Kageyama, A.; Yanase, M.; Yuguchi, Y. Structural Characterization of Enzymatically Synthesized Glucan Dendrimers. *Carbohydr. Polym.* **2019**, *204*, 104-110.

109. Peat, S.; Whelan, W. J.; Thomas. Gwen. 587. The Enzymic Synthesis and Degradation of Starch. Part XXII. Evidence of Multiple Branching in Waxy-Maize Starch. A Correction. *J. Chem. Soc.* **1956**, 3025-3030.

110. French, D. Fine Structure of Starch and its Relationship to the Organization of Starch Granule. *J. Jpn. Soc. Starch Sci.* **1972**, *19*, 8-25.

111. Greenwood, C. T.; Robertson, J. S. M. Physicochemical Studies on Starches. Part I. The Characterization of the Starch present in the Seeds of the Rubber Tree, Hevea Brasiliensis. *J. Chem. Soc.* **1954**, 3769-3778.

112. Jenkins, P. J.; Cameron, R. E.; Donald, A. M. A Universal Feature in the Structure of Starch Granules from Different Botanical Sources. *Starch/Stärke* **1993**, *45*, 417-420.

113. Robin, J. P.; Mercier, C.; Carbonniere, R.; Guilbot, A. Lintnerized Starches. Gel Filtration and Enzymatic Studies of Insoluble Residues from Prolonged Acid Treatment of Potato Starch. *Cereal Chem.* **1974**, *51*, 389-405.

114. Hizukuri, S. Polymodal Distribution of the Chain Lengths of Amylopectins, and its Significance. *Carbohydr. Res.* **1986**, *147*, 342-347.

115. Gallant, D. J.; Bouchet, B.; Baldwin, P. M. Microscopy of Starch: Evidence of a New Level of Granule Organization. *Carbohydr. Polym.* **1997**, *32*, 177-191.

116. Finch, P.; Sebesta, D. W. The Amylase of Pseudomonas Stutzeri as a Probe of the Structure of Amylopectin. *Carbohydr. Res*. **1992**, *227*, C1-C4.

117. Bertoft, E. Investigation of the Fine Structure of Alpha-Dextrins Derived from Amylopectin and their Relation to the Structure of Waxy-Maize Starch. *Carbohydr. Res*. **1991**, *212*, 229-244.

118. Bertoft, E. On the Building Block and Backbone Concepts of Amylopectin Structure. *Cereal Chem*. **2013**, *90*, 294-311.

119. Hanashiro, I.; Abe, J.-I.; Hizukuri, S. A Periodic Distribution of the Chain Length of Amylopectin as Revealed by High-Performance Anion-Exchange Chromatography. *Carbohydr. Res*. **1996**, *283*, 151-159.

120. O'Sullivan, A. C.; Perez, S. The Relationship Between Internal Chain Length of Amylopectin and Crystallinity in Starch. *Biopolymer* **1991**, *50*, 381-390.

121. Bertoft, E. Koch, K.; Aman, P. Building Block Organisation of Clusters in Amylopectin from Different Structural Types. *Int. J. Biol. Macromol.* **2012**, *50*, 1212-1223.

122. Waigh, T. A.; Kato, K. L.; Donald, A. M; Gidley, M. J.; Clarke, C. J.; Riekel, C. Side-Chain Liquid- Crystalline Model for Starch. *Starch/Stärke* **2000**, *52*, 450- 460.

123. Waigh, T. A.; Perry, P.; Riekel, C.; Gidley, M. J.; Donald, A. M. Chiral Side-Chain Liquid-Crystalline Polymeric Properties of Starch. *Macromolecules* **1998**, *31*, 7980-7984.

124. Berlman, I. B. *Handbook of Fluorescence Spectra of Aromatic Molecules*. 2nd ed. N.Y: Academic Press, **1971**.

125. Kim, D. Characterization of Hydrophobically Modified Starch Nanoparticles by Pyrene Fluorescence. M.Sc. Dissertation, University of Waterloo, Waterloo, ON, 2017**.**

126. Birks, J. B.; Dyson, D. J.; Munro, I. H.; Flowers, B. H. 'Excimer' Fluorescence II. Lifetime Studies of Pyrene Solution. *Proc. Roy. Soc. Lond. A Math. Phys. Sci.* **1963**, *275*, 575-588.

127. Duhamel, J.; Winnik, M. A.; Baros, F.; Andre, J. C.; Maritinho, J. M. G. Diffusion Effects on Pyrene Excimer Kinetics: Determination of the Excimer Formation Rate Coefficient Time Dependence. *J. Phys. Chem.* **1992**, *96*, 9805-9810.

128. Duhamel, J.; Yekta, A.; Winnik, M. A.; Jao, T. C.; Mishra, M. K.; Rubin, I. D. A Blob Model to Study Polymer Chain Dynamics in Solution. *J. Phys. Chem.* **1993**, *97*, 13708-13712.

129. Casier, R.; Duhamel, J. The Effect of Structure on Polypeptide Blobs: A Model Study Using Poly(*L*-Lysine). *Langmuir* **2020**, *36,* 7980-7990.

Chapter 2

1. Khlestkin, V. K.; Peltek, S. E.; Kolchanov, N. A. Review of Direct Chemical and Biochemical Transformations of Starch. *Carbohydr. Polym.* **2018**, *181*, 460-476.

2. Li, H.; Gilbert, R. G. Starch Molecular Structure: The Basis for an Improved Understanding of Cooked Rice Structure. *Carbohydr. Polym.* **2018**, *195*, 9-17.

3. Miculescu, F.; Maidaniuc, A.; Voicu, S. I.; Thakur, V. K.; Stan, G. E.; Ciocan, L. T. Progress in Hydroxyapatite – Starch Based Sustainable Biomaterials for Biomedical Bone Substitution Applications. *ACS Sustainable Chem. Eng.* **2017**, *5*, 8491-8512.

4. Rayner, M.; Marku, D.; Eriksson, M.; Sjöö, M.; Dejmek, P.; Wahlgren, M. Biomass-Based Particles for the Formulation of Pickering Type Emulsions in Food and Topical Applications. *Coll. Surf.*, *A* **2014**, *458*, 48-62.

5. Marshall, J. J.; Whelan, W.J. Multiple Branching in Glycogen and Amylopectin. *Arch. Biochem. Biophys.***1974**, *161,* 234-238.

6. Witt, T.; Gilbert, R. G. Causal Relation between Structural Features of Amylopectin a Semicrystlline Hyper Branched Polymer. *Biomacromolecules* **2014**, *15*, 2501−2511.

7. Millard, M. M.; Dintzis, F. R.; Willett, J. L.; Klavons, J. A. Light-Scattering Molecular Weights and Intrinsic Viscosities of Processed Waxy Maize Starch in 90% Dimethyl Sulfoxide and H2O. *Carbohydrates* **1997**, *74*, 687-691.

8. Ioan, C. E.; Aberle, T. Burchard, W. Solution Properties of Glycogen. 1. Dilute Solutions. *Macromolecules* **1999**, *32*, 7444-7453.

9. Falk, H.; Stanek, M. Two-Dimensional 1H and 13C NMR Spectroscopy and the Structural Aspects of Amylose and Amylopectin. *Monatsh. Chem.* **1997***, 128*, 777-784.

10. Peng, Q. J.; Perlin, A. S. Observations on N.M.R. Spectra of Starches in Dimethyl Sulfoxide, Iodine-Complexing, and Solvation in Water- Dimethyl Sulfoxide. *Carbohydr. Res.* **1987**, *160*, 57-72.

11. Donald, A.; Kato, K. L.; Perry, P. A.; Waight, T. A. Scattering Studies of the Internal Structure of Starch Granules. *Starch/Stärke* **2001**, *53*, 504–512.

12. French, D. Fine Structure of Starch and its Relationship to the Organization of Starch Granule. *J. Jpn. Soc. Starch Sci*. **1972**, *19*, 8-25.

13. Imberty, A.; Tran, V.; Perez, S. Recent Advances in Knowledge of Starch Structure. *Starch/Stärke* **1991**, *43*, 375-384

14. Bertoft, E. On the nature of categories of chains in amylopectin and their connection to the super helix model. *Carbohydr. Polym.* **2004**, *57*, 211–224.

15. Bertoft, E. On the Building Block and Backbone Concepts of Amylopectin Structure. *Cereal Chem.* **2013***, 90*, 294–311.

16. Waigh, T. A.; Perry, P.; Riekel, C.; Gidley, M. J.; Donald, A. M. Chiral Side Chain Liquid Crystalline Polymeric Properties of Starch. *Macromolecules* **1998**, *31*, 7980-7984.

17. Waigh, T. A.; Kato, K. L.; Donald, A. M.; Gidley, M. J.; Clarke, C. J.; Riekel, C. Side-Chain Liquid-Crystalline Model for Starch. *Starch/Stärke* **2000**, *52*, 450–460.

18. Waigh, T. A.; Gidley, M. J.; Komanshek, B. U.; Donald, A. M. The Phase Transformations in Starch during Gelatinisation: A Liquid Crystalline Approach. *Carbohydr. Res*. **2000**, *328*, 165–176.

19. Li, L.; Kim, D.; Zhai, X.; Duhamel, J. A Pyrene Excimer Fluorescence (PEF) Study of the Interior of Amylopectin in Dilute Solution. *Macromolecules* **2020**, *53*, 6850-6860.

20. Yamashita, Y.; Hirai, N. J. Single Crystals of Amylose V Complexes. II. Crystals with 71 Helical Configuration. *Polym. Sci. Part A2* **1966**, *4*, 161–171.

21. Li, L.; Duhamel, J. Conformation of Pyrene-Labeled Amylose in DMSO Characterized with the Fluorescence Blob Model. *Macromolecules* **2016**, *49*, 7965-7974.

22. Press, W. H.; Flanery, B. P.; Tenkolsky, S. A.; Vetterling, W. T. Numerical Recipes in Fortran: The Art of Scientific Computing; Cambridge University Press: Cambridge and New York, 1992; pp 523−528.

23. Li, L. *Characterization of Polysaccharides in Starch using Fluorescence Techniques*. **2020**, University of Waterloo, Ph.D. Dissertation.

24. Ryan Amos, *Hydrophobic Modification of Starch*, **2019**, University of Waterloo, Ph.D. Dissertation.

25. Li, L.; Duhamel, J. Interior of Amylopectin and Nano-Sized Amylopectin Fragments Probed by Viscometry, Dynamic Light Scattering, and Pyrene Excimer Fluorescence. *Polymers* **2020**, *12*, 2649-2661.

26. Kim, D.; Amos, R.; Gauthier, M. Duhamel, J. Application of Pyrene Fluorescence to the Characterization of Hydrophobically Modified Starch Nanoparticles. *Langmuir* **2018**, *34*, 8611-8621.

27. Kim, D.; Amos, R. C.; Gauthier, M.; Duhamel, J. Assemblies of Hydrophobically Modified Starch Nanoparticles Probed by Surface Tension and Pyrene Fluorescence. *ACS Symposium Series-Molecular Assemblies: Characterization and Applications.* Ed. Nagarajan, R. **2020**, Chapter 5, pp 61-75.

28. Casier, R.; Duhamel, J. The Effect of Structure on Polypeptide Blobs: A Model Study Using Poly(*L*-Lysine). *Langmuir* **2020**, 3*6,* 7980-7990.

29. Duhamel, J. Global Analysis of Fluorescence Decays to Probe the Internal Dynamics of Fluorescently Labeled macromolecules. *Langmuir* **2014**, *30*, 2307-2324.

30. Inouch, N. Glover, D. V.; Fuwa, H. Chain Length Distribution of Amylopectins of Several Single Mutants and the Normal Counterpart, and Sugary-1 Phytoglycogen in Maize (Zea mays L.). *Starch/Stärke* **1987**, *39*, 259-266.

31. Bertoft, E. Investigation of the Fine Structure Of Alpha-Dextrins Derived From Amylopectin and Their Relation to the Structure of Waxy-Maize Starch. *Carbohydr. Res.* **1991**, *212*, 229-244.

32. Burchard, W. Structure Formation by Polysaccharides in Concentrated Solution. *Biomacromolecules* **2001**, *2*, 342-353.

33. Thurn, A.; Burchard, W. Heterogeneity in Branching of Amylopectin. *Carbohydr. Polym.* **1985**, *5*, 441-460.

34. Gallant, D. J.; Bouchet, B.; Baldwin, P. M. Microscopy of Starch: Evidence of a New Level of Granule Organization, *Carbohydr. Polym.* **1997**, *32*, 177-191.

35. Finch, P.; Sebesta, D. The Amylase of Pseudomonas Stutzeri as a Probe of the Structure of Amylopectin. *Carbohydr. Res.* **1992**, *227*, c1-c4.

36. Bertoft, E.; Koch, K.; Åman, P. Structure of Building Blocks in Amylopectin. *Carbohydr. Res*. **2012**, *361*, 105–113.

37. Bertoft, E.; Koch, K.; Åman, Building Block Organisation of Clusters in Amylopectin from Different Structural Types. *P. Int. J. Biol. Macromol*. **2012**, *50*, 1212–1223.

38. Tetlow, I. J.; Bertoft, E. A Review of Starch Biosynthesis in Relation to the Building Block-Backbone Model. *Int. J. Mol. Sci.* **2020**, *21*, 7011-7047.

Chapter 3

1. Haworth, W. N.; Percival, E. G. V. Polysaccharides. Part X I. Molecular Structure of Glycogen. *J. Chem. Soc.* **1932,** *1932*, 2277-2282.

2. Bell, D. J. Glycogen: The Molecular Structure of Horse Muscle Glycogen. *Biochem. J.* **1937,** *31*, 1683-1691.

3. Staudinger, H.; Husemann, E. Über Hochpolymere Verbindungen. 150. Mitteilung. Über die Konstitution der Stärke. *Ann. Chem.* **1937**, *627*, 195-236.

4. Cori, G. T.; Cori, C. F. Crystalline Muscle Phosphorylase IV. Formation of Glycogen. *J. Biol. Chem.* **1943**, *151*, 57- 63.

5. Larner, J.; Illingworth, B.; Cori, G. T.; Cori, C. F. Structure of Glycogens and Amylopectins: II. Analysis by Stepwise Enzymatic Degradation. *J. Biol. Chem.* **1952**, *199*, 641-651.

6. Roach, P. J.; Depaoli-Roach, A. A.; Hurley, T. D; Tagliabracci, V. S. Glycogen and its Metabolism: Some New Developments and Old Themes. *Biochem. J.* **2012,** *441*, 763–787.

7. Madsen, N. B.; Cori, C. F. The Binding of Glycogen and Phosphorylase. *J. Biol. Chem.* **1958**, *233*, 1251-1256.

8.   Manner, D. J. Recent Developments in Our Understanding of Glycogen Structure. *Carbohydr. Polym.* **1991,** *16*, 37-82.

9.   Bathgate, G. N.; Manners, D. J. Multiple Branching in Glycogens. *Biochem. J*. **1966**, *101*, 3-5.

10. Meyer, K. H. The Chemistry of Glycogen. *Adv. Enzymol. Relat. Areas Mol. Biol.* **1943**, 109-135.

11. Gunja-Smith, Z; Marshall, J. J.; Mercier, C.; Smith, E. E.; Whelan, W. J. A Revision of The Meyer-Bernfeld Model of Glycogen and Amylopectin. *FEBS Lett.* **1970**, *12*, 101-104.

12. French, D. *Structure of Glycogen and its Amylolytic Degradation. In Control of Glycogen Metabolism*. Eds. Book: 1964; p 7-28.

13. Meléndez-Heiva, E.; Waddell, T. G.; Shelton, E. D. Optimization of Molecular Design in the Evolution of Metabolism: The Glycogen Molecule. *Biochem. J.* **1993**, *295*, 477-483.

14. Goldsmith, E.; Sprang, S.; Fletterick, R. Structure of Maltoheptaose by Difference Fourier Methods and a Model for Glycogen. *J. Mol. Biol.* **1982**, *156*, 411-427.

15. DiNuzzo, D. Kinetic Analysis of Glycogen Turnover: Relevance to Human Brain 13C-NMR Spectroscopy. *J. Cereb. Blood Flow Metab.* **2013,** *33*, 1540-1548.

16. Bertoldo, M.; Zampano, G.; Suffner, L.; Liberati, E.; Ciardelli, F. Oxidation of Glycogen "Molecular Nanoparticles" by Periodate. *Polym. Chem.,* **2013**, *4*, 653- 661.

17. Sullivan, M.A.; O'Connor, M.J.; Umana, F.; Roura, E.; Jack, K.; Stapleton, D. I.; Gilbert, R.G. Molecular Insights into Glycogen α-Particle Formation. *Biomacromolecules* **2012**, *13*, 3805−3813.

18. Marchand, I.; Chorneyko, K.; Tarnopolsky, M.; Hamilton, S.; Shearer, J.; Potvin, J.; Graham, J. E. Quantification of Subcellular Glycogen in Resting Human Muscle: Granule Size, Number, and Location. *J. Appl. Physiol.* **2002**, *93*, 1598-1607.

19. Marchand, I.; Tarnopolsky, M.; Adamo, K. B.; Bourgeois, J. M.; Chorneyko, K.; Graham, T. E. Quantitative Assessment of Human Muscle Glycogen Granules Size and Number in Subcellular Locations During Recovery from Prolonged Exercise. *J. Physiol.* **2007**, 580, 617–628.

20. Shearer. J.; Graham, T. E. Novel Aspects of Skeletal Muscle Glycogen and Its Regulation During Rest and Exercise. *Exercise Sport Sci. Rev.* **2004,** *32*, 120-126.

21. Prats, C.; Graham, T. E.; Shearer, J. The Dynamic Life of the Glycogen Granule. *J. Biol. Chem.* **2018**, *293*, 7089-7098.

22. Bezborodkina, N. N.; Chestnova1, A. Y.; Vorobev, M. L.; Kudryavtsev, B., N. Spatial Structure of Glycogen Molecules in Cells. *Biochemistry (Moscow)* **2018**, *83*, 627-644.

23. Zhang, P.; Nada, S. S.; Tan, X. Deng, B.; Sullivan, M. A.; Gilbert, R. G. Exploring glycogen biosynthesis through Monte Carlo simulation. *Int. J. Biol. Macromol.* **2018**, *116*, 364-271.

24. Simmons, J.; Nickels, J. D.; Michalsi, M.; Grossutti, M.; Shamana, H.; Stanley, C. B.; Schwan, A. L.; Katsaras, J.; Dutcher, J. R. Structure, Hydration, and Interactions of Native and Hydrophobically Modified Phytoglycogen Nanoparticles. *Biomacromolecules* **2020**, *21*, 4053-4062.

25. Baylis, B.; Shelton, E.; Grossutti, M.; Dutcher, J. R. Force Spectroscopy Mapping of the Effect of Hydration on the Stiffness and Deformability of Phytogycogen Nanoparticles. *Biomacromolecules* **2021**, *22*, 2985-2995.

26. Morris G.A; Ang S.; Hill, S.E.; Lewis, S.; Schäfer, B.; Nobbmann, U.; Harding, S.E. Molar Mass and Solution Conformation of Branched a(1 $\rightarrow$ 4), a(1 $\rightarrow$ 6)Glucans. Part I: Glycogens in Water. *Carbohydr. Polym.*, **2008**, *71*, 101–108.

27. Kageyama, A. Yanase, M.; Yuguchi, Y. Structural Characterization of Enzymatically

Synthesized Glucan Dendrimers. *Carbohydr. Polym.* **2019,** *204*, 104-110.

28. Li, L.; Kim, D.; Zhai, X.; Duhamel, J. A Pyrene Excimer Fluorescence (PEF) Study of the Interior of Amylopectin in Dilute Solution. *Macromolecules* **2020**, *53*, 6850-6860.

29. Zhang, Q. Kim, D.; Li, L.; Patel, S.; Duhamel, J. Surfactant Structure-Dependent Interactions with Modified Starch Nanoparticles Probed by Fluorescence Spectroscopy. *Langmuir* **2019,** *35*, 3432-3444.

30. Li, L.; Duhamel, J. Conformation of Pyrene-Labeled Amylose in DMSO Characterized with the Fluorescence Blob Model. *Macromolecules* **2016**, *49*, 7965-7974.

31. Mathew, A. K.; Siu, H.; Duhamel, J. A Blob Model to Study Chain Folding by Fluorescence. *Macromolecules* **1999,** *32*, 7100–7108.

32. Duhamel, J. Polymer Chain Dynamics in Solution Probed with a Fluorescence Blob Model. *Acc. Chem. Res.* **2006**, *39*, 953–960.

33. Duhamel, J. Global Analysis of Fluorescence Decays to Probe the Internal Dynamics of Fluorescently Labeled macromolecules. *Langmuir* **2014**, *30*, 2307-2324.

34. Press, W. H.; Flanery, B. P.; Tenkolsky, S. A.; Vetterling, W. T. Numerical Recipes in Fortran: The Art of Scientific Computing; Cambridge University Press: Cambridge and New York, 1992; pp 523−528.

35. Matsui, M.; Kakuta, M.; Misaki, A. Comparison of the Unit-chain Distributions of Glycogens from Different Biological Sources, Revealed by Anion Exchange Chromatography. *Biosci. Biotechnol. Biochem*. **1993**, *57*, 623-627.

36. Winnik, F. M.; Regismond, S. T. A. Fluorescence Methods in the Study of the Interactions of Surfactants with Polymers. *Colloids Surf., A* **1996**, 118, 1 – 39.

37. Basedow, A., M.; Ebert, K.H.; Feigenbut, W. Polymer-Solvent Interactions: Dextrans in Water and DMSO. *Makromol. Chem.* **1980**, *181*, 1071 -1080.

38. Manners, D. J. Recent Developments in Our Understanding of Amylopectin Structure. *Carbohydr. Polym.* **1989**, *11*, 87-112.

39. Casier, R.; Duhamel, J. The Effect of Like-Charges on the Conformation and Internal Dynamics of Polypeptides Probed by Pyrene Excimer Fluorescence. *Macromolecules* **2020**, *53*, 5147-5157.

40. Gidely, M. J.; Bulpin, P. V. Crystallisation of Malto-Oligosaccharides as Models of the Crystalline Forms of Starch: Minimum Chain Length Requirement for the Formation of Double Helices. *Carbohydr. Res.* **1987**, *161*, 291-300.

41. Cumpstey, I. Chemical modification of polysaccharides. ISRN *Org. Chem.* **2013**, 417672−417698.

42. Dicke, R. A. Straight Way to Regioselectively Functionalized Polysaccharide Esters. *Cellulose* **2004**, *11*, 255–263.

43. Chen, S. Quantitative Characterization of Pyrene-Labeled Macromolecules in Solution by Global Analysis of Fluorescence Decays. Ph.D. Dissertation, University of Waterloo, Waterloo, ON, **2012**.

Chapter 4

1. Zhang, Q.; Kim, D.; Li, L.; Patel, S.; Duhamel, J. Surfactant Structure-Dependent Interactions with Modified Starch Nanoparticles Probed by Fluorescence Spectroscopy. *Langmuir* **2019**, *35*, 3432-3444.

2. Li, L.; Kim, D.; Zhai, X.; Duhamel, J. A Pyrene Excimer Fluorescence (PEF) Study of the Interior of Amylopectin in Dilute Solution. *Macromolecules* **2020**, *53*, 6850-6860.

3. Li, L.; Duhamel, J. Interior of Amylopectin and Nano-Sized Amylopectin Fragments Probed by Viscometry, Dynamic Light Scattering, and Pyrene Excimer Fluorescence. *Polymers* **2020**, *12*, 2649-2661.

4. Li, L.; Duhamel, J. Conformation of Pyrene-Labeled Amylose in DMSO Characterized with the Fluorescence Blob Model. *Macromolecules* **2016**, *49*, 7965-7974.

5. Kim, D.; Amos, R.;Gauthier, M.; Duhamel, J. Applications of Pyrene Fluorescence to the Characterization of Hydrophobically Modified Starch Nanoparticles. *Langmuir* **2018**, *34*, 8611-8621.

6. Kim, D.; Amos, R. C.; Gauthier, M.; Duhamel, J. Assemblies of Hydrophobically Modified Starch Nanoparticles Probed by Surface Tension and Pyrene Fluorescence. *ACS Symposium Series-Molecular Assemblies: Characterization and Applications.* Ed. Nagarajan, R. 2020, Chapter 5, pp 61-75.

7. Casier, R.; Duhamel, J. Blob-Based Approach to Estimate the Folding Time of Proteins Supported by Pyrene Excimer Fluorescence Experiments. *Macromolecules* **2020**, *53*, 9823-9835.

8. Casier, R.; Duhamel, J. Pyrene Excimer Fluorescence as a Direct and Easy Experimental Means to Characterize the Length Scale and Internal Dynamics of Polypeptide Foldons. *Macromolecules* **2018**, *51*, 3450−3457.

9. Casier, R.; Duhamel, J. The Effect of Structure on Polypeptide Blobs: A Model Study Using Poly(*L*-Lysine). *Langmuir* **2020**, *36*, 7980-7990

10. Casier, R.; Duhamel, J. Effect of Like Charges on the Conformation and Internal Dynamics of Polypeptides Probed by Pyrene Excimer Fluorescence. *Macromolecules* **2020**, *53*, 5147−5157.

11. Seymore, F.D.; Soldki, M.E.; Plattner, R.D.; Jeanes, A. Six Unusual Dextrans: Methylation Structural Analysis by Combined G.L.C.-M.S. of Per-O-Acetyl-Aldononitriles. *Carbohydr. Res*. **1977**, *53*, 153-166.

12. Seymour, F., R.; Knapp, R., D. Structural Analysis of Dextrans, From Strains of Leuconostoc and Related Genera, that Contain 3-o-α-D-Glucosylated α-D-Glycopyranosyl Residues at the Branches Points, or in Consecutive, Linear Positions. *Carbohydr. Res.* **1980**, *81*, 105-129.

13. Van Cleve, J., W., Schaefer, W., C.; Rist, C., E. The Structure of NRRL B-512 Dextran. Methylation Studies[2]. *J. Am. Chem. Soc*. **1956**, *78*, 4435-4438.

14. Garg, S. K.; Stivala, S. S. Assessment of Branching in Polymers from Small Angle X-Ray Scattering (SAXS). *Polymer* **1981**, *23*, 514-520.

15. Maina, N., H.; Pitkänen, L.; Heikkinene, S.; Tuomainen, P.; Virkki, L.; Tenkanen, M. Challenges in Analysis of High-Molar Mass Dextrans: Comparison of HPSEC, AsFlFFF and DOSY NMR Spectroscopy. *Carbohydr. Polym.* **2014**, *99*, 199-207.

16. Larm, O.; Lindberg, B.; Svensson, S. Studies on the Length of the Side Chains of the Dextran Elaborated by Leuconostoc Mesenteroides NRRL B-512*. *Carbohydr. Res*. **1971**, *20*, 39-48.

17. Heinze, T.; Liebert, T.; Heublein, B.; Hornig, S. Functional Polymers Based on Dextran, *Adv. Polym. Sci*. **2006**, *205*, 199-291.

18. Kulicke, W., M.; Heinze, T. Improvements in Polysaccharides for use as Blood Plasma Expanders. *Macromol. Symp*. **2006**, *231*, 47–59.

19. Hu, Q.; Lu, Y.; Luo, Y. Recent Advances in Dextran-Based Drug Delivery Systems: From Fabrication Strategies to Applications. *Carbohydr. Polym.* **2021**, *264*, 117999.

20. Heinze, T.; Liebert, T.; Heublein, B.; Hornig, S. Functional Polymers Based on Dextran. In *Adv. Polym. Sci. 205 Polysaccharides II*. Ed. Klemm, D. Springer, Heidelberg, 2006, pp 199-291.

21. Basedow, A., M.; Ebert, K.H.; Feigenbut, W. Polymer-Solvent Interactions: Dextrans in Water and DMSO. *Makromol. Chem.* **1980**, *181*,1071 -1080.

22. Çatiker, E.; Güner, G. Unperturbed Molecular Dimensions and the Theta Temperature of Dextran in Dimethylsulfoxide (DMSO) Solutions. *Polym. Bull*. **1998**, *41*, 223-230.

23. Callaghan, P. T.; Lelievre, J. The Influence of Polymer Size and Shape on Self-Diffusion of Polysaccharides and Solvents. *Anal. Chem. Acta* **1986**, *189*, 145-166.

24. Suzuki, N.; Wada, A.; Suzuki, K. Study of Dextran Solutions by Quasielastic Light Scattering. *Carbohydr. Res.* **1982**, *109*, 249-258.

25. Press, W. H.; Flanery, B. P.; Tenkolsky, S. A.; Vetterling, W. T. Numerical Recipes in Fortran: The Art of Scientific Computing; Cambridge University Press: Cambridge and New York, 1992; pp 523−528.

26. Thoma, J.; McNelles, S. A.; Adronov, A.; Duhamel, J. Direct Measure of the Local Concentration of Pyrenyl Groups in Pyrene-Labeled Dendrons Derived from the Rate of Fluorescence Collisional Quenching. *Polymers* **2020**, *12*, 2919.

27. Duhamel, J.; Kanagalingam, S.; O'Brien, T.; Ingratta, M. Side-Chain Dynamics of an α−Helical Polypeptide Monitored by Fluorescence. *J. Am. Chem. Soc.* **2003**, *125*, 12810-12822.

28. De Belder, A., N.; Norrman, B. The Distribution of Substituents in Partially Acetylated Dextran. *Carbohydr. Res*. **1986**, *8*, 1-6.

29. Arranz, F.; Sánchez-Chaves, M. 13C Nuclear Magnetic Resonance Spectral Study on the Distribution of Substituents in Relation to the Preparation Method of Partially Acetylated Dextrans. *Polymer* **1988**, *29*, 507-512.

30. Thoma, J.; Li, M., J.; Bertocchi, M. J.; Weiss, R., G.; Duhamel, J. Long-Range Polymer Chain Dynamics of a "Stiff" Polymer. Fluorescence from Poly(isobutylene-alt-maleic anhydride) with N-(1-Pyrenylmethyl)succinimide Groups. *Macromolecules* **2017**, *50*, 3394-3403.

31. Farhangi, S.; Weiss, H.; Duhamel, J. Effect of Side-Chain Length on the Polymer Chain Dynamics of Poly(alkyl methacrylate)s in Solution. *Macromolecules* **2013**, *46*, 9738-9747.

Chapter 5

1. Liu, J., H., Y.; Brameld, K. A.; Brant, D. A.; Goddard III, W. A. Conformational Analysis of Aqueous Pullulan Oligomers: An Effective Computational Approach. *Polymer* **2002**, *43*, 509-516.

2. Marszalek, P. E.; Oberhauser, A. F.; Pang, Y. P.; Fernandez, J. M. Polysaccharide Elasticity Governed by Chair-Boat Transitions of the Glucopyranose Ring. *Nature* **1998**, *396*, 661-664.

3. Nishinari, K.; Tsutsumi, A. Studies on Molecular Motion of Polysaccharides in the Solid State by Broad-Line Nuclear Magnetic Resonance. *J. Polym. Sci., Polym. Phys. Ed.* **1984**, *22*, 95-99.

4. Dais P.; Vlachou, S.; Taravel, F. R. 13C Nuclear Magnetic Relaxation Study of Segmental Dynamics of the Heteropolysaccharide Pullulan in Dilute Solutions. *Biomacromolecules* **2001**, *2*, 1137-1147.

5. Scandola, M.; Ceccorulli, G.; Pizzoli, M. Molecular Motions of Polysaccharides in the Solid State: Dextran, Pullulan, and Amylose. *Int. J. Biol. Macromol*. **1991**, *13*, 254-260.

6. Brant, D.; Burton, B., A. The Configurational Statistics of Pullulan and Some Related Glucans. In *Solution Properties of Polysaccharide*, Brant, E., A. Ed. ACS Book:1981.

7. Burton, B. A.; Brant, D. A. Comparative Flexibility, Extension, and Conformation of Some Simple Polysaccharide Chains. *Biopolymers* **1983**, *22*, 1769-1792.

8. Muroga, Y.; Yamada, Y.; Noda, I.; Nagasawa, M. Local Conformation of Polysaccharides in Solution Investigated by Small-Angle X-ray Scattering. *Macromolecules* **1987**, *20*, 3003-3006.

9. Garg, S. K.; Stivala, S. S. Assessment of Branching in Polymers from Small Angle X-Ray Scattering (SAXS). *J. Polym. Sci. Polym. Phys. Ed*. **1978**, *16*, 1419-1434.

10. Pavlov, G. M.; Korneeva, E. V.; Yevlampieva, N. P. Hydrodynamic Characteristics and Equilibrium Rigidity of Pullulan Molecules. *Int. J. Biol. Macromol.* **1994**, *16*, 318–323.

11. Casier, R.; Duhamel, J. Effect of Like Charges on the Conformation and Internal Dynamics of Polypeptides Probed by Pyrene Excimer Fluorescence. *Macromolecules* **2020**, *53*, 5147−5157.

12. Casier, R.; Duhamel, J. Pyrene Excimer Fluorescence as a Direct and Easy Experimental Means to Characterize the Length Scale and Internal Dynamics of Polypeptide Foldons. *Macromolecules* **2018**, *51*, 3450−3457.

13. Li, L.; Duhamel, J. Conformation of Pyrene-Labeled Amylose in DMSO Characterized with the Fluorescence Blob Model. *Macromolecules* **2016**, *49*, 7965-7974.

14. Farhangi, S.; Weiss, H.; Duhamel, J. Effect of Side-Chain Length on the Polymer Chain Dynamics of Poly(alkyl methacrylate)s in Solution. *Macromolecules* **2013**, *46*, 9738-9747.

15. Thoma, J.; Li, M. J.; Bertocchi, M. J.; Weiss, R. G.; Duhamel, J. Long-Range Polymer Chain Dynamics of a "Stiff" Polymer. Fluorescence from Poly(isobutylene-alt-maleic anhydride) with N-(1-Pyrenylmethyl)succinimide Groups. *Macromolecules* **2017**, *50*, 3394-3403.

16. Duhamel, J. Polymer Chain Dynamics in Solution Probed with a Fluorescence Blob Model. *Acc. Chem. Res.* **2006**, *39*, 953-960.

17. Everett, W. W.; Foster, J. F. The Conformation of Amylose in Solution. *J. Am. Chem. Soc.* **1959**, *81*, 3464-3469.

18. Fujii, M.; Honda, K.; Fujita, H. Dilute-Solution of Amylose in Dimethylsulfoxide. *Biopolymers* **1973**, *12*, 1177-1195.

19. Li, L.; Kim, D.; Zhai, X.; Duhamel, J. A Pyrene Excimer Fluorescence (PEF) Study of the Interior of Amylopectin in Dilute Solution. *Macromolecules* **2020**, *53*, 6850-6860.

20. Gunja-Smith, Z; Marshall, J. J.; Mercier, C.; Smith, E. E.; Whelan, W. J. A Revision of The Meyer-Bernfeld Model of Glycogen and Amylopectin. *FEBS Lett.* **1970**, *12*, 101-104.

21. Kato, T.; Okamoto, T.; Tokuya, T.; Takahashi, A. Solution Properties and Chain Flexibility of Pullulan in Aqueous Solution. *Biopolymers* **1982**, *21*, 1623-1633.

22. Pavlov, G. M.; Yevlampieva, N. P.; Korneeva, E. V. Flow Birefringence of Pullulan Molecules in Solutions. *Polymer* **1998**, *39*, 235-239.

23. Press, W. H.; Flanery, B. P.; Tenkolsky, S. A.; Vetterling, W. T. Numerical Recipes in Fortran: The Art of Scientific Computing; Cambridge University Press: Cambridge and New York, 1992; pp 523−528.

24. Cumpstey, I. Chemical modification of polysaccharides. ISRN *Org. Chem.* **2013**, 417672−417698.

25. Bruneel, D.; Schacht, E.; Bruyn, A. D. Structural Analysis of Succinoylated and Chloroformate Activated Pullulan: NMR Study in DMSO Solution. *J. Carbohydr. Chem.* **1993**, *12*, 769-778.

26. De Belder, A. N.; Norrman, B. The Distribution of Substituents in Partially Acetylated Dextran. *Carbohydr. Res.* **1986**, *8*, 1-6.

27. Ioan, C. E.; Aberle, T.; Burchard, W. Structure Properties of Dextran. 2. Dilute Solution. *Macromolecules* **2000**, *33*, 5730-5739.

Chapter 6.

1. Casier, R.; Duhamel, J. Pyrene Excimer Fluorescence as a Direct and Easy Experimental Means to Characterize the Length Scale and Internal Dynamics of Polypeptide Foldons. *Macromolecules* **2018**, *51*, 3450−3457.

2. Casier, R.; Duhamel, J. Effect of Like Charges on the Conformation and Internal Dynamics of Polypeptides Probed by Pyrene Excimer Fluorescence. *Macromolecules* **2020**, *53*, 5147−5157.

3. Li, L.; Duhamel, J. Conformation of Pyrene-Labeled Amylose in DMSO Characterized with the Fluorescence Blob Model. *Macromolecules* **2016**, *49*, 7965-7974.

4. Farhangi, S.; Weiss, H.; Duhamel, J. Effect of Side-Chain Length on the Polymer Chain Dynamics of Poly(alkyl methacrylate)s in Solution. *Macromolecules* **2013**, *46*, 9738-9747.

5. Li, L.; Kim, D.; Zhai, X.; Duhamel, J. A Pyrene Excimer Fluorescence (PEF) Study of the Interior of Amylopectin in Dilute Solution. *Macromolecules* **2020**, *53*, 6850-6860.

6. Imberty, A.; Tran, V.; Perez, S. Recent Advances in Knowledge of Starch Structure. *Starch/Stärke* **1991**, *43*, 375-384.

7. Yamashita, Y.; Hirai, N. J. Single Crystals of Amylose V Complexes. II. Crystals with 71 Helical Configurations. *Polym. Sci. Part A2* **1966**, *4*, 161–171.

8. Gallant, D. J.; Bouchet, B.; Baldwin, P. M. Microscopy of Starch: Evidence of a New Level of Granule Organization, *Carbohydr. Polym.* **1997**, *32*, 177-191.

9. Gunja-Smith, Z; Marshall, J. J.; Mercier, C.; Smith, E. E.; Whelan, W. J. A Revision of The Meyer-Bernfeld Model of Glycogen and Amylopectin. *FEBS Lett.* **1970**, *12*, 101-104.

10. Cori, G. T.; Cori, C. F. Crystalline Muscle Phosphorylase IV. Formation of Glycogen. *J. Biol. Chem.* **1943**, *151*, 57- 63.

11. Larner, J.; Illingworth, B.; Cori, G. T.; Cori, C. F. Structure of Glycogens and Amylopectins: II. Analysis by Stepwise Enzymatic Degradation. *J. Biol. Chem.* **1952**, *199*, 641-651.

12. French, D. *Structure of Glycogen and its Amylolytic Degradation. In Control of Glycogen Metabolism*. Eds. Book: 1964; p 7-28.

13. Sullivan, M. A.; O'Connor, M. J.; Umana, F.; Roura, E.; Jack, K.; Stapleton, D. I.; Gilbert, R. G. Molecular Insights into Glycogen α-Particle Formation. *Biomacromolecules* **2012**, *13*, 3805−3813.

14. Marchand, I.; Tarnopolsky, M.; Adamo, K. B.; Bourgeois, J. M.; Chorneyko, K.; Graham, T. E. Quantitative Assessment of Human Muscle Glycogen Granules Size and Number in Subcellular Locations During Recovery from Prolonged Exercise. *J. Physiol.* **2007**, 580, 617–628.

15. Morris, G.A; Ang, S.; Hill, S. E.; Lewis, S.; Schäfer, B.; Nobbmann, U.; Harding, S. E. Molar Mass and Solution Conformation of Branched a(1 → 4), a(1 → 6)Glucans. Part I: Glycogens in Water. *Carbohydr. Polym.* **2008**, *71*, 101–108.

16. Simmons, J.; Nickels, J. D.; Michalsi, M.; Grossutti, M.; Shamana, H.; Stanley, C. B.; Schwan, A. L.; Katsaras, J.; Dutcher, J. R. Structure, Hydration, and Interactions of Native and Hydrophobically Modified Phytoglycogen Nanoparticles. *Biomacromolecules* **2020**, *21*, 4053-4062.

17. Zhang, P.; Nada, S. S.; Tan, X.; Deng, B.; Sullivan, M. A.; Gilbert, R. G. Exploring glycogen biosynthesis through Monte Carlo simulation. *Int. J. Biol. Macromol.* **2018**, *116*, 364-271.

18. Meléndez-Heiva, E.; Waddell, T. G.; Shelton, E. D. Optimization of Molecular Design in the Evolution of Metabolism: The Glycogen Molecule. *Biochem. J.* **1993**, *295*, 477-483.

19. Manner, D. J. Recent Developments in Our Understanding of Glycogen Structure. *Carbohydr. Polym.* **1991,** *16*, 37-82.

20. Basedow, A., M.; Ebert, K. H.; Feigenbut, W. Polymer-Solvent Interactions: Dextrans in Water and DMSO. *Makromol. Chem.* **1980**, *181*,1071 -1080.

21. Pavlov, G. M.; Yevlampieva, N. P.; Korneeva, E. V. Flow Birefringence of Pullulan Molecules in Solutions. *Polymer* **1998**, *39*, 235-239.

22. Garg, S. K.; Stivala, S. S. Assessment of Branching in Polymers from Small Angle X-Ray Scattering (SAXS). *J. Polym. Sci. Polym. Phys. Ed*. **1978**, *16*, 1419-1434.

23. Muroga, Y.; Yamada, Y.; Noda, I.; Nagasawa, M. Local Conformation of Polysaccharides in Solution Investigated by Small-Angle X-ray Scattering. *Macromolecules* **1987**, *20*, 3003-3006.

24. Kothari, D.; Das, D.; Patel, S.; Goyal, A. Dextran and Food Application. In *Polysaccharides: Bioacitivity and Biotechnology*. Ramawat, K. G.; Mérillon, J-M. Eds.; Springer: Switzerland, 2015, pp 735- 752.

25. Marchessault, R. H.; Deslandes, Y. Texture and Crystal Structure of Fungal Polysaccharides. In *Fungal Polysaccharides*. Sandford, P. A.; Matsuda, K. Eds., ACS Book: 1980.

26. Lamberts, B. L.; Meyer, T. S.; Simonson, L. G. Investigation of Possible Solvents for Extracellular Polysaccharides from *Streptococcus mutans* and *Streptococcus sanguis*. *J. Dent. Res.* **1975**, *54*, 857-866.

27. Yang, J.; Sato, T. Conformation of Pullulan in Aqueous Solution Studied by Small-Angle X-ray Scattering. *Polymers* **2020**, *12*, 1266-1276.

28. Dicke, R. A Straight Way to Regioselectively Functionalized Polysaccharide Esters. *Cellulose* **2004**, *11*, 255-263.

Appendices

S2- Appendices for Chapter 2

S2A] Global analysis of the monomer and excimer fluorescence decays according to the fluorescence blob model and equations for the molar fractions of the different pyrene species

The fluorescence decays of the pyrene monomer and excimer of the Py-NAFs and Py-Amylopectin samples were fitted with Equations S2.1 and S2.2, respectively. Equation S2.2 includes the existence of a short-lived excimer species, referred to as *ES**. The *ES** species is often encountered, when PEF takes place in rigid environments such as along the oligosaccharide backbone. Excellent fits were obtained with χ^2 values smaller than 1.3 and residuals and autocorrelation of the residuals randomly distributed around zero as shown in Figure S2.1.

$$[Py^*]_{(t)} = [Py^*_{diff}]_{(t)} + [Py^*_{k2}]_{(t)} + [Py^*_{free}]_{(t)}$$

$$= [Py^*_{diff}]_0 \exp\left(-\left(A_2 + \frac{1}{\tau_M}\right)t - A_3\left(1 - \exp(-A_4 t)\right)\right)$$

$$+ \left([Py^*_{k2}]_o + [Py^*_{diff}]_o e^{-A_3} \sum_{i=0}^{\infty} \frac{A_3^i}{i!} \frac{A_2 + iA_4}{A_2 + iA_4 - k_2}\right)\exp\left(-\left(k_2 + \frac{1}{\tau_M}\right)t\right)$$

$$- [Py^*_{diff}]_o e^{-A_3} \sum_{i=0}^{\infty} \frac{A_3^i}{i!} \frac{A_2 + iA_4}{A_2 + iA_4 - k_2} \exp\left(-\left(A_2 + iA_4 + \frac{1}{\tau_M}\right)t\right) + [Py^*_{free}]_o \exp(-t/\tau_M) \quad \text{(S2.1)}$$

$$[E^*]_{(t)} = [E0^*]_{(t)} + [ES^*]_{(t)}$$

$$= k_2\left([Py^*_{k2}]_o + [Py^*_{diff}]_o e^{-A_3} \sum_{i=0}^{\infty} \frac{A_3^i}{i!} \frac{A_2 + iA_4}{A_2 + iA_4 - k_2}\right) \times \frac{\exp\left(-\frac{t}{\tau_{E0}}\right) - \exp\left(-\left(k_2 + \frac{1}{\tau_M}\right)t\right)}{k_2 + \frac{1}{\tau_M} - \frac{1}{\tau_{E0}}}$$

$$+ [Py^*_{diff}]_o e^{-A_3} \sum_{i=0}^{\infty} \frac{A_3^i}{i!} \frac{A_2 + iA_4}{A_2 + iA_4 - k_2} \frac{\exp\left(-\left(A_2 + iA_4 + \frac{1}{\tau_M}\right)t\right) - \exp\left(-\frac{t}{\tau_{E0}}\right)}{A_2 + iA_4 + \frac{1}{\tau_M} - \frac{1}{\tau_{E0}}}$$

$$+ [E0^*]_o \exp\left(-\frac{t}{\tau_{E0}}\right) + [ES^*]_o \exp\left(-\frac{t}{\tau_{ES}}\right) \quad \text{(S2.2)}$$

The parameters, A_2, A_3, and A_4 in Equation S2.1 and S2.2 are expressed in Equations S2.3a-c.

$$A_2 = <n> \times \frac{k_{blob} k_e [blob]}{k_{blob} + k_e [blob]} \tag{S2.3a}$$

$$A_3 = <n> \times \left(\frac{k_{blob}}{k_{blob} + k_e [blob]} \right)^2 \tag{S2.3b}$$

$$A_4 = k_{blob} + k_e \times [blob] \tag{S2.3c}$$

$<n>$ in Equation S2.3b represents the average number of ground-state pyrenyl labels present in a *blob*. k_{blob} and k_e describe the rate constant for the slow diffusion of two AGUs bearing a pyrenyl label in a same *blob* and the rate constant for the exchange of ground-state pyrenes between *blobs*, respectively. [*blob*] is the local concentration of *blobs* inside the macromolecular volume.

The fluorescence *blob* model (FBM) was first applied to a series of pyrene-labeled amylopectin and NAFs with floating k_2, the rate constant for the rapid rearrangement between two pyrenyl labels in close proximity prior to PEF. The k_2 values of the pyrene-labeled amylopectin and NAF samples obtained at different NAF(56) concentrations were averaged. The average k_2 values obtained for each polysaccharide are listed in section E. The FBM analysis of the decays was repeated with the average k_2 value fixed in the analysis.

Equations S4-S6 provide the expressions for the molar fractions of the pyrene species determined from the analysis of the monomer decays. The molar fractions f_{Mdiff}, f_{Mfree}, and f_{Mk2} are expressed in Equation S4-S6, where all parameters have been defined in the main text.

$$f_{Mdiff} = \frac{[Py^*_{diff}]_o}{[Py^*_{diff}]_o + [Py^*_{k2}]_o + [Py^*_{free}]_o} \tag{S2.4}$$

$$f_{Mfree} = \frac{[Py^*_{free}]_o}{[Py^*_{diff}]_o + [Py^*_{k2}]_o + [Py^*_{free}]_o} \tag{S2.5}$$

$$f_{Mk2} = \frac{[Py^*_{k2}]_o}{[Py^*_{diff}]_o + [Py^*_{k2}]_o + [Py^*_{free}]_o} \tag{S2.6}$$

The molar fraction f_{Mfree} determined with Equation S2.5 was used to calculate the number of structural units present in a *blob* (N_{blob}^{exp}) as described by Equation 3 in Chapter 2.

Similarly, the molar fractions of the pyrene species detected in the excimer decays was retrieved by applying Equation S2.2. The expressions of the molar fractions f_{Ediff}, f_{Ek2}, f_{EE0}, and f_{EES} are given in Equations S2.7-S2.10.

$$f_{Ediff} = \frac{[Py^*_{diff}]_o}{[Py^*_{diff}]_o + [Py^*_{k2}]_o + [E0^*]_o + [ES^*]_o} \tag{S2.7}$$

$$f_{Ek2} = \frac{[Py^*_{k2}]_o}{[Py^*_{diff}]_o + [Py^*_{k2}]_o + [E0^*]_o + [ES^*]_o} \tag{S2.8}$$

$$f_{EE0} = \frac{[E0^*]_o}{[Py^*_{diff}]_o + [Py^*_{k2}]_o + [E0^*]_o + [ES^*]_o} \tag{S2.9}$$

$$f_{EES} = \frac{[ES^*]_o}{[Py^*_{diff}]_o + [Py^*_{k2}]_o + [E0^*]_o + [ES^*]_o} \tag{S2.10}$$

The contribution of each pyrene species in the monomer and excimer decays were combined to determine the molar fraction of f_{diff}, f_{k2}, f_{free}, and f_{E0} as shown in Equation S2.11-S2.14. Since the short-lived species ES^* in Equation S2 emitted with a short decay time of 3.5 ns and disappeared rapidly after excitation, the contribution of the short-lived species was not included in the derivation of the molar fractions.

$$f_{diff} = \frac{1}{1 + (f_{Mk2}/f_{Mdiff}) + (f_{Mfree}/f_{Mdiff}) + (f_{EE0}/f_{Ediff})} \tag{S2.11}$$

$$f_{k2} = f_{diff} \frac{f_{Mk2}}{f_{Mdiff}} \tag{S2.12}$$

$$f_{free} = f_{diff} \frac{f_{Mfree}}{f_{Mdiff}} \tag{S2.13}$$

$$f_{E0} = f_{diff} \frac{f_{EE0}}{f_{Ediff}} \tag{S214}$$

S2B] Example of a fit of the fluorescence decays
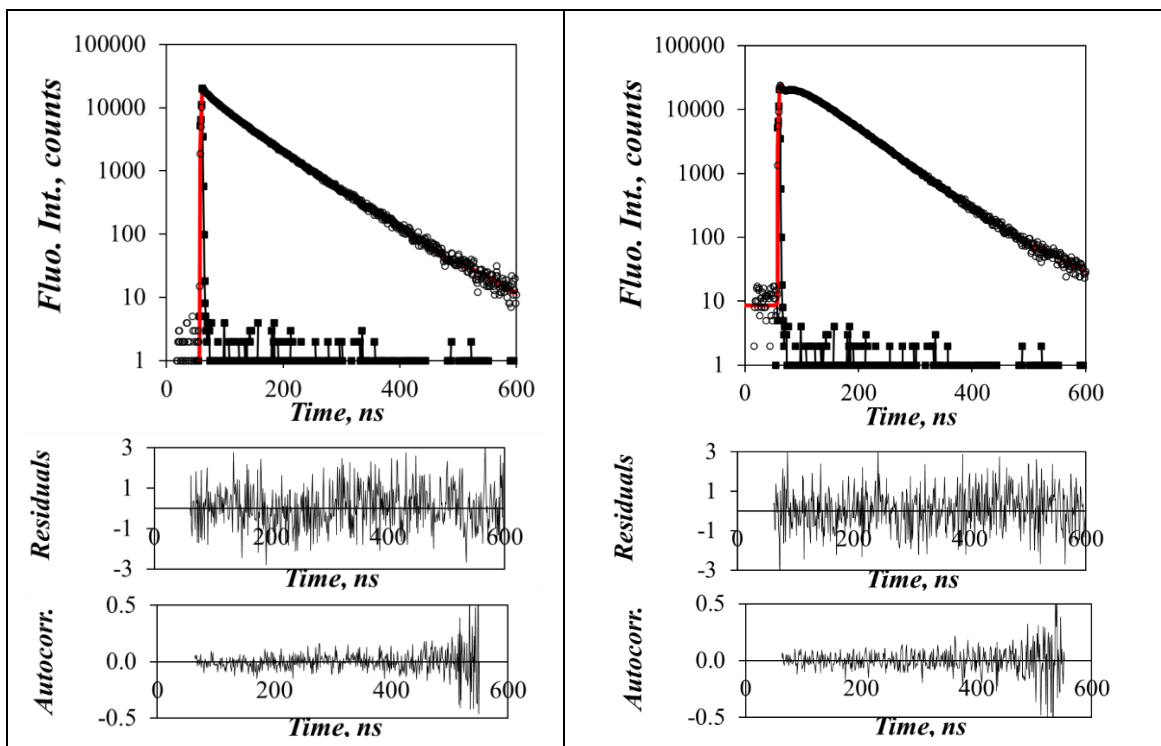
Figure S2.1. Example of the fit of the fluorescence decays of the pyrene monomer (left, λ_{em} = 375 nm) and excimer (right, λ_{em} = 510 nm) for Py(4.2)-Amylopectin labeled with 4.2 mol% of PyBA in DMSO. χ^2 = 1.16, λ_{ex} = 346 nm.

S2C] Plot of η as a function of mass concentration of amylopectin
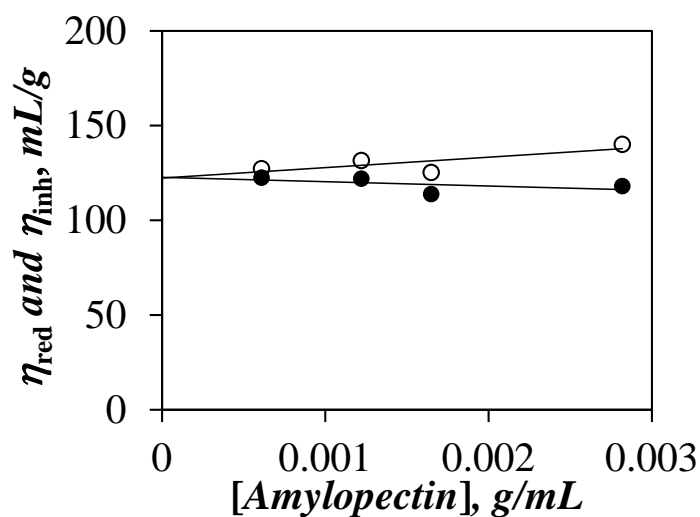
Figure S2.2. Plot of the (○) reduced and (●) inherent viscosity of amylopectin in DMSO at 25 °C as a function of amylopectin concentration.

220

S2D] Observation of a constant I_E/I_M ratio over a wide absorbance range for Py(6.7)-NAF(56)
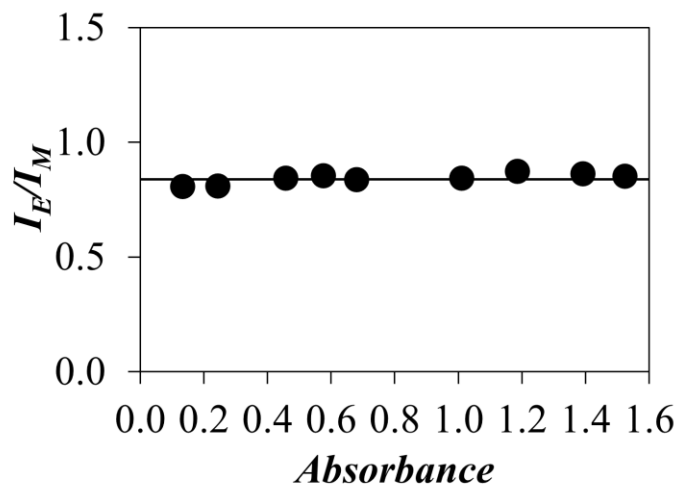
Figure S2.3. Plot of the I_E/I_M ratio as a function of absorbance for Py(6.7)-NAF(56) in DMSO.

S2E] List of parameters retrieved from the fluorescence decay analysis

Table S2.1. Parameters retrieved from the fluorescence decays of Py(0.004)-NAF(56) at different concentrations of NAF(56) and Py(0.004)-NAF(56) analyzeded with the biexponential function given in Equation S2.15.

$$[Py^*]_{(t)} = \alpha_1 \times \exp(-t/\tau_1) + \alpha_2 \times \exp(-t/\tau_2) \qquad \text{(S2.15)}$$

wt %	α_1	τ_1 (ns)	α_2	τ_2 (ns)	χ^2
0.1	0.14	20.3	0.86	100.1	1.13
1.2	0.15	25.9	0.85	99.5	1.11
4.3	0.13	31.6	0.87	100.8	1.08
4.4	0.15	25.9	0.85	100.4	1.09
8.3	0.15	23.5	0.85	100.7	1.02
8.4	0.14	27.8	0.86	100.9	1.17
13.6	0.15	23.6	0.85	102.9	1.08
15.2	0.15	24.6	0.85	103.8	1.11
16.3	0.14	22.3	0.86	105.2	1.09
21.9	0.15	23.3	0.85	110.5	1.14
23.0	0.15	29.3	0.85	109.5	1.20
42.3	0.17	26.5	0.83	126.9	1.06

Table S2.2. Parameters retrieved from the global FBM analysis of the monomer decays with the program *globmis90sbg-2* for Py(4.1)-Amylopectin and Py(6.6)-NAF(56) at different NAF(56) concentrations in DMSO with Equations S2.1 and S2.2.

Sample	wt %	f_{Mdiff}	f_{Mfree}	k_{blob} $(\times 10^7 \text{s}^{-1})$	$<n>$	f_{k2}	$k_e[blob]$ $(\times 10^6 \text{ s}^{-1})$	$\chi 2$
Py(4.1)-Amylopectin (220) $k_2=2.1\times10^8 \text{ s}^{-1}$	0.0	0.841	0.047	1.488	0.65	0.112	9.27	1.16
	0.1	0.835	0.062	1.547	0.71	0.104	10.42	1.11
	1.2	0.836	0.044	1.405	0.74	0.120	9.87	1.17
	4.9	0.825	0.050	1.092	0.82	0.125	10.92	1.13
	8.6	0.802	0.040	1.311	0.81	0.158	10.36	1.05
	11.8	0.785	0.041	1.250	0.88	0.175	10.81	1.07
	16.6	0.771	0.036	1.036	1.12	0.193	9.32	1.12
	19.9	0.751	0.040	0.917	1.24	0.210	8.45	1.17
	22.5	0.731	0.035	0.862	1.50	0.234	7.81	1.10
	26.0	0.724	0.072	0.893	1.45	0.204	7.09	1.21
	27.8	0.685	0.060	0.820	1.58	0.255	6.92	1.11
	30.8	0.681	0.074	0.766	1.78	0.245	6.79	1.22
	32.8	0.647	0.059	0.751	1.83	0.294	5.46	1.23
	34.5	0.673	0.081	0.784	1.89	0.247	6.67	1.09
	36.6	0.646	0.071	0.774	1.93	0.282	7.58	1.09
	*41.3	0.607	0.107	0.835	2.00	0.287	9.53	1.12
Py(6.6)-NAF(56) $k_2=2.0\times10^8 \text{ s}^{-1}$	0.0	0.826	0.006	1.327	1.10	0.168	9.89	1.17
	0.1	0.821	0.003	1.345	1.11	0.176	10.03	1.21
	0.5	0.817	0.014	1.374	1.10	0.170	10.22	1.25
	1.3	0.805	0.007	1.249	1.17	0.189	9.45	1.19
	1.9	0.799	0.012	1.292	1.16	0.190	9.85	1.10
	2.2	0.800	0.007	1.259	1.18	0.193	9.75	1.14
	6.2	0.769	0.000	1.185	1.22	0.231	8.98	1.08
	10.3	0.748	0.004	1.162	1.30	0.248	9.30	1.11
	10.8	0.763	0.007	1.224	1.29	0.230	9.22	1.23
	12.6	0.773	0.004	1.181	1.34	0.222	9.07	1.12
	14.7	0.742	0.005	1.095	1.49	0.253	8.49	1.12
	14.8	0.733	0.004	1.090	1.51	0.263	8.37	1.10
	17.5	0.719	0.003	0.919	1.85	0.279	6.73	1.18
	19.5	0.703	0.005	0.892	2.08	0.292	6.50	1.14
	20.7	0.677	0.008	0.852	2.22	0.315	6.26	1.16
	21.7	0.674	0.002	0.847	2.27	0.324	5.61	1.11
	24.3	0.672	0.009	0.819	2.41	0.319	5.05	1.13
	27.1	0.669	0.013	0.749	2.63	0.318	5.73	1.14
	28.9	0.668	0.011	0.783	2.67	0.321	3.55	1.09
	36.0	0.633	0.012	0.792	2.75	0.355	3.70	1.05

*The decay was fitted with *globmis90obg-2*.

Table S2.3. Parameters retrieved from the global FBM analysisof the monomer decays with the program *globmis90sbg-2* for Py(5.8)-NAF(20) and Py(5.8)-NAF(8) at different NAF(56) concentrations in DMSO with Equations S2.1 and S2.2.

Sample	wt %	f_{Mdiff}	f_{Mfree}	k_{blob} $(\times 10^7 s^{-1})$	$<n>$	f_{k2}	$k_e[blob]$ $(\times 10^6 s\text{-}1)$	$\chi 2$
Py(5.7)-NAF(20) $k_2=1.8\times10^8$ s $^{-1}$	0.0	0.815	0.014	1.204	1.04	0.172	9.66	1.14
	0.1	0.834	0.006	1.237	1.05	0.160	9.35	1.16
	1.2	0.814	0.016	1.315	1.02	0.170	10.06	1.10
	5.0	0.808	0.013	1.282	1.03	0.179	9.99	1.06
	8.6	0.780	0.014	1.130	1.14	0.205	9.65	1.14
	11.9	0.779	0.014	1.086	1.22	0.207	9.13	1.16
	16.8	0.752	0.010	0.959	1.38	0.238	7.46	1.18
	20.2	0.741	0.019	0.974	1.44	0.240	7.45	1.00
	22.4	0.727	0.016	0.950	1.53	0.257	6.30	1.17
	23.9	0.697	0.034	1.006	1.57	0.269	6.66	1.25
	27.8	0.687	0.031	0.975	1.66	0.282	5.49	1.16
	29.2	0.704	0.011	0.945	1.61	0.285	4.44	1.15
	32.2	0.687	0.020	1.038	1.58	0.282	5.06	1.16
	33.5	0.688	0.020	0.983	1.66	0.292	3.90	1.18
	37.2	0.704	0.027	0.971	1.66	0.268	5.66	1.28
Py(5.8)-NAF(8) $k_2=2.0\times10^8$ s $^{-1}$	0.1	0.802	0.041	1.335	1.01	0.156	9.33	1.29
	0.9	0.801	0.030	1.441	0.96	0.169	9.57	1.21
	4.8	0.780	0.032	1.353	0.97	0.188	9.49	1.17
	9.5	0.752	0.031	1.289	1.03	0.217	9.19	1.18
	12.9	0.735	0.026	1.131	1.15	0.239	8.32	1.22
	16.6	0.735	0.034	1.168	1.19	0.231	9.00	1.10
	19.9	0.735	0.033	1.177	1.23	0.232	9.18	1.14
	22.5	0.702	0.036	1.070	1.29	0.262	7.79	1.12
	26.2	0.688	0.073	1.173	1.19	0.239	8.54	1.29
	24.2	0.692	0.050	1.189	1.22	0.258	7.77	1.10
	31.1	0.682	0.042	1.090	1.26	0.276	6.46	1.22
	33.6	0.687	0.039	1.018	1.36	0.274	6.08	1.25
	34.8	0.665	0.042	1.069	1.32	0.292	5.47	1.17
	37.2	0.596	0.058	0.934	1.45	0.346	5.69	1.22

Table S2.4. Parameters retrieved from the global FBM analysis with the program *globmis90sbg-2* for the excimer decays of Py(4.1)-Amylopectin and Py(6.6)-NAF(56) at different NAF(56) concentrations in DMSO with Equations S1 and S2. τ_{ES} was fixed at 3.5 ns in the analysis.

Samples	wt %	τ_{E0} (ns)	τ_D (ns)	$f_{Ediff, E0}$	$f_{Ediff, D}$	f_{Ek2}	$f_{EE0, E0}$	$f_{EE0, D}$	f_{ES}	χ^2
Py(4.1)-Amylopectin (220) $k_2=2.1\times10^8$ s^{-1}	0.0	50.4		0.662		0.088	0.093		0.157	1.16
	0.1	49.3		0.632		0.079	0.105		0.184	1.11
	1.2	48.5		0.625		0.089	0.090		0.196	1.17
	4.9	48.5		0.604		0.092	0.087		0.218	1.13
	8.6	47.8		0.576		0.114	0.060		0.250	1.05
	11.8	47.5		0.553		0.123	0.051		0.273	1.07
	16.6	47.5		0.514		0.129	0.048		0.309	1.12
	19.9	48.3		0.499		0.139	0.034		0.327	1.17
	22.5	48.2		0.458		0.147	0.036		0.360	1.10
	26.0	51.7		0.450		0.127	0.072		0.351	1.21
	27.8	50.9		0.416		0.155	0.030		0.399	1.11
	30.8	51.9		0.403		0.145	0.058		0.394	1.22
	32.8	51.5		0.371		0.168	0.017		0.444	1.23
	34.5	52.7		0.383		0.140	0.083		0.394	1.09
	36.6	52.1		0.353		0.154	0.050		0.443	1.09
	*41.3	50.6	100.0	0.045	0.007	0.151	0.010	0.309	0.477	1.12
Py(6.6)-NAF(56) $k_2=2.0\times10^8$ s^{-1}	0.0	46.5		0.654		0.133	0.111		0.101	1.17
	0.1	46.3		0.648		0.139	0.105		0.109	1.21
	0.5	46.5		0.645		0.134	0.117		0.104	1.25
	1.3	46.3		0.634		0.148	0.092		0.126	1.19
	1.9	46.0		0.629		0.149	0.095		0.127	1.10
	2.2	46.3		0.626		0.151	0.093		0.130	1.14
	6.2	46.2		0.582		0.175	0.055		0.189	1.08
	10.3	46.8		0.569		0.182	0.048		0.220	1.11
	10.8	47.0		0.554		0.167	0.067		0.213	1.23
	12.6	47.1		0.553		0.159	0.081		0.208	1.12
	14.7	47.3		0.521		0.177	0.058		0.243	1.12
	14.8	47.4		0.511		0.183	0.050		0.256	1.10
	17.5	47.2		0.482		0.187	0.052		0.279	1.18
	19.5	48.0		0.459		0.191	0.061		0.289	1.14
	20.7	47.7		0.436		0.203	0.045		0.316	1.16
	21.7	47.9		0.425		0.204	0.044		0.327	1.11
	24.3	48.8		0.409		0.194	0.059		0.338	1.13
	27.1	49.5		0.413		0.196	0.074		0.316	1.14
	28.9	50.1		0.384		0.184	0.070		0.362	1.09
	36.0	51.1		0.327		0.184	0.078		0.411	1.05

*The decay was fitted with *globmis90obg-2*.

Table S2.5. Parameters retrieved from the global FBM analysis with the program *globmis90sbg-2* for the excimer decays of Py(5.7)-NAF(20) and Py(5.8)-NAF(8) at different NAF(56) concentrations in DMSO with Equations S2.1 and S2.2. τ_{ES} was fixed at 3.5 ns in the analysis.

Samples	*wt* %	τ_{E0} (ns)	f_{Ediff}	f_{Ek2}	f_{EE0}	f_{ES}	χ^2
Py(5.7)-NAF(20) $k_2{=}1.8{\times}10^8\,\mathrm{s}^{-1}$	0.0	45.3	0.659	0.139	0.092	0.110	1.14
	0.1	45.5	0.663	0.127	0.114	0.096	1.16
	1.2	45.9	0.641	0.134	0.104	0.120	1.10
	5.0	45.8	0.623	0.138	0.094	0.145	1.06
	8.6	45.1	0.591	0.156	0.066	0.187	1.14
	11.9	45.8	0.572	0.153	0.072	0.202	1.16
	16.8	46.3	0.535	0.169	0.048	0.247	1.18
	20.2	47.0	0.512	0.166	0.054	0.268	1.00
	22.4	47.7	0.484	0.172	0.047	0.297	1.17
	23.9	48.4	0.452	0.174	0.047	0.327	1.25
	27.8	49.4	0.433	0.177	0.050	0.340	1.16
	29.2	49.3	0.421	0.171	0.046	0.363	1.15
	32.2	60.7	0.400	0.162	0.062	0.376	1.16
	33.5	50.8	0.386	0.164	0.061	0.389	1.18
	37.2	49.0	0.436	0.166	0.061	0.338	1.28
Py(5.8)-NAF(8) $k_2{=}2.0{\times}10^8\,\mathrm{s}^{-1}$	0.1	47.3	0.573	0.112	0.118	0.197	1.29
	0.9	47.6	0.562	0.119	0.109	0.210	1.21
	4.8	46.6	0.542	0.130	0.084	0.243	1.17
	9.5	46.7	0.504	0.145	0.065	0.285	1.18
	12.9	46.4	0.481	0.156	0.054	0.309	1.22
	16.6	46.1	0.467	0.147	0.061	0.327	1.10
	19.9	46.3	0.457	0.144	0.066	0.333	1.14
	22.5	47.4	0.432	0.161	0.042	0.365	1.12
	26.2	51.8	0.434	0.151	0.081	0.340	1.29
	24.2	49.3	0.404	0.151	0.047	0.398	1.10
	31.1	50.0	0.384	0.155	0.036	0.424	1.22
	33.6	49.8	0.368	0.147	0.043	0.442	1.25
	34.8	51.5	0.358	0.157	0.040	0.444	1.17
	37.2	52.4	0.310	0.180	0.007	0.502	1.22

Table S2.6. Molar fractions of the pyrene species of Py(4.1)-Amylopectin(220) and Py(6.6)-NAF(56) at different NAF(56) concentrations in DMSO calculated from f_{Mfree}, f_{Mdiff}, f_{Ediff}, f_{k2} and f_{E0}.

Samples	wt %	f_{diff}	f_{k2}	f_{free}	f_{E0}
Py(4.1)-Amylopectin (220) $k_2=2.1\times10^8\,s^{-1}$	0.0	0.753	0.100	0.042	0.105
	0.1	0.733	0.091	0.054	0.122
	1.2	0.747	0.107	0.039	0.107
	4.9	0.737	0.112	0.045	0.106
	8.6	0.740	0.146	0.037	0.077
	11.8	0.731	0.163	0.038	0.068
	16.6	0.719	0.180	0.034	0.067
	19.9	0.714	0.199	0.038	0.049
	22.5	0.691	0.221	0.034	0.054
	26.0	0.649	0.183	0.065	0.103
	27.8	0.653	0.243	0.057	0.047
	30.8	0.620	0.223	0.068	0.089
	32.8	0.628	0.285	0.057	0.029
	34.5	0.587	0.215	0.070	0.128
	36.6	0.592	0.258	0.065	0.084
	41.3	0.551	0.261	0.097	0.092
Py(6.6)-NAF(56) $k_2=2.0\times10^8\,s^{-1}$	0.0	0.724	0.147	0.005	0.123
	0.1	0.725	0.155	0.003	0.117
	0.5	0.711	0.148	0.012	0.129
	1.3	0.721	0.169	0.006	0.104
	1.9	0.713	0.169	0.010	0.108
	2.2	0.715	0.172	0.006	0.107
	6.2	0.717	0.215	0.000	0.067
	10.3	0.703	0.233	0.004	0.060
	10.8	0.699	0.210	0.006	0.084
	12.6	0.695	0.200	0.004	0.101
	14.7	0.685	0.233	0.005	0.077
	14.8	0.684	0.245	0.004	0.068
	17.5	0.667	0.259	0.003	0.072
	19.5	0.643	0.267	0.005	0.086
	20.7	0.633	0.295	0.008	0.065
	21.7	0.630	0.302	0.002	0.066
	24.3	0.613	0.290	0.008	0.089
	27.1	0.597	0.284	0.012	0.108
	28.9	0.595	0.286	0.010	0.109
	36.0	0.550	0.308	0.010	0.132

Table S2.7. Molar fractions of the pyrene species of Py(5.7)-NAF(20) and Py(5.8)-NAF(8) at different NAF(56) concentrations in DMSO calculated from f_{Mfree}, f_{Mdiff}, f_{Ediff}, f_{k2} and f_{E0}.

Sample	wt %	f_{diff}	f_{k2}	f_{free}	f_{E0}
Py(5.7)-NAF(20) $k_2{=}1.8{\times}10^8\,\mathrm{s}^{-1}$	0.0	0.732	0.154	0.012	0.102
	0.1	0.730	0.140	0.005	0.125
	1.2	0.719	0.150	0.014	0.117
	5.0	0.720	0.160	0.012	0.108
	8.6	0.717	0.189	0.013	0.080
	11.9	0.709	0.189	0.013	0.090
	16.8	0.704	0.223	0.009	0.064
	20.2	0.687	0.222	0.018	0.072
	22.4	0.679	0.241	0.015	0.065
	23.9	0.650	0.251	0.032	0.067
	27.8	0.637	0.261	0.029	0.074
	29.2	0.653	0.265	0.010	0.071
	32.2	0.626	0.257	0.019	0.098
	33.5	0.620	0.264	0.018	0.098
	37.2	0.641	0.244	0.025	0.089
Py(5.7)-NAF(8) $k_2{=}2.0{\times}10^8\,\mathrm{s}^{-1}$	0.1	0.689	0.134	0.036	0.141
	0.9	0.693	0.146	0.026	0.135
	4.8	0.696	0.167	0.028	0.108
	9.5	0.685	0.197	0.029	0.088
	12.9	0.679	0.220	0.024	0.077
	16.6	0.670	0.211	0.031	0.088
	19.9	0.665	0.210	0.030	0.096
	22.5	0.657	0.245	0.034	0.063
	26.2	0.610	0.212	0.065	0.114
	24.2	0.640	0.238	0.047	0.075
	31.1	0.641	0.259	0.039	0.060
	33.6	0.637	0.254	0.036	0.074
	34.8	0.619	0.272	0.039	0.070
	37.2	0.588	0.341	0.057	0.013

Table S2.8. Parameters retrieved from the global FBM analysis with the program *globmis90sbg-2* for the monomer decays of Py(6.6)-NAF(56) at different Py(6.6)-NAF(56) concentrations in DMSO with Equations S2.1 and S2.2.

Sample	wt %	τ_M (ns)	f_{Mdiff}	f_{Mfree}	k_{blob} ($\times 10^7 s^{-1}$)	$\langle n \rangle$	f_{k2}	$k_e[blob]$ ($\times 10^6 s\text{-}1$)	$\chi2$
Py(6.6)-NAF(56) $k_2=2.0\times10^8$ s^{-1}	0.1	100.2	0.824	0.020	1.560	1.07	0.157	11.00	1.17
	0.7	100.1	0.812	0.004	1.384	1.06	0.184	9.91	1.20
	3.0	100.0	0.769	0.002	1.480	1.04	0.229	7.40	1.28
	4.2	100.0	0.774	0.007	1.419	1.09	0.219	14.19	1.14
	6.1	100.3	0.777	0.002	1.488	1.12	0.221	8.84	1.17
	6.5	100.4	0.783	0.006	1.421	1.08	0.211	7.81	1.02
	11.3	102.1	0.622	0.000	1.015	1.65	0.378	6.41	1.15
	11.3	102.2	0.725	0.000	1.047	1.52	0.275	5.97	1.28
	14.8	104.0	0.751	0.000	1.078	1.95	0.249	8.09	1.18
	21.1	108.6	0.768	0.001	0.677	2.76	0.231	7.99	1.15
	*36.1	121.9	0.592	0.000	0.876	2.86	0.408	5.30	1.14

*The decay was fitted with *globmis90obg-2*.

Table S2.8. Parameters retrieved from the global FBM analysis with the program *globmis90sbg-2* for the excimer decays of Py(6.6)-NAF(56) at different Py(6.6)-NAF(56) concentrations in DMSO with Equations S2.1 and S2.2. τ_{ES} was fixed at 3.5 ns in the analysis.

Sample	wt %	τ_{E0} (ns)	τ_{EL} (ns)	$f_{Ediff, E0}$	$f_{Ediff, D}$	f_{Ek2}	$f_{EE0, E0}$	$f_{EE0, D}$	f_{ES}	$\chi2$
Py(6.6)-NAF(56) $k_2=2.0\times10^8$ s^{-1}	0.1	47.6		0.667		0.127	0.152		0.055	1.17
	0.7	48.2		0.651		0.147	0.135		0.067	1.20
	3.0	53.0		0.589		0.175	0.138		0.099	1.28
	4.2	51.7		0.592		0.168	0.136		0.104	1.14
	6.1	51.4		0.585		0.167	0.133		0.115	1.17
	6.5	51.4		0.624		0.168	0.122		0.087	1.02
	11.3	51.1		0.470		0.286	0.007		0.236	1.15
	11.3	53.6		0.560		0.212	0.128		0.099	1.28
	14.8	49.9		0.515		0.171	0.217		0.096	1.18
	21.1	48.7		0.531		0.160	0.309		0.000	1.26
	*36.1	46.5	69.8	0.247	0.173	0.169	0.079	0.166	0.166	1.14

*The decay was fitted with *globmis90obg-2*.

Table S2.9. Molar fractions of the pyrene species of Py(6.6)-NAF(20) at different Py(6.6)-NAF(56) concentrations in DMSO calculated from f_{Mfree}, f_{Mdiff}, f_{Ediff}, f_{k2} and f_{E0}.

Sample	wt %	f_{diff}	f_{k2}	f_{free}	f_{E0}
Py(6.6)-NAF(56) $k_2 = 2.0 \times 10^8 \, s^{-1}$	0.1	0.694	0.132	0.016	0.158
	0.7	0.695	0.157	0.004	0.144
	3.0	0.652	0.194	0.002	0.153
	4.2	0.657	0.186	0.006	0.151
	6.1	0.660	0.188	0.002	0.150
	6.5	0.679	0.183	0.005	0.133
	11.3	0.616	0.375	0.000	0.009
	11.3	0.622	0.236	0.000	0.142
	14.8	0.570	0.189	0.000	0.240
	21.1	0.530	0.160	0.001	0.309
	36.1	0.294	0.202	0.000	0.504

S2F] *Number of overlapping carbons and ΔN_{blob} values retrieved from MMOs*

Table S2.10. Number of overlapping carbons between the reference pyrene attached on Helix #0 with an angle $\varphi = 30°$ and the secondary pyrene attached on Helix 2 at $\theta = 60°$ for d_{h-h} values ranging from 3.4 nm to 1.6 nm with the total number of AGUs (ΔN_{blob}) allowing a good pyrene overlap with 7 or more carbon atoms.

d_{h-h}, nm / Position	1.6 nm	1.8 nm	2.4 nm	2.5 nm	2.6 nm	2.7 nm	2.8 nm	2.9 nm	3.0 nm	3.1 nm	3.2 nm	3.3 nm	3.4 nm
-18	0	0	0	0	0	0	0	0	0	0	0	0	0
-17	0	0	0	0	0	0	0	0	0	0	0	0	0
-16	0	0	0	0	0	0	0	0	0	0	0	0	0
-15	0	0	0	0	0	0	0	0	0	0	0	0	0
-14	0	0	0	0	0	0	0	0	0	0	0	0	0
-13	0	0	0	0	0	0	0	0	0	0	0	0	0
-12	≥ 7	7	7	0	6	5	5	0	0	0	0	0	0
-11	≥ 7	≥ 7	≥ 7	≥ 7	≥ 7	≥ 7	8	≥ 7	8	6	0	0	0
-10	≥ 7	≥ 7	≥ 7	≥ 7	8	7	6	0	0	0	0	0	0
-9	0	0	0	0	0	0	0	0	0	0	0	0	0
-8	0	0	0	0	0	0	0	0	0	0	0	0	0
-7	0	0	0	0	0	0	0	0	0	0	0	0	0
-6	0	0	0	0	0	0	0	0	0	0	0	0	0
-5	≥ 7	≥ 7	≥ 7	≥ 7	≥ 7	≥ 7	7	≥ 7	7	0	0	0	0
-4	≥ 7	≥ 7	≥ 7	≥ 7	≥ 7	≥ 7	8	≥ 7	≥ 7	8	7	5	0
-3	≥ 7	≥ 7	≥ 7	≥ 7	≥ 7	≥ 7	8	≥ 7	≥ 7	7	7	6	0
-2	≥ 7	8	8	8	6	4	4	0	0	0	0	0	0
-1	0	0	0	0	0	0	0	0	0	0	0	0	0
0	0	0	0	0	0	0	0	0	0	0	0	0	0
+1	0	0	0	0	0	0	0	0	0	0	0	0	0
+2	≥ 7	≥ 7	≥ 7	≥ 7	≥ 7	≥ 7	7	6	5	0	0	0	0
+3	≥ 7	≥ 7	≥ 7	≥ 7	≥ 7	≥ 7	8	≥ 7	≥ 7	7	7	0	0
+4	≥ 7	≥ 7	≥ 7	≥ 7	≥ 7	≥ 7	10	8	5	6	0	0	0
+5	≥ 7	≥ 7	≥ 7	≥ 7	7	4	4	0	0	0	0	0	0
+6	0	0	0	0	0	0	0	0	0	0	0	0	0
+7	0	0	0	0	0	0	0	0	0	0	0	0	0
+8	0	0	0	0	0	0	0	0	0	0	0	0	0
+9	≥ 7	≥ 7	≥ 7	≥ 7	7	5	5	0	0	0	0	0	0
+10	≥ 7	≥ 7	≥ 7	≥ 7	≥ 7	≥ 7	8	≥ 7	≥ 7	7	0	8	0
+11	≥ 7	7	7	7	0	0	0	0	0	0	0	0	0
+12	0	0	0	0	0	0	0	0	0	0	0	0	0
+13	0	0	0	0	0	0	0	0	0	0	0	0	0
+14	0	0	0	0	0	0	0	0	0	0	0	0	0
+15	0	0	0	0	0	0	0	0	0	0	0	0	0
+16	0	0	0	0	0	0	0	0	0	0	0	0	0
+17	0	0	0	0	0	0	0	0	0	0	0	0	0

$N_{blob, 30}$	14	14	14	13	11	9	8	7	6	4	3	1	0

* The AGUs with $\geq$ were counted toward N_{blob} without conducting the MMO, because the pyrenyls attached at the same positions had been shown to generate a good overlap even at a larger distance.

Table S2.11. Number of overlapping carbons between the reference pyrene attached on Helix #0 with an angle $\varphi = 30°$ and the secondary pyrene attached on Helix 3 at $\theta = 120°$ for d_{h-h} values ranging from 3.4 nm to 1.6 nm with the total number of AGUs (ΔN_{blob}) allowing a good pyrene overlap with 7 or more carbon atoms.

d_{h-h}, nm / Position	1.6 nm	1.8 nm	2.5 nm	2.6 nm	2.7 nm	2.8 nm	2.9 nm	3.0 nm	3.1 nm	3.2 nm	3.3 nm	3.4 nm
-15	0	0	0	0	0	0	0	0	0	0	0	0
-14	0	0	0	0	0	0	0	0	0	0	0	0
-13	0	0	0	0	0	0	0	0	0	0	0	0
-12	0	0	0	0	0	0	0	0	0	0	0	0
-11	0	0	0	0	0	0	0	0	0	0	0	0
-10	0	0	0	0	0	0	0	0	0	0	0	0
-9	≥ 7	≥ 7	≥ 7	≥ 7	≥ 7	7	8	7	4	0	0	0
-8	≥ 7	8	7	5	4	4	0	0	0	0	0	0
-7	0	0	0	0	0	0	0	0	0	0	0	0
-6	0	0	0	0	0	0	0	0	0	0	0	0
-5	0	0	0	0	0	0	0	0	0	0	0	0
-4	0	0	0	0	0	0	0	0	0	0	0	0
-3	≥ 7	≥ 7	≥ 7	≥ 7	≥ 7	9	≥ 7	7	5	0	0	0
-2	≥ 7	≥ 7	≥ 7	≥ 7	≥ 7	8	≥ 7	≥ 7	7	6	0	0
-1	≥ 7	≥ 7	≥ 7	≥ 7	≥ 7	7	7	6	5	0	0	0
0	0	0	0	0	0	0	0	0	0	0	0	0
+1	0	0	0	0	0	0	0	0	0	0	0	0
+2	0	0	0	0	0	0	0	0	0	0	0	0
+3	0	0	0	0	0	0	0	0	0	0	0	0
+4	≥ 7	≥ 7	≥ 7	≥ 7	≥ 7	7	≥ 7	7	4	0	0	0
+5	≥ 7	≥ 7	≥ 7	≥ 7	≥ 7	8	≥ 7	≥ 7	7	8	0	0
+6	≥ 7	≥ 7	≥ 7	7	7	3	0	0	0	0	0	0
+7	0	0	0	0	0	0	0	0	0	0	0	0
+8	0	0	0	0	0	0	0	0	0	0	0	0
+9	0	0	0	0	0	0	0	0	0	0	0	0
+10	0	0	0	0	0	0	0	0	0	0	0	0
+11	≥ 7	≥ 7	≥ 7	≥ 7	≥ 7	8	5	4	0	0	0	0
+12	≥ 7	≥ 7	≥ 7	≥ 7	≥ 7	7	≥ 7	7	4	0	0	0
+13	0	0	0	0	0	0	0	0	0	0	0	0
+14	0	0	0	0	0	0	0	0	0	0	0	0

+15	0	0	0	0	0	0	0	0	0	0	0	0
+16	0	0	0	0	0	0	0	0	0	0	0	0
+17	0	0	0	0	0	0	0	0	0	0	0	0
+18	0	0	0	0	0	0	0	0	0	0	0	0
$N_{blob, 90}$	10	10	10	9	9	8	7	6	2	1	0	0

* The AGUs with ≥ were counted toward N_{blob} without conducting an MMO because the pyrenyl

labels at the same positions had been shown to generate a good overalp even at a larger distance.

S3- Appendices for Chapter 3

A] Equations for the global analysis of the fluorescence decays according to the fluorescence blob model and equations for the molar fractions of the different pyrene species

Equation S3.1 and S3.2 were applied to fit the monomer and excimer fluorescence decays of the Py-Glycogen(O/C) constructs in DMSO, respectively.

$$[Py^*]_{(t)} = [Py^*_{diff}]_{(t)} + [Py^*_{k2}]_{(t)} + [Py^*_{free}]_{(t)}$$

$$= [Py^*_{diff}]_0 \exp\left(-\left(A_2 + \frac{1}{\tau_M}\right)t - A_3\left(1 - \exp(-A_4 t)\right)\right)$$

$$+ \left([Py^*_{k2}]_o + [Py^*_{diff}]_o e^{-A_3} \sum_{i=0}^{\infty} \frac{A_3^i}{i!} \frac{A_2 + iA_4}{A_2 + iA_4 - k_2}\right) \exp\left(-\left(k_2 + \frac{1}{\tau_M}\right)t\right)$$

$$-[Py^*_{diff}]_o e^{-A_3} \sum_{i=0}^{\infty} \frac{A_3^i}{i!} \frac{A_2 + iA_4}{A_2 + iA_4 - k_2} \exp\left(-\left(A_2 + iA_4 + \frac{1}{\tau_M}\right)t\right) + [Py^*_{free}]_o \exp(-t/\tau_M) \qquad (S3.1)$$

$$[E^*]_{(t)} = [E0^*]_{(t)} + [ES^*]_{(t)}$$

$$= k_2 \left([Py^*_{k2}]_o + [Py^*_{diff}]_o e^{-A_3} \sum_{i=0}^{\infty} \frac{A_3^i}{i!} \frac{A_2 + iA_4}{A_2 + iA_4 - k_2}\right) \times \frac{\exp\left(-\frac{t}{\tau_{E0}}\right) - \exp\left(-\left(k_2 + \frac{1}{\tau_M}\right)t\right)}{k_2 + \frac{1}{\tau_M} - \frac{1}{\tau_{E0}}}$$

$$+ [Py^*_{diff}]_o e^{-A_3} \sum_{i=0}^{\infty} \frac{A_3^i}{i!} \frac{A_2 + iA_4}{A_2 + iA_4 - k_2} \frac{\exp\left(-\left(A_2 + iA_4 + \frac{1}{\tau_M}\right)t\right) - \exp\left(-\frac{t}{\tau_{E0}}\right)}{A_2 + iA_4 + \frac{1}{\tau_M} - \frac{1}{\tau_{E0}}}$$

$$+[E0^*]_o \exp\left(-\frac{t}{\tau_{E0}}\right) + [ES^*]_o \exp\left(-\frac{t}{\tau_{ES}}\right)$$ (S3.2)

The parameters A_2, A_3, and A_4 used in Equations S3.1 and S3.2 are given in Equation S3.3. The parameters $<n>$ and k_{blob} were defined in the main text. $k_e \times [blob]$ is the product of the exchange rate constant k_e of the ground-state pyrenes between *blobs* and the local *blob* concentration [*blob*] inside the macromolecule.

$$A_2 = \langle n \rangle \frac{k_{blob} k_e [blob]}{k_{blob} + k_e[blob]}$$ (S3.3.a)

$$A_3 = \langle n \rangle \left(\frac{k_{blob}}{k_{blob} + k_e[blob]}\right)^2$$ (S3.3b)

$$A_4 = k_{blob} + k_e[blob]$$ (S3.3C)

The information about the molar fractions of the different pyrene species in solution can be retrieved from the pre-exponential factors in Equations S3.1 and S3.2. Equation S1 yields the molar factions of the pyrene species, that contribute to the monomer decays and their expression for each species is given in Equations S3.4 – S3.6.

$$f_{Mdiff} = \frac{[Py_{diff}^*]_o}{[Py_{diff}^*]_o + [Py_{k2}^*]_o + [Py_{free}^*]_o}$$ (S3.4)

$$f_{Mk2} = \frac{[Py_{k2}^*]_o}{[Py_{diff}^*]_o + [Py_{k2}^*]_o + [Py_{free}^*]_o}$$ (S3.5)

$$f_{Mfree} = \frac{[Py_{free}^*]_o}{[Py_{diff}^*]_o + [Py_{k2}^*]_o + [Py_{free}^*]_o}$$ (S3.6)

Similarly, the pre-exponential factors obtained from Equation S3.2 yield the molar fractions of the pyrene species, that contribute to the excimer decay. The expressions of the molar fractions of the pyrene species, that are detected in the excimer decays are provided in Equations S3.7-S3.10.

$$f_{Ediff} = \frac{[Py_{diff}^*]_o}{[Py_{diff}^*]_o + [Py_{k2}^*]_o + [E0^*]_o + [ES^*]_o}$$ (S3.7)

$$f_{Ek2} = \frac{[Py_{k2}^*]_o}{[Py_{diff}^*]_o + [Py_{k2}^*]_o + [E0^*]_o + [ES^*]_o} \tag{S8}$$

$$f_{EES} = \frac{[ES^*]_o}{[Py_{diff}^*]_o + [Py_{k2}^*]_o + [E0^*]_o + [ES^*]_o} \tag{S9}$$

$$f_{EE0} = \frac{[E0^*]_o}{[Py_{diff}^*]_o + [Py_{k2}^*]_o + [E0^*]_o + [ES^*]_o} \tag{S10}$$

B] Example of fits of the fluorescence decays of Py-Glycogen(O) in DMSO with Equations S1 and S2
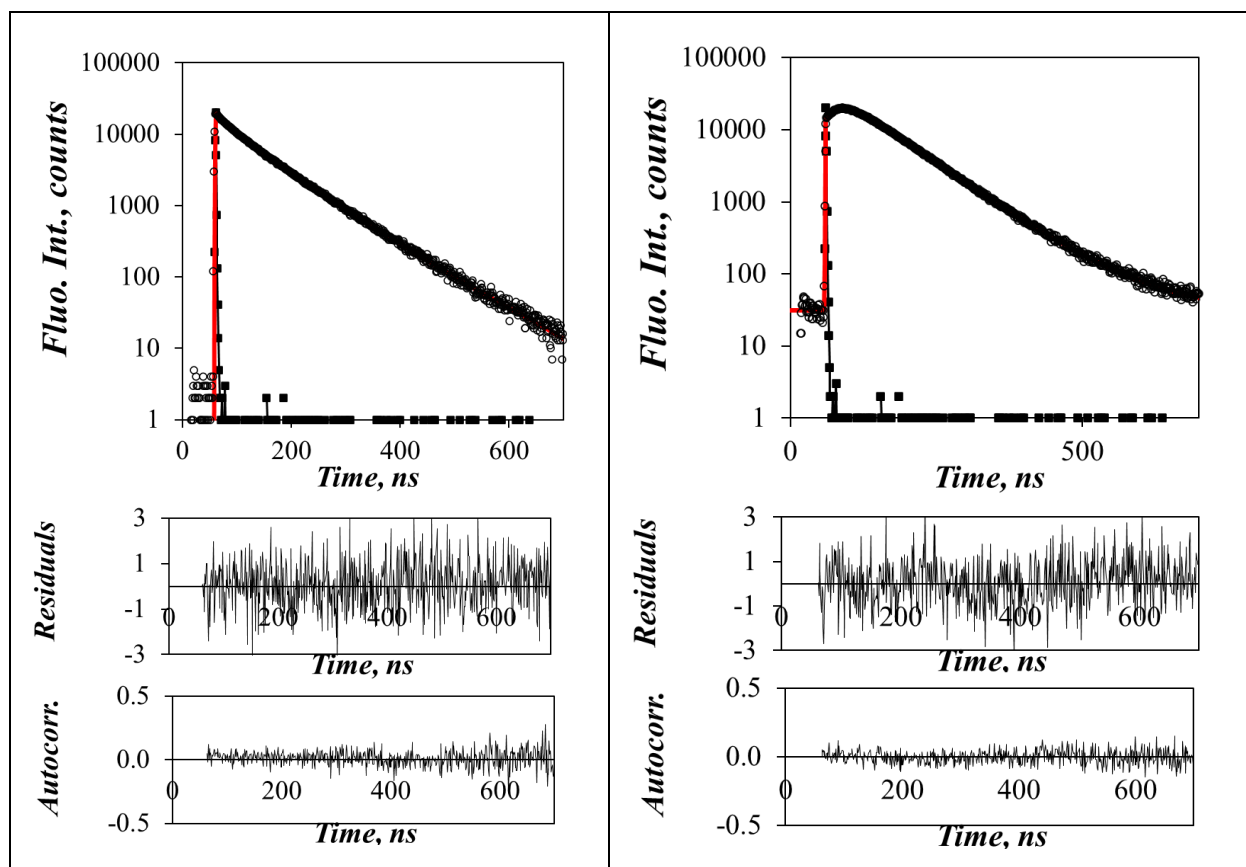
Figure S3.1. Monomer (left, λ_{em} = 375 nm) and excimer (right, λ_{em} = 510 nm) fluorescence decays of Py(2.1)-Glycogen(O) in DMSO. The decays were analyzed globally using Equations S1 and S2; [Py] = 2.5×10^{-6} M, λ_{ex} = 346 nm, χ^2 = 1.17

C] Determination of $[\eta]$ for glycogen from oyster and corn
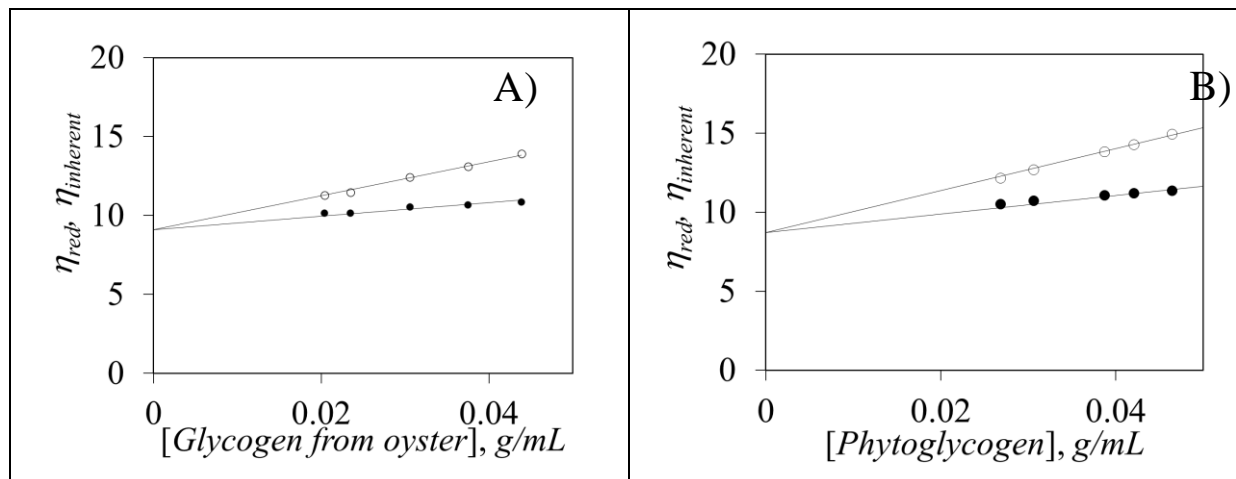
Figure S3.2. Plots of the (○) reduced and (●) inherent viscosity of A) glycogen from oyster and B) glycogen from corn as a function of glycogen concentration.

D] Calculation of $d_{\text{h-h}}$ from the experimentally determined M_n and $[\eta]$

The surface area ($S_{\text{tier}}(t)$) of an oligosaccharide helix in a given tier (t) is given in Equation S3.11 as a function of the tier radius ($R(t) = t \times tt$, where tt is the tier thickness given in Equation 3.5) and the number of tiers (t). t can be determined from the experimentally determined M_n, $[\eta]$, or R_h for a glycogen particle as shown in Table 3.1.

$$S_{tier}(t) = \frac{4\pi R(t)^2}{2^t - 2^{t-1}} \tag{S3.11}$$

The surface area of an oligosaccharide helix located in an array of hexagonally packed helices is given by Equation (S12), where the term $d_{\text{h-h}}$ is the interhelical distance.

$$S = \frac{\sqrt{3}}{2} d_{h-h}^2 \tag{S3.12}$$

Equating $S_{\text{tier}}(t)$ in Equation S3.11 with S in Equation S3.12 enables one to determine $d_{\text{h-h}}$ as a function of $R(t)$ and t, as shown in Equation S3.13.

$$d_{h-h} = \sqrt{\frac{8\pi R(t)^2}{\sqrt{3} \times (2^t - 2^{t-1})}} \tag{S3.13}$$

E] the M_n and ρ of Phytoglycogen
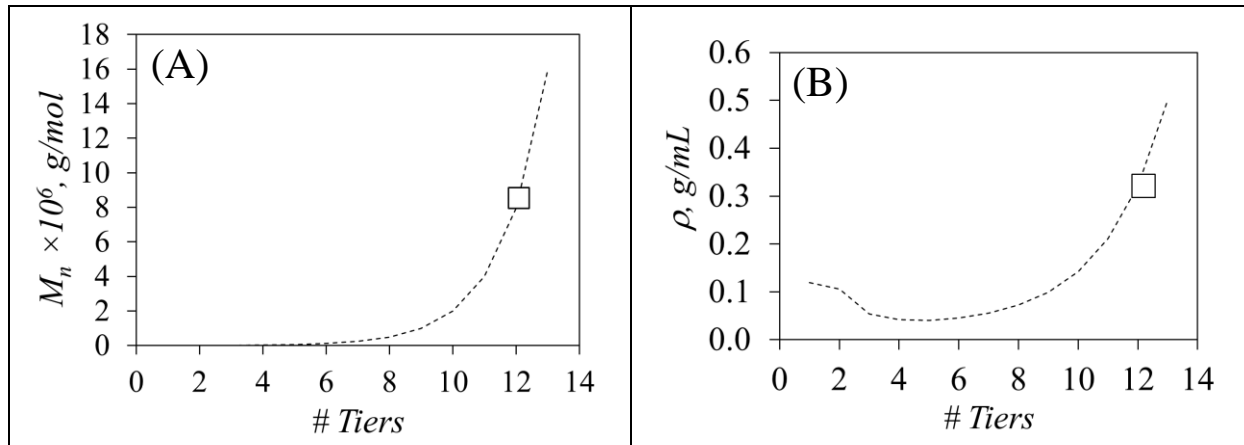
Figure S3.3. Plots of A) M_n and B) ρ (= 2.5/[η]) obtained ($\cdots\cdots$) theoretically based on Equations 3.4 – 3.6 and experimentally for glycogen from corn.

F] Fluorescence spectra of Py-Dextran and Np-Dextran
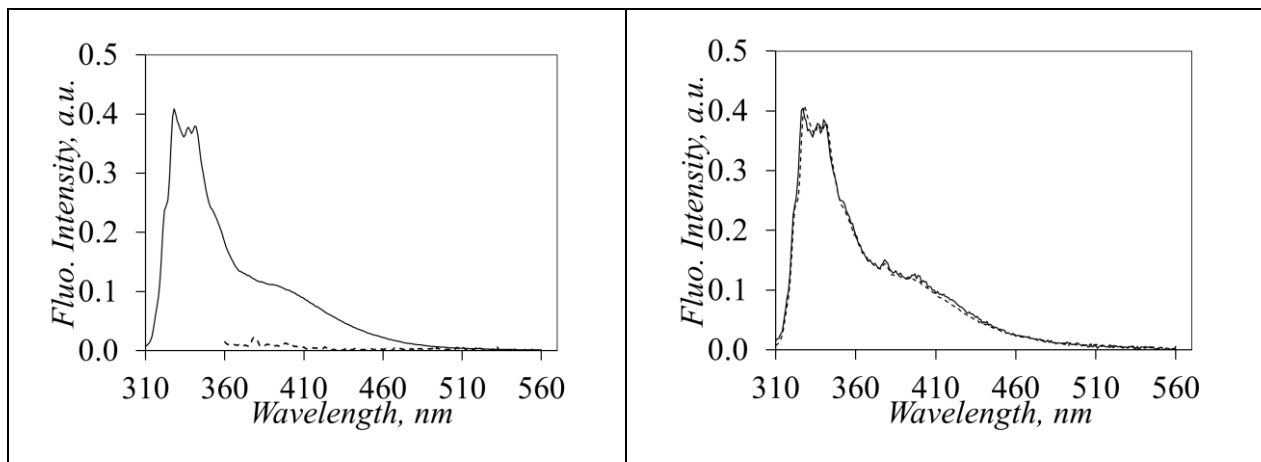
Figure S3.4 A) Individual fluorescence spectra of the ($-$) 2.1 mg/L Np(130)-Dextran and (---) 0.3 mg/L Py(7.8)-Dextran solutions in DMSO and B) fluorescence spectrum of the 2.1 mg/L Np(130)-Dextran and (---) 0.3mg/L Py(7.8)-Dextran mixture in DMSO with (---) the sum of the individual spectra shown in Figure S3A. λ_{ex} = 293 nm.

G] Fluorescence spectra of Py-Glycogen(C) in DMSO
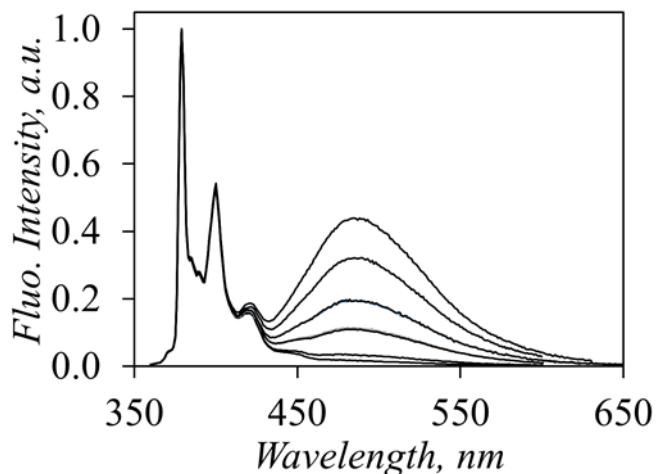
Figure S3.5. Fluorescence spectra of Py-Glycogen(C) in DMSO. $[Py] = 2.5 \times 10^{-6}$ M, $\lambda_{ex} = 346$ nm

H] Estimate of the reach of a pyrenyl derivative in Py-Glycogen

A 1-pyrenebutyryl derivative was attached on the C6-hydroxyl of an anhydroglucose unit (AGU) in HyperCchem. The pyrene moiety was induced to stretch away from the AGU and allowed to relax back to yield the structure shown in Figure S5. The carbon labeling and the centers of the pyrene and the AGU (●) were assigned in the figure.
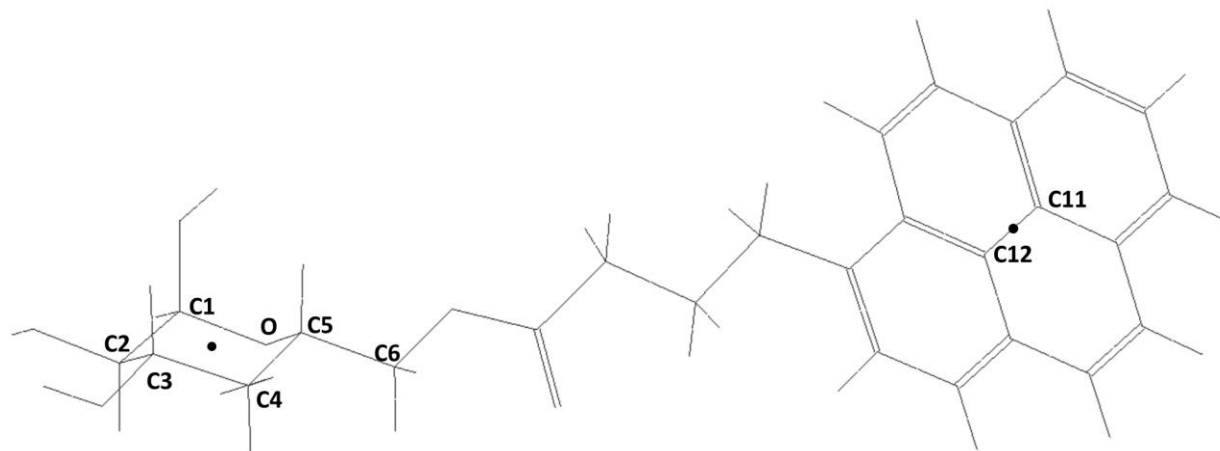
Figure S3.6. Structure of a pyrene-labeled AGU determined with HyperChem.

The coordinates of the carbons C1, C2, C4, and C5 for the AGU and C11 and C12 for pyrene were determined with HyperChem and listed in Table 1. The coordinates of the centers of mass (CoM)

of the AGU was determined with the coordinates of the carbons C1, C2, C4, and C5 and the CoM of the pyrene moiety was determined with the coordinates of C11 and C12. The distance between the two CoM was equal to 12.7Å. Since the center of a pyrenyl moiety could encounter the center of another pyrenyl moiety located 12.7 Å away, the reach of a pyrene label was estimated to equal $2\times12.7 = 25.4$ Å. Thus, a pyrenyl moiety could be viewed as being located at the center of a *blob* $25.4 \times 2 = 50.8$ Å in diameter

Table 3.1. Coordinates of the C1, C2, C3, and C4 atoms of the AGU, the C11 and C12 atoms of pyrene and the centers of mass (CoM) of C1, C2, C3, and C4 and C11 and C12

Molecule	Carbon #	x	y	z
AGU	C1	3.33	-6.47	2.93
AGU	C2	4.81	-6.06	3.00
AGU	C4	4.18	-4.01	1.73
AGU	C5	2.73	-4.54	1.73
AGU	CoM	3.76	-5.27	2.35
Pyrene	C11	-4.61	1.41	-3.45
Pyrene	C12	-5.31	2.62	-3.25
Pyrene	CoM	-4.96	2.02	-3.35

I] List of parameters retrieved from the fluorescence decay analysis

Table S3.1. Parameters retrieved from the global FBM analysis of the monomer decays of the Py-Glycogen(O/C) samples in DMSO with Equation S1.

Source	mol%	f_{Mdiff}	f_{Mfree}	k_{blob} $(\times10^7\,s^{-1})$	$<n>$	f_{Mk2}	$k_e[blob]$ $(\times10^8\,s^{-1})$	χ^2
	1.48	0.848	0.111	1.02	0.58	0.041	3.60	1.21
	2.09	0.782	0.129	1.19	0.79	0.089	8.40	1.17
Oyster	3.14	0.781	0.077	1.32	1.19	0.143	8.32	1.18
$\tau_M = 112$ ns	4.22	0.787	0.010	1.38	1.49	0.204	5.94	1.22
$k_2 = 2.6\times10^8\,s^{-1}$	4.81	0.816	0.000	1.25	1.46	0.173	6.95	1.24
	5.48	0.797	0.000	1.20	1.92	0.203	5.97	1.19
	5.62	0.759	0.000	1.11	1.94	0.241	5.43	1.15
	6.85	0.743	0.000	1.45	2.41	0.257	5.82	1.24
	7.80	0.733	0.000	1.13	2.71	0.267	4.64	1.12
	1.87	0.848	0.058	1.39	0.64	0.094	8.86	1.16
Corn	3.32	0.849	0.010	1.14	1.15	0.141	7.19	1.20
$\tau_M = 110$ ns	4.03	0.835	0.028	0.97	1.34	0.137	7.91	1.11
$k_2 = 2.6\times10^8\,s^{-1}$	5.26	0.828	0.000	1.11	1.66	0.172	7.23	1.13
	6.07	0.779	0.000	1.05	2.25	0.221	7.38	1.18

Table S3.2. Parameters retrieved from the global FBM analysis of the excimer decays of the Py-Glycogen(O/C) samples in DMSO with Equation S2.

Source	mol%	$\tau_{E,1}$ (ns)	$\tau_{E,2}$ (ns)	$f_{Ediff,\,E1}$	$f_{Ediff,\,E2}$	f_{Ek2}	$f_{EE0,\,E1}$	$f_{EE0,\,E2}$	f_{ES}	χ^2
Oyster $\tau_M = 112$ ns $\tau_S = 3.5$ ns $k_2 = 2.6\times10^8\,\text{s}^{-1}$	1.48	25.9	63.3	0.344	0.465	0.039	0.021	0.016	0.116	1.21
	2.09	42.0	66.6	0.185	0.596	0.089	0.046	0.000	0.084	1.17
	3.14	48.0	113.5	0.016	0.640	0.120	0.093	0.000	0.131	1.18
	4.22	49.2		0.598		0.155	0.101		0.147	1.22
	4.81	49.7		0.650		0.138	0.114		0.099	1.24
	5.48	49.1		0.624		0.159	0.114		0.104	1.19
	5.62	48.2		0.583		0.186	0.090		0.142	1.15
	6.85	47.6		0.608		0.210	0.176		0.005	1.24
	7.80	48.0		0.514		0.187	0.185		0.115	1.12
Corn $\tau_M = 110$ ns $\tau_S = 3.5$ ns $k_2 = 2.6\times10^8\,\text{s}^{-1}$	1.87	52.0		0.667		0.074	0.041		0.219	1.16
	3.32	47.9		0.645		0.107	0.073		0.174	1.20
	4.03	39.4	59.3	0.216	0.414	0.103	0.009	0.054	0.212	1.11
	5.26	48.0		0.568		0.118	0.091		0.222	1.13
	6.07	47.1		0.543		0.154	0.111		0.192	1.18

Table S3.3. Fractions of all pyrene species for the Py-Glycogen(O/C) samples calculated from f_{Mdiff}, f_{Mfree}, f_{Ediff}, f_{Ek2}, and f_{EE0}.

Source	mol%	f_{diff}	f_{free}	f_{E0}	f_{k2}
Oyster $\tau_M = 112$ ns $k_2 = 2.6\times10^8\,\text{s}^{-1}$	1.48	0.82	0.04	0.11	0.04
	2.09	0.75	0.08	0.12	0.04
	3.14	0.70	0.13	0.07	0.10
	4.22	0.69	0.18	0.01	0.12
	4.81	0.72	0.15	0.00	0.13
	5.48	0.70	0.18	0.00	0.13
	5.62	0.68	0.22	0.00	0.10
	6.85	0.61	0.21	0.00	0.18
	7.80	0.58	0.21	0.00	0.21
Corn $\tau_M = 110$ ns $k_2 = 2.6\times10^8\,\text{s}^{-1}$	1.87	0.81	0.09	0.05	0.05
	3.32	0.77	0.13	0.01	0.09
	4.03	0.77	0.13	0.03	0.08
	5.26	0.73	0.15	0.00	0.12
	6.07	0.67	0.19	0.00	0.14

I] Number of overlapping carbons retrieved from MMOs

Molecular mechanics optimizations (MMOs) for a single helix

Table S3.1. Number of overlapping carbons between the frame of the reference pyrene and that of a secondary pyrenyl label both attached to Helix #0 with the total number of residues $N_{\text{blob, intra}}$ allowing a pyrene-pyrene overlap with 7 or more carbon atoms.

$$< N_{blob,intra} >= \frac{\sum_{i=1}^{SCL} N_{blob}}{SCL}$$

# AGU	C6G1	C6G2	C6G3	C6G4	C6G5	C6G6	C6G7	C6G8	C2G9	C2G10	C6G11	C2G12		
C6G1	ref.	8	7	9	9	8	0	0	7	0	0	0		
C6G2	8	ref.	7	7	8	8	8	7	7	8	7	0		
C6G3	7	7	ref.	8	9	8	8	7	7	8	7	0		
C6G4	9	7	8	ref.	8	8	8	8	8	8	8	7		
C6G5	9	8	9	8	ref.	8	8	7	0	0	7	6		
C6G6	8	8	8	8	8	ref.	8	8	0	0	8	7		
C6G7	9	7	7	8	8	9	ref.	8	0	0	0	8		
C6G8	7	8	8	0	7	7	8	ref.	9	8	0	0		
C2G9	7	7	7	8	0	0	0	9	ref.	8	7	0		
C2G10	0	8	8	8	0	0	0	8	8	ref.	7	7		
C6G11	0	7	7	8	7	8	0	0	7	7	ref.	7		
C2G12	0	0	0	7	6	7	8	0	0	7	7	ref.		
SCL													$<N_{\text{blob, intra}}>$	stdev
9	9	9	9	8	8	8	7	8	6				8.0	1.0
10	9	10	10	9	8	8	7	9	7	6			8.3	1.3
11	9	11	11	10	9	9	7	9	8	7	8		8.9	1.4
12	9	11	11	11	9	10	8	9	8	8	9	6	9.1	1.5

Molecular mechanics optimizations (MMOs) for a hexagonal array of seven single helices

$$\Delta N_{blob,inter} = \sum_{i=1}^{6} \Delta N_{blob,Hi} + N_{blob,\ intra}$$

Table S3.2. Number of overlapping carbons between the frame of the reference pyrene attached to single Helix #0 and that of a secondary pyrenyl label attached to single Helix #1 for $d_{h\text{-}h}$ value of 1.8 nm with the total number of residues ΔN_{blob} allowing a pyrene-pyrene overlap with 7 or more carbon atoms.

H1	Position of the reference (# hydroxyl, #AGU, # Helix)											
# AGU	C6G1H0	C6G2H0	C6G3H0	C6G4H0	C6G5H0	C6G6H0	C6G7H0	C6G8H0	C2G9H0	C2G10H0	C6G11H0	C2G12H0
1	8	8	8	7	7	7	0	0	6	8	0	0
2	0	9	8	7	0	8	0	0	7	7	0	0
3	0	0	7	7	0	0	0	0	0	6	0	0
4	0	0	8	9	7	0	0	0	0	0	0	0
5	0	7	7	8	7	7	0	0	0	0	7	0
6	0	7	8	7	8	7	0	0	0	0	7	0
7	7	8	7	8	8	7	0	0	0	0	7	0
8	7	7	8	6	0	8	0	0	8	8	0	0
9	0	0	0	0	0	0	0	0	7	7	0	0
10	0	0	0	0	0	0	0	0	0	0	0	0
11	0	0	0	0	0	0	0	0	0	0	8	0
12	0	0	7	7	7	0	0	0	0	0	8	7
$\Delta N_{blob,\ H1}$	3	6	9	8	6	6	0	0	4	4	5	1

Table S3.3. Number of overlapping carbons between the frame of the reference pyrene attached to single Helix #0 and that of a secondary pyrenyl label attached to single Helix #2 and #3 for $d_{h\text{-}h}$ value of 1.8 nm with the total number of residues ΔN_{blob} allowing a pyrene-pyrene overlap with 7 or more carbon atoms.

H2	Position of the reference (# hydroxyl, #AGU, # Helix)											
# AGU	C6G1H0	C6G2H0	C6G3H0	C6G4H0	C6G5H0	C6G6H0	C6G7H0	C6G8H0	C2G9H0	C2G10H0	C6G11H0	C2G12H0
1	7	8	7	8	0	0	0	8	7	0	0	0
2	8	9	7	7	0	0	0	0	0	0	0	0
3	7	8	8	4	0	0	0	0	0	0	0	0
4	8	7	8	7	0	0	0	0	0	0	0	0
5	8	7	8	7	0	0	0	0	0	9	9	0
6	7	7	9	7	0	0	8	5	8	8	8	0
7	8	8	8	8	0	0	7	9	7	8	7	0
8	5	0	0	0	0	0	5	8	7	0	0	0
9	0	0	0	0	0	0	0	0	0	0	0	0
10	0	0	7	0	0	0	0	0	0	0	0	0
11	0	7	7	5	0	0	0	0	0	7	7	0
12	0	0	7	8	0	0	0	0	0	9	8	7
$\Delta N_{blob,\,H2}$	7	8	10	7	0	0	2	3	4	5	5	1
H3	Position of the reference (# hydroxyl, #AGU, # Helix)											
# AGU	C6G1H0	C6G2H0	C6G3H0	C6G4H0	C6G5H0	C6G6H0	C6G7H0	C6G8H0	C2G9H0	C2G10H0	C6G11H0	C2G12H0
1	7	8	0	0	0	0	7	7	0	0	0	0
2	7	7	6	0	0	0	8	9	0	0	0	0
3	9	8	8	7	0	8	9	7	0	0	0	0
4	8	9	8	8	7	7	8	7	8	8	5	0
5	7	7	0	8	7	7	8	7	8	9	7	0
6	7	4	0	7	7	8	7	8	8	7	0	0
7	8	0	0	3	0	7	7	7	0	0	0	0
8	0	0	0	0	0	0	0	8	0	0	0	0
9	0	7	0	0	0	0	0	0	0	0	0	0
10	7	8	8	0	0	0	0	0	8	7	0	0
11	0	0	0	7	0	7	8	0	9	10	8	0
12	0	0	0	0	0	8	8	7	7	8	8	0
$\Delta N_{blob,\,H3}$	8	7	3	5	3	7	9	9	6	6	3	0

Table S3.4. Number of overlapping carbons between the frame of the reference pyrene attached to single Helix #0 and that of a secondary pyrenyl label attached to single Helix #4 and #5 for $d_{h\text{-}h}$ value of 1.8 nm with the total number of residues ΔN_{blob} allowing a pyrene-pyrene overlap with 7 or more carbon atoms.

H4	Position of the reference (# hydroxyl, #AGU, # Helix)											
# AGU	C6G1H0	C6G2H0	C6G3H0	C6G4H0	C6G5H0	C6G6H0	C6G7H0	C6G8H0	C2G9H0	C2G10H0	C6G11H0	C2G12H0
1	7	7	0	0	0	8	7	0	0	0	0	0
2	8	8	0	0	7	7	7	8	0	0	0	0
3	7	9	8	0	8	7	8	8	0	0	0	7
4	8	7	8	0	7	8	7	7	0	0	7	8
5	8	0	0	0	7	7	8	7	0	0	0	8
6	0	0	0	0	0	7	0	9	0	0	0	0
7	0	0	0	0	0	0	0	0	0	0	0	0
8	8	0	0	0	0	0	8	0	0	0	0	0
9	7	0	0	0	0	7	8	7	0	0	0	0
10	0	0	0	0	8	7	7	8	0	0	8	7
11	0	0	0	0	7	7	8	7	0	0	7	8
12	0	0	0	0	0	0	0	8	0	0	0	8
$\Delta N_{blob, H4}$	7	4	2	0	6	9	9	9	0	0	3	6
H5	Position of the reference (# hydroxyl, #AGU, # Helix)											
# AGU	C6G1H0	C6G2H0	C6G3H0	C6G4H0	C6G5H0	C6G6H0	C6G7H0	C6G8H0	C2G9H0	C2G10H0	C6G11H0	C2G12H0
1	8	7	7	0	8	8	8	7	0	0	0	0
2	8	7	9	7	8	7	8	7	0	0	0	0
3	0	8	8	7	8	8	9	8	0	0	0	0
4	0	6	6	8	9	0	7	7	0	0	7	8
5	0	0	0	0	0	0	0	0	0	0	0	7
6	0	0	0	0	0	0	0	0	0	0	0	0
7	0	0	0	0	0	11	8	0	0	0	0	0
8	7	7	0	0	7	8	7	8	0	0	0	0
9	0	0	0	0	8	7	0	9	0	0	0	0
10	0	0	6	0	8	8	0	7	0	0	8	8
11	0	0	0	0	7	0	0	0	0	0	7	8
12	0	0	0	0	0	0	0	0	0	0	0	8
$\Delta N_{blob, H5}$	3	6	3	3	8	7	6	7	0	0	3	5

Table S3.5. Number of overlapping carbons between the frame of the reference pyrene attached to single Helix #0 and that of a secondary pyrenyl label attached to single Helix #4 and #5 for $d_{h\text{-}h}$ value of 1.8 nm with the total number of residues ΔN_{blob} allowing a pyrene-pyrene overlap with 7 or more carbon atoms.

H6	Position of the reference (# hydroxyl, #AGU, # Helix)											
# AGU	C6G1H0	C6G2H0	C6G3H0	C6G4H0	C6G5H0	C6G6H0	C6G7H0	C6G8H0	C2G9H0	C2G10H0	C6G11H0	C2G12H0
1	8	8	9	8	8	7	7	7	0	0	9	0
2	0	8	8	7	7	6	0	7	0	0	7	0
3	0	7	8	8	0	0	0	0	0	8	7	0
4	0	0	0	7	7	0	0	0	0	7	7	0
5	0	0	0	0	7	7	0	0	0	0	0	0
6	0	0	0	0	7	8	4	0	0	0	0	0
7	0	8	8	0	8	7	8	0	0	0	0	0
8	6	8	9	7	8	8	0	7	0	0	7	7
9	0	0	7	7	0	0	0	0	0	9	9	7
10	0	0	0	8	0	0	0	0	0	7	8	7
11	0	0	0	5	0	0	0	0	0	4	8	7
12	0	0	0	0	0	0	0	0	0	0	0	0
$\Delta N_{blob,\ H6}$	1	2	6	7	7	5	2	3	0	4	8	4

Table S3.6. Number of overlapping carbons between the frame of the reference pyrene attached to single Helix #0 (C6 on 1st AGU; $\theta = 0^o$, $\phi = 0^o$) and that of a secondary pyrenyl label attached to single Helix #1-#6 for d_{h-h} values between 2.4 nm and 3.4 nm with the total number of residues ΔN_{blob} allowing a pyrene-pyrene overlap with 7 or more carbon atoms.

d_{h-h}	3.40 nm							3.20 nm							3.00 nm						
# AGU	H1	H2	H3	H4	H5	H6		H1	H2	H3	H4	H5	H6		H1	H2	H3	H4	H5	H6	
1	0	0	0	0	0	0		0	0	0	0	0	0		0	0	0	0	0	0	
2	0	0	0	0	0	0		0	0	0	0	0	0		0	0	7	0	0	0	
3	0	0	3	0	0	0		0	0	8	0	0	0		0	0	8	6	0	0	
4	0	0	6	0	0	0		0	0	7	0	0	0		0	0	7	6	0	0	
5	0	0	6	0	0	0		0	6	7	0	0	0		0	7	7	0	0	0	
6	0	5	0	0	0	0		0	8	0	0	0	0		0	8	0	0	0	0	
7	0	0	0	0	0	0	$N_{blob,inter}$	0	0	0	0	0	0	$N_{blob,inter}$	0	4	0	0	0	0	$N_{blob,inter}$
8	0	0	0	0	0	0	(SCL)	0	0	0	0	0	0	(SCL)	0	0	0	0	0	0	(SCL)
9	0	0	0	0	0	0	0 (9)	0	0	0	0	0	0	4 (9)	0	0	0	0	0	0	5 (9)
10	0	0	0	0	0	0	0 (10)	0	0	0	0	0	0	4 (10)	0	0	0	0	0	0	5 (10)
11	0	0	0	0	0	0	0 (11)	0	0	0	0	0	0	4 (11)	0	0	0	0	0	0	5 (11)
12	0	0	0	0	0	0	0 (12)	0	0	0	0	0	0	4 (12)	0	0	0	0	0	0	5 (12)

d_{h-h}	2.80 nm							2.60 nm							2.40 nm						
# AGU	H1	H2	H3	H4	H5	H6		H1	H2	H3	H4	H5	H6		H1	H2	H3	H4	H5	H6	
1	0	0	0	0	0	0		6	6	5	4	0	0		7	7	7	7	7	7	
2	0	0	7	5	0	0		0	4	8	7	0	0		0	8	8	7	5	0	
3	0	0	8	8	0	0		0	7	8	7	0	0		0	7	8	7	0	0	
4	0	7	7	6	0	0		0	8	7	7	0	0		0	8	7	7	0	0	
5	0	7	7	0	0	0		0	7	7	0	0	0		0	7	7	0	0	0	
6	0	8	0	0	0	0		0	8	7	0	0	0		0	8	7	0	0	0	
7	0	8	0	0	0	0	$N_{blob,inter}$	6	8	0	0	0	0	$N_{blob,inter}$	8	8	0	0	0	0	$N_{blob,inter}$
8	0	0	0	0	0	0	(SCL)	4	0	0	0	0	0	(SCL)	7	0	0	0	0	0	(SCL)
9	0	0	0	0	0	0	9 (9)	0	0	0	0	0	0	13 (9)	0	0	0	0	0	0	22 (9)
10	0	0	5	0	0	0	9 (10)	0	0	8	0	0	0	14 (10)	0	0	8	0	0	0	23 (10)
11	0	0	0	0	0	0	9 (11)	0	0	0	0	0	0	14 (11)	0	0	0	0	0	0	23 (11)
12	0	0	0	0	0	0	9 (12)	0	0	0	0	0	0	14 (12)	0	0	0	0	0	0	23 (12)

Table S3.7. Number of overlapping carbons between the frame of the reference pyrene attached to single Helix #0 (C6 on 1st AGU; θ = 0°, ϕ = 0°) and that of a secondary pyrenyl label attached to single Helix #1-#6 for d_{h-h} values between 1.6 nm and 2.2 nm with the total number of residues ΔN_{blob} allowing a pyrene-pyrene overlap with 7 or more carbon atoms.

d_{h-h}	2.20 nm							2.00 nm							1.80 nm						
# AGU	H1	H2	H3	H4	H5	H6		H1	H2	H3	H4	H5	H6		H1	H2	H3	H4	H5	H6	
1	8	7	7	8	8	7		7	7	8	7	8	7		8	7	7	7	8	8	
2	0	8	7	7	8	0		0	7	8	8	7	0		0	8	7	8	8	0	
3	0	8	8	8	0	0		0	8	7	8	0	0		0	7	9	7	0	0	
4	0	7	8	8	0	0		0	7	7	7	0	0		0	8	8	8	0	0	
5	0	7	8	0	0	0		0	8	7	5	0	0		0	8	7	8	0	0	
6	0	7	7	0	0	0		0	8	8	0	0	0		0	7	7	0	0	0	
7	7	8	8	0	0	0	$N_{blob,inter}$	7	7	7	0	0	0	$N_{blob,inter}$	7	8	8	0	0	0	$N_{blob,inter}$
8	7	0	0	0	5	0	(SCL)	8	0	0	7	7	0	(SCL)	7	5	0	8	7	6	(SCL)
9	0	0	0	8	0	0	25 (9)	0	0	0	7	0	0	27 (9)	0	0	0	7	0	0	28 (9)
10	0	0	8	0	0	0	26 (10)	0	0	8	0	0	0	28 (10)	0	0	7	0	0	0	29 (10)
11	0	0	0	0	0	0	26 (11)	0	0	0	0	0	0	28 (11)	0	0	0	0	0	0	29 (11)
12	0	0	0	0	0	0	26 (11)	0	0	0	0	0	0	28 (12)	0	0	0	0	0	0	29 (12)

d_{h-h}	1.75 nm							1.70 nm							1.60 nm						
# AGU	H1	H2	H3	H4	H5	H6		H1	H2	H3	H4	H5	H6		H1	H2	H3	H4	H5	H6	
1	≥7	≥7	≥7	≥7	≥7	≥7		≥7	≥7	≥7	≥7	≥7	≥7		≥7	≥7	≥7	≥7	≥7	≥7	
2	0	≥7	≥7	≥7	≥7	8		0	≥7	≥7	≥7	≥7	7		6	≥7	≥7	≥7	≥7	7	
3	0	≥7	≥7	≥7	8	0		0	≥7	≥7	≥7	8	0		0	≥7	≥7	≥7	8	0	
4	0	≥7	≥7	≥7	0	0		0	≥7	≥7	≥7	0	0		0	≥7	≥7	≥7	4	0	
5	8	≥7	≥7	≥7	0	0		8	≥7	≥7	≥7	0	0		7	≥7	≥7	≥7	0	0	
6	8	≥7	≥7	0	0	0		7	≥7	≥7	0	0	7		8	≥7	≥7	0	0	8	
7	≥7	≥7	≥7	0	0	0	$N_{blob,inter}$	≥7	≥7	≥7	0	0	7	$N_{blob,inter}$	≥7	≥7	≥7	0	7	7	$N_{blob,inter}$
8	≥7	5	0	≥7	≥7	7	(SCL)	≥7	6	0	≥7	≥7	7	(SCL)	≥7	7	0	≥7	≥7	7	(SCL)
9	0	0	0	≥7	0	0	33 (9)	0	0	0	≥7	0	0	35 (9)	0	0	0	≥7	0	0	37 (9)
10	0	0	≥7	0	0	0	34 (10)	0	0	≥7	0	0	0	36 (10)	0	0	≥7	0	0	0	38 (10)
11	0	0	0	0	0	0	34 (11)	0	0	8	0	0	0	37 (11)	0	0	8	0	0	0	39 (11)
12	0	0	0	0	0	0	34 (12)	0	0	0	0	0	0	37 (12)	0	0	0	0	0	0	39 (12)

* The data with ≥ was counted toward N_{blob} without conducting an MMO. The assumption was made because the pyrenyl labels at the same positions had been shown to generate a good overlap even at a larger distance.

Table S3.8. Number of overlapping carbons between the frame of the reference pyrene attached to single Helix #0 (C6 on 1st AGU; $\theta = 0°$, $\phi = 30°$) and that of a secondary pyrenyl label attached to single Helix #1-#6 for $d_{h\text{-}h}$ values between 2.4 nm and 3.4 nm with the total number of residues ΔN_{blob} allowing a pyrene-pyrene overlap with 7 or more carbon atoms.

dh-h	3.4 nm							3.2 nm							3.0 nm						
# AGU	H1	H2	H3	H4	H5	H6		H1	H2	H3	H4	H5	H6		H1	H2	H3	H4	H5	H6	
1	0	0	0	0	0	0		0	0	0	0	0	0		0	0	0	0	0	0	
2	0	0	0	0	0	0		0	0	0	7	0	0		0	0	0	7	0	0	
3	0	0	0	0	0	0		0	0	0	7	3	0		0	0	0	7	8	0	
4	0	0	0	0	0	0		0	0	0	0	7	0		0	0	0	8	8	0	
5	0	0	0	0	0	0		0	0	0	0	7	0		0	0	0	0	7	0	
6	0	0	0	0	0	0		0	0	0	0	0	0		0	0	0	0	0	7	
7	0	0	0	0	0	0		0	0	0	0	0	0		0	0	0	0	0	0	
8	0	0	0	0	0	0	$N_{blob,inter}$	0	0	0	0	0	0	$N_{blob,inter}$	0	0	0	0	0	0	$N_{blob,inter}$
9	0	0	0	0	0	0	0	0	0	0	0	6	0	4	0	0	0	3	0	0	7
10	0	0	0	0	0	0	0	0	0	0	0	0	0	4	0	0	0	7	0	0	8
11	0	0	0	0	0	0	0	0	0	0	5	0	0	4	0	0	0	7	7	0	10
12	0	0	0	0	0	0	0	0	0	0	0	0	0	4	0	0	0	0	0	0	10

dh-h	2.8 nm							2.6 nm							2.4 nm						
# AGU	H1	H2	H3	H4	H5	H6		H1	H2	H3	H4	H5	H6		H1	H2	H3	H4	H5	H6	
1	0	0	0	0	0	0		0	0	0	0	7	0		0	0	8	6	≥ 7	8	
2	0	0	0	≥ 7	0	0		0	0	0	8	7	0		0	0	7	≥ 7	≥ 7	0	
3	0	0	0	≥ 7	≥ 7	0		0	0	0	8	7	0		0	0	7	≥ 7	≥ 7	0	
4	0	0	0	≥ 7	≥ 7	0		0	0	0	8	7	0		0	0	0	≥ 7	≥ 7	0	
5	0	0	0	0	≥ 7	7		0	0	0	7	7	7		0	0	0	≥ 7	≥ 7	≥ 7	
6	0	0	0	0	7	≥ 7		0	0	0	0	7	7		0	0	0	0	≥ 7	≥ 7	
7	0	0	0	0	0	7		0	0	0	0	0	7		0	0	0	0	8	≥ 7	
8	0	0	0	0	0	0	$N_{blob,inter}$	0	0	0	0	0	0	$N_{blob,inter}$	0	0	6	0	0	6	$N_{blob,inter}$
9	0	0	0	≥ 7	0	0	11	0	0	0	7	0	0	12	0	0	0	≥ 7	0	0	19
10	0	0	0	≥ 7	0	0	12	0	0	0	7	0	0	15	0	0	0	≥ 7	0	0	20
11	0	0	0	≥ 7	≥ 7	0	14	0	0	0	7	7	0	17	0	0	0	≥ 7	≥ 7	0	22
12	0	0	0	0	0	0	14	0	0	0	0	0	0	17	0	0	0	0	0	0	22

* The data with $\geq$ was counted toward N_{blob} without conducting an MMO. The assumption was made because the pyrenyl labels at the same positions had been shown to generate a good overlap even at a larger distance.

Table S3.9. Number of overlapping carbons between the frame of the reference pyrene attached to single Helix #0 (C6 on 1st AGU; $\theta = 0°$, $\phi = 30°$) and that of a secondary pyrenyl label attached to single Helix #1-#6 for $d_{h\text{-}h}$ values between 1.6 nm and 2.2 nm with the total number of residues ΔN_{blob} allowing a pyrene-pyrene overlap with 7 or more carbon atoms.

2.20 nm

# AGU	H1	H2	H3	H4	H5	H6	$N_{blob,inter}$
1	8	7	7	7	≥7	7	
2	0	7	8	7	≥7	5	
3	0	0	7	7	≥7	0	
4	0	0	0	8	≥7	7	
5	0	0	0	8	≥7	8	
6	0	0	0	0	≥7	8	
7	0	0	0	0	8	8	
8	0	0	7	0	0	8	$N_{blob,inter}$
9	0	0	0	7	0	0	26
10	0	0	0	8	0	0	27
11	0	0	0	8	≥7	0	29
12	0	0	0	0	0	0	29

2.00 nm

# AGU	H1	H2	H3	H4	H5	H6	$N_{blob,inter}$
1	≥7	≥7	≥7	≥7	≥7	≥7	
2	0	≥7	≥7	≥7	≥7	8	
3	0	0	≥7	≥7	≥7	0	
4	0	0	0	≥7	≥7	≥7	
5	0	0	0	≥7	≥7	≥7	
6	0	0	0	0	≥7	≥7	
7	0	0	0	0	≥7	≥7	
8	0	0	≥7	0	0	≥7	$N_{blob,inter}$
9	0	0	0	≥7	0	0	27
10	0	0	0	≥7	0	0	28
11	0	0	0	≥7	≥7	0	30
12	0	0	0	0	0	0	30

1.80 nm

# AGU	H1	H2	H3	H4	H5	H6	$N_{blob,inter}$
1	8	7	7	8	7	7	
2	0	8	7	8	7	8	
3	0	5	8	7	7	7	
4	0	0	8	7	7	7	
5	0	0	0	7	7	7	
6	0	0	0	7	7	7	
7	0	7	0	7	7	7	
8	8	8	8	7	0	7	$N_{blob,inter}$
9	0	0	0	8	0	0	35
10	0	0	0	7	0	0	36
11	0	0	0	7	7	0	38
12	0	0	0	0	6	0	38

1.75 nm

# AGU	H1	H2	H3	H4	H5	H6	$N_{blob,inter}$
1	≥7	≥7	≥7	≥7	≥7	≥7	
2	7	≥7	≥7	≥7	≥7	≥7	
3	0	7	≥7	≥7	≥7	≥7	
4	0	0	≥7	≥7	≥7	≥7	
5	0	0	0	≥7	≥7	≥7	
6	0	0	0	≥7	≥7	≥7	
7	0	≥7	0	≥7	≥7	≥7	
8	≥7	≥7	≥7	≥7	0	≥7	$N_{blob,inter}$
9	0	0	0	≥7	0	0	37
10	0	0	0	≥7	0	0	38
11	0	0	0	≥7	≥7	0	40
12	0	0	0	0	0	0	40

1.70 nm

# AGU	H1	H2	H3	H4	H5	H6	$N_{blob,inter}$
1	≥7	≥7	≥7	≥7	≥7	≥7	
2	7	≥7	≥7	≥7	≥7	≥7	
3	0	7	≥7	≥7	≥7	≥7	
4	0	0	≥7	≥7	≥7	≥7	
5	0	0	0	≥7	≥7	≥7	
6	0	0	0	≥7	≥7	≥7	
7	0	≥7	0	≥7	≥7	≥7	
8	≥7	≥7	≥7	≥7	0	≥7	$N_{blob,inter}$
9	0	0	0	≥7	0	0	37
10	0	0	0	≥7	0	0	38
11	0	0	0	≥7	≥7	0	40
12	0	0	0	0	0	0	40

1.60 nm

# AGU	H1	H2	H3	H4	H5	H6	$N_{blob,inter}$
1	≥7	≥7	≥7	≥7	≥7	≥7	
2	7	≥7	≥7	≥7	≥7	≥7	
3	0	7	≥7	≥7	≥7	≥7	
4	0	0	≥7	≥7	≥7	≥7	
5	0	0	0	≥7	≥7	≥7	
6	7	0	0	≥7	≥7	≥7	
7	7	≥7	0	≥7	≥7	≥7	
8	≥7	≥7	≥7	≥7	0	≥7	$N_{blob,inter}$
9	0	0	0	≥7	0	0	39
10	0	0	0	≥7	0	0	40
11	0	0	0	≥7	≥7	0	42
12	0	0	0	0	0	0	42

* The data with ≥ was counted toward N_{blob} without conducting an MMO. The assumption was made because the pyrenyl labels at the same positions had been shown to generate a good overlap even at a larger distance.

Table S3.10. Number of overlapping carbons between the frame of the reference pyrene attached to single Helix #0 (C2 on 9th AGU; θ = 0°, ϕ = 0°) and that of a secondary pyrenyl label attached to single Helix #1-#6 for $d_{h\text{-}h}$ values between 2.6 nm and 3.6 nm with the total number of residues ΔN_{blob} allowing a pyrene-pyrene overlap with 7 or more carbon atoms.

| dh-h	3.6 nm							3.4 nm							3.2 nm						
#AGU	H1	H2	H3	H4	H5	H6		H1	H2	H3	H4	H5	H6		H1	H2	H3	H4	H5	H6	
1	0	0	0	0	0	0		0	0	0	0	0	0		0	0	0	0	0	0	
2	0	0	0	0	0	0		0	0	0	0	0	0		0	0	0	0	0	0	
3	0	0	0	0	0	0		0	0	0	0	0	0		0	0	0	0	0	0	
4	0	0	0	0	0	0		0	0	0	0	0	0		0	0	0	0	0	0	
5	0	0	0	0	0	0		0	0	0	0	0	0		0	0	0	0	0	0	
6	0	0	0	0	0	0		0	0	0	0	0	0		0	0	0	0	0	0	
7	0	0	0	0	0	0		0	0	0	0	0	0		0	0	0	0	0	0	
8	0	0	0	0	0	0	N$_{blob,inter}$	0	0	0	0	0	0	N$_{blob,inter}$	0	0	0	0	0	0	N$_{blob,inter}$
9	0	0	0	0	0	0	0	0	0	0	0	0	0	0	0	0	0	0	0	0	0
10	0	0	0	0	0	0	0	0	0	0	0	0	0	0	0	0	0	0	0	0	0
11	0	0	0	0	0	0	0	0	0	0	0	0	0	0	0	7	0	0	0	0	1
12	0	0	0	0	0	0	0	0	7	0	0	0	0	1	0	8	0	0	0	0	2
dh-h	3.0 nm							2.8 nm							2.6 nm						
#AGU	H1	H2	H3	H4	H5	H6		H1	H2	H3	H4	H5	H6		H1	H2	H3	H4	H5	H6	
1	0	0	0	0	0	0		0	0	0	0	0	0		0	0	0	0	0	0	
2	0	0	0	0	0	0		0	0	0	0	0	0		0	0	0	0	0	0	
3	0	0	0	0	0	0		0	0	0	0	0	0		0	0	0	0	0	0	
4	0	0	0	0	0	0		0	8	0	0	0	0		0	8	8	0	0	0	
5	0	7	0	0	0	0		0	≥7	0	0	0	0		0	9	0	0	0	0	
6	7	0	0	0	0	0		7	0	0	0	0	0		9	0	0	0	0	0	
7	7	0	0	0	0	0		≥7	0	0	0	0	0		8	0	0	0	0	0	
8	7	0	0	0	0	0	N$_{blob,inter}$	≥7	0	0	0	0	0	N$_{blob,inter}$	8	0	0	0	0	8	N$_{blob,inter}$
9	0	0	0	0	0	0	4	0	0	0	0	0	0	5	0	0	0	0	0	0	7
10	0	0	7	0	0	0	5	0	0	≥7	0	0	0	6	0	0	9	0	0	0	8
11	0	7	8	0	0	0	7	0	≥7	≥7	0	0	0	8	0	7	7	0	0	0	10
12	0	8	0	0	0	0	8	0	≥7	0	0	0	0	9	0	7	0	0	0	0	11

* The data with ≥ was counted toward N_{blob} without conducting an MMO. The assumption was made because the pyrenyl labels at the same positions had been shown to generate a good overlap even at a larger distance.

Table S3.11. Number of overlapping carbons between the frame of the reference pyrene attached to single Helix #0 (C2 on 9th AGU; $\theta = 0°$, $\phi = 0°$) and that of a secondary pyrenyl label attached to single Helix #1-#6 for d_{h-h} values between 1.6 nm and 2.4 nm with the total number of residues ΔN_{blob} allowing a pyrene-pyrene overlap with 7 or more carbon atoms.

dh-h	2.4 nm							2.2 nm							2.0 nm						
#AGU	H1	H2	H3	H4	H5	H6		H1	H2	H3	H4	H5	H6		H1	H2	H3	H4	H5	H6	
1	7	0	0	0	0	0		7	0	0	0	0	0		7	0	0	0	0	7	
2	0	0	0	0	0	0		0	0	0	0	0	0		0	0	0	0	0	7	
3	0	0	5	0	0	0		0	0	8	0	0	0		0	8	7	0	0	7	
4	0	7	8	0	0	0		0	8	7	0	0	0		0	7	7	0	0	0	
5	0	8	0	0	0	0		0	7	0	0	0	0		0	7	0	0	0	0	
6	7	0	0	0	0	0		8	0	0	0	0	0		8	6	0	0	0	0	
7	7	0	0	0	0	0		8	0	0	0	0	0		8	0	0	0	0	0	
8	8	0	0	0	0	8	$N_{blob,inter}$	8	0	0	0	0	7	$N_{blob,inter}$	8	0	0	0	0	8	$N_{blob,inter}$
9	0	0	0	0	0	0	8	0	0	0	0	0	7	10	0	0	7	0	0	7	15
10	0	6	9	0	0	0	9	0	8	8	0	0	0	12	0	8	7	0	0	0	17
11	0	8	8	0	0	0	11	0	8	8	0	0	0	14	0	7	7	0	0	0	19
12	0	8	0	0	0	0	12	0	7	0	0	0	0	15	0	7	0	0	0	0	20

| dh-h	1.8 nm							1.6 nm						
#AGU	H1	H2	H3	H4	H5	H6		H1	H2	H3	H4	H5	H6	
1	≥7	0	0	0	0	≥7		7	0	0	0	0	7	
2	0	0	0	0	0	≥7		0	0	0	0	0	7	
3	0	≥7	≥7	0	0	≥7		0	7	7	0	0	7	
4	0	≥7	≥7	0	0	0		0	7	7	0	0	0	
5	0	≥7	0	0	0	0		0	7	0	0	0	0	
6	8	8	0	0	0	0		≥7	≥7	0	0	0	0	
7	≥7	0	0	0	0	0		7	0	0	0	0	0	
8	≥7	0	0	0	0	≥7	$N_{blob,inter}$	8	0	0	0	0	8	$N_{blob,inter}$
9	0	0	≥7	0	0	≥7	16	0	0	7	0	0	7	16
10	0	≥7	≥7	0	0	0	18	0	8	8	0	0	0	18
11	0	≥7	≥7	0	0	0	20	0	7	8	0	0	0	20
12	0	≥7	0	0	0	0	21	0	7	0	0	0	0	21

* The data with ≥ was counted toward N_{blob} without conducting an MMO. The assumption was made because the pyrenyl labels at the same positions had been shown to generate a good overlap even at a larger distance.

J] N_{blob}^{theo} of Glycogen with SLC=12 predicted from MMOs simulations
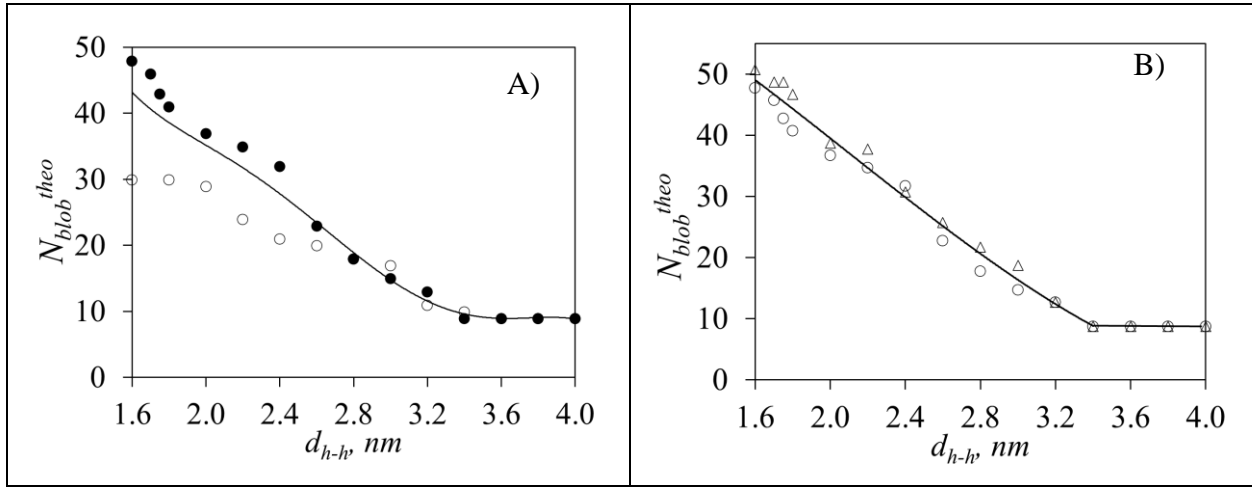
Figure S3.7. A) Plot of N_{blob}^{theo}(C6/C2) with the reference pyrene attached on (○) the C2-hydroxyl of the 9th AGU and (●) the C6- hydroxyl of the 1st AGU as a function of d_{h-h} for glycogen with SCL=12. The line represents the N_{blob}^{theo} over the three AGUs with an N_{blob}^{theo}(C2) values corresponding to the reference pyrene attached on the C2-hydroxyl of the 9th AGU and the nine AGUs with an N_{blob}^{theo}(C6) value corresponding to the reference pyrene attached on the C6-hydroxyl of the 1st AGU. B) Plot of N_{blob}^{theo}(C6) for Helix #0 with (○) $\phi = 0^{o}$ and (△) $\phi = 30^{o}$. The line represents the average of the N_{blob}^{theo}(C6) values obtained at $\phi = 0^{o}$ and 30°.

K] $N_{blob}^{theo}(\rho)$, $\rho(r)$, and $N_{blob}^{theo}(r)$ for phytoglycogen with SCL=12
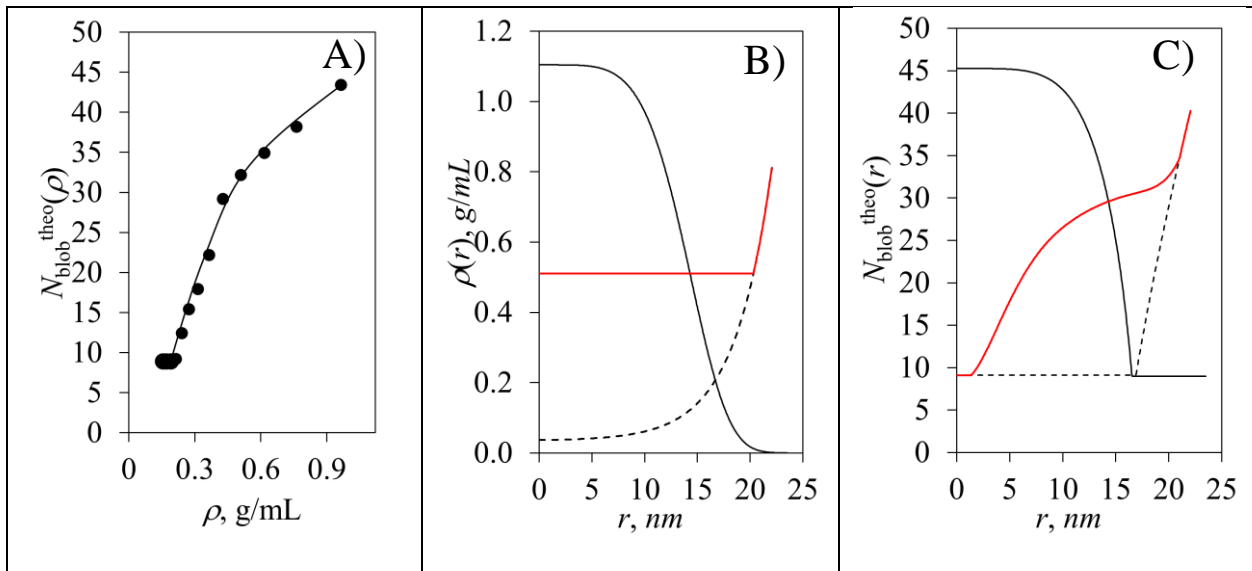
Figure S3.8. Plots of (A) N_{blob}^{theo} as a function of the local density ρ and (B) ρ and (C) N_{blob}^{theo} as a function of r, according to (▬ ▬) the Meléndez-Hevia model, (▬▬) the modified Meléndez-Hevia model, and (▬▬) the Gilbert model with ρ_{max} = 1.1 g/mL, a=1.3×10^{-6}, and b=5. SLC=12.

L] Equations describing the relationship between $\rho(r)$ based on the Meléndez-Hevia Model

The local density $\rho(r)$ of glycogen could be predicted with Equations S3.14 and S3.15 for glycogen with SCL=10 and SCL=12 AGUs, respectively.

$$\rho(r) \text{ (in g/mL)} = 0.0452 + \{exp[-0.3618\times(20.13 - r) - 48.004]\times10^{21}\} \qquad \text{(S3.14)}$$

$$\rho(r) \text{ (in g/mL)} = 0.0351 + \{exp[-0.2818\times(23.28 - r) - 48.263]\times10^{21}\} \qquad \text{(S3.15)}$$

M] Equations applied to account for the edge effects in a cluster of side chain for N_{blob}^{theo}

The total number of side chain ($n_{sc}(t)$) present in a given tier (t) of glycogen can be expressed with Equation S3.16 with the degree of branching, r, being equal to 2 as stated in the main text and based on Meléndez-Hevia model. The number of chains increases exponentially with increasing t as shown in Figure S3.9A.

$$n_{sc} = \frac{1-r^t}{1-r} \qquad \text{(S3.16)}$$

Each tier increases the diameter of the glycogen particle by $(0.126 \times SCL + 0.35)$ nm, where SCL equals 10 and 12 AGUs for glycogen from oyster and corn, respectively. The total number of tiers, when t is higher than 1, can be calculated with Equation S3.17, where $R_{glycogen}$ is the radius of glycogen. The addition of 0.5 accounts for the contribution of the 1st tier.

$$t_{total} = \frac{R_{glycogen}}{(0.126\times SCL+0.35)} + 0.5 \qquad \text{(S3.17)}$$

The number of side chains for a given t, $n_{sc}(t)$, can be calculated with Equation S3.18.

$$n_{sc}(t) = \frac{r^t - r^{(t-1)}}{1-r} \qquad \text{(S3.18)}$$

Equations S3.19 and S3.20 describe the relationship between N_{blob}^{theo} and ρ in Figure 3.9A and S3.8A for glycogen with SCL=10 AGUs and 12 AGUs, respectively. N_{blo}^{theo} is for an array with an infinite number of HCP helices and is referred to as $N_{blob}^{theo}(\infty)$ in Equations S3.19 and S3.20. The earlier study on amylopectin demonstrated that N_{blob}^{theo} for an array of a finite number of helices depends on the interhelical distance (d_{h-h}) and the number of helices. N_{blob}^{theo} increases with increasing number of helices in a cluster and with decreasing d_{h-h} as shown in Figure S3.9B. For a given d_{h-h}, N_{blob}^{theo} reaches a constant value ($N_{blob}^{theo}(\infty)$), where N_{blob}^{theo} becomes independent of the number of side chains. $N_{blob}^{theo}(\infty)$ represents the value of N_{blob}^{theo} for an infinite array of helices and was estimated with Equations S3.19 and S3.20.

$SCL=10$ $\qquad\qquad\qquad N_{blob}^{theo}(\infty) = 17.427\times Ln(\rho - 0.1) + 45.187 \qquad \text{(S3.19)}$

$SCL=10$ $\qquad\qquad\qquad N_{blob}^{theo}(\infty) = 17.322\times Ln(\rho - 0.1) + 46.193 \qquad \text{(S3.20)}$

The $N_\text{blob}^\text{theo}$-$vs$-$\rho$ relationship had to be corrected for the inner tiers, where the side chains were not dispersed homogeneously in the tier volume, but rather constituted a cluster with a finite number of helical side chains. At this point, edge effects were accounted for by multiplying $N_\text{blob}^\text{theo}(\infty)$ by the reduction factors listed in Table S3.12.
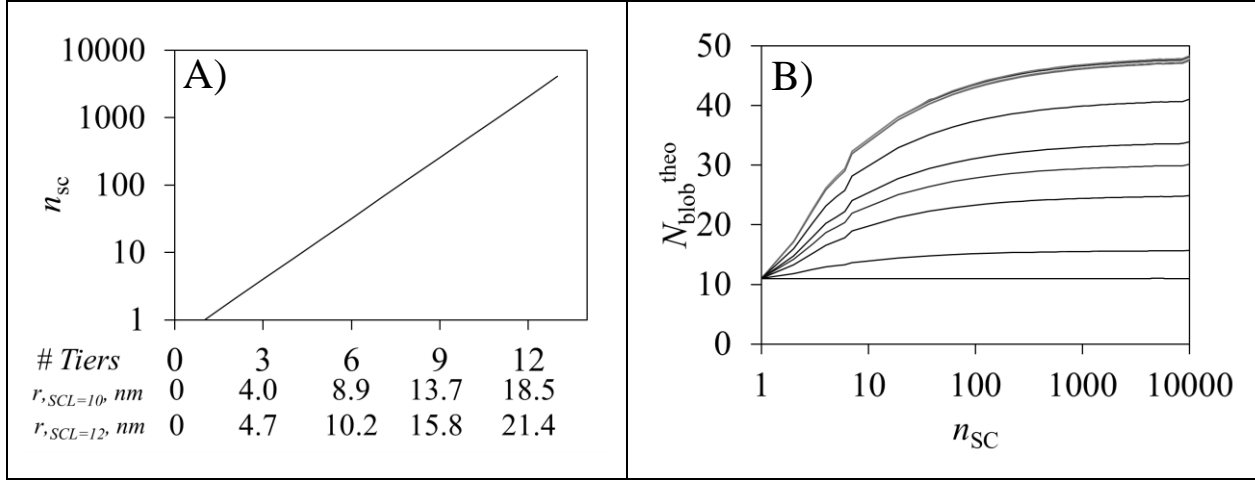

Figure S3.9. Plots of A) the number of side chains of glycogen as a function of r and B) $N_\text{blob}^\text{theo}$ for clusters comprised the different number of infinitely long helices at $d_\text{h-h}$ of 3.6, 3.4, 3.2, 3.0, 2.8, 2.6, 2.4, 2.2, 2.0, 1.8, and 1.6 nm from to bottom to top.

Table S3.12 Reduction factors that need to be applied to $N_\text{blob}^\text{theo}(\infty)$ to obtain $N_\text{blob}^\text{theo}$ for a cluster with a limited number of helices

| $d_\text{h-h}$, nm ($\rho_\text{dh-h}$, g/mL)	$N_\text{blob}^\text{theo}(\infty)$ (SCL=10)	$N_\text{blob}^\text{theo}(\infty)$ (SCL=12)	Reduction factor
3.2 nm (0.24 g/mL)	11.3	12.4	$6.43 \times 10^{-3} \times \ln(n_\text{sc,t})^3 - 0.015 \times \ln(n_\text{sc,t})^2 + 0.11 \times \ln(n_\text{sc,t}) + 0.69$
3.0 nm (0.27 g/mL)	13.9	15.4	$1.18 \times 10^{-3} \times \ln(n_\text{sc,t})^3 - 0.027 \times \ln(n_\text{sc,t})^2 + 0.21 \times \ln(n_\text{sc,t}) + 0.42$
2.8 nm (0.32 g/mL)	16.5	17.9	$1.41 \times 10^{-3} \times \ln(n_\text{sc,t})^3 - 0.032 \times \ln(n_\text{sc,t})^2 + 0.25 \times \ln(n_\text{sc,t}) + 0.30$
2.6 nm (0.37 g/mL)	20.9	22.2	$1.53 \times 10^{-3} \times \ln(n_\text{sc,t})^3 - 0.035 \times \ln(n_\text{sc,t})^2 + 0.27 \times \ln(n_\text{sc,t}) + 0.25$
2.4 nm (0.43 g/mL)	28.3	29.2	$1.60 \times 10^{-3} \times \ln(n_\text{sc,t})^3 - 0.036 \times \ln(n_\text{sc,t})^2 + 0.28 \times \ln(n_\text{sc,t}) + 0.21$
2.2 nm (0.51 g/mL)	31.3	32.2	$1.61 \times 10^{-3} \times \ln(n_\text{sc,t})^3 - 0.037 \times \ln(n_\text{sc,t})^2 + 0.29 \times \ln(n_\text{sc,t}) + 0.21$
2.0 nm (0.62 g/mL)	33.9	34.9	$1.60 \times 10^{-3} \times \ln(n_\text{sc,t})^3 - 0.036 \times \ln(n_\text{sc,t})^2 + 0.29 \times \ln(n_\text{sc,t}) + 0.21$
1.8 nm (0.76 g/mL)	37.3	38.2	$1.61 \times 10^{-3} \times \ln(n_\text{sc,t})^3 - 0.037 \times \ln(n_\text{sc,t})^2 + 0.29 \times \ln(n_\text{sc,t}) + 0.21$
1.6 nm (0.97 g/mL)	42.1	43.4	$1.63 \times 10^{-3} \times \ln(n_\text{sc,t})^3 - 0.037 \times \ln(n_\text{sc,t})^2 + 0.29 \times \ln(n_\text{sc,t}) + 0.21$

$N_\text{blob}^\text{theo}(r)$ of glycogen was plotted as a function of r or *# tiers* in Figure S3.10. The best agreement between $\langle N_\text{blob}^\text{theo}\rangle$ and $\langle N_\text{blob}^\text{exp}\rangle$ was observed when the $d_\text{h-h}$ equals 2.2 nm.
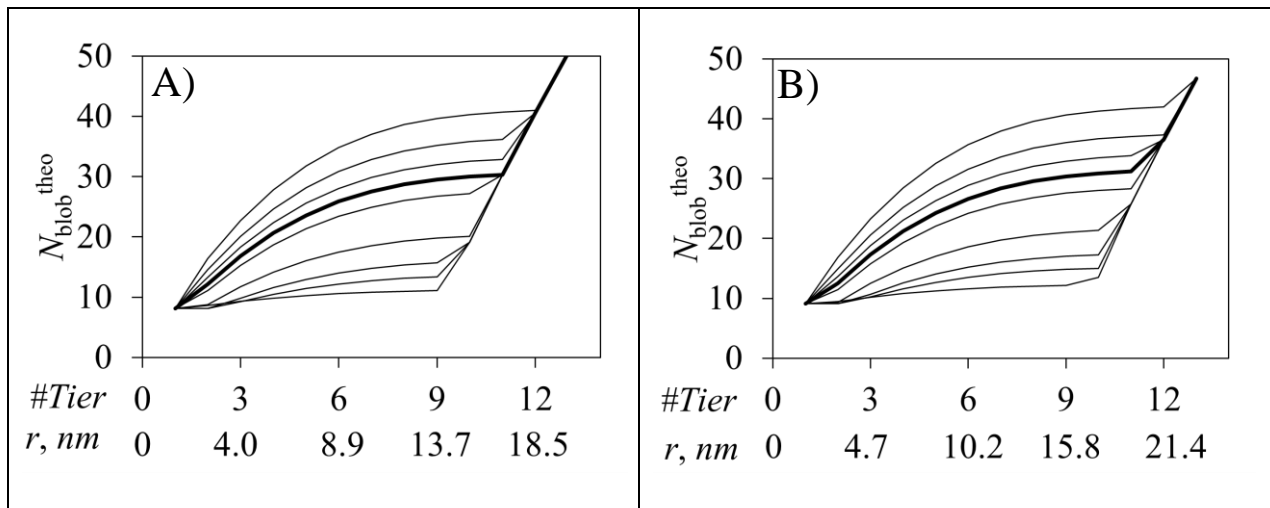
Figure S3.10. Plot of N_{blob}^{theo} of glycogen with A) SCL=10 AGUs and B) SCL=12 AGUs as a function of r when d_{h-h} equals 1.6, 1.8, 2.0, 2.2, 2.4, 2.6, 2.8, 3.0, 3.2, and 4.0 nm from top to bottom. The plot of N_{blob}^{theo} with $d_{h-h} = 2.2$ nm is represented with a bold line.

N] The effect of the parameters ρ_{max} and b on the density profile of glycogen according to the Gilbert model
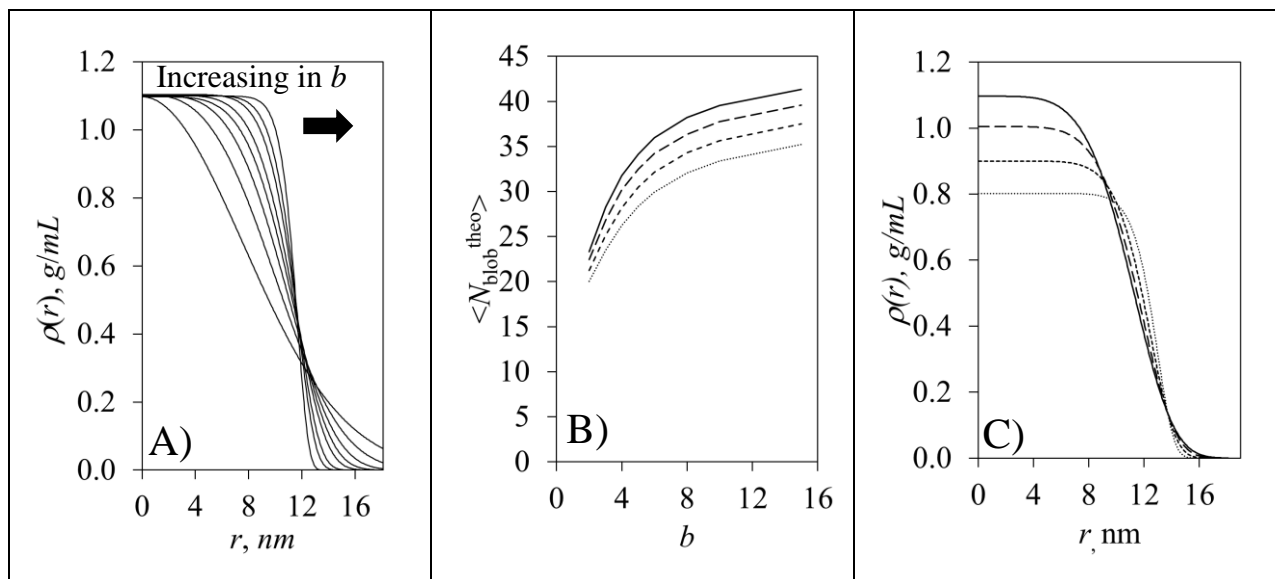
Figure S3.11. Plots of (A) $\rho(r) = 1.1 \times \exp(-ar^b)$ where the b value changes from 2 to 15, (B) $<N_{blob}^{theo}>$ of glycogen with SCL=10 AGUs as a function of b and (C) $\rho(r)$ where ρ_{max} is set to equal (_____) 1.1, (__ __) 1.0, (_ _ _) 0.9, and (...........) 0.8 g/mL.
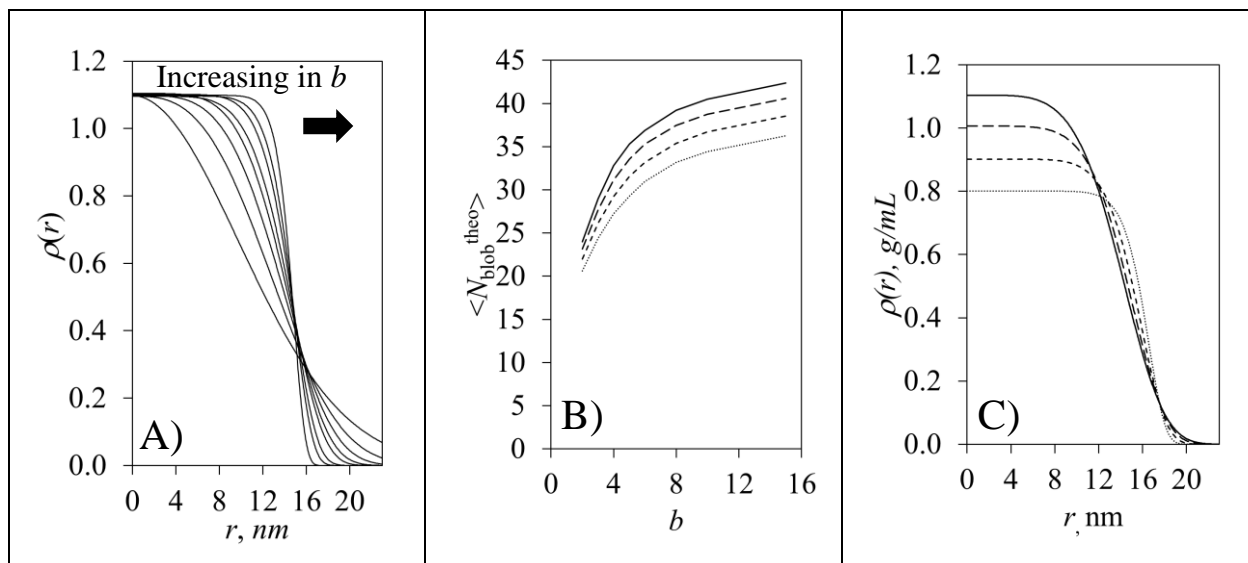
Figure S3.12. Plots of (A) $\rho(r) = 1.1 \times \exp(-ar^b)$ as a function of r. The b value change from 2 to 15, (B) $<N_{blob}^{theo}>$ for glycogen with SCL=12 AGUs as a function of b and (C) $\rho(r)$ as a function of r, where ρ_{max} equals (_____) 1.1 g/mL, (__ __) 1.0 g/mL, (_ _ _) 0.9 g.mL, and (..........) 0.8 g/mL.

S4- Appendices for Chapter 4

S4A] Equations used to fit the monomer and decays of $Py(x)$-Dextran and expressions of the molar fractions of the different pyrene species.

Equation S4.1 and S4.2 were used to globally fit the pyrene monomer and excimer fluorescence decays, respectively.

$$[Py^*]_{(t)} = [Py^*_{diff}]_{(t)} + [Py^*_{k2}]_{(t)} + [Py^*_{free}]_{(t)}$$

$$= [Py^*_{diff}]_o \exp\left(-\left(A_2 + \frac{1}{\tau_M}\right)t - A_3\left(1 - \exp(-A_4 t)\right)\right)$$

$$+ \left([Py^*_{k2}]_o + [Py^*_{diff}]_o e^{-A_3} \sum_{i=0}^{\infty} \frac{A_3^i}{i!} \frac{A_2 + iA_4}{A_2 + iA_4 - k_2}\right) \exp\left(-\left(k_2 + \frac{1}{\tau_M}\right)t\right)$$

$$-[Py^*_{diff}]_o e^{-A_3} \sum_{i=0}^{\infty} \frac{A_3^i}{i!} \frac{A_2 + iA_4}{A_2 + iA_4 - k_2} \exp\left(-\left(A_2 + iA_4 + \frac{1}{\tau_M}\right)t\right) + [Py^*_{free}]_o \exp(-t/\tau_M)$$

$$(S4.1)$$

$$[E^*]_{(t)} = [E0^*]_{(t)} + [ES^*]_{(t)}$$

$$= k_2 \left([Py_{k2}^*]_o + [Py_{diff}^*]_o e^{-A_3} \sum_{i=0}^{\infty} \frac{A_3^i}{i!} \frac{A_2 + iA_4}{A_2 + iA_4 - k_2} \right) \times \frac{\exp\left(-\dfrac{t}{\tau_{E0}}\right) - \exp\left(-\left(k_2 + \dfrac{1}{\tau_M}\right)t\right)}{k_2 + \dfrac{1}{\tau_M} - \dfrac{1}{\tau_{E0}}}$$

$$+ [Py_{diff}^*]_o e^{-A_3} \sum_{i=0}^{\infty} \frac{A_3^i}{i!} \frac{A_2 + iA_4}{A_2 + iA_4 - k_2} \frac{\exp\left(-\left(A_2 + iA_4 + \dfrac{1}{\tau_M}\right)t\right) - \exp\left(-\dfrac{t}{\tau_{E0}}\right)}{A_2 + iA_4 + \dfrac{1}{\tau_M} - \dfrac{1}{\tau_{E0}}}$$

$$+ [E0^*]_o \exp\left(-\frac{t}{\tau_{E0}}\right) + [ES^*]_o \exp\left(-\frac{t}{\tau_{ES}}\right) \tag{S4.2}$$

The equations for the parameters A_2, A_3, and A_4 used in Equations S4.1 and S4.2 are shown in Equations S3a-c, where $<n>$ represents the average number of ground-state pyrenes present in a *blob*, k_{blob} is the rate constant describing the diffusive motions of two AGUs bearing one excited and one ground-state pyrenyl labels, k_e is the rate constant of ground-state pyrenes exchanging between *blobs*, and [*blob*] represents the local concentration of *blobs* inside a macromolecule.

$$A_2 = <n> \times \frac{k_{blob} k_e [blob]}{k_{blob} + k_e [blob]} \tag{S4.3a}$$

$$A_3 = <n> \times \left(\frac{k_{blob}}{k_{blob} + k_e [blob]} \right)^2 \tag{S4.3b}$$

$$A_4 = k_{blob} + k_e \times [blob] \tag{S4.3c}$$

The decays were analyzed with the FBM twice. The first FBM analysis of the fluorescence decays allowed the parameter k_2 to float, where k_2 is the rate constant for two pyrene molecules, that are close to each other, to undergo rapid rearrangement and form an excimer. The k_2 values of the Py-Dextran samples were averaged and the fluorescence decays were re-fitted with the average k_2 value fixed in the FBM analysis.

The pre-exponential factors in Equations S4.1 and S4.2 yielded the molar fractions of the different pyrene species, that contributed to the monomer and excimer fluorescence decays, respectively.

The molar fractions of each species, f_{Mdiff}, f_{Mfree}, f_{Mk2}, f_{Ediff}, f_{Ek2}, f_{EE0}, and f_{EES} are expressed in Equation S4.4-S4.10. All parameters have been defined in the main text, with the subscripts M and E referring to parameters, that were obtained from the monomer and excimer decays, respectively.

$$f_{Mdiff} = \frac{[Py_{diff}^*]_o}{[Py_{diff}^*]_o + [Py_{k2}^*]_o + [Py_{free}^*]_o} \tag{S4.4}$$

$$f_{Mfree} = \frac{[Py_{free}^*]_o}{[Py_{diff}^*]_o + [Py_{k2}^*]_o + [Py_{free}^*]_o} \tag{S4.5}$$

$$f_{Mk2} = \frac{[Py_{k2}^*]_o}{[Py_{diff}^*]_o + [Py_{k2}^*]_o + [Py_{free}^*]_o} \tag{S4.6}$$

$$f_{Ediff} = \frac{[Py_{diff}^*]_o}{[Py_{diff}^*]_o + [Py_{k2}^*]_o + [E0^*]_o + [ES^*]_o} \tag{S4.7}$$

$$f_{Ek2} = \frac{[Py_{k2}^*]_o}{[Py_{diff}^*]_o + [Py_{k2}^*]_o + [E0^*]_o + [ES^*]_o} \tag{S4.8}$$

$$f_{EE0} = \frac{[E0^*]_o}{[Py_{diff}^*]_o + [Py_{k2}^*]_o + [E0^*]_o + [ES^*]_o} \tag{S4.9}$$

$$f_{EES} = \frac{[ES^*]_o}{[Py_{diff}^*]_o + [Py_{k2}^*]_o + [E0^*]_o + [ES^*]_o} \tag{S4.10}$$

The molar fraction of f_{diff}, f_{free}, f_{k2}, and f_{E0} representing all the pyrene species in solutions of the Py-PSs were determined by applying Equations S4.11- S4.14. f_{EES} was omitted in the calculation of the molar fractions as the short-lived pyrene ES^* species has never been found to interfere with the contributions from all other much longer-lived pyrene species.

$$f_{diff} = \frac{1}{1 + (f_{Mk2} / f_{Mdiff}) + (f_{Mfree} / f_{Mdiff}) + (f_{EE0} / f_{Ediff})} \tag{S4.11}$$

$$f_{k2} = f_{diff}\,\frac{f_{Mk2}}{f_{Mdiff}} \qquad (S4.12)$$

$$f_{free} = f_{diff}\,\frac{f_{Mfree}}{f_{Mdiff}} \qquad (S4.13)$$

$$f_{E0} = f_{diff}\,\frac{f_{EE0}}{f_{Ediff}} \qquad (S4.14)$$

S4B] Examples of the fits of decays of Py-Dextran analyzed with the FBM.
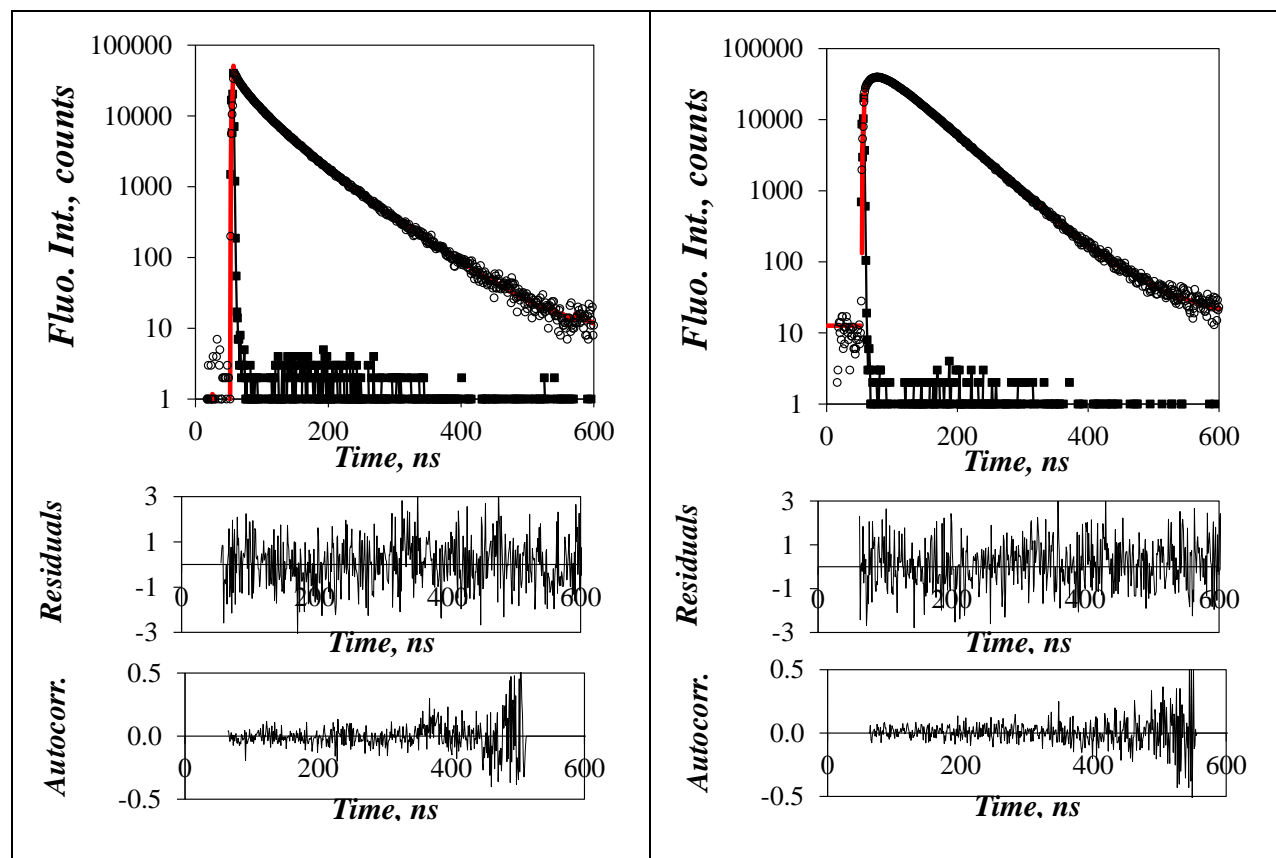
Figure S4.1. Global FBM analysis of the fluorescence decays of the pyrene monomer (left) and excimer (right) for Py-Dextran labeled with 15.6 mol% of 1-pyrenebutyric acid ($\chi^2 = 1.16$) in DMSO.

S4C] Emission spectra of Py-Dextran samples in ethylene glycol

Figure S4.2. Fluorescence spectra of Py(x)-Dextran in DMSO with x ranging from 1.7 (bottom) to 15.6 mol % (top).

S4D] Parameters retrieved from the FBM analysis of the Py-Dextran samples

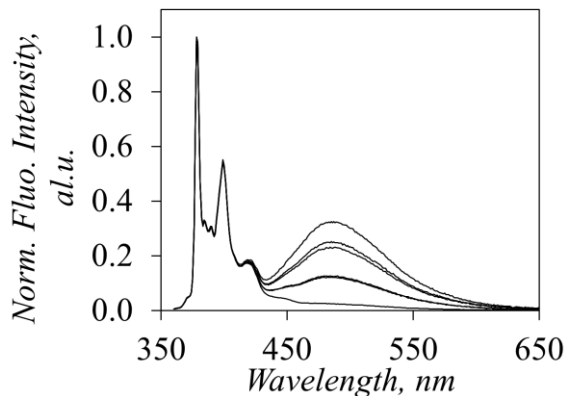**Table S4.1**. Parameters retrieved from the FBM analysis of the monomer decays of the Py-Dextran samples in DMSO and ethylene glycol.

Solvent	x	f_{Mdiff}	f_{Mfree}	k_{blob} $(\times 10^7 s^{-1})$	$<n>$	f_{k2}	$k_e[blob]$ $(\times 10^6 s^{-1})$	χ^2
DMSO τ_M= 87.7 ns k_2=1.5 $\times 10^8$ s^{-1}	7.8	0.680	0.164	1.242	0.839	0.156	7.92	1.25
	8.0	0.674	0.160	1.272	0.855	0.166	7.77	1.16
	12.2	0.698	0.084	1.359	1.202	0.218	9.04	1.20
	12.8	0.692	0.074	1.230	1.324	0.234	8.29	1.11
	15.6	0.698	0.056	1.374	1.414	0.246	9.19	1.16
Ethylene Glycol τ_M= 163.5 ns k_2=0.8 $\times 10^8$ s^{-1}	7.8	0.557	0.308	0.721	0.863	0.135	4.09	1.04
	8.0	0.579	0.262	0.728	0.826	0.158	3.86	1.02
	12.2	0.631	0.129	0.677	1.152	0.239	3.51	1.02
	12.8	0.614	0.136	0.821	1.101	0.250	4.99	1.18
	15.6	0.602	0.093	0.672	1.413	0.305	3.95	1.11

Table S4.2. Parameters retrieved from the FBM analysis of the excimer decays of $Py(x)$-Dextran in DMSO and ethylene glycol.

| Solvent	x	τ_{E0} (ns)	τ_{EL} (ns)	$f_{Ediff, E0}$	$f_{Ediff, D}$	f_{Ek2}	$f_{EE0, E0}$	$f_{EE0, D}$	$*f_{ES}$	χ^2
DMSO τ_M= 87.7 ns τ_{ES}= 3.5 ns k_2=1.5 ×10^8 s^{-1}	7.8	44.76		0.678		0.156	0.045		0.122	1.25
	8.0	45.04		0.672		0.165	0.039		0.123	1.16
	12.2	43.31		0.616		0.192	0.077		0.114	1.20
	12.8	43.16		0.618		0.209	0.073		0.099	1.11
	15.6	42.63		0.605		0.213	0.105		0.078	1.16
Ethylene Glycol τ_M= 163.5 ns τ_{ES}= 3.5 ns k_2=0.8 ×10^8 s^{-1}	7.8	47.54	88.65	0.110	0.520	0.153	0.171	0.000	0.045	1.04
	8.0	46.41	81.38	0.143	0.470	0.168	0.148	0.002	0.068	1.02
	12.2	48.18	75.46	0.101	0.432	0.205	0.209	0.000	0.047	1.02
	12.8	38.65	56.31	0.457	0.074	0.216	0.199	0.002	0.052	1.18
	15.6	50.00	91.63	0.018	0.436	0.230	0.213	0.076	0.028	1.11

* f_{ES} was not used to determine the molar fractions of the different pyrenyl species.

Table S4.3. Molar fractions of the pyrene species of $Py(x)$-Dextran calculated from f_{diff}, f_{free}, f_{Mk2}, and f_{EE0}.

Solvent	x	f_{diff}	f_{k2}	f_{free}	f_{E0}
DMSO k_2=1.5 ×10^8 s^{-1}	7.8	0.650	0.150	0.157	0.043
	8.0	0.649	0.160	0.154	0.038
	12.2	0.642	0.200	0.077	0.080
	12.8	0.639	0.216	0.069	0.076
	15.6	0.623	0.219	0.050	0.108
Ethylene Glycol k_2=0.8 ×10^8 s^{-1}	7.8	0.483	0.117	0.268	0.131
	8.0	0.507	0.139	0.230	0.124
	12.2	0.507	0.192	0.104	0.196
	12.8	0.498	0.203	0.110	0.189
	15.6	0.435	0.220	0.067	0.277

S5- Appendices for Chapter 5

S5A] Analysis of the molecular weight distribution of the pullulan sample in DMSO by gel

permeation chromatograph
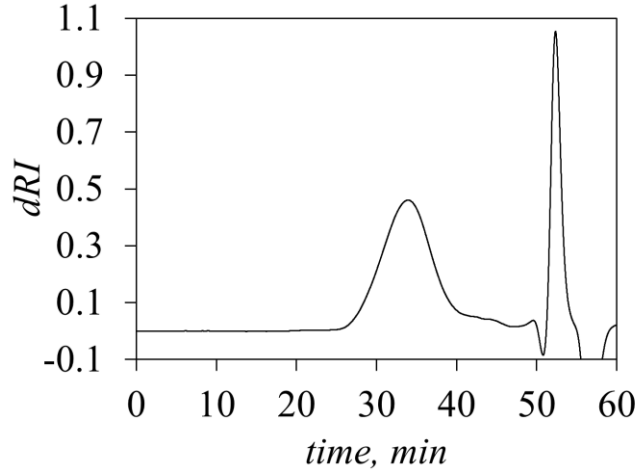
Figure S5.1. Plot of the differential refractive index of pullulan obtained by GPC in DMSO. The

peaks after 50 min elution time represent the solvent.

S5B] Equations used to fit the monomer and excimer fluorescence decays and equations used for
the molar fractions of the different pyrene species.

The monomer decays were fitted with Equation S1.

$$[Py^*]_{(t)} = [Py^*_{diff}]_{(t)} + [Py^*_{k2}]_{(t)} + [Py^*_{free}]_{(t)}$$

$$= [Py^*_{diff}]_0 \exp\left(-\left(A_2 + \frac{1}{\tau_M}\right)t - A_3\left(1 - \exp(-A_4 t)\right)\right)$$

$$+ \left([Py^*_{k2}]_o + [Py^*_{diff}]_o e^{-A_3} \sum_{i=0}^{\infty} \frac{A_3^i}{i!} \frac{A_2 + iA_4}{A_2 + iA_4 - k_2}\right) \exp\left(-\left(k_2 + \frac{1}{\tau_M}\right)t\right)$$

$$- [Py^*_{diff}]_o e^{-A_3} \sum_{i=0}^{\infty} \frac{A_3^i}{i!} \frac{A_2 + iA_4}{A_2 + iA_4 - k_2} \exp\left(-\left(A_2 + iA_4 + \frac{1}{\tau_M}\right)t\right) + [Py^*_{free}]_o \exp(-t/\tau_M)$$

$$(S5.1)$$

The excimer decays were fitted with Equation S5.2.

261

$$[E^*]_{(t)} = [E0^*]_{(t)} + [ES^*]_{(t)}$$

$$= k_2 \left([Py_{k2}^*]_o + [Py_{diff}^*]_o e^{-A_3} \sum_{i=0}^{\infty} \frac{A_3^i}{i!} \frac{A_2 + iA_4}{A_2 + iA_4 - k_2} \right) \times \frac{\exp\left(-\dfrac{t}{\tau_{E0}}\right) - \exp\left(-\left(k_2 + \dfrac{1}{\tau_M}\right)t\right)}{k_2 + \dfrac{1}{\tau_M} - \dfrac{1}{\tau_{E0}}}$$

$$+ [Py_{diff}^*]_o e^{-A_3} \sum_{i=0}^{\infty} \frac{A_3^i}{i!} \frac{A_2 + iA_4}{A_2 + iA_4 - k_2} \frac{\exp\left(-\left(A_2 + iA_4 + \dfrac{1}{\tau_M}\right)t\right) - \exp\left(-\dfrac{t}{\tau_{E0}}\right)}{A_2 + iA_4 + \dfrac{1}{\tau_M} - \dfrac{1}{\tau_{E0}}}$$

$$+ [E0^*]_o \exp\left(-\frac{t}{\tau_{E0}}\right) + [ES^*]_o \exp\left(-\frac{t}{\tau_{ES}}\right) \tag{S5.2}$$

The parameters A_2, A_3, and A_4 used in Equation S5.1 and S5.2 are expressed as a function of $<n>$, k_{blob}, and the product $k_e \times [blob]$ in Equations S3a-c.

$$A_2 = <n> \times \frac{k_{blob} k_e [blob]}{k_{blob} + k_e [blob]} \tag{S5.3a}$$

$$A_3 = <n> \times \left(\frac{k_{blob}}{k_{blob} + k_e [blob]} \right)^2 \tag{S5.3b}$$

$$A_4 = k_{blob} + k_e \times [blob] \tag{S5.3c}$$

In Equations S5.3a-c, $<n>$ is the average number of ground-state pyrene present in a *blob*, k_{blob} and k_e represent the rate constant of excimer formation between an excited and a ground-state pyrene and the exchange of ground-state pyrenes between *blobs*, respectively, and the local concentration of *blobs* in a macromolecule is represented by $[blob]$.

The Fluorescence Blob Model (FBM) was applied to analyze the fluorescence decays of a series of pyrene labeled pullulan samples (Py-Pullulan) by allowing the rate constant k_2, which describes the rapid rearrangement of pyrene groups toward PEF, to float. The k_2 value was then averaged over all Py-Pullulan samples and fixed in the FBM analysis. This procedure has been found to reduce substantially the errors on all other parameters.

The pre-exponential factors obtained from Equations S5.1 and S5.2 were used to determine the molar fractions of each pyrene species to the monomer and excimer fluorescence decays, respectively. The molar fractions f_{Mdiff}, f_{Mfree}, f_{Mk2}, f_{Ediff}, f_{Ek2}, f_{EE0}, and f_{EES} of each pyrene species defined in the main text are expressed in Equations S4-S10. The subscript, M and E, represent the monomer and excimer, respectively.

$$f_{Mdiff} = \frac{[Py^*_{diff}]_o}{[Py^*_{diff}]_o + [Py^*_{k2}]_o + [Py^*_{free}]_o} \tag{S5.4}$$

$$f_{Mfree} = \frac{[Py^*_{free}]_o}{[Py^*_{diff}]_o + [Py^*_{k2}]_o + [Py^*_{free}]_o} \tag{S5.5}$$

$$f_{Mk2} = \frac{[Py^*_{k2}]_o}{[Py^*_{diff}]_o + [Py^*_{k2}]_o + [Py^*_{free}]_o} \tag{S5.6}$$

$$f_{Ediff} = \frac{[Py^*_{diff}]_o}{[Py^*_{diff}]_o + [Py^*_{k2}]_o + [E0^*]_o + [ES^*]_o} \tag{S5.7}$$

$$f_{Ek2} = \frac{[Py^*_{k2}]_o}{[Py^*_{diff}]_o + [Py^*_{k2}]_o + [E0^*]_o + [ES^*]_o} \tag{S5.8}$$

$$f_{EE0} = \frac{[E0^*]_o}{[Py^*_{diff}]_o + [Py^*_{k2}]_o + [E0^*]_o + [ES^*]_o} \tag{S5.9}$$

$$f_{EES} = \frac{[ES^*]_o}{[Py^*_{diff}]_o + [Py^*_{k2}]_o + [E0^*]_o + [ES^*]_o} \tag{S5.10}$$

The overall contributions of each pyrene species in a solution were calculated from Equations S5.4-S5.9. Since the species ES^* is much shorter-lived than all the other species, f_{EES} was not accounted for to determine the molar fractions f_{diff}, f_{free}, f_{k2}, and f_{EE0} of the different pyrene species, whose expressions are given in Equations S11-S14.
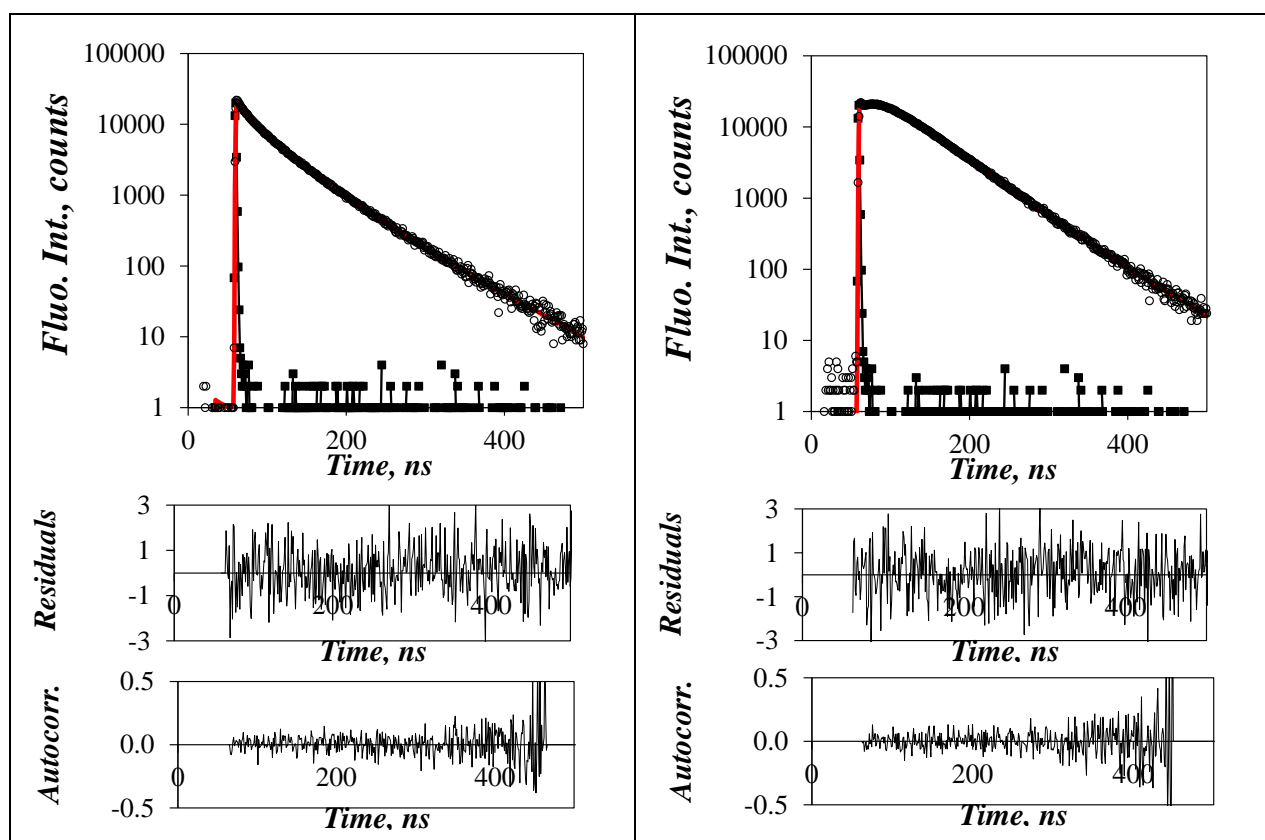
$$f_{diff} = \frac{1}{1 + (f_{Mk2} / f_{Mdiff}) + (f_{Mfree} / f_{Mdiff}) + (f_{EE0} / f_{Ediff})} \tag{S5.11}$$

$$f_{k2} = f_{diff} \frac{f_{Mk2}}{f_{Mdiff}} \tag{S5.12}$$

$$f_{free} = f_{diff} \frac{f_{Mfree}}{f_{Mdiff}} \qquad (S5.13)$$

$$f_{E0} = f_{diff} \frac{f_{EE0}}{f_{Ediff}} \qquad (S5.14)$$

S5C] Example of the fit of the monomer and excimer fluorescence decays analyzed according to the FBM.

Figure S5.2. Fit of the fluorescence decays of the pyrene monomer (left, $\lambda_{em} = 375$ nm) and excimer (right, $\lambda_{em} = 510$ nm) for Py-Pullulan labeled with 13.8 mol% of 1-pyrenebutyric acid ($\chi^2 = 1.18$) in DMSO. $\lambda_{ex} = 346$ nm.

S5D] Parameters retrieved from the FBM analysis for the Py-Pullulan samples.

Table S5.1. Parameters retrieved from the FBM analysis of the monomer decays of the Py-Pullulan samples in DMSO. k_2 was fixed to equal 1.1×10^8 s^{-1}.

χ_{py}	f_{Mdiff}	f_{Mfree}	k_{blob} $(\times 10^7 s^{-1})$	$<n>$	f_{k2}	$k_e[blob]$ $(\times 10^6 s^{-1})$	χ^2
2.50	0.667	0.249	1.679	0.267	0.084	7.56	1.18
4.02	0.746	0.129	1.118	0.490	0.126	7.58	1.14
4.77	0.744	0.117	1.017	0.592	0.139	7.59	1.13
6.59	0.765	0.066	1.283	0.710	0.170	8.15	1.10
9.27	0.754	0.028	1.324	0.961	0.218	8.08	1.02
9.41	0.717	0.024	1.144	1.219	0.259	7.66	1.15
10.31	0.716	0.036	1.049	1.207	0.248	7.53	1.03
13.08	0.697	0.011	1.182	1.468	0.291	7.96	1.18

Table S5.2. Parameters retrieved from the FBM analysis of the excimer decays of the Py-Pullulan samples in DMSO. k_2 was fixed to equal 1.1×10^8 s^{-1}.

χ_{py}	τ_E (ns)	f_{Ediff}	f_{Ek2}	f_{EE0}	f_{ES}	χ^2
2.50	54.04	0.581	0.073	0.045	0.301	1.18
4.02	46.76	0.587	0.099	0.037	0.276	1.14
4.77	44.50	0.775	0.145	0.025	0.055	1.13
6.59	45.61	0.681	0.151	0.067	0.100	1.10
9.27	44.39	0.709	0.205	0.085	0.000	1.02
9.41	43.34	0.662	0.239	0.085	0.014	1.15
10.31	44.59	0.502	0.174	0.091	0.233	1.03
13.08	44.07	0.458	0.191	0.148	0.203	1.18

Table S5.3. All molar fractions of pyrene species for the Py-Pullulan samples in DMSO calculated from f_{diff}, f_{free}, f_{k2}, and f_{EE0}. k_2 was fixed to equal 1.1×10^8 s^{-1}.

χ_{py}	f_{diff}	f_{k2}	f_{free}	f_{E0}
2.50	0.634	0.080	0.236	0.049
4.02	0.712	0.120	0.123	0.045
4.77	0.726	0.136	0.115	0.024
6.59	0.711	0.158	0.061	0.070
9.27	0.691	0.200	0.026	0.083
9.41	0.656	0.237	0.022	0.084
10.31	0.633	0.219	0.032	0.115
13.08	0.569	0.238	0.009	0.184